



UNIVERSITY OF CAPE TOWN

CENTRE FOR CATALYSIS RESEARCH

Alumina-modified cobalt catalysts for the
Fischer-Tropsch synthesis

by

Anna P. Petersen

Thesis presented to the University of Cape Town in the fulfilment of the
requirements for the degree of

DOCTOR OF PHILOSOPHY

July 11, 2018

CATALYSIS INSTITUTE
DEPARTMENT OF CHEMICAL ENGINEERING

The copyright of this thesis vests in the author. No quotation from it or information derived from it is to be published without full acknowledgement of the source. The thesis is to be used for private study or non-commercial research purposes only.

Published by the University of Cape Town (UCT) in terms of the non-exclusive license granted to UCT by the author.

*"Daß ich erkenne, was die Welt
Im Innersten zusammenhält"*
Faust, Johann Wolfgang von Goethe

*"That I may know what the world contains
In its innermost heart and finer veins"*

Declaration

I, Anna Paula Petersen, hereby declare that the work on which this thesis is based is my original work (except where acknowledgements indicate otherwise) and that neither the whole work nor any part of it has been, is being, or is to be submitted for another degree in this or any other university. I authorise the University to reproduce for the purpose of research either the whole or any portion of the contents in any manner whatsoever.

Signature:

July 11, 2018

Signed by candidate

Acknowledgements

Gratitude goes towards my supervisor Eric van Steen and co-supervisor Michael Claeys. I consider myself blessed to have been under the guidance of people with such profound knowledge and passion for science. I am especially indebted to Eric, for the generous way in which he lends his time and patience to all of his students, for the countless versions of this thesis he proofread, for his continuous encouragement, for the many, many challenging discussions we had, and foremost, for always having an open door, through which one may enter in despair but shall leave with new found inspiration.

I also want to thank the many scientists, colleagues and students, in and outside of the University of Cape Town, who accompanied and supported me along the way. My special gratitude goes to Roy Forbes, for sharing his immense knowledge about X-ray diffraction and spectroscopy with me, and for his invaluable support with the Synchrotron experiments. I am very grateful for all the support staff at the Synchrotron Light Laboratory in Campinas, Brazil, especially Santiago Figueroa and Anna Paula da Silva Sotero Levinsky, and to Roy and Sandeeran Govender for the long shifts and support they provided during that time. Thanks to Patricia Kooyman, for her help with TEM and EDS experiments, and her unequivocal eye for detail. Thanks to the support staff of the Analytical Laboratory, Zulfa Le Riche and Stephanie Hauslaib, and the Electron Microscopy Unit, especially Mohammed Jaffer.

I want to gratefully acknowledge the funding from the DST-NRF centre for excellence in catalysis (C*change), without which this work would not have been possible, as well as the Catalysis Society of South Africa (CATSA) for their financial support towards attending an international conference.

Last but not least, I want to acknowledge the unconditional support of my family and friends. To my mother: Mãe, não existem palavras suficientes no mundo para te dizer quanto eu te agradeço para tudo o teu amor, para sempre me suportar e para sempre acreditar em mim. Eu não seria a pessoa que eu estou hoje sem uma mulher como você para me mostrar o caminho.

I am especially grateful to Tracey, Thobani, Doreen, Chelsea, Colleen, Moritz, Nico, Hennie, Stefano, my coffee mates Stephen, JV, Rein and Niels, Cobus, Waldo, Gideon, Rachel and Chantal to name just a few, for their support and advice, for listening to all my stories of failure and success, and for making this experience so memorable. I will miss working with you, and I wish you all the best for your future endeavours.

I also want to express my gratitude to Shaun. Thank you for always listening and pretending so well to be interested in my work, for keeping my head free when I needed it most, and for being by my side through all of this.

Synopsis

In the Fischer-Tropsch process, valuable hydrocarbons are produced using the basic starting materials hydrogen and carbon monoxide, which can be derived from alternative carbon sources such as coal, gas or biomass. Although this process has been studied for almost a century, the effects of the support material on activity, selectivity and stability of the catalyst remain obscure.

This study aims to gain fundamental insights into the effect of metal-support interactions in cobalt alumina based Fischer-Tropsch catalysts. To accomplish this, the effects of metal-support interactions have to be isolated from possible convoluting effects of the metal crystallite size and support porosity. This is achieved by preparing inverse-model catalysts, in which the support is deposited onto the metal, in contrast to conventional supported catalysts, in which the metal phase is deposited onto a porous support.

Cobalt alumina inverse-model catalysts were prepared by incipient wetness impregnation of cobalt oxide with aluminium sec-butoxide. The alumina loading was varied systematically between 0 and 2.5 wt% Al. The catalysts were characterised by X-ray diffraction (XRD), Transmission electron microscopy (TEM), H₂ chemisorption, and X-ray absorption near edge spectroscopy (XANES). The catalyst reducibility was studied by temperature-programmed reduction (TPR), *in situ* XRD and *in situ* XANES experiments. The catalytic performance for the Fischer-Tropsch synthesis was studied in a slurry reactor under industrially relevant conditions.

The alumina modification was found to prevent sintering and decrease the reducibility of the catalysts. With increasing alumina loading, and increasing calcination temperature, reduction peaks shifted to higher temperatures and peaks with maxima above 400 °C appeared in the TPR. The kinetic evaluation showed that the decreased reducibility was due to a decrease in the pre-exponential factor, which suggests that the alumina modification hindered hydrogen activation and/or nucleation of reduced cobalt phases.

The activity of the catalysts for the FT reaction was found to increase with increasing alumina loading. This was likely an effect of the increase in metal dispersion upon alumina modification. Furthermore, alumina-modified catalysts had a higher C₅₊ and olefin selectivity, and lower methane selectivity.

Pyridine-TPD experiments showed that the alumina modification introduced Lewis acid

sites to the cobalt catalysts. Lewis acid sites may interact with adsorbed CO thereby weakening the C–O bond and facilitating CO dissociation. This was supported by CO-TPR experiments, which revealed that alumina-modified catalysts had an increased activity for the surface catalysed Boudouard reaction. It is concluded that the alumina modification increased the rate of CO dissociation on metallic cobalt. An increased rate of CO dissociation may lead to coverage of the metal surface with carbon thereby decreasing hydrogenation and shifting the product selectivity towards high molecular weight products. Hence, alumina may promote the selectivity of cobalt catalysts via a synergistic effect.

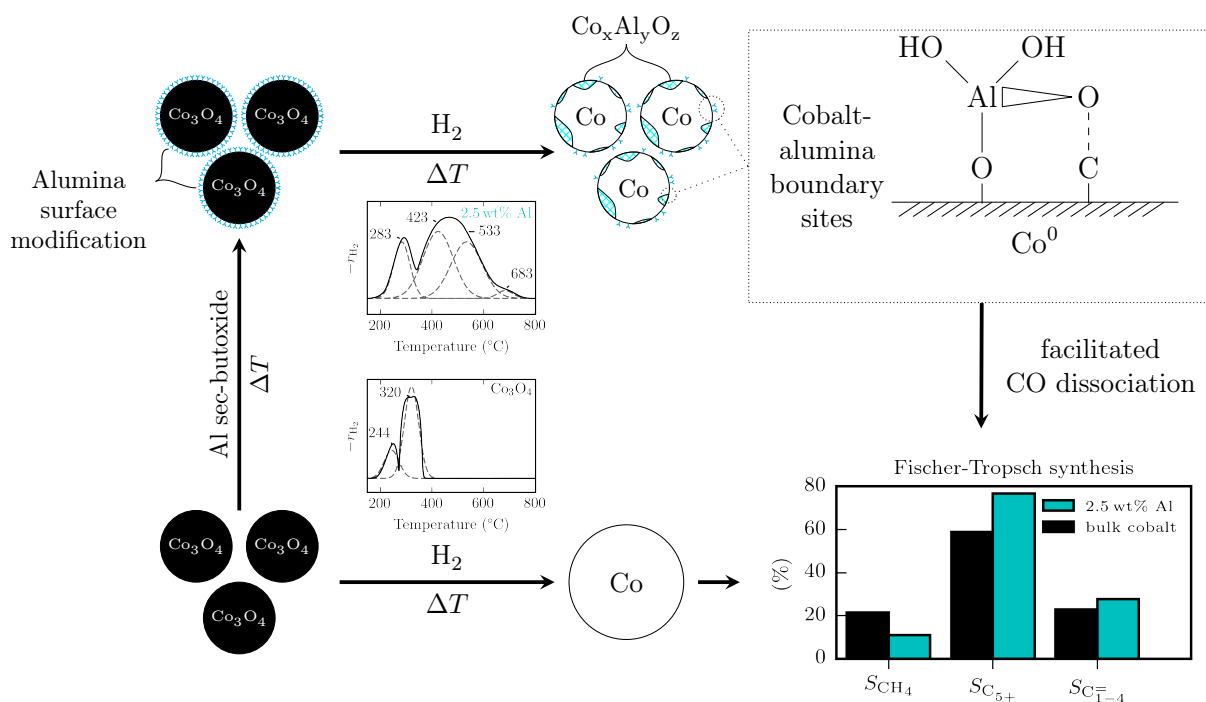


Figure 1: Schematic representation of the effect of alumina modification of cobalt.

Contents

List of Figures	iii
List of Tables	iv
Nomenclature	vi
1 Introduction	1
1.1 The Fischer-Tropsch synthesis	1
1.2 A historical perspective on the Fischer-Tropsch process	3
1.3 References	6
2 Literature Review	8
2.1 The catalyst support	8
2.2 Metal-support interactions	10
2.3 Investigating metal-support interactions	13
2.4 References	16
3 Scope and Objectives	20
4 Reducibility of alumina-modified cobalt oxide crystallites	23
4.1 Introduction	23
4.2 Literature Review - The reduction of metal oxides	25
4.2.1 Thermodynamics	25
4.2.2 Reaction mechanism and kinetics	26
4.2.3 Experimental procedure and evaluation	27
4.2.4 Reduction of bulk and supported cobalt oxides	33
4.3 Experimental	40
4.4 Results	46
4.4.1 Catalyst characterisation	46
4.4.2 Reduction experiments	53
4.5 Discussion	82
4.5.1 Crystallite size and morphology	82
4.5.2 Reducibility	83
4.6 Conclusions	90
4.7 References	93
5 Effect of alumina modification of cobalt on the Fischer-Tropsch synthesis	99
5.1 Introduction	99
5.2 Literature Review - The Fischer-Tropsch synthesis	101
5.2.1 The reaction mechanism	101

5.2.2	The product selectivity	103
5.2.3	The active phase and the intrinsic activity	106
5.2.4	Catalyst deactivation	107
5.2.5	The influence of alumina supports	108
5.3	Experimental	112
5.4	Results	122
5.4.1	Degree of reduction	122
5.4.2	Cobalt metal dispersion	125
5.4.3	Boudouard reaction	129
5.4.4	Catalyst acidity	133
5.4.5	Fischer-Tropsch synthesis	137
5.4.6	Spent catalyst characterisation	150
5.5	Discussion	155
5.5.1	Fischer-Tropsch activity	155
5.5.2	Catalyst deactivation	156
5.5.3	Fischer-Tropsch product selectivity	158
5.6	Conclusions	168
5.7	References	170
6	Concluding remarks	178
6.1	Summary and conclusions	178
6.2	Recommendations	181
6.3	References	183
A	Evaluation of TPR experiments	184
B	Effect of calcination temperature on metal dispersion	196
C	Determining degree of reduction	199
D	Conditions and GC-analysis of Fischer-Tropsch experiments	202
E	Curriculum Vitae - List of Publications	206

List of Figures

1	Graphical abstract	
4.1	Schematic representation of nucleation and contracting sphere reaction model	27
4.2	Demonstration of the effect of varying P value and $\beta/c_{0,H_2}$ ratio	30
4.3	Demonstration of the effect of the P value on a two-step reduction process	31
4.4	XRD of precipitated catalysts after drying and calcination	46
4.5	XRD of alumina-modified Co_3O_4 catalysts after calcination	48
4.6	XRD of aluminium sec-butoxide (ASB) after hydrolysis on air and calcination	49
4.7	TEM images of unmodified and alumina-modified catalysts	51
4.8	Bright-field STEM and EDS mapping of 2.5Al300	52
4.9	TPR of unmodified and alumina-modified Co_3O_4 catalysts calcined at 300 °C and 500 °C	54
4.10	Simulated TPR profile following first order kinetics fitted with a Gaussian function.	57
4.11	Results of peak deconvolution for TPR experiments conducted at 10 °C/min.	58
4.12	Computation of the TPR for the reduction of CoO to metallic cobalt	63
4.13	Computation of the reduction profile of Co_3O_4	66
4.14	Computation of the reduction profile of 0.0Al300	68
4.15	Computation of the reduction profile of 0.0Al500	69
4.16	Computation of the reduction profile of alumina-modified Co_3O_4	72
4.17	<i>In situ</i> XRD reduction pattern.	74
4.18	Crystal phase and crystallite size evolution during <i>in situ</i> XRD reduction.	76
4.19	XANES spectra of unmodified and alumina-modified Co_3O_4 catalysts calcined at 300 °C.	78
4.20	XANES of unmodified and alumina-modified Co_3O_4 reduced <i>in situ</i> in hydrogen.	79
4.21	Phase composition during <i>in situ</i> XANES reduction.	80
4.22	Reduction profile of unmodified Co_3O_4 calcined at 300 °C and 500 °C. . . .	85
4.23	Reduction curves (α vs. t)	86
5.1	Product distribution of the FT synthesis as described by the Anderson-Schulz-Flory distribution	104
5.2	Sample FID chromatogram	121
5.3	TPR experiments of catalysts after activation	123
5.4	H_2 -chemisorption experiments	126
5.5	CO-TPR experiments	131

5.6	TEM image of 0.5Al300 ex CO-TPR showing metal particles encapsulating in multiwall carbon nanotubes.	132
5.7	<i>In situ</i> XRD reduction experiments in CO atmosphere	133
5.8	Pyridine-TPD experiments	136
5.9	FT activity during start-up	137
5.10	Conversion and methane selectivity as a function of TOS	139
5.11	Arrhenius plot for FT reaction	142
5.12	FT product distribution as a function of reaction temperature.	145
5.13	Comparison of the FT product distribution of fresh and deactivated catalysts at a reaction temperature of 220 °C.	147
5.14	Product distribution as a function of alumina loading at a reaction temperature of 220 °C, 230 °C and 240 °C.	149
5.15	Chain growth probability (α_{4-7}) as a function of the reaction temperature.	150
5.16	XRD of spent catalysts	151
5.17	TEM images of spent catalysts	153
5.18	Bright-field STEM and EDS mapping of spent 2.5Al300	154
5.19	Product distribution for the fresh catalyst at a reaction temperature of 220 °C as a function of alumina loading.	160
5.20	Product distribution at a reaction temperature of 220 °C as a function of alumina loading determined at TOS \approx 250 h.	161
5.21	Schematic representation of the effects of alumina modification on the cobalt catalyst.	162
A.1	Reduction profiles as measured.	185
A.2	Peak deconvolution of TPR of catalyst 0.0Al300.	190
A.3	Peak deconvolution of TPR of catalyst 0.0Al500.	190
A.4	Peak deconvolution of TPR of catalyst 0.1Al300.	191
A.5	Peak deconvolution of TPR of catalyst 0.1Al500.	191
A.6	Peak deconvolution of TPR of catalyst 0.5Al300.	192
A.7	Peak deconvolution of TPR of catalyst 0.5Al500.	192
A.8	Peak deconvolution of TPR of catalyst 2.5Al300	193
A.9	Peak deconvolution of TPR of catalyst 2.5Al500.	193
A.10	Kissinger plot from TPR experiments.	194
A.11	Kissinger plot from TPR experiments (Peak deconvolution).	195
C.1	Oxygen titration experiments	201
D.1	Flow diagram of the slurry reactor	204

List of Tables

4.1	Co ₃ O ₄ crystallite size of catalysts after calcination.	49
4.2	Peak maxima and peak areas of TPR experiments conducted using a heating rate of 10 °C/min.	55
4.3	Kinetic evaluation of TPR profiles using the Kissinger equation after peak deconvolution.	61
5.1	Overview of reactions occurring in the FT synthesis	102
5.2	Influence of reaction conditions on product selectivity	105
5.3	Results of hydrogen chemisorption ($T_{\text{cal}} = 300\text{ °C}$)	128
5.4	FT activity at 220 °C	137
5.5	FT conditions, activity and methane selectivity.	140
A.1	Evaluation of reduction profiles measured by TPR.	186
A.2	Kinetic evaluation using Kissinger method from TPR profiles (no peak deconvolution).	187
A.3	Results of peak deconvolution for TPR of catalysts calcined at 300 °C . . .	188
A.4	Results of peak deconvolution for TPR of catalysts calcined at 500 °C . . .	189
B.1	Results of hydrogen chemisorption	197
B.2	Evaluation of hydrogen chemisorption experiments.	198
C.1	Degree of reduction determined from TPR experiments	199
D.1	Experimental conditions of GC-TCD analysis	203
D.2	Experimental conditions of GC-FID analysis	203
D.3	Overview of activity and selectivity for the FT synthesis	205

Nomenclature

Acronyms

ASB	Aluminium sec-butoxide
ASF	Anderson-Schulz-Flory (product distribution)
CSTR	Continuously stirred tank reactor
EDS	Energy-dispersive X-ray spectroscopy
FID	Flame ionisation detector
FT	Fischer-Tropsch
FWHM	Full width at half maximum
GC	Gas chromatograph
HRTEM	High resolution transmission electron microscopy
M ⁰	Metal
MO	Metal oxide
O/P	Olefin to paraffin ratio
RSS	Residual sum of squares
STEM	Scanning transmission electron microscopy
TCD	Thermal conductivity detector
TEM	Transmission electron microscopy
TGA	Thermogravimetric analysis
TPD	Temperature-programmed desorption
TPR	Temperature-programmed reduction
XANES	X-ray absorption near edge spectroscopy
XRD	X-ray diffraction

Greek Symbols

α	Conversion fraction	
α_{4-7}	Chain growth probability	
β	Heating rate	$^{\circ}\text{C}/\text{min}$

Roman Symbols

A	Arrhenius constant, pre-exponential factor	$\text{s}^{-1}, \text{min}^{-1}$
A_i	Peak area of species i in the chromatogram	
C_{5+}	Selectivity of carbohydrates with chain length $n \leq 5$	C%
c_i	Concentration of species i	
C_n	Fraction of FT product with a chain length of n carbon atoms	
$C_n^=$	Selectivity of linear olefins with chain length n	C%
C_n^Y	Selectivity of branched carbohydrates with chain length n	C%
$C_n^{1=}$	Selectivity of linear 1-olefins with chain length n	C%
$C_n^{2=}$	Selectivity of 2-olefins with chain length n	C%
C_n^{OH}	Selectivity of alcohols with chain length n	C%
C_n	Selectivity of linear carbohydrates with chain length n	C%
CTY	Cobalt time yield	s^{-1}
D	Metal dispersion	%
d	Crystallite size	nm
DOR	Degree of reduction	%
E_a	Activation energy	kJ/mol
F_i	Molar flow rate of species i	mol/s
G	Gibbs free energy	
K	Langmuir adsorption constant	
k	Rate constant	$\text{s}^{-1}, \text{min}^{-1}$
M	Molar mass	g/mol
m	Mass	g
n	Chain length of hydrocarbon, number of carbon atoms	

N_i	Number of moles of species i	
p	Pressure or partial pressure	bar
q	Reaction order	
R	Universal gas constant	J/mol/K
$-r_i$	Rate of disappearance of species i	
S	Amount of reducible species	
S_i	Selectivity of species i	C%, mol%
T	Temperature	°C, K
t	Time	s, min
TOF	Turn over frequency or site time yield	s^{-1}
w_i	Weight fraction of species i	
x	Molefraction	
y_i	Volume fraction of species i	

Subscripts

0	Initial
ad	Adsorbed
cal	Calcination
g	Gas phase
max	Maximum
Py	Pyridine

Chapter 1

Introduction

1.1 The Fischer-Tropsch synthesis

The Fischer-Tropsch (FT) synthesis is a surface catalysed polymerisation reaction of hydrogen and carbon monoxide to form higher hydrocarbons. The main FT products, besides water, are linear paraffins and 1-olefins, but branched hydrocarbons and oxygenated products are formed in smaller quantities as well. The large spectrum of compounds formed make the reaction versatile and the product selectivity may be adjusted to suit different needs. For example, a combination of FT and hydrocracking catalysts is being investigated in order to optimise the yield of middle-distillate products (diesel) [1], and Dow has been funding research focussed on achieving a high selectivity for short-chain olefins (FTO) [2, 3]. Maximising the yield of high molecular weight products can significantly improve the plant profitability [4, 5]. Hence, increasing the selectivity for high molecular weight products is a main focus of research in the FT synthesis.

The product yield and product selectivity are dependent on the reaction conditions, the metal catalyst and catalyst composition, as well as the choice of the reactor [6]. The most commonly used reactors for the FT synthesis are fixed-bed reactors and slurry reactors. Fixed-bed reactors are convenient for research purposes, as they can be scaled down easily, requiring only the use of small amounts of catalyst and are fairly simple to operate. However, fixed-bed reactors may exhibit hot spots and concurrently a change in partial pressures over the reactor bed [6]. Slurry reactors are commercially applied at Sasol, and therefore specifically relevant to research efforts in South Africa. Furthermore,

slurry reactors or continuous stirred tank reactors (CSTR) present a constant temperature throughout the reactor and perfect mixing of reactants and products, making them particularly suitable for kinetic studies [6]. In slurry reactors, a high temperature-resistant wax is used as reaction medium. The thermal stability of the hydrocarbons composing the wax imposes a temperature restriction of $\approx 300^\circ\text{C}$.

Iron and cobalt are the only metals which are commercially applied as catalysts, but nickel and ruthenium also show FT activity [7]. Nickel catalysts have a high activity but predominantly produce methane. The platinum group metals have a relatively low catalytic activity, except for ruthenium, which is active for the FT reaction and has a high selectivity for very high molecular weight products [8].

The FT synthesis is operated at pressures around 20 bar and temperatures between 200°C and 350°C . The selectivity for methane, which is an undesired product, increases sharply with an increase in reaction temperature when cobalt is used as a catalyst [9]. Therefore, cobalt-based FT synthesis is typically carried out at $220\text{--}240^\circ\text{C}$ (low-temperature FT), while iron-based FT synthesis is carried out at temperatures around 350°C (high-temperature FT). When liquid fuels are the desired products, metallic cobalt is the catalyst of choice, due to its high conversion rate, high selectivity for linear hydrocarbons and low selectivity for carbon dioxide [10].

Several catalyst promoters may be added to the catalyst to improve its performance. The first commercial catalyst applied consisted of a mixture of $\text{Co}:\text{ThO}_2:\text{Kieselguhr} = 100:18:100$ [8]. Catalyst promoters can be classified as structural promoters, selectivity promoters, and reduction promoters.

Reduction promoters increase the availability of the active metallic phase, which may increase the activity. For cobalt-based catalysts, noble metals such as gold or platinum are typically used as reduction promoters. They facilitate the reduction by increasing the rate of hydrogen dissociation [11]. For iron-based catalysts, copper can be used as a reduction promoter [12]. Whether reduction promoters play an active role during the FT synthesis is still a matter of debate [11].

Selectivity promoters are typically alkaline or rare-earth metals, added in small quantities to improve the selectivity for high molecular weight products or olefins. The mechanism of action of selectivity promoters is not entirely understood. The optimal concentration of

promoters in the catalyst is strongly dependent on the catalyst composition (e.g. type of support) and metal dispersion [13]. Often high promoter concentrations lead to catalyst deactivation possibly by blocking of active sites [14].

Structural promoters are catalyst supports; they aid in increasing metal catalyst dispersion as well as providing a homogeneous heat distribution and stability to attrition. The support is commonly a porous refractory oxide. Only titania, silica, zirconia and alumina have been used in commercial or pilot scale applications [15].

Cobalt-based catalysts are typically supported on alumina or other ceramic materials, and contain noble metal as reduction promoter. Iron-based catalysts are typically unsupported, bulk iron catalysts containing several chemical promoters such as potassium. Although the majority of heterogeneous catalysts are supported catalysts, there is no consensus on the effects of the support on the catalytic activity and selectivity [16].

1.2 A historical perspective on the Fischer-Tropsch process

The Fischer-Tropsch process was originally developed in Germany to produce synthetic fuel from coal. It was named after Franz Fischer and Hans Tropsch who were working at the Karl-Wilhelm Institute in Mühlheim and published their findings in 1926 [17]. The catalytic hydrogenation of carbon monoxide was actually discovered some 20 years earlier by the French scientists Paul Sabatier and Jean-Baptiste Senderens [18]. However, the French scientists were not exactly overlooked by history. Both of them are renowned chemists, and Paul Sabatier did even receive the Nobel Prize in 1912 for his work on catalytic hydrogenation [19]. Fischer and Tropsch were rightly credited for this discovery, as it was their research which led to the implementation of a large-scale synthetic fuel industry in Nazi-Germany, which brought the FT synthesis to its (in)famous reputation.

Germany is of particular historical relevance for the FT synthesis, not just as its birthplace, but as the first country that developed a synthetic fuel industry with 12 coal liquefaction and 9 FT plants producing 23 million barrels of synthetic fuel in the year 1944 [20]. Germany's plentiful coal reserves, but inaccessibility to petroleum drove the development

of the FT process to obtain liquid fuels during World War II. After the Potsdam Conference of 16 July 1945 the FT synthesis was considered war technology and synthetic fuel production in Germany was prohibited. Thereafter, most plants were dismantled. Apart from Germany, Britain, France and Japan synthesised liquid fuels from coal, and the United States had a significant research interest in FT process from the 1920s to the 1940s [8, 20].

After World War II, synthetic fuel became economically non-viable due to the low oil prices. Research and development ceased until the global energy crises of the 1970s and 1990s, in all countries except for South Africa. South Africa's desire for energy independence led to the development of their first FT plant in 1955 in Sasolburg, and two more in 1973 and 1976 in Secunda. Today, Germany produces no synthetic fuel anymore, and only eight FT plants are active worldwide, operated by Sasol in South Africa, Sasol/Chevron in Nigeria, Shell in Malaysia and Qatar and Synfuel China/Shenhua Group in China [21, 22].

At the moment any carbon-based fuel technology is suffering from an image problem. In much of the developed world, the public is pushing away from carbon-based fuels towards renewable energy sources. In Australia and the UK, even the implementation of plastic-to-fuel conversion plants, which convert (non-recyclable) plastic-waste into liquid fuel by pyrolysis encountered major protests [23]. They argue that any technology that produces petrol or diesel fuel acts as life support for an outdated carbon economy, and hinders the development of alternative, environmentally friendly and renewable energy and fuel sources. This sort of reasoning finds itself confirmed by the inability of technologically advanced countries, such as Germany and the United States, to stir away from coal. The reasons are mainly socio-political. Coal, despite posing substantial environmental problems, still offers employment, often in remote areas, where unemployment is typically high.

Throughout history the interest in FT has flared up and ceased several times, depending on the price of crude oil. In late 2013 the crude oil price plummeted, after Saudi Arabia flooded the market with an overproduction, in an attempt to hinder the United States's efforts to drive the shale gas industry [24]. This led to a dead halt of projects to build Gas-To-Liquid plants using FT technology in the United States by Shell and Sasol [25]. As a consequence research efforts concerning FT may decline in the coming years.

The incentive for South Africa and sub-saharan Africa to pursue FT technology are still many-fold. Much of the continent is still struggling to fulfil its energy demands with

633 million people still lacking access to electricity in the year 2014 [26]. At the same time, the continent is rich in coal and mineral resources. Many of these resources are currently mined by international companies, exported and processed to the benefit of the developed world leaving African economies behind [27]. The conversion of Africa's large coal reserves to synthetic fuel may provide the continent with much-needed access to a reliable fuel and energy source. Good arguments may be brought forward for the implementation of solar or wind-craft as energy sources instead. However, in the absence of a railway network in Africa, long-distance transportation of goods and people rely mainly on trucks and buses, which, for the foreseeable future, will still depend on diesel. Moreover, Sasol, which is a South African company, is a driving force in research and development of FT technology. In an African context, it is thus hoped that the development of a new FT based fuel economy may pave the road to something Africa needs above all: more access to higher education and true autonomy over the use of their own resources.

1.3 References

- [1] Brosius, R. and Fletcher, J. C. Q. *Journal of Catalysis*, 317:(2014) 318–325
- [2] Torres Galvis, H. M. and de Jong, K. P. *ACS Catalysis*, 3(9):(2013) 2130–2149
- [3] Torres Galvis, H. M., Koeken, A. C. J., Bitter, J. H., Davidian, T., Ruitenbeek, M., Dugulan, A. I. and de Jong, K. P. *Journal of Catalysis*, 303:(2013) 22–30
- [4] LeViness, S., Deshmukh, S. R., Richard, L. A. and Robota, H. J. *Topics in Catalysis*, 57(6):(2014) 518–525
- [5] Rytter, E. and Holmen, A. *Catalysis Today*, 275:(2016) 11–19
- [6] Laan, G. P. V. D. and Beenackers, A. A. C. M. *Catalysis Reviews*, 41(3):(1999) 255–318
- [7] Schulz, H. *Applied Catalysis A: General*, 186:(1999) 3–12
- [8] Anderson, R. B. *The Fischer-Tropsch Synthesis*. Academic Press (1984)
- [9] Schulz, H. *Catalysis Today*, 214:(2013) 140–151
- [10] Dry, M. E. *Applied Catalysis A: General*, 276(1–2):(2004) 1–3
- [11] Nabaho, D., Niemantsverdriet, J. W., Claeys, M. and van Steen, E. *Catalysis Today*, 275:(2016) 27–34
- [12] de Smit, E. *Iron-based Fischer-Tropsch synthesis: new insights from in-situ (Micro-)Spectroscopy, Diffraction and Theory*. Ph.D. thesis, Universiteit Utrecht (2010)
- [13] van Steen, E. and Claeys, M. *Chemical Engineering and Technology*, 31(5):(2008) 655–666
- [14] Dinse, A., Aigner, M., Ulbrich, M., Johnson, G. R. and Bell, A. T. *Journal of Catalysis*, 288:(2012) 104–114
- [15] Oukaci, R., Singleton, A. H. and Goodwin Jr., J. G. *Applied Catalysis A: General*, 186(1–2):(1999) 129–144
- [16] Liu, P., Qin, R., Fu, G. and Zheng, N. *Journal of the American Chemical Society*, 139(6):(2017) 2122–2131
- [17] Fischer, F. and Tropsch, H. *Brennstoff-Chemie*, 7:(1926) 97–104
- [18] Sabatier, P. and Senderens, J. *Journal of the Society of Chemical Industry*, 21:(1902) 504
- [19] Sabatier, P. and Nye, M. J. *Chemistry World*, 1(12):(2004) 46–49
- [20] Stranges, A. N. *Studies in Surface Science and Catalysis*, 163:(2007) 1–28

- [21] Mallik, A. and Mantri, V. Gas-to-liquids plants face challenges in the U.S. market. <https://www.eia.gov/todayinenergy/detail.php?id=15071> (2014)
- [22] SyngasChem. News: Synfuels China demonstrates First Fischer-Tropsch products from the new Shenhua Ningxia Coal-to-Liquids plant. <http://www.syngaschem.com/news/synfuels-china-ningxia-plant> (2016)
- [23] Opray, M. Campaigners reject plastics-to-fuel projects: but are they right? <https://www.theguardian.com/sustainable-business/2017/feb/20/campaigners-reject-plastics-to-fuel-projects-but-are-they-right> (2017)
- [24] Purvis, D. Why saudi arabia has no intention to end the oil glut. <https://oilprice.com/Energy/Energy-General/Why-Saudi-Arabia-Has-No-Intention-To-End-The-Oil-Glut.html> (2016)
- [25] Burkhardt, P. Sasol slows progress on first US GTL project, citing lower oil prices. <http://www.gasprocessingnews.com/news/sasol-slows-progress-on-first-us-gtl-project,-citing-lower-oil-prices.aspx> (2015)
- [26] Morrissey, J. *The energy challenge in sub-Saharan Africa: A guide for advocates and policy makers*. Oxfam (2017)
- [27] Kimani, M. Mining to profit africa's people. <http://www.un.org/africarenewal/magazine/april-2009/mining-profit-africa's-people> (2009)

Chapter 2

Literature Review

2.1 The catalyst support

A supported metal catalyst typically contains only 10-30 wt% of the active metal phase. The bulk of the catalyst is made up of the catalyst support material. The main function of the catalyst support is to maintain a high dispersion of the catalytically active metal phase, but it also improves heat distribution and provides stability against abrasion. Support materials are typically refractory oxides such as silica, alumina or titania, but also non-refractory materials such as carbon or silicon carbide can be used [1–3].

Catalyst supports are characterised by their crystal structure, surface area, porosity and to a lesser extent by their surface chemistry (e.g. hydrophobicity, OH-surface groups) [4]. The support preparation, especially heat treatment of the support has major effects on the available surface area, porosity and surface chemistry. A high-temperature heat treatment is commonly associated with a denser but more chemically inert support material [5].

The physical characteristics of catalyst supports affect the catalytic performance. For example, the pore structure may introduce mass-transport limitations with consequently alters the product selectivity. Supports with narrow pores, such as γ -Al₂O₃, may restrict water removal in CO hydrogenation resulting in a high partial pressure of water inside the pores, which may cause catalyst deactivation by reoxidation [5]. Shimura et al. [6] investigated the effect of several metal promoters, as well as different crystalline phases of titania on cobalt-based FT catalysts and found that the rutile phase positively affected catalytic activity and selectivity.

It is well established, that the physical properties of the support, such as the surface area and porosity, correlate with the properties of the active metal phase, such as the metal dispersion and degree of reduction. For catalysts prepared by conventional impregnation methods (which is by far the most common preparation method and the only preparation method applied for supported catalysts on a commercial scale), the metal dispersion is expected to increase with decreasing pore diameter [5, 7], increasing surface area [8] and decreasing metal loading [9]. Increasing the support surface area and porosity may affect the structural integrity of the support. Hence, a compromise needs to be found between the desired surface area for best metal particle characteristics and the structural integrity of the catalyst. This is especially relevant for the use in slurry reactors, which requires catalysts with strong attrition resistance.

The metal dispersion may also be affected by the surface chemistry of the support [10]. Van Steen et al. [11] reported that during catalyst preparation by impregnation silanol groups on the silica surface may be polarised (SiOH , SiO^+ , SiOH_2^+) depending on the pH of the impregnation solution. The interaction between the solvated cobalt complexes and surface silanol groups may govern the metal dispersion. It has been postulated, that the surface chemistry of the support also influences the catalytic activity and selectivity [12, 13]. However, these effects are not yet completely understood [14, 15].

Studies reporting the effect of surface acid sites on the catalytic performance of supported cobalt catalysts have produced contradictory results. Xiong et al. [16] studied the effect of several carbon supports containing weak acidic sites (introduced by pre-treatment of carbon in nitric acid). They found an increase in metal dispersion with decreasing support acidity. Cobalt supported on carbon nanotubes showed intermediate surface acidity, and had the highest activity. Zhang et al. [17] reported an increase in activity with decreasing acidity of $\gamma\text{-Al}_2\text{O}_3$ supports. Lualdi et al. [18] reported no correlation between the surface acidity and the catalytic performance of cobalt supported on SBA-15, when the surface acidity was increased by Al- and Ti-doping of the support.

A better understanding of the interaction between the metal and the support may be the missing link towards finding an optimal catalyst composition.

2.2 Metal-support interactions

Although metal-support interactions have been reported for over 30 years, and the literature on this topic is extensive, the picture of what actually constitutes a metal-support interaction is still vague. In this study, metal-support interactions shall refer to a form of chemical interaction between the metal/metal-oxide which may alter its reactivity. This definition excludes the effect of physical properties of the support, such as porosity and surface area, which may also affect the catalytic performance.

Metal-support interactions may lead to the formation of mixed-metal support compounds resulting in a decreased catalyst reducibility. Intuitively a decrease in reducibility is expected to result in a decrease in overall catalytic activity. However, metal-support interactions may also increase the metal dispersion, which increases the activity for structure-insensitive reactions. Hence a complex relationship between reducibility and catalytic activity may be observed [19], and some degree of metal-support interaction may be desirable.

Strong metal-support interactions were first associated with the formation of mixed metal-support compounds of group VIII noble metals supported on titania [20], and were later extended to other metal support systems [21]. The term strong metal-support interactions is sometimes more loosely used to describe the tendency of a support to decrease the reducibility or influence the metal phase.

The tendency of a catalyst to form mixed metal-support compounds directly decreases in the order $\text{Al}_2\text{O}_3 > \text{TiO}_2 > \text{SiO}_2$ [22, 23]. The reducibility is found to decrease, and metal dispersion increases with increasing metal-support interaction [23, 24]. Therefore, alumina in combination with a reduction promoter, is still the best choice, as it provides the highest number of Co surface sites after reduction, even though the reducibility is low.

The formation of mixed metal-support compounds involves diffusion of metal ions into the support lattice. Ion mobility increases with temperature and at high partial pressures of water [25]. Therefore, the formation of mixed metal-support compounds typically occurs at high calcination temperatures, during reduction or during the FT reaction [26]. Large surface area supports, low cobalt loadings and high cobalt dispersions facilitate the formation of strong metal-support interaction, presumably due to the increased contact area between the metal and the support [22, 24, 27–30].

The mixed metal-support phase is often restricted to a few outer layers of the surface, and is non-stoichiometric [25, 31, 32]. This makes characterisation of this phase inherently difficult [33]. A non-stoichiometric mixed metal-support phase is essentially a diluted solid solution. Kung et al. [34] found that a cation in a solid solution can experience a change in the ionicity as well as possible lattice distortions compared to the cation in the pure metal oxide, which change its surface chemistry and catalytic properties.

Electronic metal-support interactions - An electronic promoter affects the electronic structure of the catalytically active metal by adding or withdrawing electron density near the Fermi level in the metal's valence band [35]. This changes the chemisorption properties of the metal and thus affects the surface coverage, and reactivity of reactants on the catalyst surface. Electronic promotion can only occur when there is a direct contact between the promoter and the metal surface.

Whether a charge transfer occurs is dependent on the chemistry of the support as well as the metal [36]. Non-reducible oxide supports, such as magnesia, alumina and silica are insulators with a large band gap and show ionic bonding. The oxygen ions are fully reduced and have a high ionisation potential. They are true O^{2-} species and therefore act as basic centres (charge donors). Transition metals on non-reducible oxides can form covalent bonds, but usually, show no or only very little amount of charge-transfer. The strength of the bonding is dependent on the mixing of metal d-electrons with oxygen 2p-orbitals. 5d elements interact stronger than 3d and 4d elements. Metals with full d-orbital interact less with the support. Transition metal oxides, rare earth metal oxides and titania belong to the reducible oxides. The oxygen is not in the fully reduced state and can thus accept negative charge which is transferred to the d- or f-orbitals of the metal formally reducing it from the M^{n+} to a $M^{(n-1)+}$ state. Interaction of non-reducible oxides with metals can lead to charge transfer from the metal to the support and vice versa.

The number of crystal defects (especially hydroxyl groups, and defect oxygen) strongly affect the electronic metal-support interaction [36]. Hydroxyl groups can trap electrons and thus ionise metal atoms or clusters in its vicinity. The presence of hydroxyl groups is generally associated with an increased reactivity of the surface with the metal.

Electronic metal-support interactions have been mainly reported for supported noble

metal catalysts [37, 38]. It is not clear whether these effects play a role in supported transition metal catalysts with a relatively large crystallite size, such as cobalt [35].

Synergistic effects - Some promoters, although not themselves catalytically active, may alter the catalytic performance of the catalyst by changing the local feed composition or overall product distribution [35]. Synergistic effects are typically attributed to chemical promoters. For example, addition of noble metals may increase hydrogen dissociation thereby promoting hydrogenation reactions [39], or addition of transition metal oxides which may promote the water-gas shift reaction [35]. However, the support may introduce synergistic effects by influencing the reactivity of exposed metal sites at the metal-support interface.

The lattice mismatch at the metal-support interface can cause lattice distortions and crystal strain of the metal phase, which may affect the strength of the metal-adsorbate bonding [40–42]. Wong et al. [41] used density functional theory calculations (DFT) to investigate the metal-support interface of Fe- and Ni-monometallic or bimetallic adlayers on α -Al₂O₃. They found that the metal phase was significantly strained at the metal-support interface resulting in expansion of the metal-metal bond, which was associated with enhanced catalytic activity. However, Rytter et al. [5] hypothesised that strain induced by high surface area supports on cobalt crystallites have detrimental effects on the catalytic selectivity for the FT synthesis.

Surface decoration or ligand effect - Dissolution and precipitation of support-molecules may occur during catalyst preparation in wet media, essentially covering (decorating) the metal/metal-oxide surface with support-ligands. Such a metal-support ligand bond may also be present at the interface or boundary site between the metal and the support.

Kunz [43] found parallels in the application of ligand modification of metal nanoparticles in heterogeneous catalysis to the use and functionalities of ligands in homogeneous catalysts. In metalorganic homogeneous catalysts, a single metal atom or ion is surrounded by stabilising ligands that bind to the metal centre leaving free coordination sites available for adsorption and catalytic reaction. The main purpose of the ligand is to stabilise

and tune the solubility as well as the reactivity of the metal centre. In heterogeneous catalysis, ligands are not necessary for stabilisation as the metal particles are deposited onto a support material. Ligands are often believed to be non-beneficial to heterogeneous catalysts as they may self-assemble on the metal surface blocking active sites. However, ligands may influence the catalytic activity and selectivity either by steric or electronic interaction of the ligands with the reactants, or by electronic interaction of the ligands with the catalytically active metal centre itself. It was suggested that ligands might aid in controlling chemo- and stereo-selectivity, which may be one of the largest challenges for heterogeneous catalysis in the coming decade [43].

According to Stakheev et al. [44], the chemistry of the support may affect morphology and catalytic performance of metal particles. The particle morphology determines which crystalline planes are exposed on the surface, which may affect the catalytic reaction. Liu et al. [45] showed that adsorption of ligands during the synthesis of metal nanocrystals may significantly reduce the surface energy of facets, which led to the formation of non-Wulff shaped particles. They found that during the hydrogenation of nitrobenzene ultrathin Pt nanowires modified with ethylenediamine show a high selectivity towards N-hydroxyanilines, rather than the thermodynamically favoured anilines. DFT calculations suggested electron donation from the amine to the Pt surface favouring the adsorption of electron-deficient reactants and preventing the full hydrogenation into anilines. The electron enrichment of the surface also led to enhanced CO binding by electron back-donation which was confirmed by CO stripping voltammetry [45].

Thus, support-ligands in contact with the metal phase may lead to a synergistic or electronic promotion. It is evident that metal-support interactions affect the metal dispersion and reducibility, but the role of metal-support interaction in determining the catalytic selectivity is not well understood.

2.3 Investigating metal-support interactions

Traditionally, metal-support interactions have been investigated by modifying the support properties (e.g. heat treatment, chemical treatment) and studying the effect on the catalyst

properties and the catalytic performance. However, it is quite difficult to draw reliable conclusions in this manner, because the physical properties of the support are strongly correlated with each other and the properties of the metal phase. For example, increasing the severity of the heat treatment of a γ - Al_2O_3 support increases the alumina crystal size, which results in a reduction of the porosity and surface area and an increase of the pore diameter, as well as an increase in the cobalt crystallite size [5]. This coincides with an increase in the selectivity of high molecular weight products. This may be attributed to an increase in pore diameter, a change in the metal-support interaction due to the change of the cobalt crystallite size, or a combination of both effects.

The properties of the support and the properties of the metal phase can be decoupled by preparing the metal-oxide particles ex-situ, for example via the reverse-micelle technique [46, 47] or similar colloidal preparation methods [48], and then depositing the particles onto the support [49]. These methods, involve the use surfactants, which may be strongly attached to the particle surface, and thus difficult to remove. Moreover, homogeneous deposition of these particles on the support is challenging, and the preparation is typically restricted to very small weight loadings, in order to avoid particle-agglomeration. These methods typically achieve low yields, making catalyst preparation time consuming and expensive.

Therefore, model systems are used to study metal-support interaction. Known model systems are flat-model catalysts, encapsulated catalysts and inverse-model catalysts [21].

Flat-model catalysts are typically thin films of supports modified with a metals or vice versa [50, 51]. These systems are interesting for surface science studies, but cannot be used for catalytic testing. This makes it difficult to relay the results to real-world catalysts.

Encapsulation of metal nanoparticles with support material in a core-shell, core-tube or similar structure, is a recent trend in catalysis research. Tian et al. [52] wrote an excellent review on encapsulated group VIII base-metal catalysts. This technique provides an interesting means to study metal-support interaction as the contact interface between the metal and support is very large. Encapsulation of iron in CNT has been found to have an electronic effect on the iron particles, facilitating the reduction of iron oxide and altering their catalytic behaviour [53]. It is not clear whether this, so-called confinement effect is specific to carbon materials or whether it might also occur on oxidic support materials.

Nonetheless, it is an interesting example of the occurrence of electronic metal-support interactions in base-metal catalysts.

A trending topic is also the modification of a non-refractory support such as carbon or silicon carbides with a classical refractory material such as titania or alumina in order to achieve better dispersions and investigate metal-support interactions. Venezia et al. [54] investigated the effect of titania modification and cobalt loading on silica-supported cobalt catalysts for the FT synthesis. Sol-gel derived silica supports were grafted with titania by impregnation with titanium iso-propoxide in hexane solution followed by calcination. The titania modification reduced the cobalt oxide crystallite size marginally from 15 nm to 11-13 nm for a weight loading of 6 and 12 wt% cobalt respectively. The reducibility of the catalysts dropped from 76 % to 47 % after titania modification, while CO conversion and TOF drastically increased. The increase in activity was ascribed to the presence of unreduced cobalt oxides in the sample, which prevented initial deactivation due to cobalt particle sintering in the early phase of the FT reaction.

In this study, the support effect is studied using inverse-model catalysts. This method involves depositing a varying amount of the support material around the metal/metal-oxide phase [21]. These systems are closer to real catalysts than for example thin-film models, while still providing the means to exclude the influence of crystallite size and the physical properties of the support, such as porosity [55]. Inverse-model systems were successfully used by Mogorosi et al. [56, 57] for the study of support effects on iron-based FT catalyst.

Inverse catalyst systems may not only be useful as model systems but have applications in industrial processes. Some reactions may proceed preferentially at the metal-support interface [58], in which case inverse catalysts may have an enhanced catalytic performance. Hornes et al. [59] studied the use of inverse CeO_2/CuO catalysts for preferential oxidation of CO and found enhanced catalytic activity when small CeO_2 particles were supported on large CuO particles, compared to a conventional reference catalyst. As possible explanation, they offered a decreased reducibility of large CuO and stronger metal-support interaction which was beneficial to the catalytic reaction. This illustrates that there are potential real-world applications for inverse catalyst systems.

2.4 References

- [1] Gates, B. C. *Chemical Reviews*, 95(3):(1995) 511–522
- [2] Xiong, H., Motchelaho, M. A. M., Moyo, M., Jewell, L. L. and Coville, N. J. *Journal of Catalysis*, 278(1):(2011) 26–40
- [3] Lacroix, M., Dreibine, L., de Tymowski, B., Vigneron, F., Edouard, D., Bégin, D., Nguyen, P., Pham, C., Savin-Poncet, S., Luck, F., Ledoux, M.-J. and Pham-Huu, C. *Applied Catalysis A: General*, 397(1–2):(2011) 62–72
- [4] Acres, G. J. K., Bird, A. J., Jenkins, J. W., King, F., Kemball, C. and Dowden, D. A. *The design and preparation of supported catalysts*, volume 4, 1–30. The Royal Society of Chemistry (1981)
- [5] Rytter, E. and Holmen, A. *Catalysis Today*, 275:(2016) 11–19
- [6] Shimura, K., Miyazawa, T., Hanaoka, T. and Hirata, S. *Applied Catalysis A: General*, 460–461:(2013) 8–14
- [7] Storsæter, S., Tøtdal, B., Walmsley, J. C., Tanem, B. S. and Holmen, A. *Journal of Catalysis*, 236(1):(2005) 139–152
- [8] Bessell, S. *Applied Catalysis A: General*, 96(2):(1993) 253 – 268
- [9] Reuel, R. C. and Bartholomew, C. H. *Journal of Catalysis*, 85(1):(1984) 78–88
- [10] Khodakov, A. Y., Chu, W. and Fongarland, P. *Chemical Reviews*, 107(5):(2007) 1692–1744
- [11] Steen, E. v., Sewell, G. S., Makhothe, R. A., Micklethwaite, C., Manstein, H., de Lange, M. and O’Connor, C. T. *Journal of Catalysis*, 162(2):(1996) 220–229
- [12] Johnson, B. G., Bartholomew, C. H. and Goodman, D. W. *Journal of Catalysis*, 128(1):(1991) 231–247
- [13] Borg, Ø., Dietzel, P. D. C., Spjelkavik, A. I., Tveten, E. Z., Walmsley, J. C., Diplas, S., Eri, S., Holmen, A. and Rytter, E. *Journal of Catalysis*, 259(2):(2008) 161–164
- [14] Iglesia, E., Soled, S. L. and Fiato, R. A. *Journal of Catalysis*, 137(1):(1992) 212–224
- [15] Borg, Ø., Eri, S., Blekkan, E. A., Storsæter, S., Wigum, H., Rytter, E. and Holmen, A. *Journal of Catalysis*, 248(1):(2007) 89–100
- [16] Xiong, H., Motchelaho, M. A. M., Moyo, M., Jewell, L. L. and Coville, N. J. *Catalysis Today*, 1:(2013) 50–60
- [17] Zhang, J., Chen, J., Ren, J., Li, Y. and Sun, Y. *Fuel*, 82(5):(2003) 581–586
- [18] Lualdi, M., Di Carlo, G., Lögdberg, S., Järås, S., Boutonnet, M., La Parola, V., Liotta, L. F., Ingo, G. M. and Venezia, A. M. *Applied Catalysis A: General*, 443–444:(2012) 76–86

- [19] Holm, V. C. F. and Clark, A. *Journal of Catalysis*, 11(4):(1968) 305–316
- [20] Tauster, S. J. *Accounts of Chemical Research*, 20(11):(1987) 389–394
- [21] Fu, Q. and Wagner, T. *Surface Science Reports*, 62(11):(2007) 431–498
- [22] van de Loosdrecht, J., van der Haar, M., van der Kraan, A. M., van Dillen, A. J. and Geus, J. W. *Applied Catalysis A: General*, 150(2):(1997) 365–376
- [23] Jacobs, G., Das, T. K., Zhang, Y., Li, J., Racoillet, G. and Davis, B. H. *Applied Catalysis A: General*, 233(1–2):(2002) 263–281
- [24] Ji, L., Lin, J. and Zeng, H. C. *The Journal of Physical Chemistry B*, 104(8):(2000) 1783–1790
- [25] Jongsomjit, B., Panpranot, J. and Goodwin, J. G. *Journal of Catalysis*, 204(1):(2001) 98–109
- [26] Das, T. and Deo, G. *Catalysis Today*, 198(1):(2012) 116–124
- [27] Wang, W. J. and Chen, Y. W. *Applied Catalysis*, 77(2):(1991) 223–33
- [28] van de Water, L. G. A., Bezemer, G. L., Bergwerff, J. A., Versluijs-Helder, M., Weckhuysen, B. M. and de Jong, K. P. *Journal of Catalysis*, 242(2):(2006) 287–298
- [29] Jacobs, G., Ma, W. and Davis, B. H. *Catalysts*, 4:(2014) 49–76
- [30] Roe, G. M., Ridd, M. J., Cavell, K. J., Larkins, F. P., D. M. Bibby, R. F. H., C. D. Chang and Yurchak, S. *Studies in Surface Science and Catalysis*, 36:(1988) 509–515
- [31] Lojacono, M., Verbeek, J. L. and Schuit, G. C. A. *Journal of Catalysis*, 29(3):(1973) 463–474
- [32] Zhang, Y., Wei, D., Hammache, S. and Goodwin Jr., J. G. *Journal of Catalysis*, 188(2):(1999) 281–290
- [33] Chin, R. L. and Hercules, D. M. *The Journal of Physical Chemistry*, 86(3):(1982) 360–367
- [34] Kung, H. H. *Journal of Catalysis*, 73(2):(1982) 387–395
- [35] Morales, F. and Weckhuysen, B. M. *Catalysis*, volume 19, chapter Promotion Effects in Co-based Fischer-Tropsch Catalysis, 1–40. The Royal Society of Chemistry (2006)
- [36] Pacchioni, G. *Physical Chemistry Chemical Physics*, 15(6):(2013) 1737–1757
- [37] Libuda, J., Frank, M., Sandell, A., Andersson, S., Brühwiler, P. A., Bäumer, M., Mårtensson, N. and Freund, H. J. *Surface Science*, 384(1–3):(1997) 106–119
- [38] Heemeier, M., Stempel, S., Shaikhutdinov, S. K., Libuda, J., Bäumer, M., Oldman, R. J., Jackson, S. D. and Freund, H. J. *Surface Science*, 523(1):(2003) 103–110

-
- [39] Nabaho, D., Niemantsverdriet, J. W., Claeys, M. and van Steen, E. *Catalysis Today*, 275:(2016) 27–34
- [40] Mavrikakis, M., Hammer, B. and Nørskov, J. K. *Physical Review Letters*, 81(13):(1998) 2819–2822
- [41] Wong, K., Zeng, Q. and Yu, A. *The Journal of Physical Chemistry C*, 115(28):(2011) 13796–13803
- [42] Campbell, C. T. *Nature Chemistry*, 4(8):(2012) 597–598
- [43] Kunz, S. *Topics in Catalysis*, 59(19):(2016) 1671–1685
- [44] Stakheev, A. Y. and Kustov, L. M. *Appl. Catal., A*, 188(1,2):(1999) 3–35
- [45] Liu, P., Qin, R., Fu, G. and Zheng, N. *Journal of the American Chemical Society*, 139(6):(2017) 2122–2131
- [46] Fischer, N., Minnermann, M., Baeumer, M., van Steen, E. and Claeys, M. *Catalysis Letters*, 142(7):(2012) 830–837
- [47] Martínez, A. and Prieto, G. *Journal of Catalysis*, 245(2):(2007) 470–476
- [48] Shi, N., Cheng, W., Zhou, H., Fan, T. and Niederberger, M. *Chemical Communications*, 51(7):(2015) 1338–1340
- [49] Wolf, M., Kotze, H., Fischer, N. and Claeys, M. *Faraday Discussions*, 197:(2017) 243–268
- [50] Rainer, D. R. and Goodman, D. W. *Journal of Molecular Catalysis A: Chemical*, 131(1–3):(1998) 259–283
- [51] Boffa, A. B., Lin, C., Bell, A. T. and Somorjai, G. A. *Catalysis Letters*, 27(3):(1994) 243–249
- [52] Tian, H., Li, X., Zeng, L. and Gong, J. *ACS Catal.*, 5(8):(2015) 4959–4977
- [53] Xiao, J., Pan, X., Guo, S., Ren, P. and Bao, X. *Journal of the American Chemical Society*, 137(1):(2015) 477–482
- [54] Venezia, A. M., La Parola, V., Liotta, L. F., Pantaleo, G., Lualdi, M., Boutonnet, M. and Järås, S. *Catalysis Today*, 197(1):(2012) 18–23
- [55] Hayek, K., Fuchs, M., Klotzer, B., Reichl, W. and Rupprechter, G. *Topics in Catalysis*, 13(1-2):(2000) 55–66
- [56] Mogorosi, R. P. *Metal-Support Interactions on Fe-based Fischer-Tropsch Catalysts*. Ph.D. thesis, University of Cape Town (2012)
- [57] Mogorosi, R. P., Fischer, N., Claeys, M. and van Steen, E. *Journal of Catalysis*, 289:(2012) 140–150

- [58] Hayek, K., Kramer, R. and Paál, Z. *Applied Catalysis A: General*, 162(1–2):(1997) 1–15
- [59] Hornés, A., Hungría, A. B., Bera, P., Cámara, A. L., Fernández-García, M., Martínez-Arias, A., Barrio, L., Estrella, M., Zhou, G., Fonseca, J. J., Hanson, J. C. and Rodríguez, J. A. *Journal of the American Chemical Society*, 132(1):(2010) 34–35

Chapter 3

Scope and Objectives

A major focus of research in catalysis is the development of catalysts with improved activity and selectivity. Ever new catalyst formulations and increasingly complicated preparation techniques are being continuously developed. Despite all the research efforts, development of new catalysts still largely follows a trial-and-error approach. This is in part because fundamental understanding of many processes underlying the catalytic reaction, such as the nature of the active site, is still lacking. In order to be able to design catalysts with high activity and selectivity, the complicated interplay between all catalyst components needs to be understood better.

The objective of this study is to gain fundamental insights into the role of cobalt-alumina metal-support interactions in Fischer-Tropsch catalysts. The FT synthesis is a complex reaction involving a myriad of products, side reactions and active sites. This makes it particularly suitable to study catalyst selectivity. Furthermore, the FT process is of particular relevance to South-African research efforts, due to the existing FT plants in the country [1].

The focus of this study is the *chemical* interaction between the metal and the support. This includes the formation of mixed-metal support compounds, as well as a possible ligand or synergistic effects. This excludes effects of the physical properties of the support, such as support porosity, which have been extensively studied in the past [2].

In order to establish a clear relationship between the metal-support interaction and the catalytic performance, crystallite size effects and effects of micro-porosity, which may cloud the effect of metal-support interactions, need to be excluded. Therefore, an inverse-

model catalyst system was designed to isolate the contribution of metal-support interactions. Unlike conventional catalysts, where the metal is deposited onto the support, in the inverse-model catalyst support molecules are introduced to the metal surface (without encapsulating the metal). In this way the quantity of support in the catalyst can be varied. The metal/metal oxide crystallite size can be controlled and the porosity is not altered by the modification. The use of inverse-model catalysts is a novel way to study the effect of alumina on cobalt-based FT catalysts. No systematic study of the cobalt-alumina metal support interaction in inverse-model catalysts was found in the literature.

In this study, a facile technique for the preparation of inverse-model catalysts is described. A synthesis method for cobalt oxide crystallites in the size range of 15 nm to 30 nm with good dispersion and appropriate morphology was developed. The cobalt oxide was then modified with alumina by incipient wetness impregnation using a suitable alumina precursor. The content of alumina on cobalt oxide was varied in order to study the effect of different alumina loadings. This technique is easily transferred to other cobalt-support systems or may even be applied for the study of other catalyst promoters (e.g. noble metals, manganese, potassium).

This study focusses on the effect of metal-support interactions on catalyst reducibility and the effect on the FT performance under industrially relevant conditions. Catalyst reducibility is one of the key issues in the design of efficient cobalt alumina-supported FT catalysts [3]. Metal-support interactions are known to effect catalyst reducibility, e.g. by the formation of mixed-metal support compounds [4]. Therefore, temperature-programmed reduction experiments are often used to characterise metal-support interactions [5]. Furthermore, correlations between catalyst reducibility and catalyst activity and selectivity have been reported [6–8]. The reduction experiments were performed using conventional temperature-programmed reduction techniques, which measure the hydrogen consumption during reduction, as well as novel techniques, which allow for catalyst characterisation during reduction such as *in situ* X-Ray diffraction and *in situ* X-ray absorption near edge spectroscopy.

The effect of alumina on cobalt-based FT synthesis was studied in a slurry reactor under industrially relevant conditions. A special focus was placed on the catalyst selectivity, in order to establish a possible synergistic effect of alumina, which may promote the FT reac-

tion. The activity and selectivity of the catalysts were correlated with the characterisation of the activated and spent catalysts.

References

- [1] van de Loosdrecht, J., Ciobîcă, I. M., Gibson, P., Govender, N. S., Moodley, D. J., Saib, A. M., Weststrate, K.-J. and Niemantsverdriet, J. W. *ACS Catalysis*, 6(6):(2016) 3840–3855
- [2] Borg, Ø. *Role of Alumina Support in Cobalt Fischer-Tropsch Synthesis*. Ph.D. thesis, Norwegian University of Science and Technology (2007)
- [3] Chu, W., Chernavskii, P. A., Gengembre, L., Pankina, G. A., Fongarland, P. and Khodakov, A. Y. *Journal of Catalysis*, 252(2):(2007) 215–230
- [4] Tauster, S. J. *Accounts of Chemical Research*, 20(11):(1987) 389–394
- [5] Jongsomjit, B., Panpranot, J. and Goodwin, J. G. *Journal of Catalysis*, 204(1):(2001) 98–109
- [6] Nabaho, D. *Hydrogen spillover in the Fischer-Tropsch synthesis*. Ph.D. thesis, University of Cape Town (2015)
- [7] Iqbal, S., Davies, T. E., Hayward, J. S., Morgan, D. J., Karim, K., Bartley, J. K., Taylor, S. H. and Hutchings, G. J. *Catalysis Today*, 272:(2016) 74–79
- [8] Johnson, G. R., Werner, S. and Bell, A. T. *ACS Catalysis*, 5:(2015) 5888–5903

Chapter 4

Reducibility of alumina-modified cobalt oxide crystallites

4.1 Introduction

The majority of industrial chemical processes involve the application of heterogeneous catalysts. In a typical heterogeneous catalyst, an active phase is dispersed on an inert carrier material, the catalyst support, in order to optimise catalytic activity and minimise the cost of the catalyst. The catalyst support is used to improve heat distribution, stability against abrasion and foremost improve and maintain the dispersion of the catalytically active (metal) phase. The metal dispersion is defined as the number of metal sites present on the surface in relation to the amount of metal in the bulk of the metal crystallite. As catalytic processes occur on the metal surface, an increase in the metal dispersion is expected to increase the catalytic activity. Consequently, small metal crystallites are desired for catalytic processes. In an attempt to stabilise small metal crystallites under harsh reaction conditions, such as high temperatures and pressures, the metal phase is dispersed on a support material. Such support materials are typically refractory oxides such as silica, alumina or titania, but also non-refractory materials such as carbon or silicon carbide can be used [1–3]. To achieve a good contact and high stability of small metal crystallites, supports with large surface areas around 200-300 m²/g are typically chosen. Despite the high chemical inertness of the materials used, the support may interact

with the metal phase. Such strong metal-support interactions were first described as the formation of mixed metal-support compounds of group VIII noble metals supported on titania [4], and were later found to extend to other metal support systems [5]. These mixed metal-support compounds may form during catalyst preparation or activation.

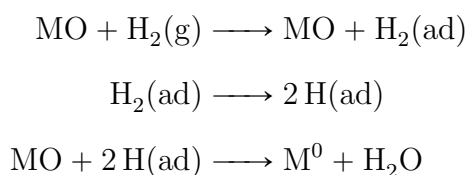
In the case of alumina supported cobalt catalysts the mixed metal-support compound cobalt aluminate (CoAl_2O_4) may be formed, which only reduces in hydrogen at temperatures higher than 850 °C [6, 7]. At those temperatures, metal sintering takes place which leads to a decrease in metal dispersion and a loss of activity. To prevent metal sintering, the reduction is typically performed at a temperature between 300 °C and 450 °C. Therefore, mixed-metal support compounds are termed 'irreducible', and are viewed as being undesirable, because they lead to a loss in the availability of the catalytically active material.

The aim of this study is to gain fundamental insights into the effect of metal-support interactions on cobalt-alumina-based catalysts. The concept is to use inverse model catalysts, in which the inert material is deposited onto the metal phase (similar to encapsulated catalysts) in contrast to conventional, supported catalysts, where the metal phase is deposited onto a porous inert material. This allows for a systematic study of metal-support interactions while excluding effects related to the physical properties of the support, such as porosity. The effect on the reducibility of cobalt oxide crystallites by introducing small amounts of alumina to their surface was studied using temperature-programmed reduction (TPR), X-ray diffraction (XRD), scanning transmission electron microscopy coupled with energy-dispersive X-ray spectroscopy (STEM-EDS) and *in situ* X-ray absorption near edge spectroscopy (XANES).

4.2 Literature Review - The reduction of metal oxides

4.2.1 Thermodynamics

The reduction of metal oxides to metals can theoretically be accomplished with several different reducing agents, the most commonly used being hydrogen. The reduction of metal oxides (MO) with hydrogen to form metals (M) follows the general chemical equation [8]:



Reduction of metal oxides is thermodynamically feasible if:

$$\Delta G = \Delta G^\circ + RT \log \left(\frac{p_{\text{H}_2\text{O}}}{p_{\text{H}_2}} \right) < 0 \quad (4.1)$$

$$\Delta G^\circ = \Delta G_{\text{M}^0}^f + \Delta G_{\text{H}_2\text{O}}^f - \Delta G_{\text{H}_2}^f - \Delta G_{\text{MO}}^f \quad (4.2)$$

, where ΔG is the Gibbs free energy, R is the universal gas constant, T is the temperature and $p_{\text{H}_2\text{O}}$ and p_{H_2} is the partial pressure of water and hydrogen, respectively [8].

This means that for metal oxides with a positive value of ΔG° the partial pressure of water must be kept sufficiently low to allow the reduction. Metal oxides with a very large value of ΔG° cannot be reduced with hydrogen. This is true for alumina as well as most of the common support materials, except for titania and ceria, which can be partially reduced at high temperatures [9, 10]. Many oxides have negative values of ΔG° and can easily be reduced. Amongst those are the oxides of cobalt, nickel and the noble metals [11].

It should be noted, that contradictory to common belief, the metal-oxygen bond strength is not directly correlated to the rate of reduction (e.g. rate of reduction of bismuth molybdates is three orders of magnitude higher than cobalt molybdates but oxygen bond-strength as determined by FTIR measurements is the same) [12].

4.2.2 Reaction mechanism and kinetics

For a metal oxide to be reduced, hydrogen has to adsorb and dissociate on the metal oxide surface [13]. Adsorbed hydrogen reacts with lattice oxygen, which is removed as water resulting in the formation of lattice vacancies. The vacancies are removed by lattice rearrangement leading to nucleation of a metal phase. The outward diffusion of oxygen from the lattice to the surface is often the rate-limiting step [12].

Several mathematical models can be used to describe solid-state reactions. They are tentatively categorised into nucleation models, models based on geometrical contraction, diffusion models and models based on the reaction order [14]. Figure 4.1 depicts schematics of the nucleation and shrinking core model, which describe most metal oxide reduction reactions.

The nucleation model is followed when hydrogen dissociation is the rate-limiting step [8]. The reduction proceeds slowly until a metal nucleus is formed. The newly formed metal surface may dissociate hydrogen faster so that the reduction becomes autocatalytic. As the metal nuclei grow, they start merging, at which point the reaction follows the contracting sphere or shrinking core model. The reaction curve has a characteristic S-shape. The nucleation model can mathematically be described by Avrami type equations [15].

The shrinking core or contracting volume model is followed when hydrogen dissociation on the metal oxide is fast, and nucleation of a metal phase occurs rapidly [8]. The metal nuclei form a thin layer of metal encapsulating the metal oxide. This layer will grow inwards until the metal oxide is completely consumed. In this case, the reaction interface is largest at the beginning and decreases continuously as the reduction proceeds. It follows that the rate of reaction is initially high and then decreases, opposite to the expected behaviour for the nucleation model. Different mathematical models can be derived to describe the reaction kinetics depending on the crystal shape (e.g. cubic, spherical). For catalysts, a spherical system is most frequently used.

In diffusion-controlled reactions, the rate of product formation decreases proportionally with the thickness of the product layer [14]. Many solid-state reactions, such as merging of two solids, are diffusion controlled, but diffusion control plays a minor role in the reduction

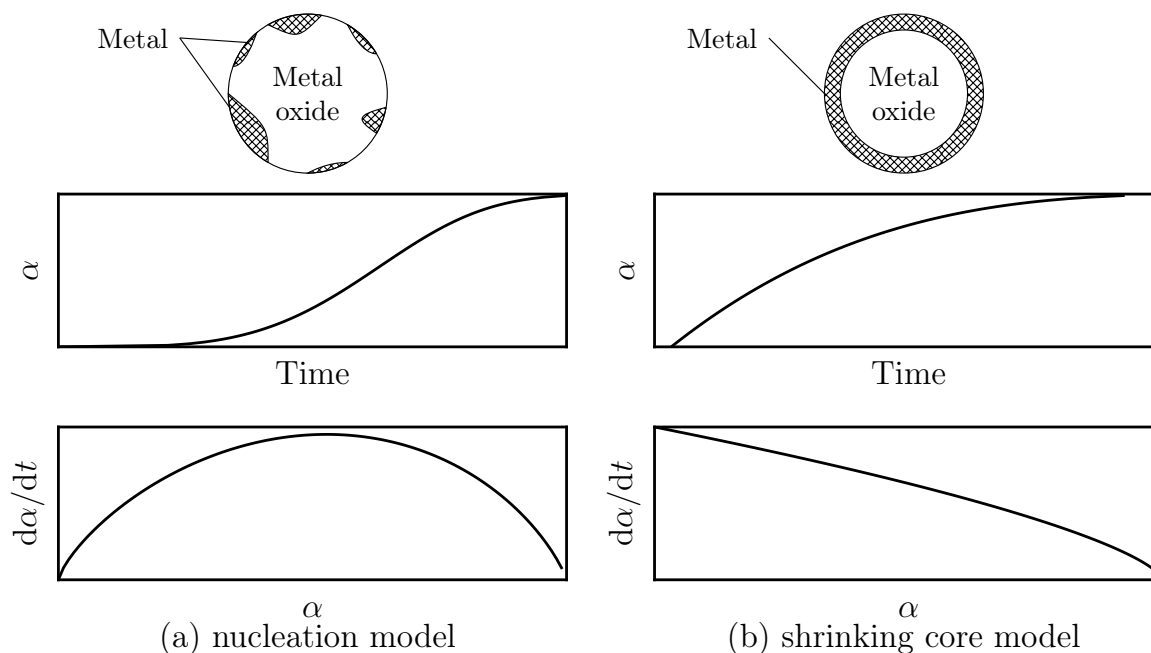


Figure 4.1: Schematic representation of metal oxide reduction by a nucleation and shrinking core model redrawn from [8]. The conversion fraction (α) and the expected reaction rate ($\frac{d\alpha}{dt}$) were calculated as $f(\alpha) = \frac{1}{k} \frac{d\alpha}{dt}$ using a rate constant of 0.049 min^{-1} . The fourth order Avrami-Erofeev equation ($f(\alpha) = 4(1 - \alpha)(-\ln(1 - \alpha)^{3/4})$) [14] was used for the nucleation model (a) and the contracting volume equation ($f(\alpha) = 3(1 - \alpha)^{2/3}$) [14] was used for the shrinking core model (b).

of metal oxides.

Most noble metal oxides, which generally form small crystallites follow the shrinking core model, while most transition metal oxides follow the nucleation model [11]. When transition metal oxides are deposited on inert carrier materials, their crystallite size may be very small, and the reduction mechanism may follow the shrinking core model.

4.2.3 Experimental procedure and evaluation

The reduction of metal oxides is commonly studied by measuring the sample weight during reduction via thermogravimetric analysis (TGA), or by measuring the concentration of the reducing gas (H_2) using a thermal conductivity detector (TCD). TGA experiments are often carried out isothermally. The change in the concentration of the reducing gas is more easily determined non-isothermally. Therefore, such experiments are referred to as temperature-programmed reduction (TPR). Commercial TPR instruments are now widely available, and replaced TGA as the most popular technique to investigate the reducibility

of bulk or supported metal oxides [16].

In recent years, it has become possible to measure the oxidation state or crystalline phases during the reduction *in situ*, for example by using, X-ray diffraction (XRD) or X-ray absorption near edge spectroscopy (XANES) [17, 18]. However, such instrumental set-ups are not as ubiquitously available as TPR instruments.

The main purpose of a TPR experiment is to determine a temperature at which the reduction kinetics are rapid enough to proceed to completion. Furthermore, the reduction profile can be evaluated to investigate the reduction kinetics and mechanism, as well as the degree of metal-support interaction. The technique has even been used to indicate the formation of bimetallic compounds [19].

The experimental conditions applied (e.g. reducing gas concentration, heating rate) may vary; however, in a typical TPR experiment 5-10 vol% H₂ in Ar is used as the carrier gas, and heating rates of 5-10 °C/min are applied [8]. The choice of reaction conditions may be restricted by practical concerns, such as availability of the carrier gas or cost of sample preparation. However, inappropriate reaction conditions may result in a loss of information [20].

The rate of reduction of a solid in hydrogen at a temperature T can be described by

$$\frac{d\alpha}{dt} = k(T)f(\alpha)\phi(c_{\text{H}_2}) \quad (4.3)$$

, where c_{H_2} is the mean hydrogen concentration, k is the rate constant and α is the conversion fraction (degree of reduction), which is defined as S/S_0 , where S is the amount of reduced species, and S_0 is the initial amount of reducible species [20]. $f(\alpha)$ accounts for the dependency of the rate on the conversion fraction and $\phi(c_{\text{H}_2})$ accounts for the dependency of the rate on the hydrogen concentration [20].

The hydrogen mass balance is given by

$$F c_{0,\text{H}_2} = F c_{\text{H}_2} + S_0 \frac{d\alpha}{dt} \quad (4.4)$$

$$\frac{d\alpha}{dt} = \frac{F c_{0,\text{H}_2} - F c_{\text{H}_2}}{S_0} \quad (4.5)$$

, where F is the molar flow of the carrier gas and c_{0,H_2} is the initial hydrogen concentration at the reactor inlet [20].

Assuming that the reduction obeys first order kinetics with respect to hydrogen, it follows that [20]:

$$\phi(c_{H_2}) = c_{H_2} \quad (4.6)$$

$$c_{H_2} = c_{0,H_2} - \frac{S_0}{F} \frac{d\alpha}{dt} \quad (4.7)$$

$$\frac{d\alpha}{dt} = k(T)f(\alpha) \left(c_{0,H_2} - \frac{S_0}{F} \frac{d\alpha}{dt} \right) \quad (4.8)$$

$$\frac{d\alpha}{dt} = \frac{c_{0,H_2} k(T) f(\alpha)}{\left(1 + \frac{S_0}{F} \right) k(T) f(\alpha)} \quad (4.9)$$

Assuming a constant heating rate is applied, the temperature at time t can be calculated as:

$$T(t) = T_0 + \beta t \quad (4.10)$$

The rate constant can be described by the Arrhenius equation

$$k = Ae^{\frac{-E_a}{RT}} \quad (4.11)$$

, where E_a is the activation energy and A is the Arrhenius constant or pre-exponential factor.

By substituting Equation (4.10) and (4.11) into (4.9) the rate equation can be simplified to

$$\frac{d\alpha}{dT} = \frac{Ae^{\frac{-E_a}{RT}} f(\alpha)}{\frac{\beta}{c_{0,H_2}} + PAe^{\frac{-E_a}{RT}} f(\alpha)} \quad (4.12)$$

, where P is defined as $\beta S_0 / F c_{0,H_2}$ [20].

It follows that the reduction profile will be affected by the values of the ratio $\beta/c_{0,H_2}$ and P . This is shown in Figure 4.2, where the peaks shift to a higher temperature with increasing $\beta/c_{0,H_2}$ ratio. The extent of the peak shift can render information on the reaction kinetics. The peak shape is not affected by the $\beta/c_{0,H_2}$ ratio, but may be significantly affected by large values of P [20]. Thus, using large amounts of sample may lead to peak

distortions. A loss of peak resolution when using large amounts of sample has been reported but is usually ascribed to a temperature and hydrogen concentration gradient within the sample bed, resulting in non-homogeneous reduction [8, 21].

Malet et al. [20] suggested keeping the P value below 20. It was also suggested to keep the P values constant when measuring TPR profiles at different heating rates, as this may improve the accuracy of the kinetic analysis. However, this may not always be possible due to experimental limitations, e.g. decreasing the heating rate from $10\text{ }^\circ\text{C}/\text{min}$ to $1\text{ }^\circ\text{C}/\text{min}$ would require a tenfold increase in sample mass. It should also be noted, that the goodness of fit obtained in their experiments when the P value was not kept constant was still very high ($R^2 > 0.994$) [20].

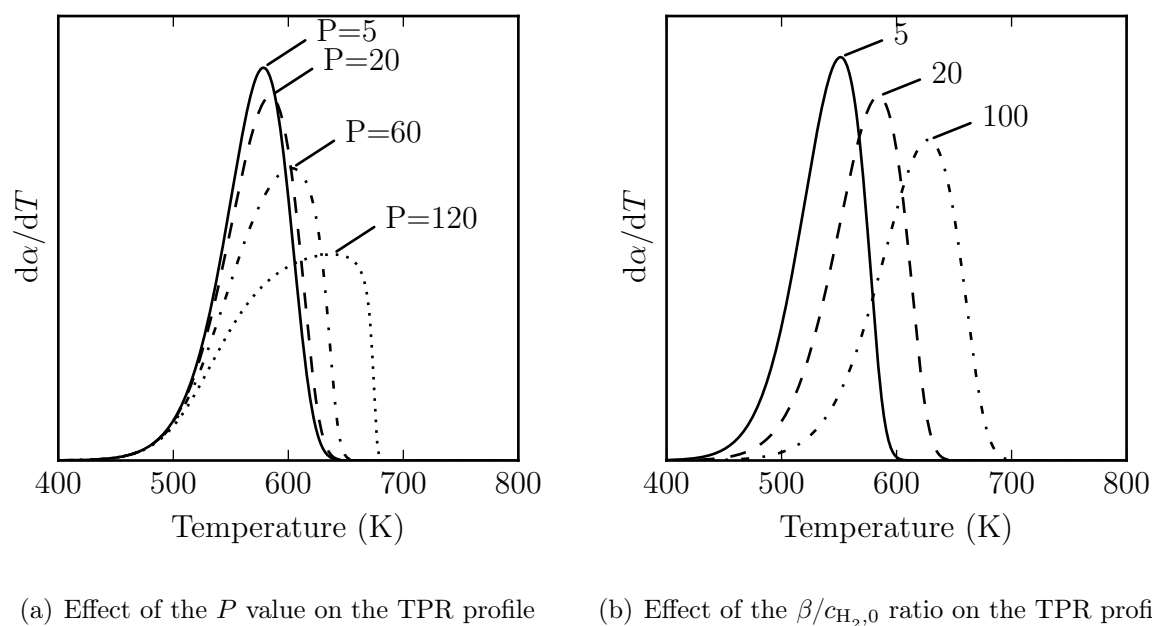


Figure 4.2: Simulated TPR profiles for a single step reduction following first order kinetics with respect to hydrogen with activation energy $E_a=100\text{ kJ/mol}$, pre-exponential factor $A=5 \cdot 10^{10}\text{ s}^{-1}$ showing the effect of varying the P value (a) for $\beta/c_{0,\text{H}_2}=20$ and varying the $\beta/c_{0,\text{H}_2}$ ratio (b) for $P = 20$, redrawn from [20].

Figure 4.3 depicts the effect of the parameter P on the TPR profile for a two-step reduction process. The separation of the two reduction peaks varies in relation to the difference in the kinetic parameters. When the difference in the kinetic parameters is large, the peak overlap is small, and the peaks may be resolved as long as the P value is low. When the two reduction steps have similar kinetic parameters, the peak overlap is

large, and peak resolution is poor, even at low values of P . Increasing the P value results in a substantial broadening of the peaks. Broad reduction peaks are usually interpreted as the result of a peak overlap, and have been reported as an indication for simultaneously occurring reduction processes [7, 22]. Therefore, a high P value may indirectly aid the identification of two simultaneous reduction processes.

In conclusion, TPR profiles are highly sensitive to the experimental conditions chosen, especially the sample mass, the concentration of the reducing gas and the heating rate. For complicated reduction profiles, it is advisable to vary the reaction conditions and be attentive to changes in the peak position as well as the peak shape.

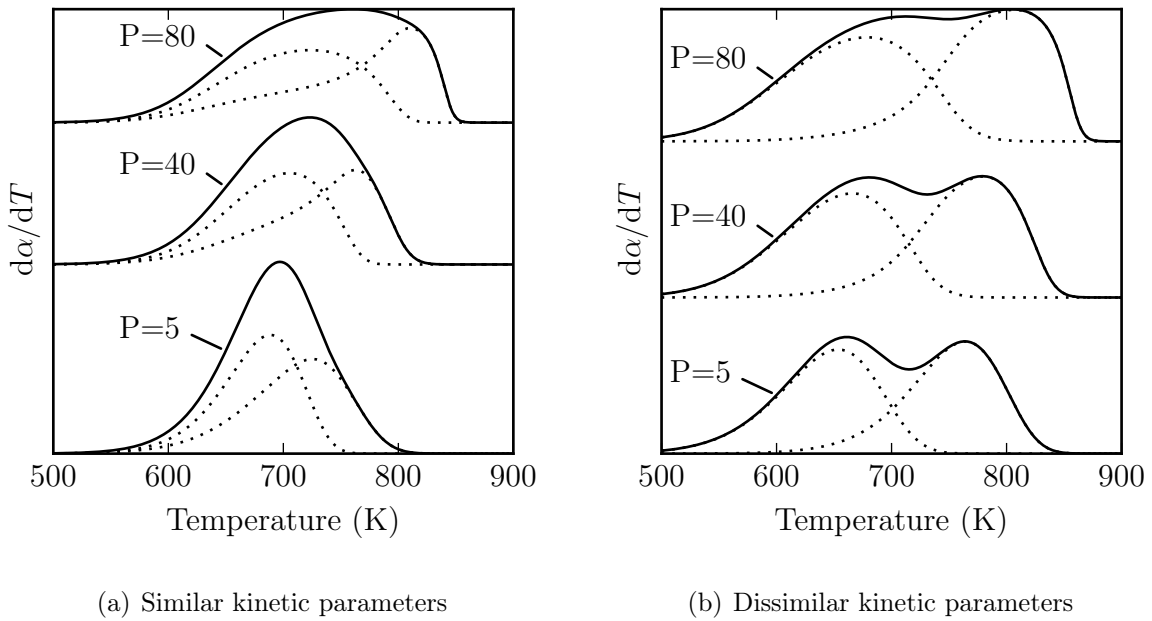


Figure 4.3: Demonstration of the effect of the P -value on a two-step reduction process. TPR profiles were computed for two reduction steps following first order kinetics: (a) kinetic parameters are similar ($E_{a,1}=100$ kJ/mol, $A_1=5 \cdot 10^8$ s $^{-1}$ and $E_{a,2}=120$ kJ/mol, $A_2=5 \cdot 10^{10}$ s $^{-1}$); (b) kinetic parameters are dissimilar ($E_{a,1}=80$ kJ/mol, $A_1=7 \cdot 10^7$ s $^{-1}$ and $E_{a,2}=120$ kJ/mol, $A_2=5 \cdot 10^9$ s $^{-1}$).

It is often desired to gain insights into the reduction kinetics as well as the reaction mechanism of the reduction. For a full kinetic evaluation, isothermal measurements are often preferred, but procedures using non-isothermal or isoconversional methods have been described in the literature [23, 24].

The kinetic parameters can be extracted from TPR experiments using a method de-

veloped by Kissinger [25]. The Kissinger equation says that the peak maximum (T_{max}) is a function of the heating rate, assuming the reaction follows a power law with respect to hydrogen:

$$\ln \frac{\beta}{T_{max}^2} = -\ln \frac{E_a}{A \cdot R \cdot p_{H_2}^q} - \frac{E_a}{R} \cdot \frac{1}{T_{max}} \quad (4.13)$$

, p_{H_2} is the partial pressure of H_2 and q is the reaction order. E_a and A can be calculated from the slope and intercept of a linear plot of $\ln \frac{\beta}{T_{max}^2}$ over $\frac{1}{T_{max}}$, respectively. Although the Kissinger equation was developed assuming a rate expression following a power law (n^{th} order kinetics), it was found empirically that the method gives reliable results irrespective of the underlying reduction mechanism [26].

When the activation energy and pre-exponential factors are known, the reduction mechanism can be established by fitting or simulating the reduction profile. Wimmers et al. [26] described a method to determine the reduction mechanism from non-isothermal TPR experiments based on solving the rate equation (Equation (4.3)). Integration of the rate equation yields:

$$\int_0^\alpha f(\alpha) = g(\alpha) = \frac{A}{\beta} \int_{T_0}^T e^{\frac{-E_a}{RT}} dT \quad (4.14)$$

Functions of $f(\alpha)$ and $g(\alpha)$ have been derived for many solid-state reaction mechanisms, and are described, for example, in the work of Khawam and Flangan [14].

Equation (4.14) can be rewritten and approximated using a Taylor series [27]:

$$g(\alpha) = \frac{AE_a}{R\beta} v(x) \quad (4.15)$$

$$x = \frac{E_a}{RT} \quad (4.16)$$

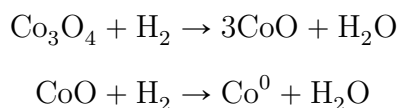
$$\begin{aligned} v(x) &= \frac{e^{-x}}{x} - \int_x^\infty \frac{e^{-u}}{u} du \\ &= \frac{e^{-x}}{x} \frac{674.5 + 57.4x - 6.0x^2 - x^3}{1699.0 + 841.6x + 49.3x^2 - 8.0x^3 - x^4} \end{aligned} \quad (4.17)$$

When E_a and A are known, the reduction profile can be simulated using Equation (4.14), (4.15) and (4.17). However, it should be noted, that TPR experiments are often poorly

described by simulated reduction profiles, and thus, the results may be ambiguous. For example, Wimmers et al. [26] concluded that the reduction of $\text{Fe}_2\text{O}_3 \rightarrow \text{Fe}_3\text{O}_4$ proceeds via a three-dimensional nucleation model according to Avrami-Erofeev, while Lin et al. [28] applied the same method and concluded that the reduction proceeds via a unimolecular model.

4.2.4 Reduction of bulk and supported cobalt oxides

It has been established that the reduction of Co_3O_4 proceeds in two sequential steps, first Co_3O_4 reduces to CoO , and then CoO reduces to metallic cobalt [17]:



Therefore, a H_2 -TPR experiment is expected to show two peaks, with a peak area of 1:3. Several authors have indeed reported two peaks appearing around 250-300 °C and 300-400 °C for the reduction of bulk Co_3O_4 [29–32]. The exact peak position may vary depending on the experimental conditions (e.g. heating rate, reducing gas composition). The two main reduction peaks often strongly overlap [33], and are sometimes completely merged resulting in only one visible peak [6, 7, 22, 34]. A small and broad peak at temperatures below 250 °C has frequently been reported, and may be ascribed to remaining precursor material, which was not completely oxidised during calcination, such as $\text{Co}(\text{NO}_3)_2 \cdot 6\text{H}_2\text{O}$ [35–37] or CoOOH [38]. It should be noted, that a cobalt nitrate reduction peak can be visible in the TPR, even when no such phase is detectable in the XRD [34]. Assignment of a low-temperature TPR peak to cobalt nitrate can be achieved by coupling the TPR with a mass spectrometer, which detects the presence of nitrate ions [39]. Reductive decomposition of NO_3^- leads to the formation of NO_2 . If the temperature of the exit lines are low, NO_2 may dimerise to form N_2O_4 , which has a higher thermal conductivity than hydrogen, and thus a negative peak may be visible in the TPR [39].

It should be noted, that metal oxides supported on inert carriers, as is the case for a typical cobalt catalyst, may exhibit drastically different reduction patterns compared to

bulk metal oxides [40]. Metal oxides may be homogeneously dispersed as small crystallites, in close contact with the support or as isolated islands of larger crystallites, in which case the reduction may be similar to that of the bulk oxide. When the metal oxide crystallite size is very small, the reduction is expected to follow the shrinking core instead of the nucleation model [8].

Due to the large discrepancies observed in the reduction profile, of what is believed to be a pure sample of Co_3O_4 , certain ambiguities in the interpretation of the reduction profile exist in the literature. One point of discussion has been whether there is a direct transition from Co_3O_4 to metallic cobalt, ergo a reduction of Co^{3+} to Co^0 in a single step. Most groups favour the explanation of a sequential reduction of Co_3O_4 to CoO , corresponding to the first peak and reduction to metallic cobalt resulting in the second peak, supported by a peak ratio close to 1:3 [41, 42]. Even when only one peak was observed in the TPR of Co_3O_4 , it has been argued that the broadness of the peak suggests merging of two peaks had taken place, and it was concluded that reduction of Co_3O_4 is a two-step process [7, 22]. However, Arnoldy et al. [6] postulated that a direct transition of Co_3O_4 to metallic cobalt is possible.

Since then modern techniques have been developed, which allow coupling of reduction experiments with analytical techniques which render direct information on the cobalt phase and oxidation state present during the reduction process. Jacobs et al. [17] used synchrotron X-ray radiation to perform TPR-XANES and EXAFS on unsupported and alumina supported cobalt catalysts. They conclusively showed that the reduction proceeds via CoO as an intermediate product with the onset of metallic cobalt formation after depletion of Co_3O_4 . This was confirmed by Plessis et al. [18], who applied synchrotron X-ray diffraction to gain crystallographic insights into the reduction of alumina-supported cobalt catalysts, and found a sequential transition from Co_3O_4 to CoO followed by formation of fcc cobalt.

Hence, it is concluded that the reduction of Co_3O_4 is a two-step process proceeding via the formation of CoO , and direct reduction of Co_3O_4 to metallic cobalt does not take place. This is expected to result in two peaks visible in a H_2 -TPR experiment, with the first peak corresponding to the reduction of Co_3O_4 forming CoO , while the second one corresponds to the reduction of CoO forming metallic cobalt. However, depending on the

experimental conditions, the reduction of $\text{Co}_3\text{O}_4 \rightarrow \text{CoO}$ and $\text{CoO} \rightarrow \text{Co}^0$ may take place simultaneously [43, 44], so that the two reduction peaks may strongly overlap or even merge into a single peak [33, 34].

This discrepancy in the observed reduction profile of Co_3O_4 may be explained by the strong dependence of the observed rate of reaction on the experimental conditions, as well as the method of Co_3O_4 preparation (e.g. calcination temperature). For example, the addition of water vapour during the reduction leads to narrower peaks, shifted to higher temperatures resulting in an improved peak resolution [44]. Tang et al. [30] showed that a bulk CoO sample prepared by heat treatment of Co_3O_4 at 950 °C, shows one reduction peak at 482 °C, while the corresponding Co_3O_4 (prior to the heat treatment) shows two reduction peaks at 300 °C and 367 °C. This shows that bulk CoO reduces at a much higher temperature than the CoO phase formed during H_2 -TPR of Co_3O_4 . This may be due to a crystallite size effect. A peak shift to higher temperatures upon increasing the Co_3O_4 crystallite size has been reported by Okamoto et al. [45] for bulk Co_3O_4 with crystallite sizes of 50-1200 nm, and by Hilmen et al. [29] for alumina- and silica-supported Co_3O_4 with crystallite sizes of 7-25 nm. However, an increase in the *catalyst particle* size, unlike an increase in the *cobalt oxide crystallite* size, was shown to have no effect on the reduction profile [29].

The formation of a metallic cobalt phase enhances hydrogen dissociation which has an autocatalytic effect on the reduction process and drastically reduces the induction period [46]. An increase in metal oxide crystallite size decreases the metal oxide surface area which influences the reduction kinetics and may lead to a change from linear to S-shaped reaction curves [47, 48]. This implies that upon increasing the crystallite size, the induction period is prolonged. This leads to the retardation of the nucleation of the metal phase. The reaction interface evolves more slowly thereby slowing crystal growth, which explains the observed peak shift to higher temperatures.

The main issue regarding the interpretation of reduction profiles of Co_3O_4 catalysts surrounds the interpretation of the second peak around 300-400 °C, as well as high-temperature features. It has been established that, for supported cobalt catalysts, the position and broadness of the second reduction peak are strongly dependent on the properties of the support [17]. Furthermore, the position of both reduction peaks shift to lower temperatures

with increasing cobalt loading [7, 33], and decreasing calcination temperature suggesting that the peak position is related to the strength of the cobalt-support interaction [33, 49]. In some cases, the formation of mixed metal-support compounds such as CoAl_2O_4 or CoSi_2O_4 occurs which introduces a sharp third reduction peak at temperatures above 850°C [7]. Jongsomjit et al. [34] suggested the formation of a non-stoichiometric compound ($\text{Co}_X\text{O}_Y \cdot \text{Al}_2\text{O}_3$), which reduces at temperatures between 400°C and 600°C . They believe to be able to distinguish this $\text{Co}_X\text{O}_Y \cdot \text{Al}_2\text{O}_3$ from a CoAl_2O_4 phase using Raman spectroscopy. Zhang et al. [44] reported that high partial pressures of water increase the mobility of cobalt ions, and promote diffusion of cobalt ions into the alumina support, thus forming highly dispersed cobalt aluminate surface species. Increasing the amount of water vapour during reduction to 20.7% shifted the second reduction peak from 483°C to 696°C [44]. Formation of a cobalt aluminate surface species is also promoted by high cobalt dispersions [50], and the availability of tetrahedral and octahedral defect sites near the support surface necessary for incorporation of Co^{2+} ions [51]. High-surface area supports may exhibit a higher number of defect sites near the surface, thus promoting metal-support interactions [51].

Cobalt ions may also diffuse into the alumina matrix during calcination, but the diffusion has been reported to be limited to the first few outer layers of the support [52]. These surface species lack long-range order which renders them XRD amorphous [53]. Richardson et al. [54] performed magnetic measurements of mixed cobalt-alumina metal oxides with varying cobalt content. When the cobalt content was low ($<12\text{ wt}\%$), cobalt was present as Co^{2+} occupying only tetrahedral sites, while at higher cobalt concentrations both Co^{2+} and Co^{3+} occupying both tetrahedral and octahedral sites were found [54]. It has been suggested, that cobalt ions occupying octahedral sites in the alumina structure are reducible, while those occupying tetrahedral sites are irreducible [53]. The authors came to this conclusion by evaluating EXAFS measurements of calcined $\text{Co}/\text{Al}_2\text{O}_3$ catalysts with varying weight loadings. Catalysts with low loadings, which generally have a low reducibility showed a stronger presence of tetrahedrally coordinated Co ions [55]. Arnoldy et al. [6] suggested that Al^{3+} ions polarise the Co-O bond. This increases the effective charge of the Co ions, thereby increasing the lattice energy, which increases the temperature necessary for reduction.

A broad reduction peak at temperatures above 400 °C and below 800-850 °C is generally assigned to cobalt-support interactions [6, 7]. Most authors seem to agree that the formation of a mixed cobalt-support phase does occur, but may be limited to the support surface, and can therefore only be characterised with great difficulty. Hence, the literature often refers to strongly or weakly interacting cobalt-support species, or cobalt-support surface species, rather than describing a specific chemical compound or crystal phase [42].

A sharp reduction peak at temperatures above 750 °C to 800 °C can generally be assigned to stoichiometric CoAl_2O_4 . CoAl_2O_4 is often formed during the TPR experiment [29], but can be present in calcined catalysts, when the metal loading is very low (< 2 wt%), or the calcination temperature is above 750 °C [56].

The reducibility of supported cobalt catalysts depends on the properties of the support, the metal loading and the method of preparation [57]. The reducibility generally increases in the order $\text{Co}/\text{Al}_2\text{O}_3 < \text{Co}/\text{TiO}_2 < \text{Co}/\text{SiO}_2$ [42, 58]. When the catalyst is prepared by impregnation, the cobalt salt, polarity and pH of the solvent, the drying procedure and the calcination temperature may influence the reducibility [32, 59]. These effects have been rationalised using interfacial coordination chemistry [59]. Steen et al. [59] investigated the preparation of silica supported cobalt catalysts by incipient wetness impregnation. Silanol groups on the silica surface may be polarised (SiOH , SiO^+ , SiOH_2^+) depending on the pH of the impregnation solution. The interaction of solvated cobalt complexes with surface silanol groups may govern the metal dispersion and the metal-support interactions. The use of nitrate and acetate salt, as well as the use of solvents with a low polarity, increased metal-support interactions and resulted in high-temperature peaks at 900 °C in the TPR [59]. Interestingly, the use of cobalt chloride resulted in a high reducibility with hardly any metal-support interactions and the reduction profile of unsupported and silica supported CoCl_2 appear to be almost identical [32]. Increasing the drying temperature, or duration increased the amount of cobalt species reducing at intermediate temperatures of 300-500 °C, and decreased the amount of cobalt species reducing at 900 °C, indicating that metal-support interactions can be destroyed during drying [59]. Increasing the surface area of the support, or calcination temperature may also increase the metal-support interactions. These effects seem to be strongly correlated with the metal dispersion. Catalysts with high metal dispersions (small metal crystallite size) generally show stronger metal-support

interactions [7, 58, 60].

This demonstrates that, although the support materials have a high chemical inertness, they may drastically affect the reducibility of metal oxides. Essentially, the support may influence the reduction process by either interacting with metal ions, or by affecting hydrogen dissociation. If the mobility of metal-atoms on the support surface is reduced, the reduction may be hindered by preventing nucleation [8]. When activated hydrogen species are immobilised on the support surface, the autocatalytic effect of the metal phase may be suppressed, and the reaction kinetics slowed, thereby inducing a shift of the reduction peaks to higher temperatures [8].

Supported catalysts often contain reduction promoters, which typically are noble metals, such as Pt or Pd, to enhance the reducibility of the metal catalyst. Batley et al. [48] investigated the influence of noble metal promoters on the reduction kinetics of several metal oxides (Co_3O_4 , Fe_2O_3 , UO_3 , Ni_3O_4 , MnO_2 and V_2O_5) by isothermal reduction in pure hydrogen. The influence of the promoter was ascribed to the ability of noble metals to dissociate hydrogen. Spillover of hydrogen from the noble metal to the metal oxide takes place via the surface. Transfer of activated hydrogen by diffusion through the gas phase is only possible at temperatures exceeding 350°C . The change in activation energy upon Pt promotion was not significant for the reduction of Fe_2O_3 , UO_3 , NiO and MnO_2 , although a strong decrease in the temperature required for reduction was observed. A similar correlation has been observed for the promotion of CuO with Pt or Pd [21]. This implies that the promoting effect is associated with an increase in the 'pre-exponential' factor, due to an increased number of nucleation sites or active hydrogen species available, rather than by a decrease in the activation barrier of the reduction [8, 61].

Reduction promoters are also associated with a decreased formation of mixed metal-support compounds. This can be explained by a decrease in the temperature at which metallic cobalt is formed, which prevents the diffusion of cobalt ions into the support matrix [29].

In summary, it seems as if almost anything may influence the reducibility of metal oxides. Supported oxides show different characteristics than unsupported oxides [40]. The mode of catalyst preparation, impregnation, deposition-precipitation or ion exchange, the pH of the solution, the solvent and the type of metal salt used will influence the reducibil-

ity [59], as does the type of the support, the surface area and the porosity [42]. The time and temperature during drying and calcination have significant contributions too. To make things worse, it is difficult to draw generalised conclusions. For supported cobalt oxide the reducibility increases in the order of $\text{Al}_2\text{O}_3 < \text{TiO}_2 < \text{SiO}_2$ [42, 58]. The same holds for supported nickel oxide catalysts, but chromium oxide on silica has a lower reducibility than chromium oxide on alumina [62]. Moreover, the specific experimental conditions when measuring the reduction profile such as the heating rate, the concentration and flow rate of the reducing gas, the partial pressure of water, the amount and distribution of sample in the sample tube, possible contaminants and even the temperature of the exit lines may influence the resulting reduction profile [20, 39]. This makes it extremely difficult to directly compare the results of different studies. Hence, the absolute values of the peak maxima or kinetic parameters derived from TPR experiments may have limited significance, and interpretation of these results should be focussed on the change of these values relative to the variable investigated in the experiment (e.g. metal loading, support porosity).

4.3 Experimental

Catalyst preparation - Cobalt oxide with a crystallite size of 15-30 nm was prepared by calcination of a cobalt carbonate precursor. The resulting cobalt oxide crystallites were impregnated with aluminium sec-butoxide to render the cobalt-alumina inverse-model catalyst. This method of preparation was necessary to prepare material in the desired crystallite size range. Cobalt carbonate was synthesised from a 0.5 M cobalt containing solution prepared by adding 29.17 g $\text{Co}(\text{NO}_3)_2 \cdot 6 \text{H}_2\text{O}$ to 200 ml demineralised water in a 1 l beaker. The pH of the solution was found to be between 5.6 and 5.8. Gaseous CO_2 was bubbled via a sparger through the solution until the pH had reached 3.6. The solution was stirred, and 83.3 ml of a 0.25 M ammonia solution was added dropwise over the course of 10-15 min while bubbling CO_2 through the solution. A precipitate formed when the pH rose above 6. After ammonia had been added, the CO_2 flow was stopped, and the suspension was stirred for another 10 min before pressure filtration. Filtration led to a slight increase in the pH of the filtrate, resulting in the formation of further precipitate. For that reason, the filtrate was collected and re-filtered three times. The combined precipitate was collected, and the filtrate was re-saturated with CO_2 until a steady pH was reached (pH=5.8-6). 83.3 ml of a 0.25 M ammonia solution was added, and the suspension was stirred for 10 min before the filtration procedure was repeated. The filtrate was collected, and the procedure was repeated until a total of 500 ml ammonia solution had been added to the solution. This sequential precipitation and filtration procedure was necessary, as keeping the precipitate in the preparation mixture for extended periods, or adding ammonia quickly, may result in the formation of an $(\text{NH}_4)_2\text{Co}_8(\text{CO}_3)_6(\text{OH})_6$ phase instead of the desired $\text{Co}(\text{CO}_3)_{0.5}(\text{OH}) \cdot 0.11\text{H}_2\text{O}$ phase, which has a more favourable morphology. The combined precipitate was washed three times with 500 ml demineralised water. The precipitate was dried in air at room temperature for 48 h. After drying, the cobalt carbonate powder was ground and calcined in a static oven at 300 °C for 16 h. The resulting black Co_3O_4 powder was modified with alumina by impregnation with a dry solution of aluminium sec-butoxide in hexane, in an argon atmosphere, to achieve a weight loading of 0.1, 0.5 or 2.5 wt% Al followed by calcination at 300 °C or 500 °C for 4 h. Pristine Co_3O_4 was also calcined at 300 °C and 500 °C to obtain unmodified reference samples. The cata-

lysts are denoted 0.0Al300, 0.1Al300, 0.5Al300, 2.5Al300 and 0.0Al500, 0.1Al500, 0.5Al500, 2.5Al500 according to their aluminium weight loading and calcination temperature.

X-ray diffraction (XRD) measurements were performed on a Bruker D8 advance AXS with Co-K α radiation ($\lambda = 1.78897 \text{ \AA}$) at 40 kV and 30 mA between 20 and 80 $^{\circ}2\theta$ with a scanning speed of 0.056 $^{\circ}2\theta/s$. Line broadening of the Co₃O₄(220) diffraction peak was used to estimate the crystallite size using the Scherrer equation [63, 64].

For the *in situ* XRD reduction experiments the catalyst was loaded into a borosilicate capillary. The capillary was fitted into a cell developed in-house, which is heated with infrared heaters [65, 66]. 4 ml/min H₂ was flown through the capillary. The catalyst temperature was increased at a heating rate of 1 $^{\circ}C/min$ from 50 $^{\circ}C$ to 400 $^{\circ}C$, and measurements were taken in intervals of 50 $^{\circ}C$. The temperature was kept constant for the duration of the scan. The phase content and crystallite size was determined by Rietveld refinement performed using TOPAS.

Transmission electron microscopy (TEM) was performed on a FEI Tecnai G² high resolution microscope with a LaB₆ filament operated at 200 keV. Samples were dispersed in methanol, ultra-sonicated for 2 min and transferred to a carbon coated copper grid.

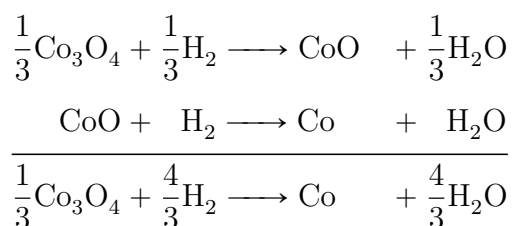
Scanning transmission electron microscopy-energy-dispersive X-ray spectroscopy (STEM-EDS) was performed using a JEOL JEM-ARM200F double Cs-corrected TEM equipped with an FEG, a STEM unit and a high angle annular dark-field (HAADF) detector, operated at 200 kV. Samples were dispersed in methanol, ultra-sonicated for 2 min and transferred to a carbon coated copper grid. Samples on TEM grids were plasma cleaned for 45 s using a Gatan Solarus model 950 plasma cleaner at 25 W under 20 ml/min Ar. EDX mapping was performed using an Oxford X-Max^N 100TLE detector and the Aztec software package.

X-ray absorption near edge spectroscopy (XANES) experiments were carried out at the Brazilian Synchrotron Light Laboratory in Campinas, Brazil at the XAFS2 Beamline. The line uses a bending magnet (D08B@15 $^{\circ}$) and can be operated in an energy range of 4-17 keV. The beamline is equipped with a double crystal - Si(111) monochromator

and has an energy resolution of $\Delta E/E = 1.71 \cdot 10^{-4}$ eV at 7 keV. A cylindrical mirror and a bendable and cooled toroidal mirror are used as focusing elements to produce a beam size of $450 \times 250 \mu\text{m}^2$. All experiments were carried out in transmission mode at the cobalt K-edge of 7709 eV, and a Co metallic foil spectrum was collected simultaneously for energy calibration.

XANES experiments were performed by collecting the background region from 7650-7700 eV in intervals of 2 eV, the XANES region from 7700-7800 eV was collected in intervals of 0.3 eV and the post-edge region from 7800-7900 eV at intervals of 2 eV for 1 sec/step. For the *in situ* experiments, 15 mg of sieved catalyst was diluted with 85 mg of boron nitride and then pressed into a disk. The disk was transferred onto a stainless-steel sample holder and placed in a tubular furnace. While collecting XANES, the catalyst was reduced in a flow of 50 ml/min of 5 vol% H_2 in He by heating to 150 °C at a heating rate of 10 °C/min and then further to 550 °C at a heating rate of 2 °C/min. Extraction of the XANES signal from the collected absorption spectra was carried out using the Demeter software package [67]. The background was removed using a second order polynomial for the pre-edge region and a third order polynomial for the post-edge region. The spectra were normalised by dividing by the height of the absorption edge. The phase composition during the reduction was determined via linear combination fitting in the region of -20 eV to 38 eV relative to the cobalt edge with the reference spectra.

For a better comparability of the results to the TPR experiments, a reduction profile (in terms of hydrogen consumption) can be calculated from the phase composition determined by the XANES experiments. The reduction of Co_3O_4 to CoO and metallic cobalt follows:



The hydrogen consumption (X_{H_2}) and the rate of hydrogen consumption ($-r_{\text{H}_2}$) can then

be calculated according to

$$X_{\text{H}_2} = \frac{1}{3}N_{\text{CoO}} + \frac{4}{3}N_{\text{Co}} \quad (4.18)$$

$$-r_{\text{H}_2} = \frac{dX_{\text{H}_2}}{dt} \quad (4.19)$$

, where N_{CoO} and N_{Co} is the quantity of CoO and metallic cobalt, respectively, and t is the time. The rate of hydrogen consumption as a function of time or temperature corresponds to the reduction profile measured in TPR experiments.

Temperature-programmed reduction (TPR) measurements were performed by weighing 45 mg catalyst into a quartz tube plugged with quartz wool and placed into a Micromeritics AutoChem HP-2950 TPR instrument. H_2 consumption was monitored with a thermal conductivity detector (TCD). The catalysts were dried at 120 °C for 1 h under 10 ml/min Ar flow and then cooled to 60 °C. Then the gas flow was switched to 5 vol% H_2 in Ar (flow rate 50 ml/min), and the samples were heated from 60 °C to 900 °C. Experiments were performed at a heating rate of 10 °C/min, 5 °C/min, 3 °C/min and 1 °C/min. The position of the peak maxima in the measured reduction profiles change as a function of heating rate according to the Kissinger equation [25]

$$\ln \frac{\beta}{T_{max}^2} = -\ln \frac{E_a}{A \cdot R \cdot p_{\text{H}_2}^q} - \frac{E_a}{R} \cdot \frac{1}{T_{max}} \quad (4.20)$$

, where β is the heating rate, T_{max} the temperature at peak maximum, E_a the activation energy, A the pre-exponential factor (or frequency factor), R the universal gas constant, p_{H_2} the hydrogen partial pressure and q the reaction order. The activation energy and the pre-exponential factor were determined from the slope and the intercept of the plot of $\ln(\beta/T_{max}^2)$ against $1/T_{max}$, respectively, assuming that the partial pressure of hydrogen is constant.

The rate constant (k) can then be determined using the Arrhenius equation:

$$k = A \cdot e^{-\frac{E_a}{RT}} \quad (4.21)$$

In order to achieve a better comparison of the reduction profiles performed at different

heating rates the TCD signal was normalised by the sample mass and heating rate according to:

$$\text{TCD}_{\text{normalised}} = \frac{\text{TCD}_{\text{measured}}}{m_{\text{sample}}} * \frac{\beta}{10^{\circ}\text{C}/\text{min}} \quad (4.22)$$

The TCD signal measured is recorded as the difference between the thermal conductivity of the effluent gas from the reactor tube compared to the thermal conductivity of a reference gas.

$$\text{TCD}_{\text{measured}} = \text{TCD}_{\text{reference}} - \text{TCD}_{\text{effluent gas}} \quad (4.23)$$

The thermal conductivity of the effluent gas decreases when hydrogen is consumed by the reduction of the sample. This leads to an increase of the measured TCD signal. Therefore, the peak area of the TPR profile should correlate to the amount of hydrogen consumed during the reduction. However, the thermal conductivity could be influenced by other factors, such as a temperature difference of the effluent gas to the reference channel or gaseous by-products, such as water. Water has a high thermal conductivity, which can lead to a decrease in the measured TCD signal. Similarly, carbon dioxide or nitrous oxide could form if metal carbonates or nitrates are present in the sample, which can have strong effects on the TCD signal. The TCD signal is often found to increase with time and temperature, which may be caused by a gas leak, whose magnitude increases with increasing temperature, or an increase in temperature (of the effluent gas) which causes a decrease of the thermal conductivity of the effluent gas. The effluent gas is generally passed through a cold trap, to prevent fluctuations of temperature and condense unwanted by-products. When the time of the experiment is excessively large (for example when the heating rate is very low), the cooling might fail with time causing a strong upwards slope of the TCD signal at high temperatures. Additionally, the signal of the reference detector may fluctuate, for example, due to small variations in the flow of the reference gas or temperature of the TCD detector. This outlines the importance of a correct background subtraction, when the hydrogen consumption of an experiment is to be evaluated. The difficulty lies in determining the background accurately, as different effects may result in a baseline drift to higher or lower values and the magnitude of the background drift may

change with time or temperature. Therefore, there is no standard procedure that can be applied for the background subtraction. Depending on the heating rate, and the shape of the observed background shift, the background was removed by linear regression, by using a polynomial or a combination of the above.

4.4 Results

4.4.1 Catalyst characterisation

XRD

Alumina-modified Co_3O_4 crystallites were prepared by impregnation of Co_3O_4 crystallites with varying amounts of alumina using aluminium sec-butoxide as the precursor. Co_3O_4 crystallites were obtained by calcination of a basic cobalt carbonate precursor at 300°C . Elemental analysis¹ of the obtained basic cobalt carbonate showed the compound corresponded to $\text{Co}(\text{CO}_3)_{0.45}(\text{OH})_{1.09} \cdot 0.64\text{H}_2\text{O}$. The XRD of the catalyst after drying and calcination is shown in Figure 4.4.

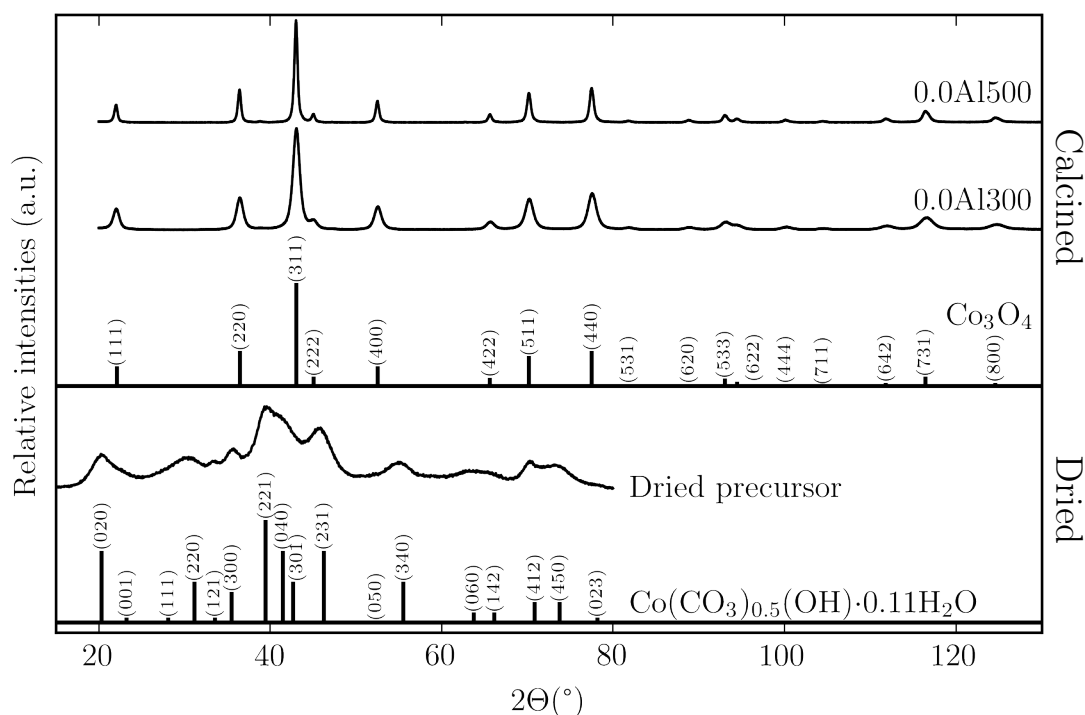


Figure 4.4: XRD of precipitated catalyst after drying and calcination. Dried precursor corresponds to crystalline phase of basic cobalt carbonate (PDF - 00-048-0083). Calcined catalysts correspond to crystalline phase of Co_3O_4 (PDF - 00-042-1467).

The XRD of the dried catalyst shows broad features which indicate that the com-

¹The carbon, hydrogen and nitrogen (no nitrogen was found) content was determined by elemental analysis (CHNO analyser). The cobalt content was determined by thermogravimetric analysis and the oxygen content was calculated from the mass balance.

pound was not well crystallised. The pattern corresponds to the crystalline phase of $\text{Co}(\text{CO}_3)_{0.5}(\text{OH}) \cdot 0.11 \text{H}_2\text{O}$, which is in close agreement with the chemical formula of the synthesised compound determined by elemental analysis. After calcination at 300°C , the precipitate was oxidised to Co_3O_4 . The XRD shows relatively broad peaks which indicate that small crystallites were formed. The average crystallite size as determined from the line width at half maximum from the (220) diffraction peak using the Scherrer equation was 14 nm. The (220) diffraction peak was chosen for determining the crystallite size because the peak with the highest intensity, the (311) diffraction peak is not suitable due to the overlap with the (222) diffraction peak.

The XRD of unmodified Co_3O_4 catalyst calcined at 500°C shows sharp peaks indicating a significant increase in crystallite size, which was determined to be 30 nm. This is expected as an increase in temperature increases the mobility of ions within a crystallite which may induce crystal growth [68].

The XRD of Co_3O_4 after modification with alumina, shown in Figure 4.5, shows no additional peaks, with the only detectable crystalline phase being that of Co_3O_4 . The alumina weight loading with a maximum of 2.5 wt% may be too low to be detectable in the XRD. Furthermore, alumina is expected to be very well dispersed on the surface of the catalyst, so that the alumina phase may not be crystalline enough to diffract the X-ray beam coherently.

As a comparison, the alumina precursor used for impregnation (aluminium sec-butoxide) was hydrolysed on air and then calcined at 300°C and 500°C . Figure 4.5 shows the XRD of the hydrolysed alumina compounds. After calcination at 300°C the hydrolysed alumina precursor formed a boehmite structure ($\gamma\text{-AlOOH}$), which began to transform into $\gamma\text{-Al}_2\text{O}_3$ when the calcination temperature was increased to 500°C . Thus, the catalysts contained Al^{3+} ions, which could be present as an aluminium oxide hydroxide or alumina phase².

The Co_3O_4 crystallite sizes determined by XRD are shown in Table 4.1. The Co_3O_4 crystallite size of the catalysts calcined at 300°C was 14 nm, independent of the alumina loading. The crystallite size of the catalysts calcined at 500°C was between 16 nm and

²Technically more correct would be to refer to an 'Al-phase' in order to avoid specifying the aluminium compound present. However, some readers may interpret this as a metallic aluminium rather than Al^{3+} -phase. To avoid this confusion, the catalysts are simply referred to as being 'alumina-modified' meaning that an aluminium oxide or aluminium oxide hydroxide of unknown crystalline structure and composition is present in the catalyst.

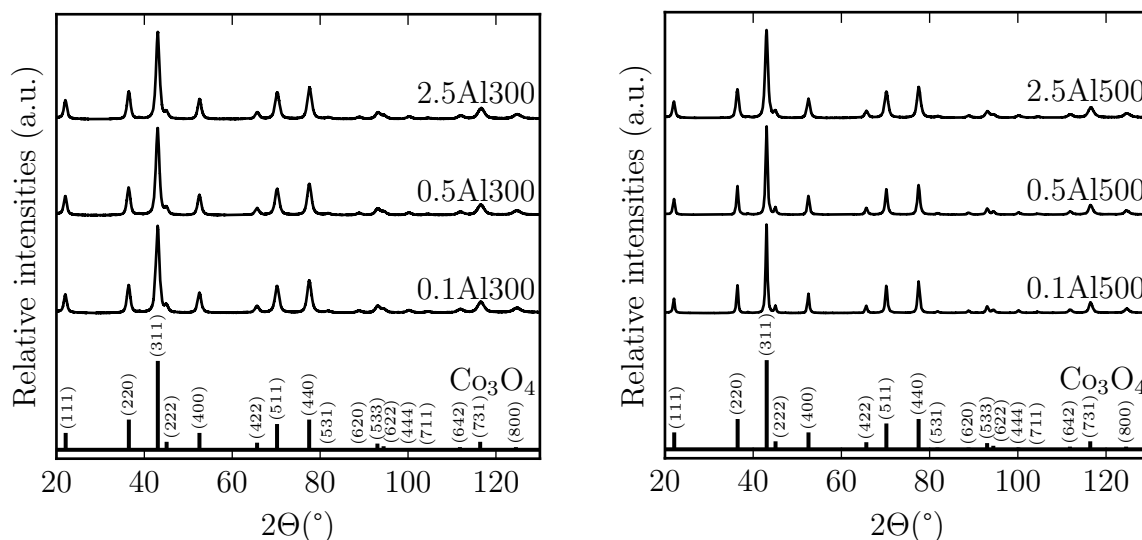


Figure 4.5: XRD of modified Co_3O_4 catalysts after calcination at 300°C and 500°C showing Co_3O_4 (PDF - 00-042-1467) as the only crystalline phase visible.

30 nm, and decreased with increasing alumina loading. The catalysts were prepared by calcining cobalt carbonate at 300°C followed by impregnation and re-calcination of the catalysts at 300°C or 500°C . For the series of catalysts calcined at 300°C , the temperature of the heat treatment before and after impregnation was the same. Hence, no crystallite growth was observed after impregnation, and the crystallite size was independent of the alumina loading. However, when the calcination temperature after impregnation was increased to 500°C , the Co_3O_4 crystallite size increased. The Co_3O_4 crystallite size in catalyst 0.0Al500 was 30 nm, which is more than twice as large as that of the 0.0Al300 catalyst. However, the crystallite size of Co_3O_4 in catalyst 2.5Al500 was 16 nm, which is only slightly larger than for catalysts calcined at 300°C . This shows that small quantities of alumina can significantly reduce sintering during calcination.

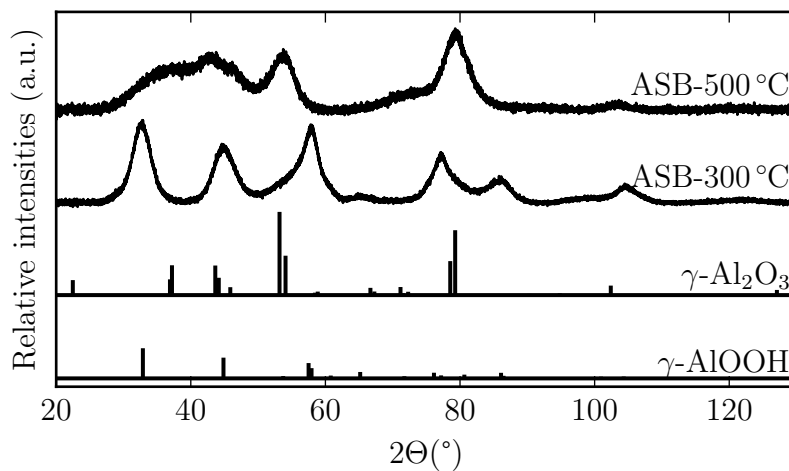


Figure 4.6: XRD of aluminium sec-butoxide (ASB) after hydrolysis on air and calcination at 300 °C and 500 °C. The sample calcined at 300 °C contains mainly γ -AlOOH (PDF-01-073-6509), while the sample calcined at 500 °C contains a mixture of γ -AlOOH and γ -Al₂O₃ (PDF - 01-074-4629).

Table 4.1: Co₃O₄ crystallite size of catalysts after calcination.

w _{Al} ^a (wt%)	T _{cal} (°C)	Crystallite size ^b (nm)
0.0	300	14
0.1		14
0.5		14
2.5		14
0.0	500	30
0.1		29
0.5		25
2.5		16

^aAl weight loading calculated as g(Al) per g(Co₃O₄)

^bDetermined by XRD from FWHM of the (220) reflection peak using the Scherrer equation.

TEM imaging

Figure 4.7 shows TEM images of unmodified and alumina modified catalysts after calcination at 300 °C and 500 °C. Catalysts calcined at 300 °C showed small crystallites of undefined shape. When the calcination temperature was increased to 500 °C, the crystallite size visibly increased, in accordance with the XRD experiments. The crystallite shape became slightly more defined with some of the crystallites displaying clearly defined edges. Furthermore, lattice fringes were visible in the TEM images, even at relatively low magnifications indicating a high crystallinity of these Co_3O_4 crystallites. An interlayer distance of 4.6 Å was determined from the lattice fringes, which corresponds to the interlayer distance of the (111) crystal plane of Co_3O_4 [69].

The TEM images of alumina-modified catalysts were in the first instance indistinguishable from the unmodified catalysts. No changes to the Co_3O_4 crystallite morphology or any signs of a distinguishable alumina phase was observed. The only observable difference was a change in crystallite size upon alumina modification, which is consistent with results obtained from XRD experiments. Therefore, only images of the catalysts with the highest alumina loading are discussed here.

Theoretically, an average crystallite size can be estimated by measuring the size of a sufficiently large number of crystallites in TEM images and performing a statistical analysis. However, the undefined shape and strong overlap of the crystallites in the bulk Co_3O_4 catalysts prepared in this work do not warrant an objective size determination by visual analysis, which is why crystallite size statistics are not provided.

STEM-EDS mapping was performed for catalyst 2.5Al300, and is shown in Figure 4.8. The EDS mapping showed that Al was homogeneously distributed as small clusters over the catalyst. The image shows a higher concentration of Al on the edges of the crystallites which indicates that the alumina phase was located on the Co_3O_4 surface. This illustrates that the impregnation procedure was successful in preparing a cobalt-alumina inverse-model catalyst.

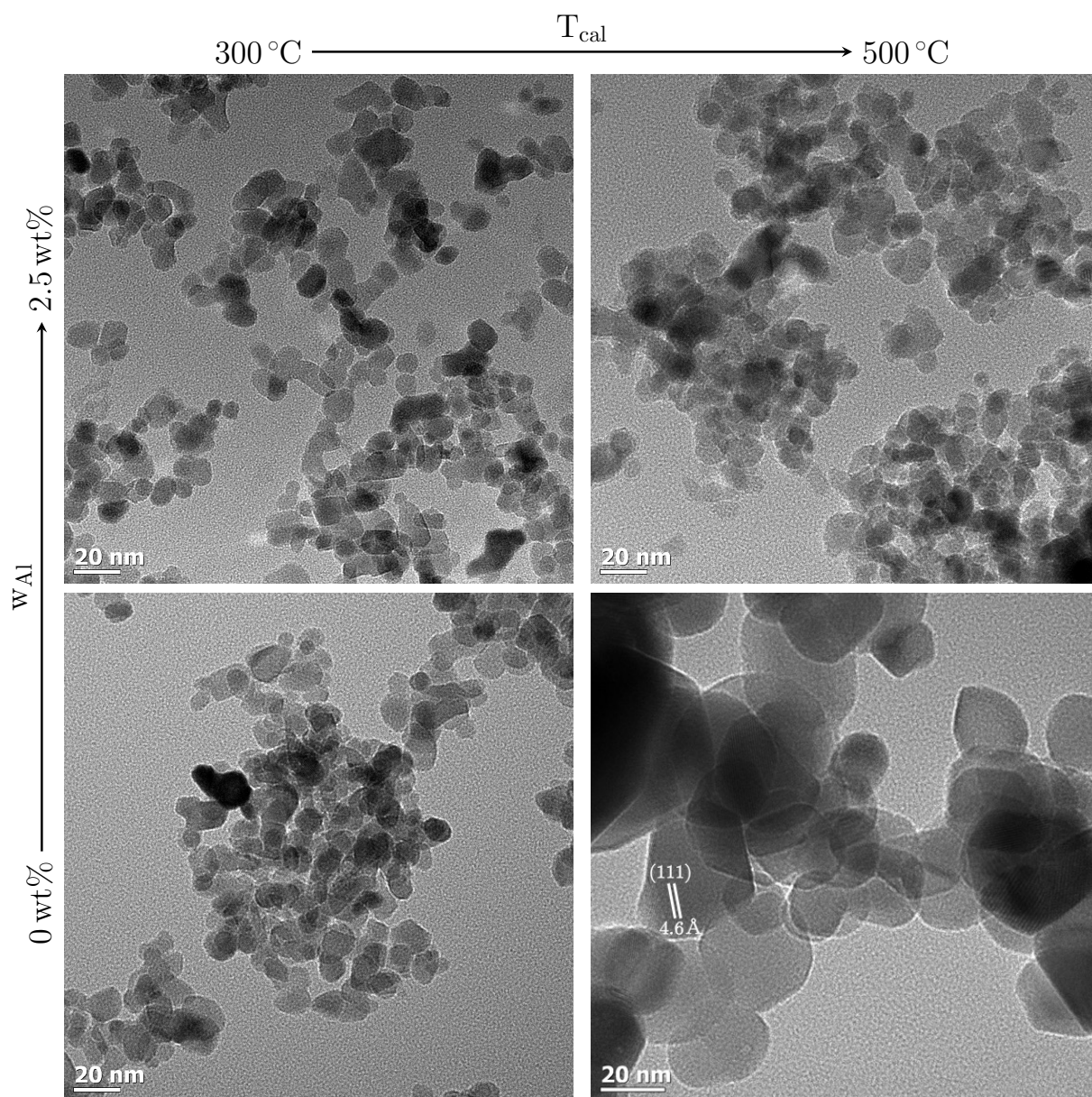
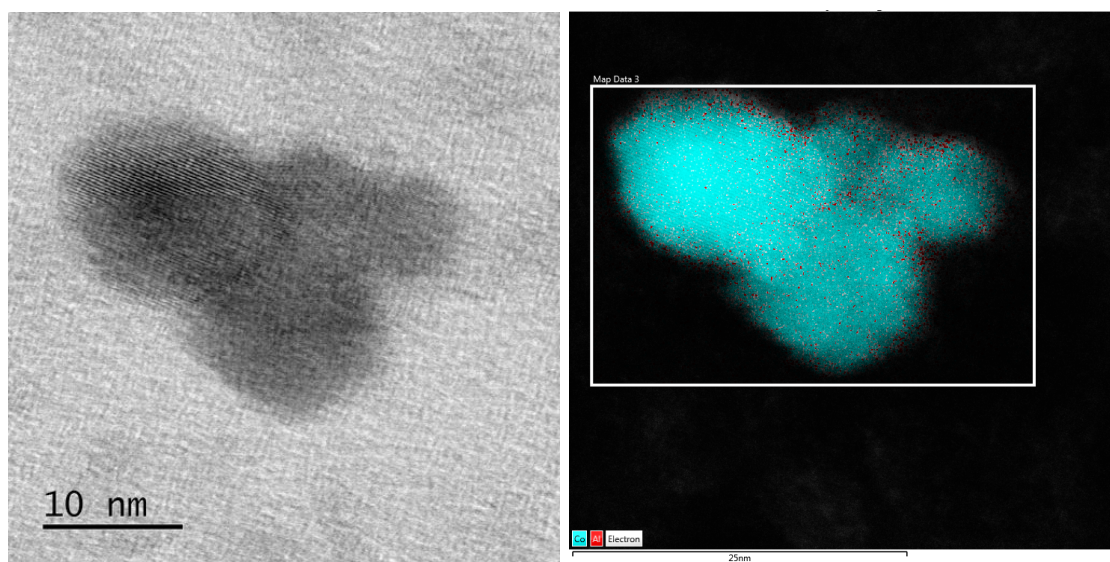


Figure 4.7: TEM images of unmodified Co_3O_4 and Co_3O_4 modified with 2.5 wt% Al calcined at 300 °C and 500 °C. Catalyst 0.0Al500 shows large crystallites with visible lattice fringes and clearly defined edges. No alumina phase is visible in the modified catalysts.



(a) 2.5Al300 bright field STEM.

(b) Co and Al mapped using EDS

Figure 4.8: Bright-field STEM and EDS mapping of 2.5Al300 showing Co in blue and Al in red. EDS mapping shows homogeneous distribution of the alumina phase on the surface of the Co_3O_4 crystallites.

4.4.2 Reduction experiments

Temperature-programmed reduction

The catalysts were reduced in 5 vol% H₂ in Ar at heating rates of 1, 3, 5 and 10 °C/min, and the hydrogen consumption was monitored with a TCD detector. The resulting reduction profiles are shown in Figure 4.9. The reduction profiles have been background corrected and normalised with respect to sample mass and heating rate according to Equation (4.22). The uncorrected reduction profiles are shown in Appendix A.

The peak area obtained by integrating the measured TCD signal as a function of time is expected to correspond to the hydrogen consumption, and hence the degree of reduction. This assumption does not hold when the catalyst contains impurities, such as remaining metal precursor [35–38]. Table 4.2 shows the evaluation of reduction profiles measured at a heating rate of 10 °C/min. The areas determined after background subtraction fluctuated considerably. This may be caused by errors in accurately determining the sample mass and difficulties in background subtraction. The underlying issue is that TPR as an experimental technique requires the use of very small amounts of sample, as a high sample quantity may skew the reduction profile [20]. This renders the technique very useful for the analysis of supported catalysts, which generally contain small quantities of < 20 wt% metal, but constitutes a difficulty when analysing bulk metal oxides, as done in this study. Small variations of 1-2 mg while weighing a bulk metal oxide sample may easily result in a difference of 5-10 % in the total amount of metal loaded into the instrument. Therefore, only minor importance is attributed to the measured peak areas. However, the peak areas determined for the catalyst containing 2.5 wt% Al calcined at 300 °C appear to be consistently larger, compared to the catalysts containing less alumina, or calcined at 500 °C. It is speculated that some organic material, from the aluminium sec-butoxide precursor used for impregnation, possibly butanol remained on the catalyst surface after calcination and is reduced to methane during the experiment leading to an increase in the total peak area. A similar trend has been observed in a study using titanium butoxide for impregnation [70].

The peak position and shape are the most important features of a reduction profile, as they give insights into the reduction mechanism and kinetics. Table 4.2 shows the temperature of the peak maxima and peak shoulders obtained by visual examination of

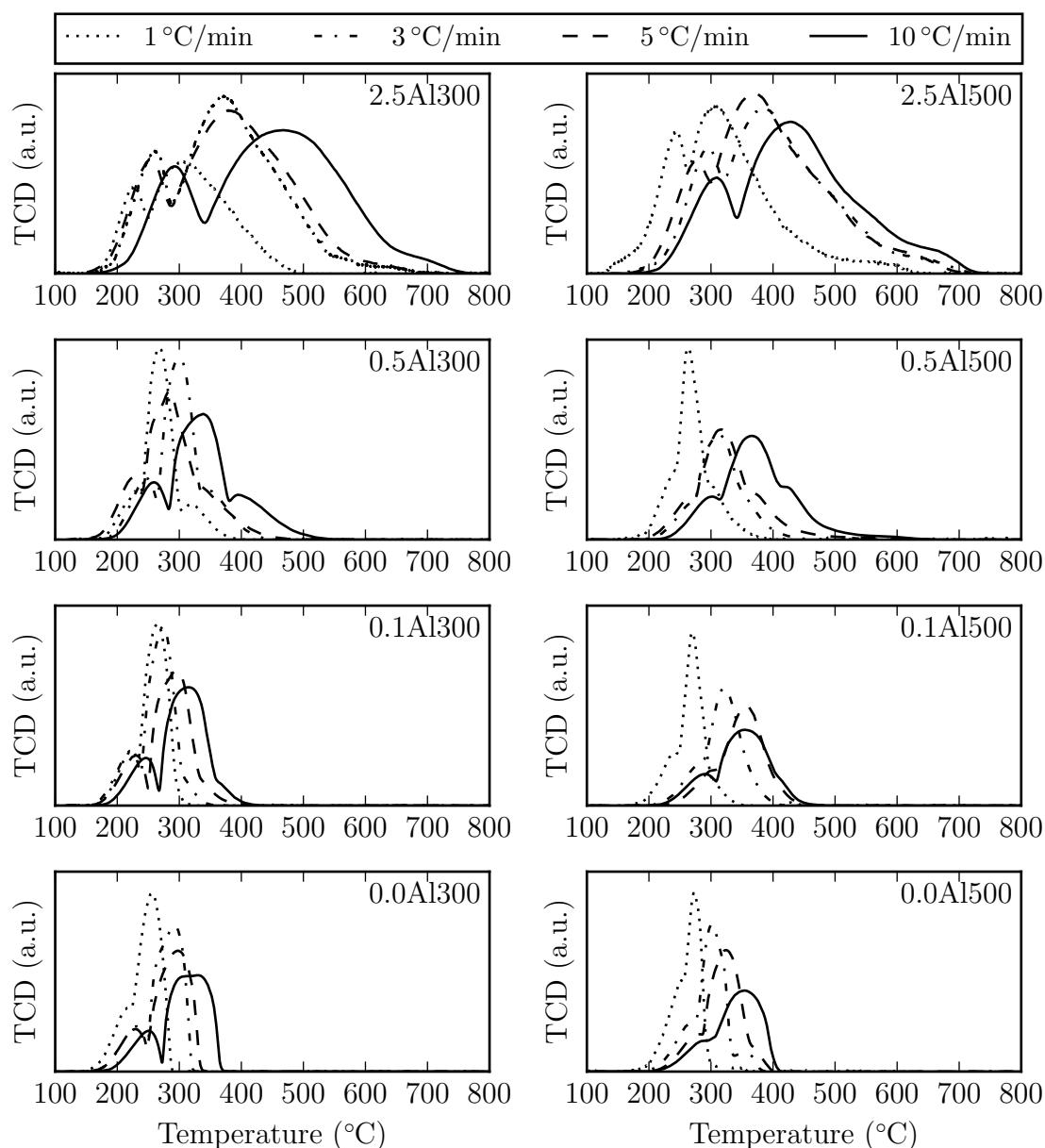


Figure 4.9: Reduction profile of unmodified and alumina-modified Co_3O_4 catalysts calcined at 300 °C and 500 °C measured at heating rates between 1 and 10 °C/min. The TCD signal has been background corrected and normalised with respect to the sample mass and heating rate.

the reduction profiles³.

³Peak maxima and inflexion points (shoulder) were estimated using the python package `signal.argrextrema` [71] to obtain all y_n in y for which $y_n \geq y_{n+x}$ (with x the window size). `Signal.argrextrema` was performed on the first derivative to estimate the position of inflexion points. The results were plotted, and adequate points for peak maxima and peak shoulders were selected manually. This crude selection process was followed because common peak finding algorithms are (surprisingly) bad at determining peak maxima of flat peaks in data with a low noise level.

Table 4.2: Peak maxima and peak areas of TPR experiments conducted using a heating rate of 10 °C/min.

T_{cal} (°C)	Al (wt%)	T_1^a (°C)	T_2^a (°C)	T_3^a (°C)	T_4^a (°C)	Area (TCD*min)
300	0	250	329	-	-	63
	0.1	246	314	369	-	63
	0.5	259	338	394	-	61
	2.5	292	468 ^b	468 ^b	685	72
500	0	288	354	-	-	58
	0.1	291	354	412	-	63
	0.5	302	366	417	-	73
	2.5	309	428	537	647	57

^aTemperature at peak maximum determined by visual examination

^bThe broadness of this peak suggests two strongly overlapping peaks

The following section will focus on the results obtained at a heating rate of 10 °C/min for a better comparison with literature, as TPR experiments are routinely performed using this heating rate.

The reduction profile of all catalysts shows two main reduction peaks, corresponding to the formation of CoO and metallic cobalt, respectively. For catalyst 0.0Al300, which is essentially bulk Co₃O₄, these peaks had maxima at 250 °C and 329 °C. For 0.0Al500, the two reduction peaks strongly overlapped and shifted to higher temperatures with maxima at 288 °C and 354 °C.

The peaks became broader and shifted towards higher temperatures with increasing alumina loading of the catalyst. For catalysts containing 0.1 wt% Al and 0.5 wt% Al a shoulder became visible with $T_{max} = 369 - 417$ °C and for the catalysts with the highest loading of 2.5 wt% Al, a high-temperature peak at $T_{max} = 647 - 685$ °C was observed. The first peak was shifted by 9-42 °C and the second peak was shifted by 9-139 °C compared to the unmodified catalysts. The peak shift increased with increasing alumina loading, except for catalyst 0.1Al300, where the peaks were shifted to slightly lower temperatures, compared to catalyst 0.0Al300. The magnitude of the shift of the catalysts calcined at 500 °C was smaller than for the catalysts calcined at 300 °C, whereas the absolute value of T_{max} was larger. The catalysts were all completely reduced at temperatures below 800 °C which suggests that CoAl₂O₄ was not formed [29]. However, the shift in the peak

temperature and the appearance of high-temperature peaks are clear indicators for the presence of metal-support interactions [33, 49].

This shows that minute amounts of alumina present on the cobalt oxide surface affect its reducibility significantly. The broadness of the peak for the alumina modified catalysts indicates that there were multiple simultaneously occurring reduction processes. This would suggest the presence of a range of more weakly to more strongly interacting cobalt-alumina species formed during the reduction process.

The kinetic parameters of each reduction process can be estimated by using the Kissinger equation, which describes the shift of the peak maximum as a function of the heating rate. This requires accurate and unbiased determination of the peak maxima. Due to the large peak overlap in most of the experiments (see Figure 4.9), the exact position of the peak maxima were determined by peak deconvolution using a Gaussian function⁴. Although Gaussian functions are commonly used in peak deconvolution, it should be noted, that the Gaussian function is in principle a poor descriptor for reduction profiles, whose peak shapes do not follow a normal distribution. This is demonstrated in Figure 4.10, which compares a typical reaction curve obeying first order kinetics with a fitted Gaussian function. It is shown that the Gaussian fitting slightly underestimates the peak maximum. The reduction profile cannot be simulated using more suitable kinetic reaction equations, without a priori knowledge of the activation energy and pre-exponential factor. Alternative fitting functions, such as Lorentzian- or pseudo-Voigt functions are, equal to the Gaussian function, symmetric functions, and therefore, do not accurately describe kinetic processes either. In the absence of a better descriptor, and in line with the literature, the peak deconvolution was performed using a Gaussian function [73].

In order to obtain meaningful results, constraints need to be imposed on the peak fitting. For example, a fitting resulting in a small peak which is completely contained within a larger peak would suggest that a very slow side reaction was occurring. This is not a reasonable description for a consecutive reduction reaction. Hence, such a result is physically meaningless and should be disregarded. Therefore, restrictions on the broadness of the fitted peaks were imposed, where necessary.

⁴Peak deconvolution was performed using the `least_squares()` function of the SciPy python package [71] which carries out the least squares minimisation of the residuals using the Trust Region Reflective algorithm [72].

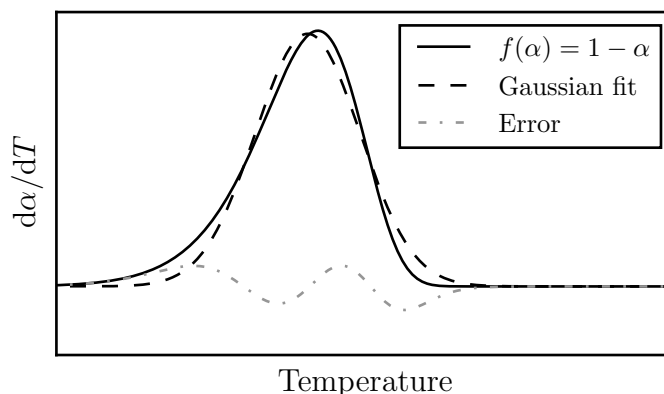


Figure 4.10: Simulated TPR profile following first order kinetics fitted with a Gaussian function. The peak maximum is slightly underestimated by the Gaussian fit.

From the hydrogen mass balance, it is expected that the first peak corresponding to the reduction of Co_3O_4 to CoO contributes to 25 % of the total peak area. To ensure, that the peak deconvolution reflects this behaviour a penalty was imposed to the residuals function to restrict results to those that provide a correct ratio of the peak areas. This measure was very successful in ensuring a good, automated peak deconvolution for all catalysts, except those containing 2.5 wt% Al. Catalyst 2.5Al300 and 2.5Al500 could only be fitted accurately when the penalty was lifted, which resulted in a peak area for the first peak of about 15 to 20 % of the total peak area. The detailed results of the peak deconvolution are provided in Appendix A.

The peak deconvolution for TPR experiments conducted using a heating rate of $10^\circ\text{C}/\text{min}$ is shown in Figure 4.11. The reduction profile of the unmodified bulk Co_3O_4 catalysts, show two narrow overlapping peaks, which were fitted using two Gaussian functions. When alumina was introduced to the catalyst, a third Gaussian function was necessary to resolve the appearing shoulder. The reduction profile of catalysts containing 2.5 wt% Al show very broad peaks, which were well fitted using four Gaussian functions. The peak maxima obtained from the peak deconvolution were taken as the basis for calculating the activation energy (E_a) and the pre-exponential factor (A) using the Kissinger method [25], and the results are tabulated in Table 4.3.

The activation energies calculated for the reduction of Co_3O_4 to CoO in the unmodified catalysts were 126 kJ/mol and 95 kJ/mol for the catalysts calcined at 300°C and 500°C ,

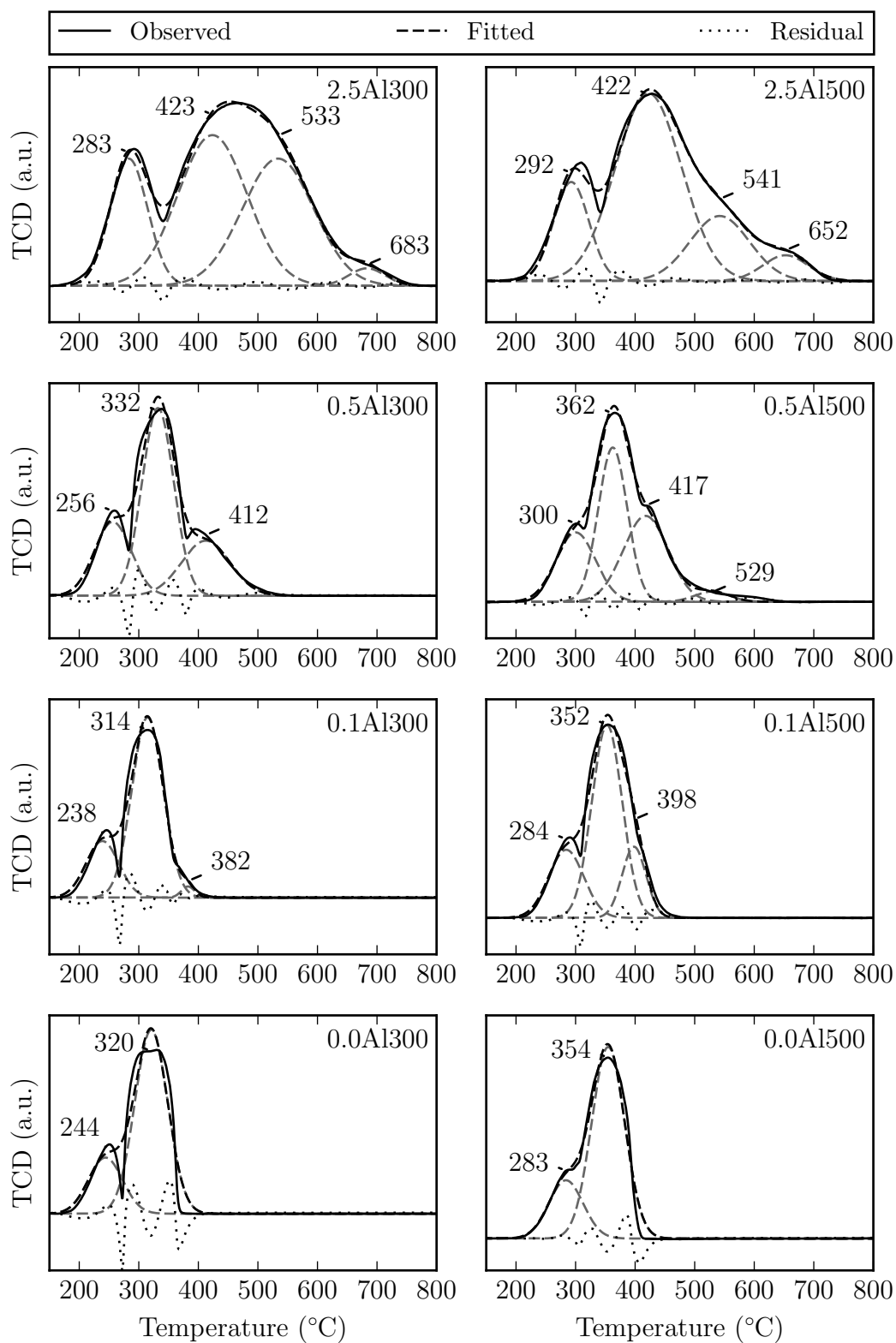


Figure 4.11: Results of peak deconvolution for TPR experiments conducted at 10°C/min.

respectively. The activation energy calculated for the consecutive reduction of CoO to metallic cobalt was lower; namely 84 kJ/mol and 69 kJ/mol for calcination at 300 °C and 500 °C, respectively. Values reported in the literature vary widely, between 25 kJ/mol and 133 kJ/mol for the reduction of Co₃O₄ and 25 kJ/mol to 87 kJ/mol for the consecutive reduction of CoO [33, 48, 74]. This suggests that the activation energy, similarly to the reduction profiles, can vary widely with the method of Co₃O₄ preparation. Despite the variations in the absolute value of the activation energy, the activation energies reported for the reduction of Co₃O₄ are consistently larger than those reported for the consecutive reduction of CoO to metallic cobalt.

When alumina was introduced, the activation energy of both reduction steps drastically decreased, except for catalyst 0.1Al300. Its activation energy was at 146 kJ/mol slightly larger compared to 126 kJ/mol for catalyst 0.0Al300. The margin of error for these calculations may be high, due to the difficulty in accurately determining peak maxima of highly overlapping peaks, reflected in low values for the goodness of fit (R^2) for the Kissinger plot. Taking into account the high error margin the activation energies of the alumina-modified catalysts were in the same order of magnitude (except for catalyst 0.1Al300) and varied between 60 and 73 kJ/mol for the reduction to CoO, and between 54 and 70 kJ/mol for the reduction to metallic cobalt. For all catalysts, the activation energy of the reduction of CoO to metallic cobalt was lower, than the activation energy of the reduction of Co₃O₄ to CoO.

The observed shift of the reduction peaks to higher temperatures suggest that the rate of the reaction decreased with increasing alumina content. The rate of reaction, as defined by the Arrhenius equation (4.24), is not only dependent on the activation energy (E_a), but also on the pre-exponential factor, or frequency factor (A).

$$k = A \cdot e^{-\frac{E_a}{RT}} \quad (4.24)$$

The retardation of the reduction observed here is expressed, not in the change in the activation energy, but in a decrease of the pre-exponential factor. The pre-exponential factor decreased by at least one order of magnitude when alumina was introduced, and a clear trend was observed between the increase in alumina loading and calcination temperature,

and a decrease in the pre-exponential factor. Table 4.3 shows the reaction constant k , calculated at the temperature of the peak maximum observed at a heating rate of 10 °C/min. The reaction rate was found to decrease with increasing alumina loading and increasing calcination temperature. This leads to the conclusion that the addition of alumina to cobalt oxide did not result in a thermodynamic but rather in a kinetic hindrance of the reduction process.

This may be different for the catalysts containing 2.5 wt% Al. The high-temperature peak appearing above 600 °C had a slightly higher activation energy of 83 kJ/mol and 117 kJ/mol, for catalyst 2.5Al300 and 2.5Al500, respectively, and equal or higher pre-exponential factors than prior reduction steps.

Table 4.3: Kinetic evaluation of TPR profiles using the Kissinger equation after peak deconvolution.

T_{cal} (°C)	w_{Al} (wt%)	Peak	E_a (kJ/mol)	A (s^{-1})	k^a (min^{-1})	R^{2b}	
300	0	1	126	4.1E+12	38.0	0.96	
		2	84	8.0E+06	18.0	0.99	
	0.1	1	146	5.8E+14	41.3	0.76	
		2	99	2.7E+08	23.1	0.93	
		3	53	2.3E+03	8.2	0.97	
	0.5	1	71	2.2E+06	11.8	0.47	
		2	70	3.0E+05	14.1	0.79	
		3	58	4.2E+03	9.3	0.74	
		4	83	4.3E+03	6.8	0.93	
	500	0	1	95	2.8E+08	18.8	0.98
			2	69	1.4E+05	13.2	1.00
		0.1	1	60	5.9E+04	6.9	0.83
2			54	4.2E+03	6.4	0.92	
3			50	6.6E+02	5.0	0.91	
0.5		1	73	1.4E+06	16.3	0.95	
		2	59	1.5E+04	11.6	0.98	
		3	60	5.7E+03	9.8	0.99	
		4	37	1.9E+01	4.3	0.97	
2.5		1	61	8.6E+04	10.4	0.83	
		2	54	1.5E+03	7.6	0.91	
		3	59	6.8E+02	6.2	0.93	
	4	117	7.1E+05	9.4	0.90		

^aReaction constant k determined from Arrhenius equation at the temperature of the peak maximum observed at a heating rate of 10 °C/min.

^bCoefficient of determination for the linear regression analysis of the Kissinger plot.

Kinetic modelling of TPR data

In theory, it should be possible to compute a reaction profile obtained by TPR or gravimmetrical experiments using available kinetic models for solid-state reactions. Several different computational methods have been reported [23, 24, 26]. In the case of non-isothermal experiments, the general route involves determining the activation energy, and then fitting the pre-exponential factor using kinetic expressions for a set of possible reaction mechanisms. This method was applied by Wimmers et al. [26] to determine the reaction mechanism for the reduction of Fe_3O_4 . The TPR profile was fitted by choosing appropriate kinetic expressions and varying the pre-exponential factor (while keeping the activation energy constant), until the peak maximum of the modelled and experimental dataset matched.

This procedure is demonstrated in Figure 4.12. It is evident that different reaction mechanisms result in drastically different peak shapes. Wimmers et al. [26] chose the best matching reaction mechanism by comparing the full width at half maximum (FWHM) of the modelled and observed peak.

This procedure is only appropriate for the evaluation of a single-step reduction mechanism. In multi-step reduction processes, where peak overlap occurs, the FWHM can not be accurately determined. In these cases, a least-square analysis may be better suited. The residual sum of squares (RSS) for the least-square analysis can be calculated as

$$\text{RSS} = \sum_{i=1}^n (y_i - f(x_i))^2 \quad (4.25)$$

, where y_i is the i^{th} experimental value and $f(x_i)$ is the value of the modelled function at x_i .

It is not reasonable to treat each reduction step as completely autonomous. For example, to correctly describe the rate of metallic cobalt formation, the increase in the concentration of CoO due to the reduction of Co_3O_4 needs to be taken into account. However, in order to obtain a high-quality fit, a good initial guess of the fitting parameters should be obtained. An initial guess of the fitting parameters was obtained by treating each reduction step as autonomous, and applying the method described by Wimmers et al. [26].

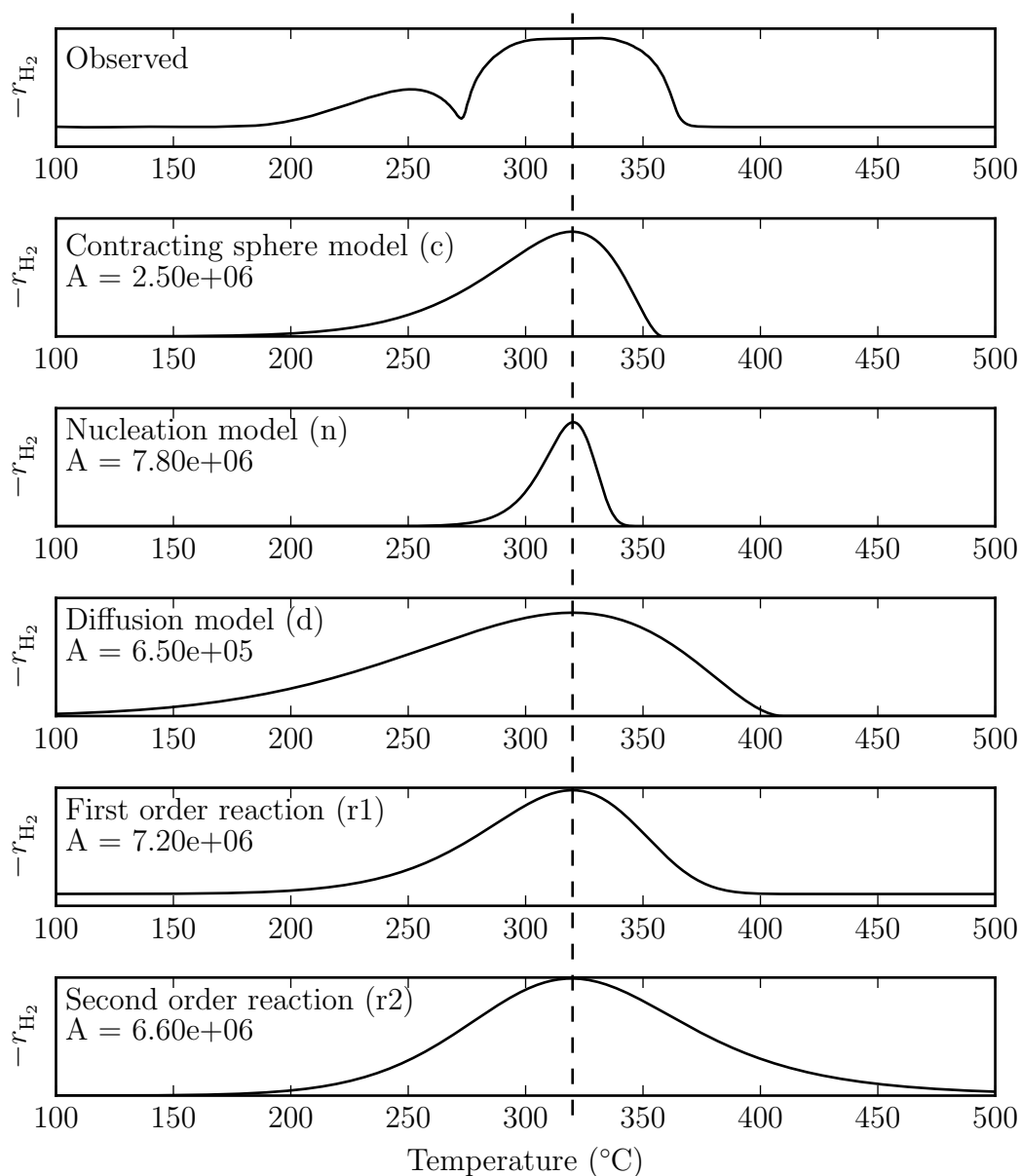
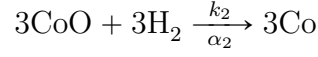
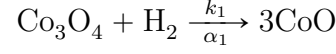


Figure 4.12: Computation of the TPR profile for the reduction of CoO to metallic cobalt compared to the reduction profile of bulk Co_3O_4 . The hydrogen consumption was calculated by computing the pre-exponential factor at an activation energy of 84 kJ/mol, so that the computed peak maximum matches the peak maximum of the measured TPR profile ($T_{max} = 320^\circ\text{C}$).

The reduction of bulk Co_3O_4 is described by the following reaction equations



and the rate of reaction (defined per mole Co) can be described by:

$$-r_{\text{Co}_3\text{O}_4} = -\frac{d[\text{Co}_3\text{O}_4]}{dt} = k_1 f(\alpha_1) \quad (4.26)$$

$$-r_{\text{CoO}} = -\frac{d[\text{CoO}]}{dt} = \frac{1}{3}k_2 f(\alpha_2) - k_1 f(\alpha_1) \quad (4.27)$$

$$r_{\text{Co}} = \frac{d[\text{Co}]}{dt} = \frac{1}{3}k_2 f(\alpha_2) \quad (4.28)$$

For known values of the activation energy and pre-exponential factor, the conversion fraction (α) can be calculated for a chosen reaction mechanism by solving the set of differential equations (4.26)-(4.28)⁵. It is important to realise, that the conversion fraction α , is not equal to the extent of reaction, but is defined such that:

$$\alpha_{1,t} = \frac{N_{\text{Co}_3\text{O}_4,0} - N_{\text{Co}_3\text{O}_4,t}}{N_{\text{Co}_3\text{O}_4,0}} \quad \text{and} \quad \alpha_{1,t=0} = 0 \quad (4.29)$$

$$\alpha_{2,t} = \frac{3N_{\text{Co}_3\text{O}_4,0} - N_{\text{CoO},t}}{3N_{\text{Co}_3\text{O}_4,0}} \quad \text{and} \quad \alpha_{2,t=0} = 1 \quad (4.30)$$

Taking into account the mass balance,

$$3N_{\text{Co}_3\text{O}_4,t} + N_{\text{CoO},t} + N_{\text{Co},t} = 3N_{\text{Co}_3\text{O}_4,0} \quad (4.31)$$

⁵The differential equations were solved using python's `scipy.integrate.odeint()` package [71]. The differential equations can only be solved when the initial value of α at the start of the reaction ($t = 0$) is known. The conversion fraction α is defined such that α_1 at $t = 0$ must be 0 and all subsequent products $\alpha_{i>1}$ must be 1. However, the equation for the reaction mechanism ($f(\alpha)$) may not be defined at $\alpha = 0$ or $\alpha = 1$ (e.g. Avrami-equation). Therefore, the initial values were chosen to be $1E - 10$ and $1 - 1E - 10$, respectively.

the amount of reactants can be calculated by:

$$N_{\text{Co}_3\text{O}_4,t} = N_{\text{Co}_3\text{O}_4,0} - \alpha_1 \cdot N_{\text{Co}_3\text{O}_4,0} \quad (4.32)$$

$$N_{\text{CoO},t} = 3N_{\text{Co}_3\text{O}_4,0} - 3\alpha_2 \cdot N_{\text{Co}_3\text{O}_4,0} \quad (4.33)$$

$$N_{\text{Co},t} = 3N_{\text{Co}_3\text{O}_4,0} - 3N_{\text{Co}_3\text{O}_4,t} + N_{\text{CoO},t} \quad (4.34)$$

Taking into account the hydrogen mass balance, the hydrogen consumption ($-r_{\text{H}_2}$) can be described by:

$$\begin{aligned} -r_{\text{H}_2} &= \frac{1k_1f(\alpha_1) + 3\frac{1}{3}k_2f(\alpha_2)}{4} \\ &= \frac{k_1f(\alpha_1) + k_2f(\alpha_2)}{4} \end{aligned} \quad (4.35)$$

The reduction profile can be computed by solving Equation (4.35). The reduction profiles were fitted using the value of the activation energy derived by the Kissinger method, and varying the pre-exponential factor. Figure 4.13 shows an example of the computation performed assuming a first order reaction mechanism for both reaction steps. The α curve shows how the conversion of Co_3O_4 runs from 0 to 1 and the conversion of CoO , as an intermediate product runs from 1 through a minimum back to 1. Hence, the consecutive reaction from Co_3O_4 to CoO to metallic cobalt shows a steady decrease of the Co_3O_4 concentration and a steady increase of the cobalt concentration, while the CoO concentration goes through a maximum.

This demonstrates that this reaction model gives a qualitatively correct representation of the reduction process. However, the computed reduction profile does not compare well with the observed reduction profile, indicating that either the reduction does not obey first order reaction kinetics, or that the kinetic parameters were chosen incorrectly.

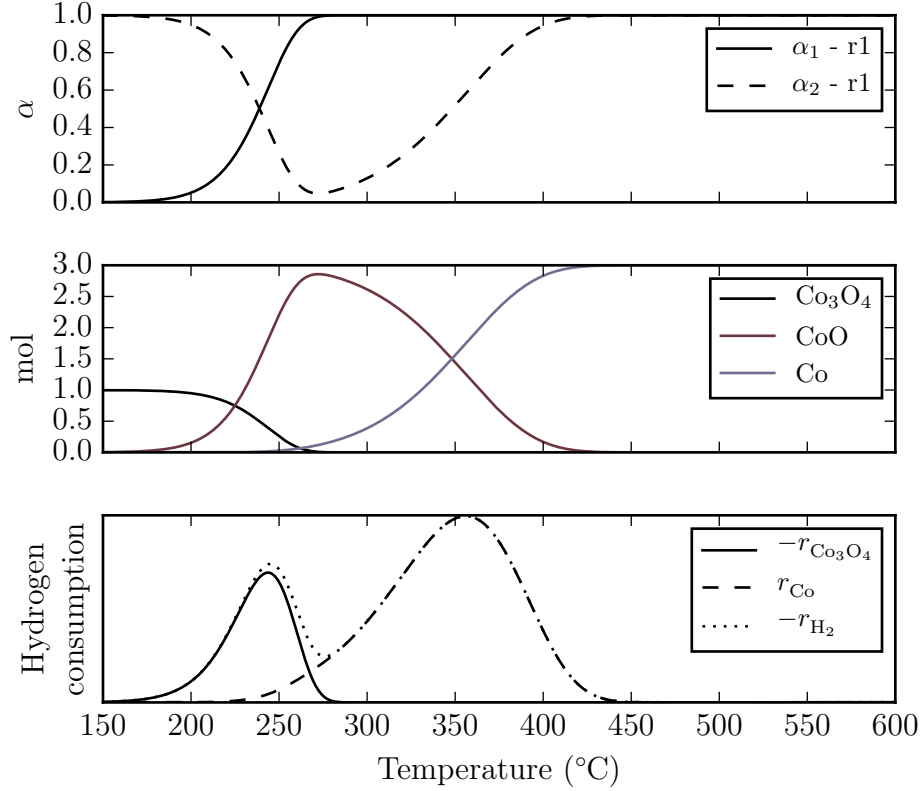


Figure 4.13: Computation of the reduction profile of 1 mol of Co_3O_4 , if the reduction was to follow first order reaction kinetics. Reduction of $\text{Co}_3\text{O}_4 \rightarrow \text{CoO}$ was computed with $E_a=126 \text{ kJ/mol}$ and $A=3.08 \cdot 10^{12} \text{ s}^{-1}$, and reduction of $\text{CoO} \rightarrow \text{Co}^0$ was computed with $E_a=84 \text{ kJ/mol}$ and $A=7.20 \cdot 10^6 \text{ s}^{-1}$.

The following kinetic reaction mechanisms were used for the computation of the experimentally observed TPR profiles [14]:

$$\text{First order reaction :} \quad f(\alpha) = 1 - \alpha \quad (\text{r1})$$

$$\text{Second order reaction:} \quad f(\alpha) = (1 - \alpha)^2 \quad (\text{r2})$$

$$\text{Contracting sphere model:} \quad f(\alpha) = 3(1 - \alpha)^{\frac{2}{3}} \quad (\text{c})$$

$$\text{Nucleation model:} \quad f(\alpha) = 3(1 - \alpha)[-\ln(1 - \alpha)]^{\frac{2}{3}} \quad (\text{n})$$

$$\text{Diffusion model:} \quad f(\alpha) = \frac{3(1 - \alpha)^{\frac{2}{3}}}{2 \left(1 - (1 - \alpha)^{\frac{1}{3}}\right)} \quad (\text{d})$$

This renders five possible reaction mechanisms for each of the two reduction steps, which results in $5^2 (=25)$ possible combinations of reaction mechanisms.

Figure 4.14 shows the four kinetic models with the lowest RSS values for the reduction of 0.0Al300. It can be seen, that the model predicting a second order reaction followed by a contracting sphere model results in the best fit. However, the model predicting a second order reaction followed by a first order reaction gives an almost equally good fit. Hence, it is not possible to distinguish whether the reaction of CoO to metallic cobalt follows the contracting sphere model or a first order reaction. This demonstrates the difficulty in establishing the correct reaction model following this procedure.

Figure 4.15 shows the fitting results for catalyst 0.0Al500. In this case, the best result was obtained for a diffusion controlled reaction followed by a contracting sphere model. It is tempting to ascribe this to the increased Co_3O_4 crystallite size of the catalyst. However, applying a second order reaction model to the data gives a reasonable fit as well. Again the results do not allow to unambiguously assign a reaction model to the reduction process.

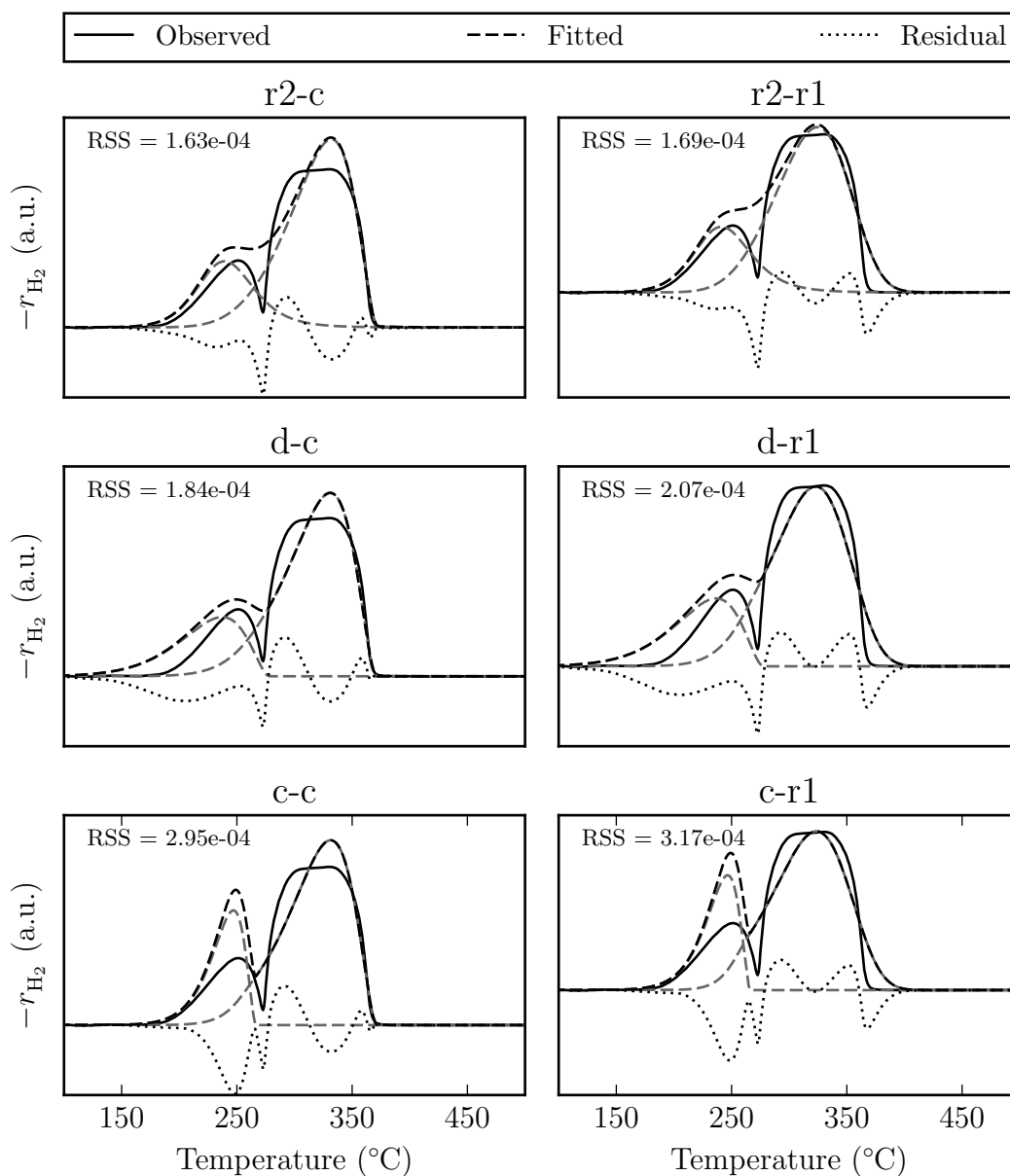


Figure 4.14: Computation of the reduction profile of catalyst 0.0Al300 (observed at a heating rate of $10^{\circ}C/min$). The plot title represents the reaction model used for each reduction step: first order reaction (r1), second order reaction (r2), contracting sphere model (c), nucleation model (n) and diffusion model (d).

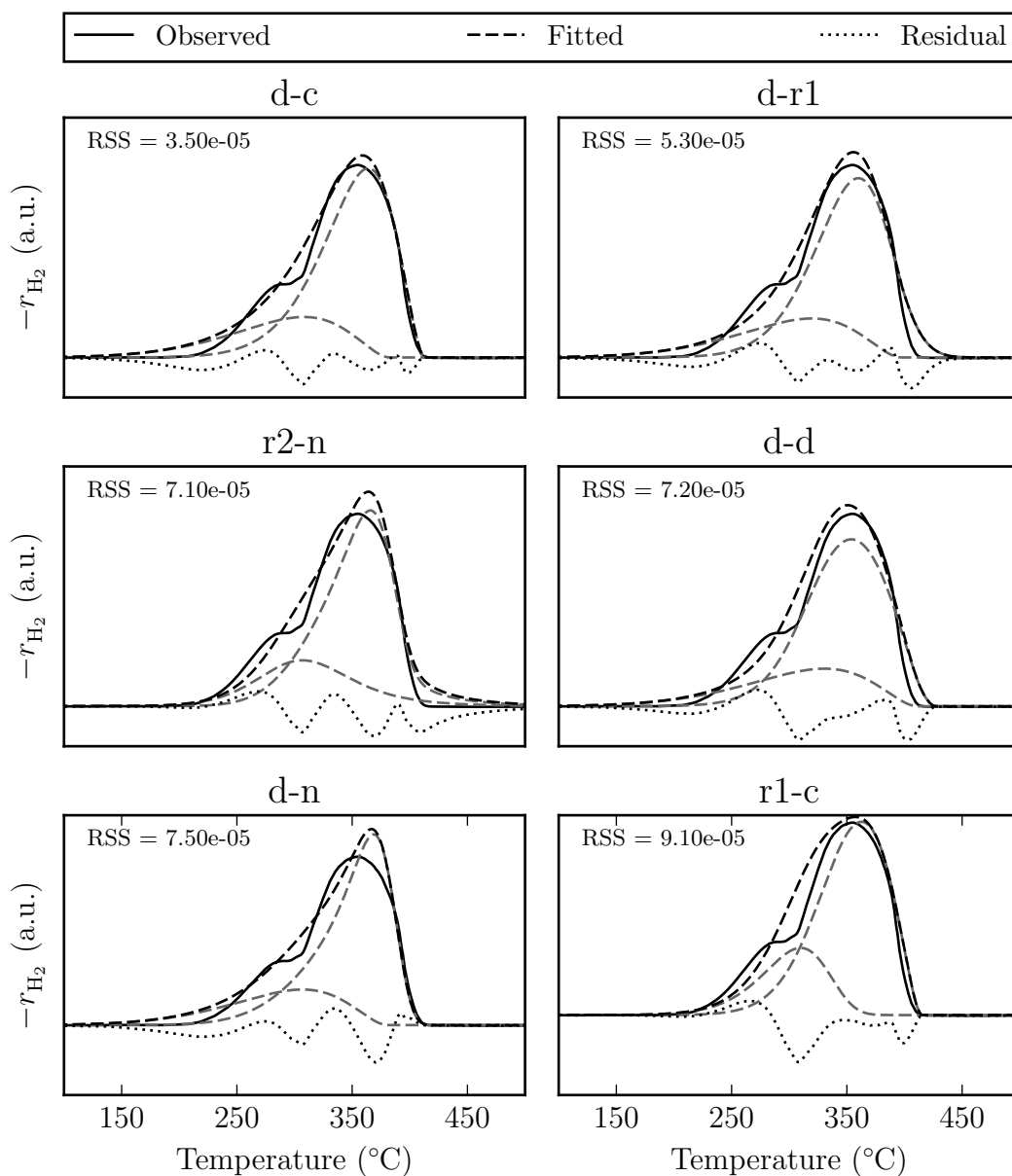
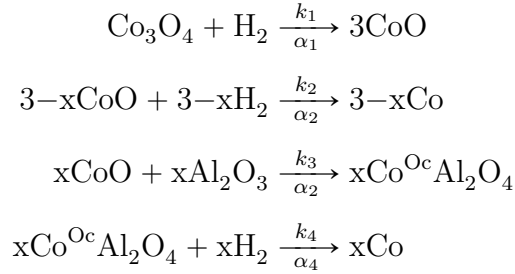


Figure 4.15: Computation of the reduction profile of catalyst 0.0Al500 (observed at a heating rate of 10 °C/min). The plot title represents the reaction model used for each reduction step: first order reaction (r1), second order reaction (r2), contracting sphere model (c), nucleation model (n) and diffusion model (d).

Catalysts containing 0.1 wt% Al showed three peaks during reduction (see Figure 4.11 on page 58). This indicates the formation of a mixed cobalt-alumina phase. It is assumed that this mixed cobalt-alumina phase forms from pre-reduced CoO interacting with alumina at high temperatures, where ion mobility is large. The mixed cobalt-alumina phase is denoted $\text{Co}^{\text{Oc}}\text{Al}_2\text{O}_4$ indicating that the Co^{2+} ions may occupy octahedral sites, and that the phase is not equivalent to CoAl_2O_4 . It should be noted, that the mixed cobalt-alumina phase is expected to be a non-stoichiometric surface phase, but for the purpose of this analysis a stoichiometry of $\text{Co}:\text{Al} = 1:2$ is assumed. The proposed reaction scheme consists of four consecutive reactions:



, where x is the fraction of CoO which reacts with alumina and α is defined as:

$$\alpha_{1,t} = \frac{N_{\text{Co}_3\text{O}_4,0} - N_{\text{Co}_3\text{O}_4,t}}{N_{\text{Co}_3\text{O}_4,0}} \quad \text{and} \quad \alpha_{1,t=0} = 0 \quad (4.36)$$

$$\alpha_{2,t} = \frac{3N_{\text{Co}_3\text{O}_4,0} - N_{\text{CoO},t}}{3N_{\text{Co}_3\text{O}_4,0}} \quad \text{and} \quad \alpha_{2,t=0} = 1 \quad (4.37)$$

$$\alpha_{4,t} = \frac{3N_{\text{Co}_3\text{O}_4,0} - N_{\text{Co}^{\text{Oc}}\text{Al}_2\text{O}_4,t}}{3N_{\text{Co}_3\text{O}_4,0}} \quad \text{and} \quad \alpha_{4,t=0} = 1 \quad (4.38)$$

The rate of reaction is then described by:

$$-r_{\text{Co}_3\text{O}_4} = -\frac{d\text{Co}_3\text{O}_4}{dt} = k_1 f(\alpha_1) \quad (4.39)$$

$$-r_{\text{CoO}} = -\frac{d\text{CoO}}{dt} = \frac{1}{3}k_2 f(\alpha_2) + \frac{1}{3}k_3 f'(\alpha_2) - k_1 f(\alpha_1) \quad (4.40)$$

$$-r_{\text{Co}^{\text{Oc}}\text{Al}_2\text{O}_4} = -\frac{d\text{Co}^{\text{Oc}}\text{Al}_2\text{O}_4}{dt} = \frac{1}{3}k_4 f(\alpha_4) - \frac{1}{3}k_3 f'(\alpha_2) \quad (4.41)$$

$$r_{\text{Co}} = \frac{d\text{Co}}{dt} = \frac{1}{3}k_2 f(\alpha_2) + \frac{1}{3}k_4 f(\alpha_4) \quad (4.42)$$

The reaction of CoO to metallic cobalt and the reaction of CoO with alumina to form

the mixed cobalt-alumina phase are both a function of the CoO concentration, which is defined by α_2 . However, the two reaction steps may follow a different reaction mechanism, which is why the rate of the reactions are described by $f(\alpha_2)$ and $f'(\alpha_2)$, respectively. It should be noted, that the formation of $\text{Co}^{\text{Oc}}\text{Al}_2\text{O}_4$ is non-reductive and does therefore not contribute to the total hydrogen consumption.

The hydrogen consumption is described by:

$$\begin{aligned} -r_{\text{H}_2} &= \frac{-r_{\text{Co}_3\text{O}_4} + 3r_{\text{Co}}}{4} = \frac{k_1f(\alpha_1) + 3(\frac{1}{3}k_2f(\alpha_2) + \frac{1}{3}k_4f(\alpha_4))}{4} \\ &= \frac{k_1f(\alpha_1) + k_2f(\alpha_2) + k_4f(\alpha_4)}{4} \end{aligned} \quad (4.43)$$

Figure 4.16 shows the computed reduction profile of a Co_3O_4 catalyst forming a mixed cobalt-alumina phase. In the computed profile, the concentration of the mixed cobalt-alumina phase remains very small. Attempts to apply such a reduction model to fit the experimental reduction profile of catalysts containing 0.1 wt% Al did not result in any satisfactory results.

Although the formation of $\text{Co}^{\text{Oc}}\text{Al}_2\text{O}_4$ does not contribute to the hydrogen consumption, it influences the rate of formation of metallic cobalt, which affects the reaction kinetics. The kinetic parameters for the formation of $\text{Co}^{\text{Oc}}\text{Al}_2\text{O}_4$ cannot be estimated from the reduction profile, and must be guessed.

The choice of kinetic parameters (even if it is only a first guess, for a fitting parameter), does drastically influence the reaction profile. If the formation of $\text{Co}^{\text{Oc}}\text{Al}_2\text{O}_4$ is slow in comparison to its reduction to metallic cobalt ($k_3f'(\alpha_2) \ll k_4f(\alpha_4)$), then its concentration in the sample will be negligible, as any $\text{Co}^{\text{Oc}}\text{Al}_2\text{O}_4$ formed is immediately reduced to metallic cobalt. If however, the reduction of $\text{Co}^{\text{Oc}}\text{Al}_2\text{O}_4$ is slow in comparison to its formation ($k_3f'(\alpha_2) \gg k_4f(\alpha_4)$), the concentration profile of $\text{Co}^{\text{Oc}}\text{Al}_2\text{O}_4$ should go through a maximum. As the TPR profile does not contain any information on the concentration of $\text{Co}^{\text{Oc}}\text{Al}_2\text{O}_4$ during the reaction, the kinetic evaluation cannot be used to adjudicate which of these two cases is correct. At this point, an objective analysis of the data is no longer possible.

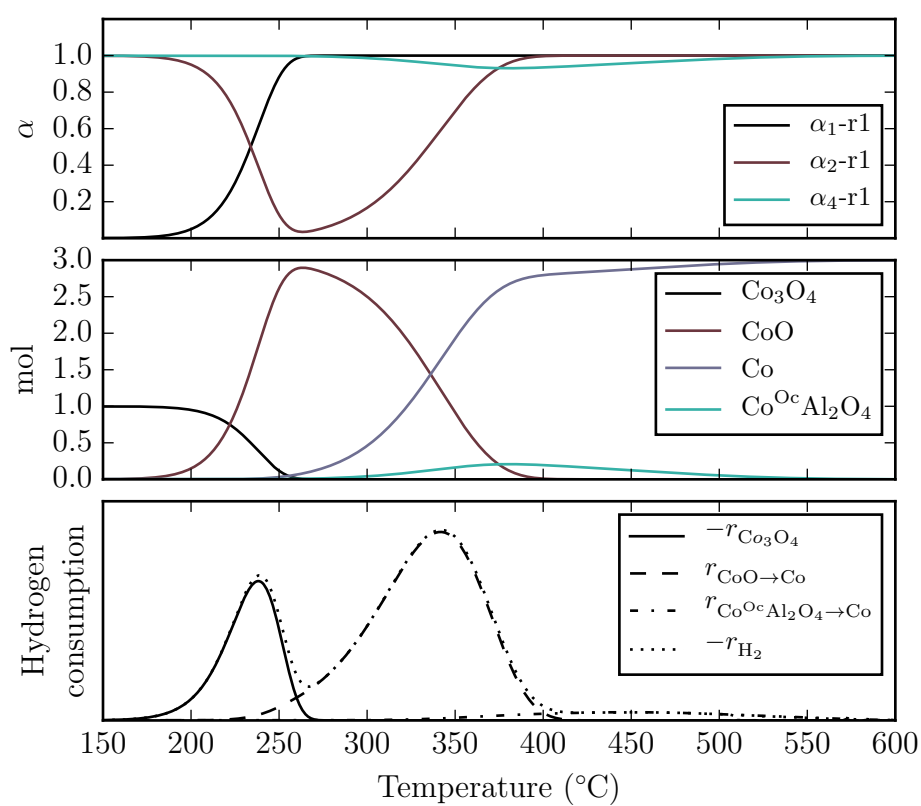


Figure 4.16: Computation of the reduction profile of alumina-modified Co_3O_4 including the formation of a mixed-metal support phase ($\text{Co}^{\text{O}^c}\text{Al}_2\text{O}_4$).

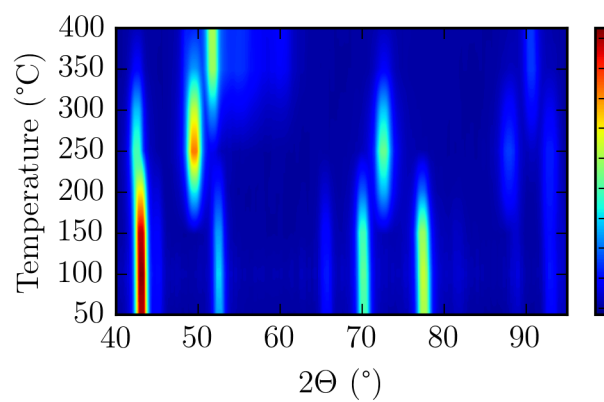
***In situ* XRD reduction**

In situ XRD reduction experiments were performed on the set of catalysts calcined at 300 °C, by reducing the catalysts in pure hydrogen while increasing the temperature and taking XRD measurements every 50 °C. The diffraction patterns as a function of time are plotted in Figure 4.17. It can be seen, that the catalysts reduced from the initial Co_3O_4 phase into a mixture of fcc and hcp cobalt. The phase content at each reduction step and crystallite sizes were determined by Rietveld refinement. The results of the Rietveld refinement are shown in Figure 4.18.

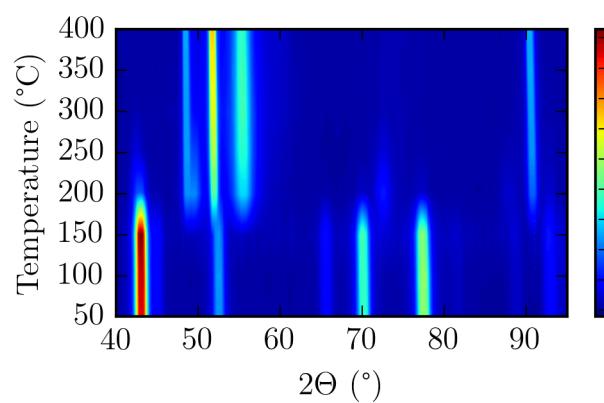
The onset of reduction was observed between 150 °C and 200 °C. At 200 °C, catalyst 0.0Al300 already showed a high degree of reduction. It contained 67 wt% metallic cobalt, in roughly equal amounts of fcc and hcp cobalt, 7 wt% CoO, and 24 wt% of Co_3O_4 . The catalyst was completely reduced at 250 °C. With increasing temperature the relative content of hcp cobalt increased to 70 wt%, while its crystallite size remained fairly constant at 5 nm to 6 nm; the size of fcc crystallite size increased to 55 nm.

For the catalyst containing 0.5 wt% Al, the reduction process was slowed down, and full reduction was only achieved at 300 °C. When the alumina content was increased to 2.5 wt%, the reduction was slowed down even more severely, and the catalyst did not reach complete reduction. At 400 °C, 8 wt% CoO were detected. Here, the sequential reduction of Co_3O_4 to CoO and metallic cobalt could be observed. Initially, the Co_3O_4 crystallite size and phase content decreased, while the CoO crystallite size and phase content increased, reaching a maximum of 8 nm and 91 wt% at 300 °C. At this point, no crystalline Co_3O_4 phase was detected, and the onset of metallic cobalt formation was observed. It is interesting to note that the maximum crystallite size of CoO observed in all catalysts was in a narrow range between 8 nm and 10 nm, independent of the alumina content. This seems to suggest that there is a minimum crystallite size necessary for nucleation of the metal phase. Hence, if the nucleation and crystallite growth of CoO is hindered, the formation of metallic cobalt is delayed, as the necessary crystallite size is only achieved at higher temperatures.

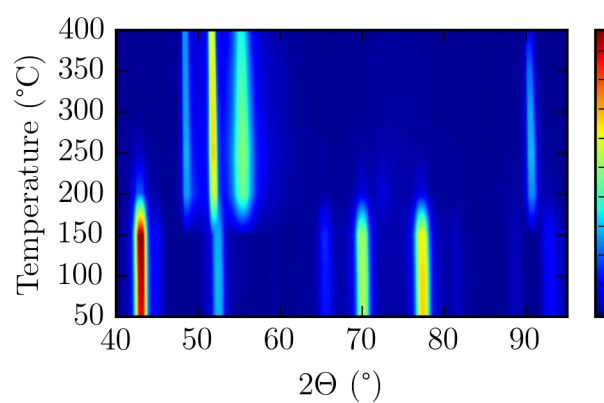
Furthermore, it was observed that the size of the fcc phase decreased, whereas the ratio of hcp to fcc cobalt decreased with increasing alumina loading. Hence, the alumina modification decreased the rate of metal sintering.



(a) 2.5Al300



(b) 0.5Al300



(c) 0.0Al300

Figure 4.17: XRD pattern for unmodified and alumina-modified catalysts calcined at 300 °C *in situ* reduced in hydrogen.

Fcc cobalt has been reported as the preferred crystal structure for small crystallites $d_{\text{Co}} < 20$ nm, while larger crystallites form hcp cobalt and crystallites with a diameter of 20 nm to 40 nm contain both crystal phases [75]. At temperatures above 420 °C fcc cobalt is thermodynamically the most stable phase [76]. Hence, catalysts with smaller metal crystallites are expected to have a larger content of fcc cobalt. This was indeed observed here, where the decrease in hcp cobalt correlated with a decrease in the metal crystallite size. However, for all catalysts, the crystallite size of fcc cobalt was much larger than the crystallite size of hcp cobalt. This indicates that the formation of the cobalt metal phase was not thermodynamically controlled.

When the cobalt crystallites coalesce during sintering, shear stress within the crystallite causes the formation of twinning defects which may nucleate hcp domains within the crystallite [77]. Cobalt metal nanoparticles are believed to contain both hcp and fcc cobalt domains, which may be inter-grown through stacking faults [78]. Some authors suggested that a new cobalt phase is formed within the crystallite, which is different from pure fcc and hcp, and the results of the Rietveld refinement are therefore inaccurate [79, 80]. Tsakoumis et al. [81] observed formation of a (101) hcp plane on the edges of a (111) fcc cobalt plane supported on alumina indicating that metal crystallites may consist of an fcc core surrounded by an hcp shell. Therefore, it is common to report cobalt crystallite sizes as the crystallite size obtained from fcc cobalt, even when both fcc and hcp phases are observed.

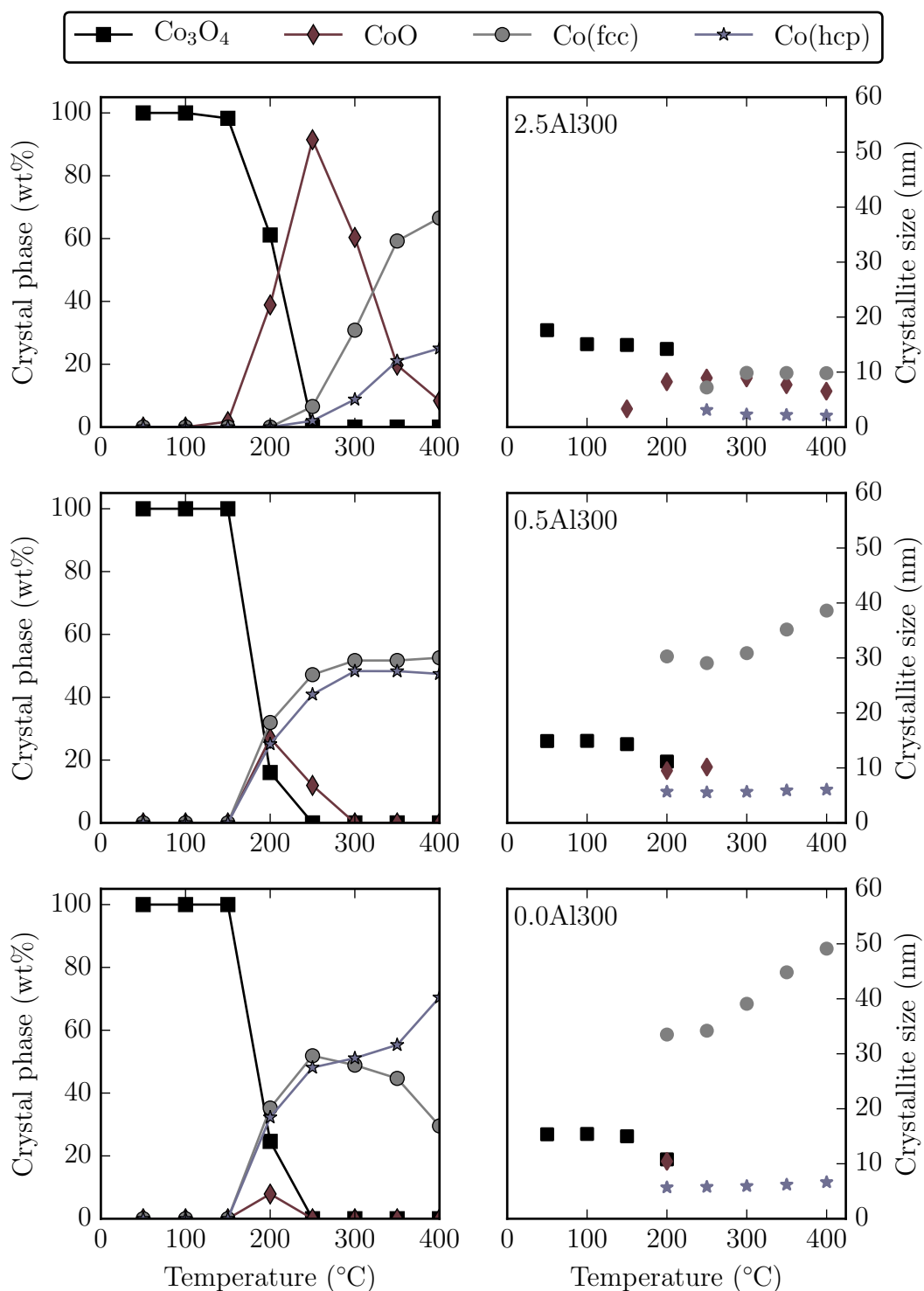


Figure 4.18: Crystal phase and crystallite size evolution during *in situ* XRD reduction in hydrogen of catalysts 0.0Al300, 0.5Al300 and 2.5Al300.

***In situ* XANES reduction**

XANES experiments were performed at the Brazilian Synchrotron Light Laboratory in Campinas, Brazil at the XAFS2 Beamline. The catalysts were diluted with boron nitride, pressed into a disk and reduced in a hydrogen in helium mixture (5 vol% H₂) by increasing the temperature from 150 °C to 550 °C at a heating rate of 2 °C/min. Figure 4.19 shows the XANES spectra of catalysts calcined at 300 °C. The spectra were consistent with a Co₃O₄ phase. The intensity of the pre-edge feature can be an indication for metal-support interaction in supported catalysts, as the pre-edge is more intense for cobalt in tetrahedral coordination, which is believed to interact more strongly with the support [55]. In this study, very small variations in the position and intensity of the pre-edge feature were observed, which are believed to be caused by the uncertainty of the measurement and small variations in the normalisation of the spectra.

Figure 4.20 shows the XANES spectra of catalysts during reduction in hydrogen compared to reference spectra. The white line intensity first increased, as the catalyst was reduced to CoO, and then decreased, as it was further reduced to metallic cobalt. For the modified catalysts a spike in the white line intensity corresponding to the formation of CoO was clearly visible. This feature was less pronounced in the spectrum of the unmodified catalyst. The phase composition at each point was calculated by deconvolution of the scans with measured reference compounds of Co₃O₄, CoO, CoAl₂O₄ and metallic cobalt, which is shown in Figure 4.21. No CoAl₂O₄ phase was detected. It should be noted that unlike XRD, XANES measurements cannot distinguish between fcc and hcp cobalt [82, 83].

All catalysts showed sequential reduction of Co₃O₄ to CoO and then to metallic cobalt. For catalyst 0.0Al300 and catalyst 0.5Al300, CoO started to form around 100 °C, whereas CoO was only detected at around 200 °C for catalyst 2.5Al300. For all catalysts, metallic cobalt started to form around 300 °C. The rate of formation of metallic cobalt, however, decreased with increasing alumina content. At 550 °C, catalyst 0.0Al300 had been almost completely reduced to metallic cobalt, while the catalyst 2.5Al300 still contained 14.5 wt% CoO.

Comparison of the *in situ* XANES (see Figure 4.21 on page 80) and the *in situ* XRD (see Figure 4.18 on page 76) reduction studies showed some discrepancies in the rate of

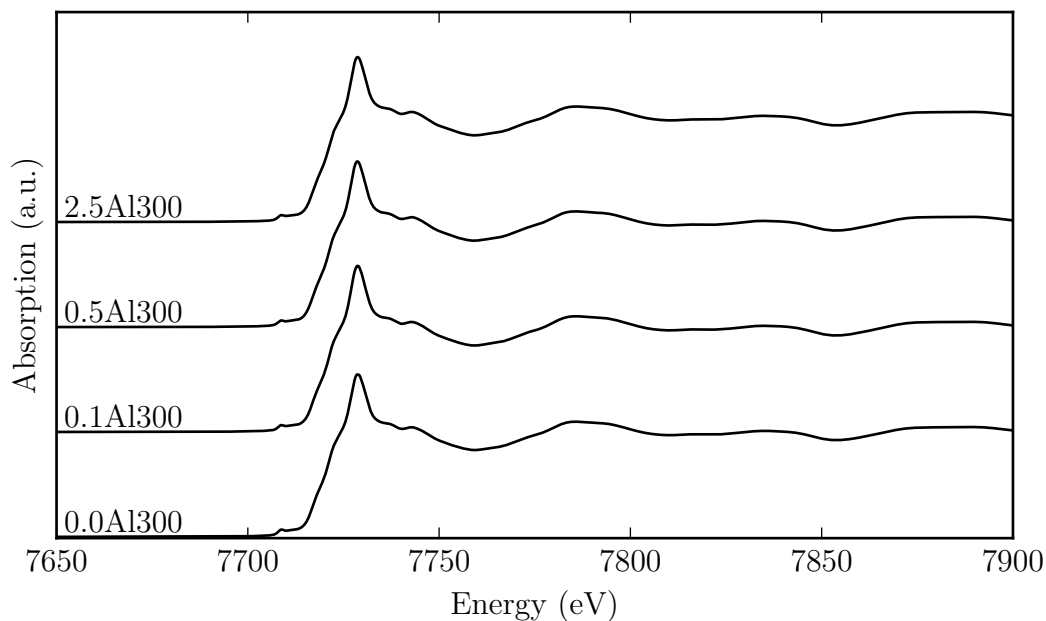


Figure 4.19: XANES spectra of unmodified and alumina-modified Co₃O₄ catalysts calcined at 300 °C.

reduction. The onset of the formation of metallic cobalt in the *in situ* XANES experiments is about 100 °C above the temperature for the *in situ* XRD experiments. This may be due to the differences in the experimental set-up of the two experiments. The XRD experiments were conducted in a capillary cell in a stream of pure hydrogen. The XANES experiments were conducted in a tubular furnace in a stream of diluted hydrogen on catalysts diluted with boron nitride and pressed into a disc. The use of a capillary system was not possible, as this led to a strong attenuation of the X-ray beam due to the strong absorption of the cobalt oxide material. Measurements in fluorescent mode were also unsuccessful due to self-absorption of the material. The use of a diluted hydrogen stream was necessary due to the safety restrictions of the synchrotron facility. The low hydrogen concentration in the reducing gas, and possible mass-transport limitations in the catalyst disk may have led to a lower rate of reduction in the *in situ* XANES experiments. This would explain the shift of the reduction to metallic cobalt to higher temperatures and the lower final degree of reduction observed in the *in situ* XANES experiments, compared to the *in situ* XRD experiments. Interestingly though, the formation of CoO in the unmodified Co₃O₄ catalyst during the *in situ* XANES experiments was observed at lower temperatures. The first CoO

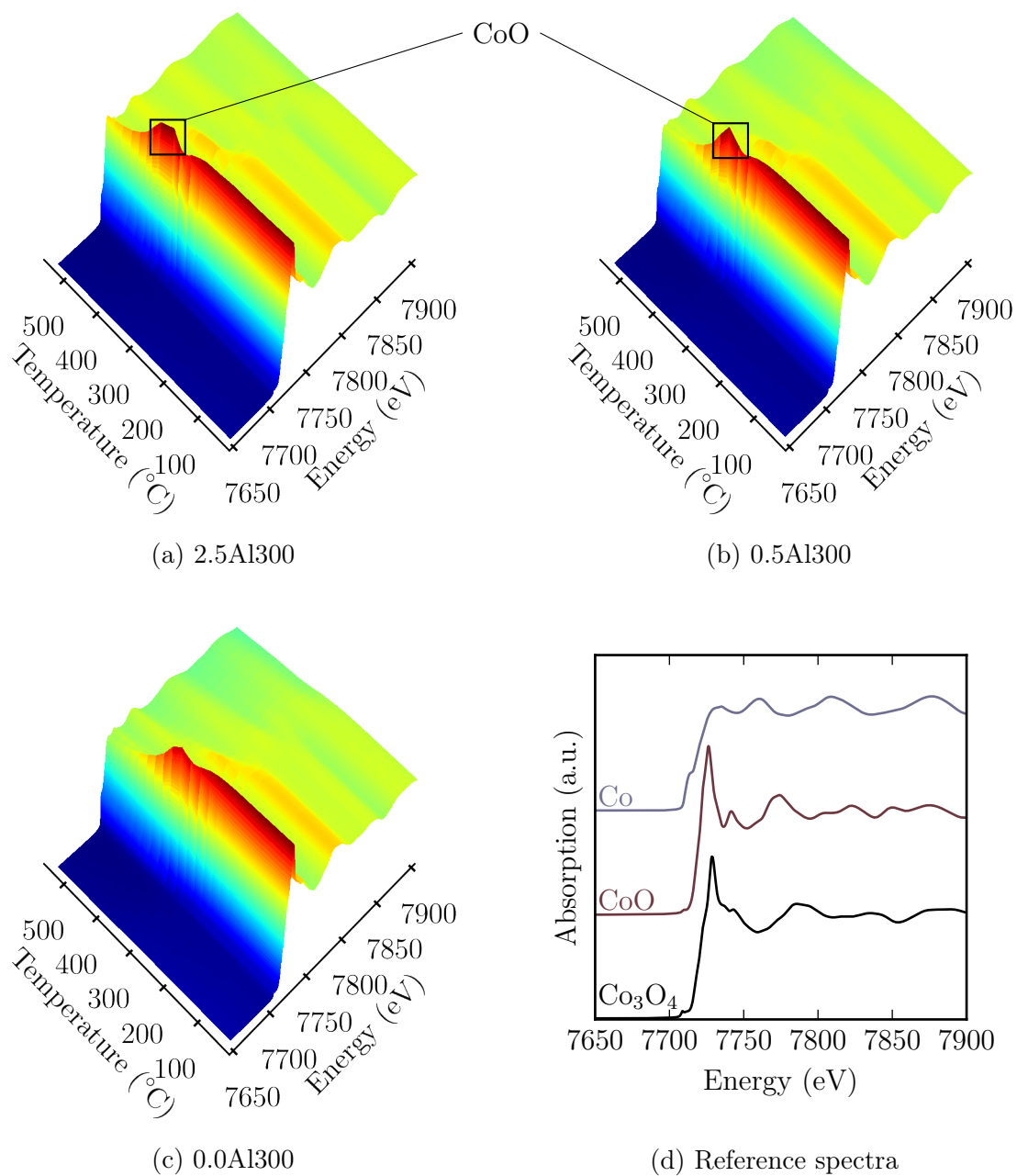


Figure 4.20: XANES of unmodified and alumina-modified Co_3O_4 reduced *in situ* in hydrogen.

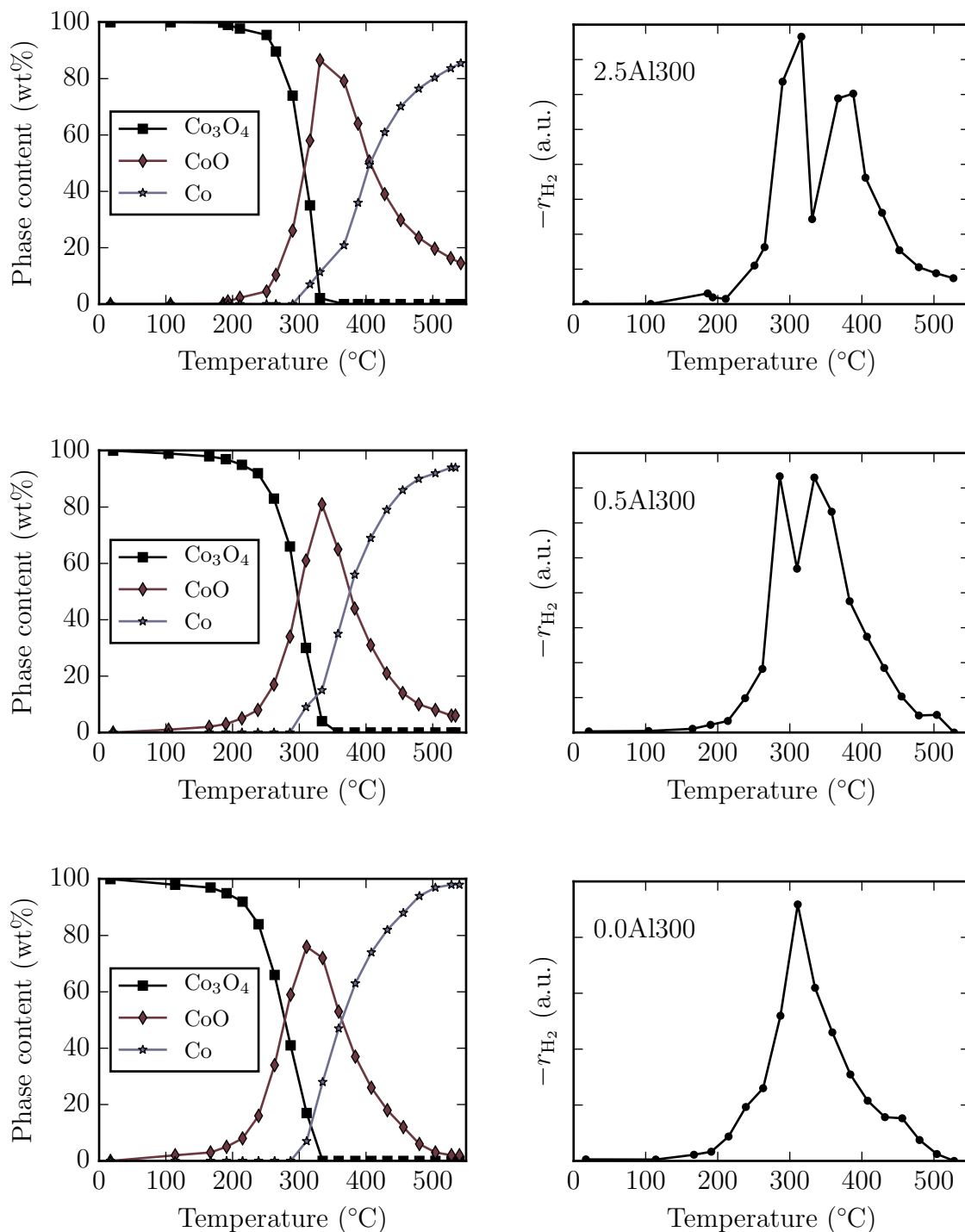


Figure 4.21: Degree of reduction of 2.5 wt%, 0.5 wt% Al and Co_3O_4 (top to bottom) as calculated from linear combination fit of XANES spectra during reduction in hydrogen.

phase was detected at around 100 °C in the XANES experiment, while no CoO was visible in this catalyst until 200 °C in the XRD experiment, at which point only 24 wt% Co_3O_4 remained in the catalyst.

This is consistent with results from Tsakoumis et al. [79], who reported that XRD experiments of reduced catalysts did not show a CoO phase which was clearly visible in XANES experiments. This could be routed in the fact that XRD does only detect crystalline phases, while XANES probes the electronic state and is therefore capable of identifying amorphous material. Therefore, it is possible, that an amorphous CoO phase forms in the early stages of catalyst reduction, which cannot be detected by XRD experiments. Similar observations have been made by Clausen et al. [84]. When comparing the reduction of a Cu/Zn/ Al_2O_3 catalysts using XRD and EXAFS, metallic copper was visible in the EXAFS, before it was detected in the XRD.

Furthermore, it should be noted, that the main CoO and Co_3O_4 diffraction peaks in the XRD are relatively close to each other. XANES is more sensitive in distinguishing Co_3O_4 from CoO and might therefore just be able to pick up small quantities of very small crystallites, which would result in a strongly overlapping and therefore indistinguishable peak in the XRD.

In order to compare the *in situ* XANES and TPR experiments, the rate of hydrogen consumption during the XANES experiments was calculated (see Figure 4.21 on page 80), which corresponds to the reduction profiles determined during TPR experiments (see Figure 4.11 on page 58) . When comparing the results of the XANES and the TPR experiments, the same trends can be seen. The reduction peaks shift to higher temperatures with increasing alumina loading and the reduction of unmodified Co_3O_4 shows only one broad peak.

4.5 Discussion

4.5.1 Crystallite size and morphology

The XRD experiments revealed a pure Co_3O_4 crystal structure for all catalysts. No alumina or cobalt-alumina compounds were detected in the alumina-modified catalysts. It should be noted, that XRD experiments can not distinguish between a Co_3O_4 and CoAl_2O_4 phase, as both have a spinel structure with similar lattice parameters [85]. However, XANES experiments confirmed the absence of a CoAl_2O_4 phase in the calcined catalysts. The alumina modification resulted in no apparent change in the bulk Co_3O_4 crystal structure, and affected merely the crystallite size. This is consistent with observations made by Iqbal et al. [86], who observed no changes in the bulk structure of unsupported CoMnOx catalyst after impregnation with La and P.

The Co_3O_4 crystallite size of the set of catalysts calcined at 300°C was about 14 nm, independent of the alumina loading. The crystallite size for the unmodified catalyst increased to 30 nm upon increasing the calcination temperature to 500°C . This is due to sintering, which may be caused by Ostwald ripening or merging/coalescence of crystallites. Ostwald ripening as a sintering process in metal powders is only associated with the growth of isolated pores in the final stage of sintering, or the growth of solid crystallites in the coarsening stage of liquid-phase sintering [87]. Sintering of supported metal crystallites by Ostwald ripening is only expected in an atmosphere capable of forming relatively volatile metal compounds (e.g. $\text{Co} + \text{CO}$) [88]. This is because the metal-support bond is energetically less favoured than the metal-metal bond, which means that metal dissociation does not occur. Therefore, coalescence of neighbouring Co_3O_4 crystallites is believed to be the predominant mechanism for the crystallite growth observed here.

TEM images of unmodified Co_3O_4 showed a change in crystallite morphology from an undefined, slightly spherical shape to more cubic shaped crystals, with well-defined edges when the calcination temperature was increased from 300°C to 500°C . This form of crystal faceting is frequently observed in the initial stages of sintering [89]. The particle density increases and surface defects are eliminated leading to the formation of crystalline planes with the lowest surface energy.

The crystallite size of catalysts calcined at 500°C decreased with increasing alumina

loading. Hence, alumina prevented sintering of Co_3O_4 crystallites during calcination. During the reduction process, an increase in crystallite size was only observed once the cobalt metal phase was formed, as shown by the *in situ* XRD reduction experiments. This is because the rate of crystal growth at a defined temperature is dependent on its melting point, and the melting point of metal oxides is much higher than that of metals [68]. The same as during calcination, the crystallite size during reduction was found to decrease with increasing alumina loading. For catalyst 0.0Al300, the fcc cobalt size domain grew from 30 nm to 50 nm, while the fcc cobalt size domain of catalyst 2.5Al300 only increased from 8 nm to 10 nm. This indicates that the alumina and cobalt phase remained in intimate contact with each other throughout the reduction process.

The effect of alumina modification on the sintering of Co_3O_4 and metallic cobalt may be explained by solute drag. Merging of two spheres in contact with each other is facilitated by increasing surface diffusion and surface tension [90]. A soluble impurity may decrease the surface tension which leads to a stronger interaction thereby decreasing the rate of sintering [91]. As alumina ions are soluble in cobalt oxide, and vice versa, a decrease in sintering with increasing alumina loading, may be explained by a decrease in surface tension. In general, a solute present at the crystal surface is expected to occupy low energy sites. When the crystal grows, the surface or grain boundary moves outwards. The solute is apt to remain at its low energy site and therefore, diffuses along the grain boundary to a low energy site at the surface. This effect is called solute drag, and it works against the boundary movement slowing down crystal growth. The extent of drag a solute imposes is dependent on the mobility of the solute atoms [68]. Hence, introducing alumina to the cobalt/cobalt oxide surface may decrease the mobility of cobalt ions, which suppress sintering and stabilise small crystallites of Co_3O_4 and metallic cobalt during calcination and reduction.

4.5.2 Reducibility

The influence of the calcination temperature and the alumina modification on the reducibility of Co_3O_4 crystallites was studied using conventional TPR, as well as *in situ* XRD and *in situ* XANES experiments. The experiments showed that increasing the calcination

temperature and increasing the alumina loading increased the temperature necessary for reduction, and hence, decreased the reducibility of Co_3O_4 .

The reduction profiles of unmodified Co_3O_4 catalysts are shown in Figure 4.22. For catalyst 0.0Al300, two reduction peaks were visible corresponding to the formation of CoO and metallic cobalt, respectively. It was observed that increasing the calcination temperature shifted the peaks to a higher temperature and decreased the peak resolution. This is consistent with the literature, where both one broad reduction peak and two reduction peaks have been reported for the reduction of bulk Co_3O_4 [6, 7, 22, 29–32, 34]. Results from *in situ* XRD and XANES showed that the reduction of Co_3O_4 proceeds via the formation of CoO as an intermediate phase and direct reduction of Co_3O_4 to metallic cobalt could be ruled out. Reduction profiles computed from *in situ* XANES experiments showed that the merging of the peaks was merely a result of the reduction kinetics allowing the formation of metallic cobalt to begin before the reduction of Co_3O_4 was completed.

In most studies, the reduction of bulk Co_3O_4 is merely reported for reference purposes, and little to no information is provided on its preparation or characterisation. However, it appears as though Co_3O_4 preparation involving harsh calcination conditions, such as high temperatures above 400 °C and long calcination times, lead to a reduction profile showing only one peak [7], while milder calcination conditions result in a good resolution of the reduction peaks [30], in agreement with the results obtained here.

Increasing the calcination temperature from 300 °C to 500 °C resulted in a decrease of the rate constant for reduction by about 20 % to 40 % when comparing catalysts with the same alumina loading. These observations may be attributed to a change in crystallite size [45]. The crystallite size of Co_3O_4 calcined at 300 °C was 14 nm and increased to 30 nm upon increasing the calcination temperature to 500 °C. The surface area available for hydrogen dissociation decreases with increasing crystallite size. This may lead to an increase in the induction period for the nucleation of a reduced phase [47, 48]. Figure 4.23 shows the conversion fraction (α), calculated by integration of the TPR profile, as a function of time. For TPR experiments, the conversion fraction is equivalent to the degree of reduction. The induction period for the reduction of 0.0Al300 was 15 min. This was about 5 min less than the induction time for 0.0Al500, corresponding to a difference in reduction temperature of about 50 °C. As a result, the estimated rate constant for Co_3O_4 reduction

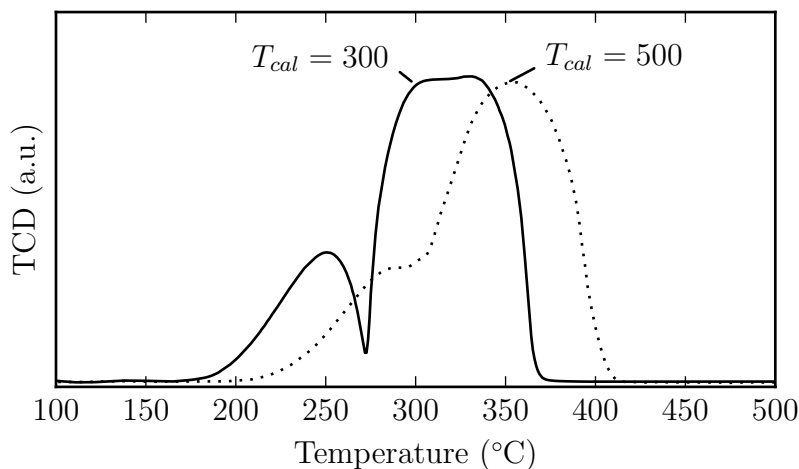


Figure 4.22: Reduction profile of unmodified Co_3O_4 calcined at $300\text{ }^\circ\text{C}$ and $500\text{ }^\circ\text{C}$.

(*k*) at peak maximum decreased from 38 min^{-1} for 0.0Al300 to 19 min^{-1} for 0.0Al500.

The reduction curves of catalyst 0.0Al300 showed an S-curve, visible in the time range of 15 min to 30 min, for the first reduction step corresponding to the formation of CoO. S-curves are characteristic of a nucleation type process [8]. This suggests that hydrogen dissociation is slow, leading to a long induction period and slow nucleation. The freshly formed CoO nuclei grow until they form a layer around the unreduced Co_3O_4 core. At that point, the reduction slows down, due to mass-transport limitations through the CoO shell. The shell thickness increases with increasing size of the original Co_3O_4 crystallite. This increases mass-transport limitations by increasing the diffusion layer, and the reaction rate slows down. It may be concluded that the nucleation of the cobalt metal phase may occur before the Co_3O_4 core is completely reduced to CoO. This results in the strong overlap of the reduction processes and the merging of the reduction peaks visible in the TPR. This may also be a contributing factor to the observation that supported cobalt catalysts, which generally contain small Co_3O_4 crystallites, unlike bulk Co_3O_4 , typically show two well-resolved reduction peaks in the TPR.

Interestingly, the alumina modification seems to have had the same effect on the induction period as increasing the calcination temperature. The onset of the CoO formation, for both catalysts 2.5Al300 and 2.5Al500, was at about 20 min, similar to that of 0.0Al500, and larger than that of 0.0Al300. The crystallite size of catalyst 0.0Al300, 2.5Al300 and

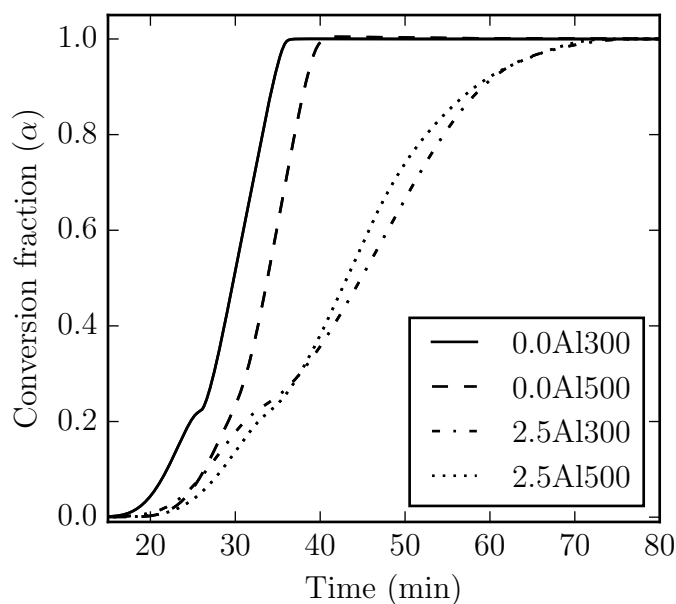


Figure 4.23: Reduction curves of unmodified catalysts, and catalysts containing 2.5 wt% Al obtained at a heating rate of 10 °C/min. The conversion fraction (α) was calculated by integration of the TPR profile, and is equivalent to the degree of reduction.

2.5Al500 was practically identical (14 nm and 16 nm). Nonetheless, the surface area of Co_3O_4 crystallites might be partly reduced due to the alumina surface modification, which could explain the increased induction period. Moreover, the Al ions on the surface of the Co_3O_4 crystallites are not just expected to reduce the exposed Co_3O_4 surface but also occupy low energy sites, such as defect or step sites. Surface defects minimise the activation energy necessary for nucleation and are therefore good nucleation sites [92]. Ward et al. [93] imaged the reduction of Co_3O_4 to CoO using HRTEM, which showed that formation of CoO regions started on step sites and corners of the Co_3O_4 crystallites.

Hence, non-metallic additives⁶ could, in general, decrease the reducibility of metal oxides, by blocking defect sites thereby hindering hydrogen activation and nucleation of the reduced phase. This in agreement with studies by Jacobs et al. [42], who showed that the reducibility of supported cobalt catalysts decreased when irreducible metal oxides (B, La, K) were introduced by incipient wetness impregnation, without affecting the cobalt dispersion.

⁶Addition of a metal phase (especially noble metals) enhance the reducibility by facilitating hydrogen dissociation [48].

However, the effect of impurities on the number of defects and their effect on the reaction kinetics is complex and may be specific to the type of reaction investigated and the quantity and type of impurity [94]. In some cases, an impurity may introduce lattice defects and increase the rate of reaction. This may explain the slight acceleration of the reduction observed for catalyst 0.1Al300. The very small quantity of Al present in this catalyst may have introduced, rather than blocked defect sites. This suggests that the effect may be strongly dependent on the concentration of the additive. This observation is also commonly made when studying the effect of chemical promoters in catalysts. Small promoter concentrations often positively affect the catalytic performance, while higher concentrations may reverse the effect resulting in an element-specific optimal promoter/Co-ratio [95].

The most prominent effects of the alumina modification on the reduction profile were the peak-broadening, shift of the reduction peaks to higher temperatures and additional peaks appearing above 400 °C. High-temperature features below 800 °C in cobalt oxide reduction profiles have been attributed to strongly interacting metal-support species with uncertain Co/Al stoichiometry [34]. Diffusion of cobalt ions into the alumina structure, or vice versa, may create a strongly diluted solid-solution of cobalt and alumina which reduces at a higher temperature compared to pure CoO, but at a lower temperature than CoAl_2O_4 . Such a phase is expected to lack long range order, be localised at the Co_3O_4 -alumina interface and may be only a few layers thick [52]. Arnoldy et al. [6] proposed that Al^{3+} ions polarise the Co-O bond increasing the effective charge of the Co ions, thereby increasing the lattice energy, which increases the reduction temperature. This may be possible due to the partly covalent character of transition metal ions in spinels, such as CoAl_2O_4 .

These studies suggested that the presence of the Al ions changed the electronic properties around the cobalt ions, which led to the decreased reducibility. If this was the case, an increase in the activation energy for the cobalt oxide reduction should be expected. However, the alumina modification in this study was found to affect the kinetics of the reduction by decreasing the pre-exponential factor, and not the activation energy.

Solid-state reactions are often dominated by kinetic restrictions which may express themselves in the pre-exponential factor. This is because the rate of reduction of metal

oxides is dominated by the rate of hydrogen activation and nucleation, which are correlated to the pre-exponential factor. In fact, it is a common misconception that the reducibility of an oxide is directly related to the metal-oxygen bond strengths and thus the activation energy [12]. However, it should be noted that Ji et al. [33] made the opposite observation of metal-support interactions increasing the activation energy of the reduction.

The unmodified catalysts were completely reduced to metallic cobalt at about 380 °C to 400 °C, whereas the alumina-modified catalysts still contained considerable amounts of CoO, because of their decreased rate of reduction. At these temperatures, the ion mobility is large, and diffusion of Al ions into the CoO matrix forming a non-stoichiometric cobalt-alumina surface phase is possible. Co_3O_4 , CoO and CoAl_2O_4 all form crystal structures in which the oxygen anions form an fcc lattice and the metal cations occupy a fraction of the octahedral and tetrahedral vacancies. Tetrahedrally coordinated Co^{2+} ions can be probed by XANES, showing a distinct, very intense pre-edge peak [96]. The *in situ* XANES experiments showed no evidence for the presence of tetrahedrally coordinated Co^{2+} ions. It can be deduced that the Co^{2+} ions were octahedrally coordinated with the alumina phase. This is supported by Tsakoumis et al. [97], who investigated the reduction of a Re promoted Co/ Al_2O_3 catalyst using *in situ* synchrotron XRD and reported a sudden expansion the γ - Al_2O_3 lattice parameter at the onset of CoO formation at 190 °C. This lattice expansion was explained by diffusion of Co^{2+} ions into octahedral vacancies in the γ - Al_2O_3 lattice forming a mixed cobalt-alumina phase.

However, it should be emphasised, that the decrease in the reducibility of Co^{2+} ions in the mixed cobalt-alumina phase does not stem from a change in the cobalt-oxygen bond strengths. The results showed that the activation energy of this phase was similar to the activation energy required for reduction of pure CoO. Instead, the pre-exponential factor was decreased. The Al ions in the cobalt-alumina matrix may simply decrease the rate of diffusion of cobalt ions, which hinders nucleation of a metal phase. This was responsible for the third peak, appearing as a shoulder or broadening of the CoO peak in the reduction profile of alumina-modified cobalt catalysts.

This may be different for the catalysts containing 2.5 wt% Al. For these catalysts, a fourth peak appeared at temperatures above 600 °C, which had a slightly higher activation energy of 83 kJ/mol and 117 kJ/mol, for calcination at 300 °C and 500 °C, respectively, and

equal or higher pre-exponential factors than previous reduction steps. XANES experiments were only conducted up to a temperature of 550 °C so that no information on the coordinative environment of the cobalt ions above 600 °C is available.

Kurajica et al. [85] investigated the formation of sol-gel derived CoAl_2O_4 after annealing at different temperatures. They described the formation of an intermediate phase corresponding to Co_2AlO_4 at temperatures between 500 °C to 600 °C with Co^{3+} and a part of Co^{2+} ions in octahedral coordination. Annealing at 700 °C led to the formation of a CoAl_2O_4 spinel phase with a substantial degree of inversion (Co^{2+} ions in octahedral and tetrahedral coordination). According to Chin et al. [53], cobalt ions occupying tetrahedral sites in the alumina matrix (as in CoAl_2O_4) are more difficult to reduce than cobalt ions occupying octahedral sites.

The activation energy calculated for this reduction step was larger compared to previous reduction steps, but the observed reduction temperature was too low for the reduction of stoichiometric CoAl_2O_4 . Presumably, the concentration of Al ions in the system was not high enough to allow the nucleation of a CoAl_2O_4 phase. However, it is hypothesised that at this point a non-stoichiometric cobalt-alumina phase was formed which may have Co^{2+} ions in tetrahedral coordination, which are more difficult to reduce.

Furthermore, it is speculated, that for the catalysts containing 2.5 wt% Al, a non-stoichiometric cobalt-alumina surface phase may have formed during the calcination. For these catalysts, peak deconvolution of the TPR profiles indicated a lower than expected peak area, and hence, hydrogen consumption, for the first reduction peak. This may indicate, that less Co_3O_4 was present in the catalyst than expected. Hence, the formation of a non-stoichiometric cobalt-alumina surface phase may have occurred during the calcination. However, it should be noted that XANES showed no differences in the properties of the calcined catalysts.

4.6 Conclusions

In order to establish the effect of alumina modification and calcination temperature on the reducibility of cobalt oxide, alumina-modified cobalt oxide catalysts containing ≤ 2.5 wt% Al were prepared by incipient wetness impregnation of cobalt oxide with aluminium sec-butoxide, followed by calcination at 300 °C or 500 °C.

Alumina modification did not affect the structure of bulk Co_3O_4 , but stabilised small cobalt oxide crystallites, preventing metal sintering. The reducibility of the catalysts decreased with increasing calcination temperature and increasing alumina loading.

The decrease in reducibility with increasing calcination temperature was attributed to an increase in the Co_3O_4 crystallite size. It should be noted, that this effect is opposite to a common observation in supported catalysts, where reducibility decreases with *decreasing* the cobalt oxide crystallite size. This is because in supported catalysts the reducibility is dominated by metal-support interactions, which increase with decreasing crystallite size, due to a larger contact area of the metal oxide crystallite with the support. This emphasises the difference in the reduction behaviour of bulk and supported cobalt oxide. Astonishingly, the reduction profile of Co_3O_4 containing small amounts of 2.5 wt% Al has a stronger resemblance to the reduction profile of a supported cobalt catalyst, than the reduction profile of bulk Co_3O_4 .

The cobalt-alumina interaction decreased the rate of reduction of Co_3O_4 and CoO, which resulted in a shift of the reduction peaks in the TPR to higher temperatures. In conclusion, the position of the Co_3O_4 and CoO peaks in the TPR profile is an indication of the strength of the metal-support interaction. This is because alumina may block defect sites at the cobalt-alumina interface, which hinders hydrogen activation and the nucleation of reduced cobalt phases.

Furthermore, alumina modification led to the appearance of additional reduction peaks at temperatures between 400 °C to 600 °C, which may be assigned to a cobalt-alumina phase with cobalt in octahedral positions. Reduction peaks at temperatures between 600 °C and 800 °C were assigned to a cobalt-alumina phase with cobalt in tetrahedral position. Unlike previous reports that suggested the presence of alumina increases the activation energy for cobalt oxide reduction, this research leads to the conclusion that small quantities of

alumina mainly have a kinetic effect, by decreasing the pre-exponential factor and thus decreasing the overall rate of cobalt oxide reduction.

It was also shown that alumina modification reduces the rate of sintering for both Co_3O_4 during calcination and metallic cobalt during reduction. This may be explained by the effect of solute drag [68]. Impurities on metal/metal oxide surfaces occupy low energy/defect sites. When the crystallite grows, the impurities want to remain at their low energy site and drag behind. They move with the crystallite surface which retards crystal growth. When low energy sites at the metal oxide surface are blocked, this leads to a reduced rate of nucleation and therefore a decrease in the reducibility. In conclusion, it appears as if the same effect that leads to the stability of small metal crystallites on the support surface also results in the decrease of the reducibility. This is in agreement with previous reports that established that in supported catalysts a certain amount of metal-support interaction is required to achieve high metal dispersions [98].

Hence, a loss in reducibility may well be the unavoidable cost of achieving high metal dispersions. Therefore, the preparation of supported catalysts should aim to introduce predominantly weak metal-support interactions. This may be accomplished by keeping calcination temperatures low and choosing less reactive supports to avoid the formation of mixed metal-support species, which are more difficult to reduce. A promising approach seems to be the modification of non-reactive supports such as carbon or silicon carbide with a coating of a more reactive support such as alumina [99–101]. In these cases, a good metal dispersion is achieved at a high degree of reduction, presumably, because similarly to this study the support-ion concentration is too low to form irreducible stoichiometric metal-support compounds.

The following general statements can be made from the results obtained in this study:

1. Increasing the crystallite size of bulk metal oxide crystallites decreases the rate of reduction by decreasing the surface area.
2. Surface modification of Co_3O_4 with alumina causes blockage of defect sites which hinders the nucleation of CoO and reduces the rate of reduction.

3. Prevention of cobalt sintering and decreased Co_3O_4 reducibility are both linked to blockage of defect sites. A loss in reducibility is therefore unavoidable if a high metal dispersion is desired.
4. Non-metallic impurities, such as chemical promoters, may decrease reducibility.

4.7 References

- [1] Gates, B. C. *Chemical Reviews*, 95(3):(1995) 511–522
- [2] Xiong, H., Motchelaho, M. A. M., Moyo, M., Jewell, L. L. and Coville, N. J. *Journal of Catalysis*, 278(1):(2011) 26–40
- [3] Lacroix, M., Dreibine, L., de Tymowski, B., Vigneron, F., Edouard, D., Bégin, D., Nguyen, P., Pham, C., Savin-Poncet, S., Luck, F., Ledoux, M.-J. and Pham-Huu, C. *Applied Catalysis A: General*, 397(1–2):(2011) 62–72
- [4] Tauster, S. J. *Accounts of Chemical Research*, 20(11):(1987) 389–394
- [5] Fu, Q. and Wagner, T. *Surface Science Reports*, 62(11):(2007) 431–498
- [6] Arnoldy, P. and Moulijn, J. A. *Journal of Catalysis*, 93(1):(1985) 38–54
- [7] Wang, W. J. and Chen, Y. W. *Applied Catalysis*, 77(2):(1991) 223–33
- [8] Hurst, N. W., Gentry, S. J. and Jones, A. *Catalysis Reviews*, 24(2):(1982) 233–309
- [9] Tauster, S. J., Fung, S. C. and Garten, R. L. *Journal of American Chemical Society*, 100(1):(1987) 170–175
- [10] Rao, G. R. and Mishra, B. G. *Bulletin of the Catalysis Society of India*, 2:(2003) 122–134
- [11] Niemantsverdriet, J. W. *Spectroscopy in Catalysis*. Wiley-VCH, 2nd edition (2000)
- [12] Haber, J. *Journal of the Less Common Metals*, 54(1):(1977) 243–261
- [13] Kung, H. *Studies in Surface Science and Catalysis*, 45:(1989) 91–109
- [14] Khawam, A. and Flangan, D. R. *The Journal of Physical Chemistry B*, 110(35):(2006) 17315–17328
- [15] Avrami, M. *The Journal of Chemical Physics*, 8(2):(1940) 212–224
- [16] Kanervo, J. *Kinetic analysis of temperature programmed reactions*. Ph.D. thesis, Helsinki University of Technology (2003)
- [17] Jacobs, G., Ji, Y., Davis, B. H., Cronauer, D., Kropf, A. J. and Marshall, C. L. *Applied Catalysis A: General*, 333(2):(2007) 177–191
- [18] du Plessis, H. E., Forbes, R. P., Barnard, W., Erasmus, W. J. and Steuwer, A. *Physical Chemistry Chemical Physics*, 15(28):(2013) 11640–11645
- [19] van 't Blik, H. F. J. and Prins, R. *Journal of Catalysis*, 97(1):(1986) 188–199
- [20] Malet, P. and Caballero, A. *Journal of the Chemical Society, Faraday Transactions 1: Physical Chemistry in Condensed Phases*, 84(7):(1988) 2369–2375

-
- [21] Gentry, S. J., Hurst, N. W. and Jones, A. *Journal of the Chemical Society, Faraday Transactions 1: Physical Chemistry in Condensed Phases*, 77(3):(1981) 603–619
- [22] Lapidus, A., Krylova, A., Kazanskii, V., Borovkov, V., Zaitsev, A., Rathousky, J., Zukal, A. and Jančálková, M. *Applied Catalysis*, 73(1):(1991) 65–81
- [23] Vyazovkin, S. and Wight, C. A. *Thermochimica Acta*, 340–341:(1999) 53–68
- [24] Janković, B., Adnadević, B. and Mentus, S. *Chemical Engineering Science*, 63(3):(2008) 567–575
- [25] Kissinger, H. E. *Analytical Chemistry*, 29(11):(1957) 1702–1706
- [26] Wimmers, O. J., Arnoldy, P. and Moulijn, J. A. *Journal of Physical Chemistry*, 90(7):(1986) 1331–1337
- [27] Doyle, C. D. *Journal of Applied Polymer Science*, 5(15):(1961) 285–292
- [28] Lin, H.-Y., Chen, Y.-W. and Li, C. *Thermochimica Acta*, 400(1–2):(2003) 61–67
- [29] Hilmen, A. M., Schanke, D. and Holmen, A. *Catalysis Letters*, 38(3):(1996) 143–147
- [30] Tang, C.-W., Wang, C.-B. and Chien, S.-H. *Thermochimica Acta*, 473:(2008) 68–73
- [31] Sexton, B. A., Hughes, A. E. and Turney, T. W. *Journal of Catalysis*, 97(2):(1986) 390–406
- [32] Rosynek, M. P. and Polansky, C. A. *Applied Catalysis*, 73(1):(1991) 97–112
- [33] Ji, Y., Zhao, Z., Duan, A., Jiang, G. and Liu, J. *The Journal of Physical Chemistry C*, 113(17):(2009) 7186–7199
- [34] Jongsomjit, B., Panpranot, J. and Goodwin, J. G. *Journal of Catalysis*, 204(1):(2001) 98–109
- [35] Nabaho, D., Niemantsverdriet, J. W., Claeys, M. and van Steen, E. *Catalysis Today*, 275:(2016) 27–34
- [36] Borg, Ø., Eri, S., Blekkan, E. A., Storsæter, S., Wigum, H., Rytter, E. and Holmen, A. *Journal of Catalysis*, 248(1):(2007) 89–100
- [37] Kogelbauer, A., Goodwin, J. G., Jr. and Oukaci, R. *Journal of Catalysis*, 160(1):(1996) 125–133
- [38] van de Loosdrecht, J., Barradas, S., Caricato, E. A., Ngwenya, N. G., Nkwanyana, P. S., Rawat, M. A. S., Sigwebela, B. H., van Berge, P. J. and Visagie, J. L. *Topics in Catalysis*, 26(1–4):(2003) 121–127
- [39] Sewell, G., van Steen, E. and O’Connor, C. *Catalysis Letters*, 37:(1996) 255–260
- [40] Bhatia, S., Beltramini, J. and Do, D. D. *Catalysis Today*, 7(3):(1990) 309–438

- [41] Khodakov, A. Y., Lynch, J., Bazin, D., Rebours, B., Zanier, N., Moisson, B. and Chaumette, P. *Journal of Catalysis*, 168(1):(1997) 16–25
- [42] Jacobs, G., Das, T. K., Zhang, Y., Li, J., Racoillet, G. and Davis, B. H. *Applied Catalysis A: General*, 233(1–2):(2002) 263–281
- [43] Ernst, B., Bensaddik, A., Hilaire, L., Chaumette, P. and Kiennemann, A. *Catalysis Today*, 39(4):(1998) 329–341
- [44] Zhang, Y., Wei, D., Hammache, S. and Goodwin Jr., J. G. *Journal of Catalysis*, 188(2):(1999) 281–290
- [45] Okamoto, Y., Nagata, K., Adachi, T., Imanaka, T., Inamura, K. and Takyu, T. *The Journal of Physical Chemistry*, 95(1):(1991) 310–319
- [46] Zabala, J. M., Grange, P. and Delmon, B. *Comptes rendus de L'Académie de Sciences series C*, 279:(1974) 561
- [47] Bracconi, P. and Dufour, L. C. *Comptes rendus de L'Académie de Sciences series C*, 270:(1970) 1152–1155
- [48] Batley, G. E., Ekstrom, A. and Johnson, D. A. *Journal of Catalysis*, 34(3):(1974) 368–375
- [49] Ji, L., Lin, J. and Zeng, H. C. *The Journal of Physical Chemistry B*, 104(8):(2000) 1783–1790
- [50] Schanke, D., Hilmen, A. M., Bergene, E., Kinnari, K., Rytter, E., Ådnanes, E. and Holmen, A. *Catalysis Letters*, 34(3-4):(1995) 269–284
- [51] Roe, G. M., Ridd, M. J., Cavell, K. J., Larkins, F. P., D. M. Bibby, R. F. H., C. D. Chang and Yurchak, S. *Studies in Surface Science and Catalysis*, 36:(1988) 509–515
- [52] Lojacono, M., Verbeek, J. L. and Schuit, G. C. A. *Journal of Catalysis*, 29(3):(1973) 463–474
- [53] Chin, R. L. and Hercules, D. M. *The Journal of Physical Chemistry*, 86(3):(1982) 360–367
- [54] Richardson, J. T. and Vernon, L. W. *The Journal of Physical Chemistry*, 62(10):(1958) 1153–1157
- [55] Greigor, R. B., Lytle, F. W., Chin, R. L. and Hercules, D. M. *The Journal of Physical Chemistry*, 85(9):(1981) 1232–1235
- [56] Chung, K. S. and Massoth, F. E. *Journal of Catalysis*, 64(2):(1980) 320–331
- [57] Acres, G. J. K., Bird, A. J., Jenkins, J. W., King, F., Kembell, C. and Dowden, D. A. *The design and preparation of supported catalysts*, volume 4, 1–30. The Royal Society of Chemistry (1981)

-
- [58] van de Loosdrecht, J., van der Haar, M., van der Kraan, A. M., van Dillen, A. J. and Geus, J. W. *Applied Catalysis A: General*, 150(2):(1997) 365–376
- [59] Steen, E. v., Sewell, G. S., Makhothe, R. A., Micklethwaite, C., Manstein, H., de Lange, M. and O'Connor, C. T. *Journal of Catalysis*, 162(2):(1996) 220–229
- [60] van de Water, L. G. A., Bezemer, G. L., Bergwerff, J. A., Versluijs-Helder, M., Weckhuysen, B. M. and de Jong, K. P. *Journal of Catalysis*, 242(2):(2006) 287–298
- [61] Il'chenko, N. I. *Russian Chemical Reviews*, 41(1):(1972) 47
- [62] Holm, V. C. F. and Clark, A. *Journal of Catalysis*, 11(4):(1968) 305–316
- [63] Scherrer, P. *Nachrichten von der Gesellschaft der Wissenschaften zu Göttingen, Mathematisch-Physikalische Klasse*, 98–100
- [64] Langford, J. I. and Wilson, A. J. C. *Journal of Applied Crystallography*, 11(2):(1978) 102–113
- [65] Claeys, M. and Fischer, N. PCT patent WO 2013/005180 A1 (2013)
- [66] Fischer, N., Clapham, B., Feltes, T., van Steen, E. and Claeys, M. *Angewandte Chemie International Edition*, 53(5):(2014) 1342–1345
- [67] Ravel, B. and Newville, M. *Journal of Synchrotron Radiation*, 12:(2005) 537–541
- [68] Kang, S.-J. L. *Sintering*. Elsevier Butterworth Heinemann (2005)
- [69] Su, D., Dou, S. and Wang, G. *Scientific Reports*, 4:(2014) 5767
- [70] Stracey, R. *Metal-support interactions in Co/TiO₂ Fischer-Tropsch catalysts*. Master's thesis, University of Cape Town (2013)
- [71] Jones, E., Oliphant, T., Peterson, P. et al. SciPy: Open source scientific tools for Python. <http://www.scipy.org/>
- [72] Byrd, R. H., Schnabel, R. B. and Shultz, G. A. *Mathematical Programming*, 40(1):(1988) 247–263
- [73] van de Loosdrecht, J., Ciobîcă, I. M., Gibson, P., Govender, N. S., Moodley, D. J., Saib, A. M., Weststrate, K.-J. and Niemantsverdriet, J. W. *ACS Catalysis*, 6(6):(2016) 3840–3855
- [74] Liu, J., Zhang, H., Zhou, T. and Wei, S. *Jinshu Xuebao*, 36(8):(2000) 837–841
- [75] Kitakami, O., Sato, H., Shimada, Y., Sato, F. and Tanaka, M. *Physical Review B*, 56(21):(1997) 13849–13854
- [76] de la Peña O'Shea, V. A., Homs, N., Fierro, J. L. G. and Ramírez de la Piscina, P. *Catalysis Today*, 114(4):(2006) 422–427
- [77] Thölen, A. R. In *Materials Science Research - Sintering Processes*. Plenum Press (1979)

- [78] Ducreux, O., Rebours, B., Lynch, J., Roy-Auberger, M. and Bazin, D. *Oil & Gas Science and Technology - Rev. IFP*, 64(1):(2009) 49–62
- [79] Tsakoumis, N. E., Voronov, A., Rønning, M., Beek, W. v., Borg, Ø., Rytter, E. and Holmen, A. *Journal of Catalysis*, 291:(2012) 138–148
- [80] Braconnier, L., Landrивon, E., Clémentçon, I., Legens, C., Diehl, F. and Schuurman, Y. *Catalysis Today*, 215:(2013) 18–23
- [81] Tsakoumis, N. E., Dehghan-Niri, R., Rønning, M., Walmsley, J. C., Borg, Y., Rytter, E. and Holmen, A. *Applied Catalysis A: General*, 479:(2014) 59–69
- [82] Cheng, G., Carter, J. D. and Guo, T. *Chemical Physics Letters*, 400(1–3):(2004) 122–127
- [83] Khodakov, A. Y., Chu, W. and Fongarland, P. *Chemical Reviews*, 107(5):(2007) 1692–1744
- [84] Clausen, B. S., Gråbæk, L., Steffensen, G., Hansen, P. L. and Topsøe, H. *Catalysis Letters*, 20(1):(1993) 23–36
- [85] Kurajica, S., Popović, J., Tkalčec, E., Gržeta, B. and Mandić, V. *Materials Chemistry and Physics*, 135(2–3):(2012) 587–593
- [86] Iqbal, S., Davies, T. E., Hayward, J. S., Morgan, D. J., Karim, K., Bartley, J. K., Taylor, S. H. and Hutchings, G. J. *Catalysis Today*, 272:(2016) 74–79
- [87] Masude, Y. and Watanabe, R. In *Materials Science Research - Sintering Processes*, volume 13, 3–22. Plenum Press (1979)
- [88] Geus, J. W. In *Materials Science Research - Sintering and Catalysis*, volume 10, 29–62. Plenum Press (1975)
- [89] Porter, R. L. In *Materials Science Research - Sintering Processes*, volume 13, 129–134. Plenum Press (1979)
- [90] Kuczynski, G. C. *Transactions of the metallurgical society of AIME*, 185:(1949) 169–174
- [91] Ruckenstein, E. and Pulvermacher, B. *Journal of Catalysis*, 29(2):(1973) 224–245
- [92] Burnham, A. K., Weese, R. K. and Weeks, B. L. *The Journal of Physical Chemistry B*, 108(50):(2004) 19432–19441
- [93] Ward, M. R., Boyes, E. D. and Gai, P. L. *Journal of Physics: Conference Series*, 522:(2014) 012009/1–012009/4
- [94] Boldyrev, V. V. *Thermochimica Acta*, 100(1):(1986) 315–338
- [95] Johnson, G. R. and Bell, A. T. *Journal of Catalysis*, 338:(2016) 250–264

- [96] Shulman, G. R., Yafet, Y., Eisenberger, P. and Blumberg, W. E. *Proceedings of the National Academy of Sciences*, 73(5):(1976) 1384–1388
- [97] Tsakoumis, N. E., Johnsen, R. E., Van Beek, W., Rønning, M., Rytter, E. and Holmen, A. *Chemical Communications*, 52(15):(2016) 3239–3242
- [98] Coulter, K. E. and Sault, A. G. *Journal of Catalysis*, 154(1):(1995) 56–64
- [99] Jongsomjit, B., Panpranot, J. and Goodwin, J. G. *Journal of Catalysis*, 215(1):(2003) 66–77
- [100] Koo, H.-M., Lee, B. S., Park, M.-J., Moon, D. J., Roh, H.-S. and Bae, J. W. *Catalysis Science & Technology*, 4:(2014) 343–351
- [101] Labuschagne, J., Meyer, R., Chonco, Z. H., Botha, J. M. and Moodley, D. J. *Catalysis Today*, 275:(2016) 2–10

Chapter 5

Effect of alumina modification of cobalt on the Fischer-Tropsch synthesis

5.1 Introduction

In the Fischer-Tropsch process, a metal catalyst is used to produce hydrocarbons from the very basic starting materials hydrogen and carbon monoxide, which can be derived from alternative carbon sources such as coal, natural gas or biomass [1]. New legislation limiting flaring of natural gas as well as increasing concerns about the environmental issues around the use of coal are driving the (re-)exploration of the use of the Fischer-Tropsch process to convert natural gas to liquid fuels. For this purpose metallic cobalt is the catalyst of choice, due to its high conversion rate, high selectivity towards linear hydrocarbons and low selectivity towards carbon dioxide [2]. Due to the high cost of metallic cobalt, very small cobalt crystallites are typically used to optimise the amount of catalytically active metal surface area. This is achieved by dispersing the metal catalyst onto a support material, such as alumina (Al_2O_3), silica (SiO_2), titania (TiO_2), ceria (CeO_2) or carbon [3–5].

In general, high surface area supports, such as alumina, which strongly interact with the metal catalyst provide high metal dispersions but lower the catalyst reducibility, which may decrease catalytic activity [6]. The loss of reducibility is caused by the formation of mixed metal-support compounds such as CoAl_2O_4 . CoAl_2O_4 only reduces in H_2 at temperatures above 850°C and therefore remain intact after catalyst activation, which is

typically performed at 350 °C to 450 °C [6–8]. The reducibility may be increased by adding noble metal promoters, but this leads to a significant cost increase.

Although the majority of heterogeneous catalysts are supported catalysts, fundamental understanding of the effect of the support is still lacking [9]. This is partially due to the difficulty in the characterisation of effects taking place on surfaces on a sub-nanometer scale. The investigation of surface effects has been largely limited to flat, single crystal models, where either metal nanoparticles were deposited onto supports or support molecules were deposited onto a flat metal surface. This study aimed to follow a more realistic approach. An inverse-model catalyst was prepared by surface modification of cobalt oxide, with varying amounts of alumina. The effect of the alumina loading on the Fischer-Tropsch synthesis was studied, in a slurry reactor under industrially relevant conditions. The catalysts were characterised by H₂-chemisorption, H₂- and CO-temperature-programmed reduction (TPR), Pyridine-temperature-programmed desorption (TPD), transmission electron microscopy (TEM) and X-ray diffraction (XRD).

5.2 Literature Review - The Fischer-Tropsch synthesis

5.2.1 The reaction mechanism

The Fischer-Tropsch (FT) synthesis is a surface catalysed polymerisation reaction of H_2 and CO (syngas) to hydrocarbons. The reaction is catalysed by iron, cobalt, nickel and ruthenium, of which only iron and cobalt are commercially applied [10]. The reaction is operated at pressures around 20 bar and temperatures between 200 °C and 350 °C, depending on the desired product selectivity. The main FT products, besides water, are linear paraffins and 1-olefins, and branched hydrocarbons and oxygenated products are formed in smaller quantities. Table 5.1 gives an overview of the main and side reactions taking place in the FT synthesis.

A variety of reaction mechanisms have been proposed for the FT synthesis. Among them, the alkyl mechanism, CO insertion and the alkylidyne mechanism are the most popular [12]. To account for the variety of products formed one might have to accept that not just one, but many reaction pathways may be operating in parallel.

The FT synthesis is essentially a polymerisation reaction. Therefore, the following reaction steps are expected to occur [11]:

1. Reactant adsorption and dissociation
2. Chain initiation
3. Chain growth
4. Chain termination
5. Product desorption
6. Product re-adsorption leading to further growth or isomerisation

The '**alkyl**'-mechanism was developed from the 'carbide'-mechanism, which was originally proposed by Fischer and Tropsch [13] themselves, and remains the most widely accepted reaction mechanism to explain the formation of linear paraffins and olefins [12]. The term 'carbide'-mechanism has been rejected, as the FT reaction can proceed on metals that do not form stable metal carbides under FT conditions, such as cobalt or ruthenium. The 'alkyl'-mechanism is based on the dissociation of hydrogen and carbon monoxide, producing surface hydrogen, surface carbon and surface oxygen. Surface carbon reacts with

Table 5.1: Overview of reactions occurring in the Fischer-Tropsch synthesis, adapted from [11].

Main reactions			
Paraffin formation	$(2n + 1)H_2 + nCO$	\longrightarrow	$C_nH_{2n+2} + nH_2O$
Olefin formation	$2nH_2 + nCO$	\longrightarrow	$C_nH_{2n} + nH_2O$
Side reactions			
Water-gas-shift ^a	$CO + H_2O$	\longrightarrow	$CO_2 + H_2$
Alcohol formation	$2nH_2 + nCO$	\longrightarrow	$C_nH_{2n+2}O + (n - 1)H_2O$
Catalyst reduction/oxidation	$M_xO_y + yH_2$	\longleftrightarrow	$xM + yH_2O$
	$M_xO_y + yCO$	\longleftrightarrow	$xM + yCO_2$
Carbide formation	$xM + yC$	\longleftrightarrow	$yCO_2 + M_xC_y$
Boudouard reaction	$2CO$	\longleftrightarrow	$C + CO_2$

^aThe water-gas shift reaction is classified as a side reaction with low importance for Co, Ni and Ru catalysts. However, Fe catalysts have large water-gas shift activities, warranting the classification as a main reaction

surface hydrogen to form successively CH, CH₂ and CH₃. Methyl species (CH₃) may act as a chain starter which incorporates methylene species (CH₂) acting as a monomer, to form a linear hydrocarbon chain. Chain termination occurs by reaction of the chain with hydrogen forming a linear paraffin, or β -hydrogen abstraction forming a 1-olefin. Linear paraffins and 1-olefins are thus primary FT products, and their selectivity is expected to increase with decreasing conversion or increasing space velocity [14]. The 'alkyl' mechanism is supported by experimental evidence. The existence of the proposed species on the metal surface upon CO hydrogenation has been reported [15, 16]. The 'alkyl'-mechanism cannot explain the formation of oxygenated products.

Formation of oxygenated products is often explained by the **CO insertion mechanism** [17]. Here, methyl acts as the chain starter. It is formed by hydrogenation of CO to methanol and subsequent elimination of water. The chain is propagated by CO insertion forming a surface acyl species. Surface acyl species can be hydrogenated to a surface alcohol species. Formation of oxygenates is accomplished either by α -hydrogenation of the surface alcohol species, which forms linear alcohols or by hydrogen elimination, which forms aldehydes. Ketones may be formed primarily by the addition of a surface alkyl group.

Furthermore, non-polymerising side reactions such as the water-gas shift reaction and the Boudouard reaction may take place. The Boudouard reaction may contribute to catalyst deactivation by carbon deposition [18]. The water-gas shift activity only plays a

significant role for iron-based catalysts, as cobalt and ruthenium have a low water-gas shift activity. The water-gas shift reaction is desirable when a feedstock with a non-stoichiometric syngas ratio is used [11].

5.2.2 The product selectivity

The product distribution of the FT synthesis is determined by the catalyst, the reaction conditions and type of reactor [11]. The product selectivity of cobalt-based catalysts is typically expressed in terms of the chain growth probability (α), the C_{5+} selectivity and the olefin to paraffin ratio (O/P). The selectivity for branched products may also be described but, due to the low amount of branching on cobalt-based catalysts, it is often disregarded. Usually, only a fraction of the FT product is analysed. In most instances analysis is limited to the C_1 to C_{16} fraction. Kinetic analysis of the FT synthesis requires evaluating the product up to at least C_{30} [11].

The FT product distribution can be described by the Anderson-Schulz-Flory distribution (ASF):

$$x_n = (1 - \alpha)\alpha^{n-1} \quad (5.1)$$

, where x_n is the mole fraction of the product containing n carbon atoms and α is the chain-growth probability. The chain growth probability α can be determined by a semi-logarithmic plot of the mole fraction of linear hydrocarbons versus the carbon number n , as shown in Figure 5.1.

The experimentally obtained FT product distribution may show some deviations from the ASF distribution. On cobalt catalysts, the methane selectivity is typically larger, while the ethene (and C_2) selectivity is typically lower than expected from the ASF distribution. To explain the large amount of methane in the FT product the existence of a separate site, or alternative pathways for methane formation have been proposed [19, 20].

The low C_2 selectivity can be explained by the difference in the desorption barrier for ethene and propene on the cobalt surface [21]. Propene is slightly more stable than ethene, due to the stabilising effect of the additional methyl group by hyperconjugation with the π -double bond. Furthermore, the methyl group causes a slight steric repulsion for propene adsorption. In conclusion, propene is found to desorb at lower temperatures

and have shorter residence times than ethene. This results in ethene having a slower rate of termination as olefin and a larger rate of hydrogenation and potential chain growth, resulting in the low C_2 selectivity and lower olefin to paraffin ratio for C_2 products observed on cobalt catalysts.

The product selectivity is often observed to be carbon number dependent. For example, the olefin content in a carbon number fraction decreases with increasing carbon number [22]. This is caused by the increased retention time of long-chain olefins, due to their increased solubility in the FT product, which increases the probability of secondary olefin reactions [22].

In general, the product selectivity is a function of the CO conversion, so that the selectivity of different catalysts should actually be compared at the same level of conversion. The olefin selectivity decreases with increasing CO conversion [23]. The C_{5+} selectivity typically increases with increasing conversion, up to a threshold [24]. In slurry reactors, a sharp decline of the C_{5+} selectivity can be observed at very high conversions, accompanied by a strong increase in CO_2 production [24]. This may be due to increased catalyst deactivation caused by catalyst oxidation due to increased back-mixing of water in the slurry reactor.

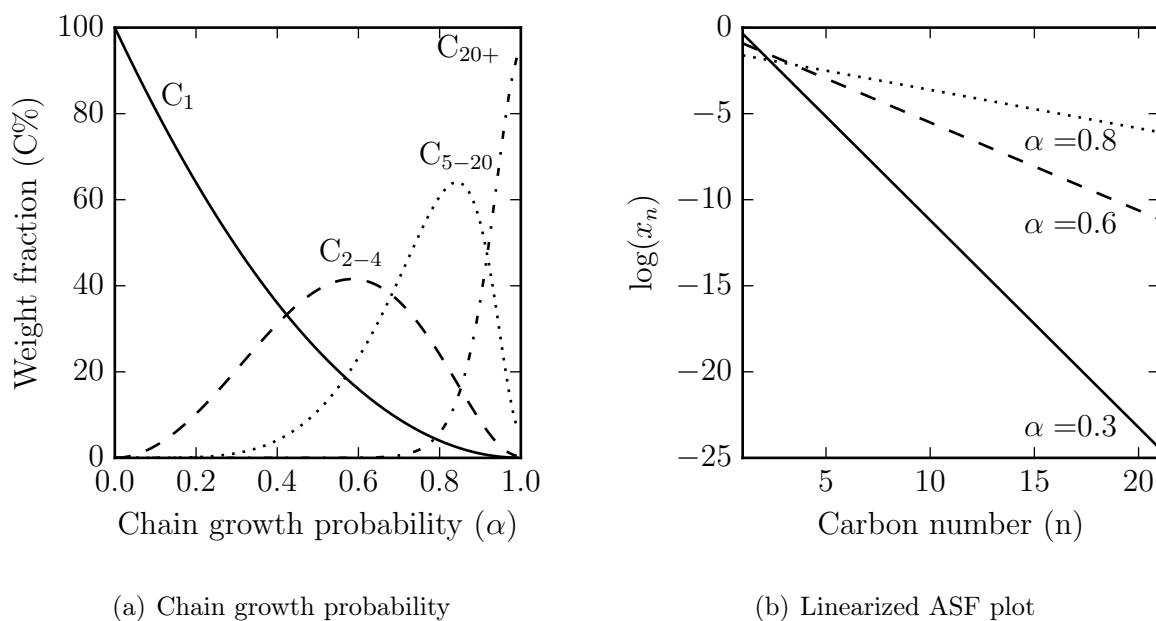


Figure 5.1: Product distribution of the FT synthesis as described by the Anderson-Schulz-Flory distribution (ASF).

Furthermore, the product selectivity is dependent on the reaction conditions, and much like the choice of the reactor and metal catalyst, the choice of reaction conditions is determined by the available feedstock (H_2/CO ratio) and the desired products. Table 5.2 summarises the effect of reaction conditions on the product selectivity.

Table 5.2: Influence of reaction conditions on product selectivity in the Fischer-Tropsch synthesis, adapted from [11]. \uparrow : Increase with increasing parameter. \downarrow : Decrease with decreasing parameter. *: Complex relationship.

Parameter	Chain length	Chain branching	Olefin selectivity	Alcohol selectivity	Carbon deposition	Methane selectivity
Temperature	\downarrow	\uparrow	*	\downarrow	\uparrow	\uparrow
Pressure	\uparrow	\downarrow	*	\uparrow	*	\downarrow
H_2/CO	\downarrow	\uparrow	\downarrow	\downarrow	\downarrow	\uparrow
Conversion	*	*	\downarrow	\downarrow	\uparrow	\uparrow
Space velocity	*	*	\uparrow	\uparrow	*	\downarrow

An increase in the reaction temperature increases the CO conversion and the yield of light hydrocarbons (chain growth probability decreases) [25]. For cobalt-based catalysts, the methane selectivity is found to increase sharply with reaction temperature [20].

Increasing the H_2/CO ratio increases the number of adsorbed hydrogen atoms on the cobalt surface and decreases the CH_2^* monomer concentration, which increases hydrogenation activity and leads to more methane and paraffin production at the expense of C_{5+} selectivity [25]. The H_2/CO ratio is typically defined by the feedstock used for syngas generation, and can not be varied over a wide range [12].

However, intra-particle diffusion limitations within large catalyst particles may increase the H_2/CO ratio in the vicinity of the metal surface (H_2 diffusivity $>$ CO diffusivity). This may increase the secondary reactions of 1-olefins and lead to a higher C_{5+} selectivity and lower olefinicity [26, 27]. Diffusion limitations imposed by the physical structure of the support are one example of how the support may affect the product distribution. It has also been postulated, that the surface chemistry of the support may contribute to the selectivity [28, 29]. However, the effects of the support on the product selectivity are not yet fully understood.

5.2.3 The active phase and the intrinsic activity

The metal phases present during the FT reaction may vary depending on the catalyst activation procedure, catalyst composition and reaction conditions [30]. Catalysts are typically incompletely reduced during the activation treatment, so that metallic, as well as oxidic or carbidic phases, may be present in the activated catalyst.

In cobalt-based catalysts, metallic cobalt is the active phase, whereas carbides are believed to be the active phase for iron-based FT catalysts [10]. The question whether the intrinsic activity, the rate of reaction per active site or site time yield, is constant; or may be affected by the crystallite size of the active phase (structure sensitivity), interaction of the metal and the support, or the degree of reduction, has been widely discussed [26, 29].

For all steps of the catalytic reaction to take place, not a single metal atom, but an ensemble of adjacent atoms may be required [31]. The number of ensembles present may decrease with decreasing crystallite size, which may give rise to a crystallite size effect.

Hence, for very small cobalt crystallites the intrinsic activity and C_{5+} selectivity are often found to decrease [32, 33]. For cobalt crystallite sizes above 6-10 nm, the cobalt-based FT synthesis is believed to be structure insensitive [25, 29, 34–36].

Furthermore, small crystallites also have a large contact area with the support, which leads to increased metal-support interaction (e.g. formation of mixed-metals support compounds) [37]. Hence, crystallite size effects and support effects are strongly intercorrelated [32]. In order to study crystallite size effects, supports with low metal-support interactions, such as carbon materials may be preferred [34]. In order to study metal-support interactions, the metal crystallite size should be kept above 10 nm so that crystallite size effects can be excluded.

Early studies indicated that the intrinsic activity might be affected by metal support interactions. Bartholomew and Reuel [38] reported a decrease in the cobalt site time yield in the order $Co/TiO_2 > Co/SiO_2 > Co/Al_2O_3 > Co/C > Co/MgO$. They postulated that the high intrinsic activity of cobalt supported on TiO_2 was a result of strong metal-support interactions. However, Johnson et al. [28] found that the intrinsic activity was more closely related to the extent of reduction, than the metal dispersion and postulated that the surface chemistry of the support might be the controlling factor in determining the intrinsic activity

of supported cobalt catalysts. More recent work by Iglesia et al. [26], Oukaci et al. [39] and Storsæter et al. [40] reported that cobalt site time yields were independent of the catalyst support and metal dispersion (for $d_{Co} > 10$ nm).

5.2.4 Catalyst deactivation

Catalyst deactivation, the loss of activity during the catalytic reaction with time on stream, is a large contributor to the costs of the FT process and therefore a much-discussed research topic [41]. The main mechanisms for catalyst deactivation in the FT synthesis are poisoning, metal sintering, metal reoxidation as well as metal-support compound formation and carbon deposition. Surface reconstruction upon exposure of cobalt to CO or syngas has also been postulated [42], and is frequently reported as a cause for catalyst deactivation. However, experimental evidence for surface reconstruction is at present limited to DFT calculations or surface science studies, so that the extent to which it contributes to catalyst deactivation is not clear.

Catalyst poisons are compounds that adsorb strongly and irreversibly on the catalyst surface rendering it inactive. Among the most common catalyst poisons for the FT synthesis, are sulphur [43], halides [44] and NH_3/HCN [45]. Poisons are introduced as contaminants of the synthesis gas, which can be minimised by synthesis gas purification.

Sintering describes the loss of catalytic surface area due to an increase in crystallite size (decrease of metal dispersion). It can account for up to 30% of catalyst deactivation in supported cobalt catalysts [46]. Sintering can take place by Ostwald ripening or crystallite migration/coalescence. Ostwald ripening proceeds via the formation of relatively volatile cobalt carbonyl or mobile sub-carbonyl species [47]. Metal-support interactions hinder sintering by decreasing the rate of formation of volatile carbonyl species [48]. Sintering is promoted by high CO conversions and high partial pressures of water [49]. A sintered catalyst can be regenerated by a reduction-oxidation-reduction (ROR) treatment [46], which causes large crystallites to split and re-disperse [50].

Carbon deposition can lead to deactivation of catalysts by encapsulation [51], active site blocking [52], the formation of subsurface carbon which may alter the electronic structure of the metal [53], the formation of filamentous carbon resulting in stress and possible

disintegration of the catalyst [51].

Reoxidation of cobalt is the most frequent explanation for deactivation during the FT reaction [41, 46]. In general, the FT environment is reductive. Hence, bulk reoxidation of cobalt to CoO is only feasible for metal crystallites smaller than 4.4 nm at elevated partial pressures of water (high conversion) [54]. The formation of cobalt support compounds although thermodynamically feasible is kinetically hindered [55]. Moodley et al. [56] found only small amounts of CoAl_2O_4 in spent catalysts and suggested that CoAl_2O_4 is formed from residual CoO and does not contribute to a large extent towards catalyst deactivation.

5.2.5 The influence of alumina supports

Alumina supports vary largely in their surface area, porosity, as well as surface chemistry. This is because alumina can form several different crystal structures. The alumina phases can be divided into those with an hcp oxygen sublattice and those with an fcc oxygen sublattice [57]. $\alpha\text{-Al}_2\text{O}_3$ is the most stable phase; it possesses trigonal symmetry with a rhombohedral Bravais centring (space group R-3c). The oxygen anions form an hcp sublattice, and the aluminium cations occupy 2/3 of the octahedral interstices. $\alpha\text{-Al}_2\text{O}_3$ has a low surface area and porosity, combined with a low attrition resistance and is therefore not well suited as catalyst support [25].

The most commonly used alumina in catalysis is the metastable form $\gamma\text{-Al}_2\text{O}_3$. This is due to the large surface area and porosity of the structure, which can be tuned by the choice of the aluminium hydroxide precursor, heat treatment and forming technology [25]. $\gamma\text{-Al}_2\text{O}_3$ crystallises in a spinel structure, with oxygen forming a fcc sub lattice and alumina randomly distributed over the octahedral and tetrahedral interstices.

The transformation of the metastable γ - phase to $\alpha\text{-Al}_2\text{O}_3$ may be direct or may proceed via δ - and $\theta\text{-Al}_2\text{O}_3$. Transformation of the metastable phases proceeds via movement of the aluminium cations while the oxygen anions remain in their position. The process thus follows chemical displacement of the aluminium cations rather than re-constructive re-crystallisation [58]. Doping of alumina with sodium impedes phase transformation because sodium occupies octahedral interstices and impedes diffusion of aluminium cations.

Furthermore, alumina may react with metals oxides at high temperatures (800-1200 °C),

or high partial pressures of water to form metal-aluminates [59, 60]. Formation of cobalt aluminate (CoAl_2O_4), or non-stoichiometric mixed cobalt-alumina phases during reductive treatment of alumina-supported cobalt catalysts decreases catalyst reducibility and thus negatively affects the activity (per gram catalyst) [61]. Zn-, Ni- or Mg-aluminate are being investigated as potential catalyst supports, due to their increased attrition resistance [25]. Mg- and Zn- aluminates form regular spinels with 1/8 of the tetrahedral holes occupied by the di-valent ions, while half of the octahedral positions are occupied by the tri-valent ions. Ni-aluminate forms an inverse spinel, where half of the di-valent ions occupy octahedral positions. Mg-aluminate is a promising support material due to low costs and high strength. However, traces of MgO present in the support material were found to adversely affect the catalytic performance [25].

The physical properties of alumina (e.g. surface area, pore volume, pore diameter) may affect the metal dispersion and reducibility but not the intrinsic activity or cobalt site time yield [62, 63]. The effect of the support on the product selectivity is not entirely understood. Although variations in product selectivity as a function of the support have frequently been reported, it is not entirely clear whether these effects are mainly caused by transport limitations [26] or the surface chemistry of the support (e.g. acidity) [28, 29] and thus metal-support interactions.

Rane et al. [62, 64] studied the effect of the Co crystallites size and alumina phase on the selectivity of the FT reaction. The crystallite size of alumina increased in the order $\gamma < \delta < \theta < \alpha\text{-Al}_2\text{O}_3$. Pore volume and surface area decreased with increasing alumina crystallite size. It was found that the degree of reduction was dependent on the crystal phase, pore size and crystallite size of alumina. Cobalt supported on α -alumina had the highest degree of reduction but lowest metal dispersion. Cobalt supported on medium pore catalysts were reduced at lower temperatures as compared to the small pore catalysts. For a constant crystallite size the C_{5+} selectivity was found to increase linearly with the mean pore diameter [64]. Hence, $\alpha\text{-Al}_2\text{O}_3$ usually shows a higher C_{5+} selectivity than $\gamma\text{-Al}_2\text{O}_3$ [29]. $\delta\text{-Al}_2\text{O}_3$ was found to have an unexpected high C_{5+} selectivity, which they speculated may be due to the low acidity of the support [62]. When the particle size was larger than 40-45 nm, the support was found to not affect the product selectivity [64].

Liu et al. [65] studied the effect of the morphology of alumina-supported cobalt catalyst

on the FT synthesis. γ - Al_2O_3 nanorods, nanofibers and spherical particles were synthesized via a sol-gel route. The difference in the stacking of the alumina particles was found to influence the porosity, which was the determining factor for the cobalt crystallite size. The alumina morphology influenced the stability of the catalyst during FT. Nanofiber supported catalysts were found to have the highest C_{5+} selectivity and were the least prone to sintering. Nanorod supported cobalt catalysts had the highest metal dispersions and catalytic activity.

The different alumina phases have different surface chemistry. In particular differences in the number of hydroxyl groups and the surface acidity, can be observed [66], which may affect the catalytic performance [64]. The number and strength of Lewis acid sites decrease with increasing surface hydration [66]. The number of Lewis acid sites was found to decrease in the order $\gamma > \theta > \delta > \alpha$ - Al_2O_3 [67]. Rane et al. [64] noted that, as the expected support acidity decreases, the observed olefin to paraffin ratio and the C_{5+} selectivity increase. However, support acidity was not experimentally determined.

Zhang et al. [68, 69] studied the effect of surface acidity of alumina. The surface acidity was varied by hydrothermal treatment of alumina with water, ethanol, acetic acid, ammonium and ammonium nitrate [68]. Treatment with acetic acid was found to increase the number of Brønsted acid sites. This led to a decrease in reducibility, a decrease in CO conversion and increased the selectivity to oxygenated compounds in particular CO_2 . The high CO_2 selectivity of the catalyst (30%), was explained by water-gas shift activity of unreduced surface cobalt compounds. Treatment with ammonia resulted in a drastically decreased surface area and enlarged pore structure. Formation of a boehmite phase was evident, which showed low acidity. The ammonia-treated catalysts showed high reducibility, an increase in CO conversion and C_{5+} selectivity. The same trends were observed when γ - Al_2O_3 catalysts with different amount of acid sites were compared [69]. The C_{5+} selectivity was found to increase, and methane selectivity decreased with decreasing acidity of the alumina support.

Rytter et al. [70] modified γ - Al_2O_3 supports by silylation in order to study the effect of hydrophobicity of the support on the catalytic performance of cobalt-based catalysts. They hypothesised that silylation would decrease the number of hydroxyl species on the alumina surface rendering it more hydrophobic, which may be similar to α - Al_2O_3 , which

shows high C_{5+} selectivities. The silylation had unpredictable effects on the surface area, porosity, dispersion and reducibility of the catalyst. Silylation after cobalt deposition resulted in a catalyst with lower C_{5+} selectivity, due to the introduction of mass-transport limitation. When the silylation was performed before cobalt deposition, the hydrophobicity of the surface was increased, and a slightly improved C_{5+} selectivity was observed. However, the hydrophobicity was not found to directly correlate with the selectivity, as the modification with chloromethyl trimethyl silane improved the C_{5+} selectivity without significantly altering the hydrophobicity of the catalyst.

It is concluded that the crystal structure, morphology and surface chemistry of alumina directly affect the reducibility and cobalt metal dispersion and may thus be a determining factor in understanding the overall catalytic performance.

5.3 Experimental

Catalyst preparation - Cobalt oxide with a crystallite size of 15-30 nm was prepared by calcination of a cobalt carbonate precursor. The resulting cobalt oxide crystallites were impregnated with aluminium sec-butoxide to render the cobalt-alumina inverse-model catalyst. This method of preparation was necessary to prepare material in the desired crystallite size range. Cobalt carbonate was synthesised from a 0.5 M cobalt containing solution prepared by adding 29.17 g $\text{Co}(\text{NO}_3)_2 \cdot 6\text{H}_2\text{O}$ to 200 ml demineralised water in a 1 l beaker. The pH of the solution was found to be between 5.6 and 5.8. Gaseous CO_2 was bubbled via a sparger through the solution until the pH had reached 3.6. The solution was stirred, and 83.3 ml of a 0.25 M ammonia solution was added dropwise over the course of 10-15 min while bubbling CO_2 through the solution. A precipitate formed when the pH rose above 6. After ammonia had been added, the CO_2 flow was stopped, and the suspension was stirred for another 10 min before pressure filtration. Filtration led to a slight increase in the pH of the filtrate, resulting in the formation of further precipitate. For that reason, the filtrate was collected and re-filtered three times. The combined precipitate was collected, and the filtrate was re-saturated with CO_2 until a steady pH was reached (pH=5.8-6). 83.3 ml of a 0.25 M ammonia solution was added, and the suspension was stirred for 10 min before the filtration procedure was repeated. The filtrate was collected, and the procedure was repeated until a total of 500 ml ammonia solution had been added to the solution. This sequential precipitation and filtration procedure was necessary, as keeping the precipitate in the preparation mixture for extended periods, or adding ammonia quickly, may result in the formation of an $(\text{NH}_4)_2\text{Co}_8(\text{CO}_3)_6(\text{OH})_6$ phase instead of the desired $\text{Co}(\text{CO}_3)_{0.5}(\text{OH}) \cdot 0.11\text{H}_2\text{O}$ phase, which has a more favourable morphology. The combined precipitate was washed three times with 500 ml demineralised water. The precipitate was dried in air at room temperature for 48 h. After drying, the cobalt carbonate powder was ground and calcined in a static oven at 300 °C for 16 h. The resulting black Co_3O_4 powder was modified with alumina by impregnation with a dry solution of aluminium sec-butoxide in hexane in an argon atmosphere to achieve a weight loading of 0.1, 0.5 and 2.5 wt% Al^1 followed by calcination at 300 °C for 4 h. The catalysts were

¹Al weight loading (w_{Al}) calculated as g Al per g Co_3O_4

denoted 0.0Al300, 0.1Al300, 0.5Al300, 2.5Al300 by their aluminium weight loading and calcination temperature.

X-ray diffraction (XRD) was performed on a Bruker AXS D8 advance diffractometer with Co-K α radiation ($\lambda = 1.78897 \text{ \AA}$) operating at 40 kV and 30 mA between $20^\circ 2\theta$ and $120^\circ 2\theta$ with a scanning speed of $0.056^\circ 2\theta/\text{s}$. The phase content and crystallite size was determined by Rietveld refinement performed using TOPAS.

Transmission electron microscopy (TEM) was performed on a FEI Tecnai G² high resolution microscope with a LaB₆ filament operated at 200 keV. Catalysts were dispersed in methanol, ultra-sonicated for 2 min and transferred to a carbon coated copper grid.

Scanning transmission electron microscopy-energy-dispersive X-ray spectroscopy (STEM-EDS) was performed using a JEOL JEM-ARM200F double Cs-corrected TEM equipped with an FEG, a STEM unit and a high angle annular dark-field (HAADF) detector, operated at 200 kV. The catalyst was dispersed in methanol, ultra-sonicated for 2 min and transferred to a carbon coated copper grid. The catalyst on TEM grids were plasma cleaned for 45 s using a Gatan Solarus model 950 plasma cleaner at 25 W under 20 ml/min Ar. EDX mapping was performed using an Oxford X-Max^N 100TLE detector and the Aztec software package.

The degree of reduction (DOR) was determined by performing a TPR experiment on the activated catalyst. Experiments were performed on an Autochem HP-2920 from Micromeritics by weighing 50 mg of the catalyst into a quartz tube plugged with quartz wool. The catalyst was activated in a flow of 10 ml/min pure H₂, by increasing the temperature at a heating rate of $1^\circ\text{C}/\text{min}$ to 350°C and holding for 10 h. Afterwards, the temperature was decreased to 60°C while flowing hydrogen to prevent reoxidation of the catalyst. Then the catalyst was purged for 60 min in a flow of 50 ml/min of 5 vol% H₂ in Ar. The catalyst temperature was increased to 900°C at a heating rate of $10^\circ\text{C}/\text{min}$ while monitoring the hydrogen consumption with a thermal conductivity detector (TCD). The hydrogen consumed during the reduction was determined from the peak area. The hydrogen consumption per peak area was calibrated using Ag₂O. The DOR was determined

according to:

$$\text{DOR (\%)} = 100 - \frac{H_{2,consumed}}{4N_{Co_3O_4,sample}} \cdot 100 \quad (5.2)$$

Hydrogen chemisorption was performed on an ASAP 2020 from Micromeritics. A sample of 100 mg catalyst were weighed into a quartz tube, sandwiched in between glass wool, and dried for 12 h at 120 °C prior to the experiment. The catalyst was reduced in hydrogen by increasing the temperature at a heating rate of 1 °C/min to 350 °C and holding for 10 h. After reduction, the temperature was decreased and the chamber was evacuated for 30 min at 330 °C and 140 °C. A leak test was performed before the start of the chemisorption experiment at 120 °C. The hydrogen uptake was measured at a temperature of 120 °C, by dosing hydrogen to 5, 25, 60, 120, 160, 215, 400 and 500 mmHg. The volume of hydrogen adsorbed at a monolayer coverage ($V_{H_2,mono}$) was calculated by performing an empirical fit according to

$$V_{H_2,ad} = \frac{V_{H_2,mono} \sqrt{K p_{H_2}}}{1 + \sqrt{K p_{H_2}}} + cf \cdot p_{H_2} \quad (5.3)$$

,where K is the adsorption constant and cf is an empirical correction factor.

The metal dispersion (D) was calculated by taking into account the degree of reduction according to:

$$D[\%] = \frac{N_{Co,surface}}{N_{Co,bulk}} \cdot 100 = \frac{N_{H,ad}}{N_{Co,bulk}} \cdot 100 \quad (5.4)$$

$$= \frac{\frac{2V_m}{22.411/\text{mol}}}{\frac{g_{cat} \cdot w_{Co}}{M_{Co}}} \cdot \text{DOR} \cdot 100 \quad (5.5)$$

The cobalt metal crystallite size was estimated as:

$$d_{Co} = \frac{96}{D(\%)} (nm) \quad (5.6)$$

CO reduction experiments were performed in an Autochem 2950 from Micromeritics. A sample of 50 mg catalyst were loaded into a quartz tube. The catalyst temperature was increased to 120 °C at a heating rate of 10 °C/min in a flow of 50 ml/min Ar, and the

catalyst was dried for 1 h. The catalyst temperature was decreased to 60 °C, and the gas was switched to 10 ml/min CO. The temperature was increased at a heating rate of 10 °C to 900 °C, and the TCD signal was recorded.

In order to establish the phase transitions occurring during the temperature programmed reduction experiment, an *in situ* CO reduction XRD experiment was performed. XRD measurements were performed on a Bruker D8 advance AXS with Co-K α radiation ($\lambda = 1.78897 \text{ \AA}$) at 40 kV. The catalyst was loaded into a borosilicate capillary. The capillary was fitted into a cell, which was developed in-house [71, 72]. The capillary was flushed with 4 ml/min carbon monoxide and heated with infra-red heaters. The temperature was increased at a heating rate of 1 °C/min from 50 °C to 450 °C and measurements were taken every 5 min.

Pyridine temperature programmed desorption (TPD) was performed in an Autochem 2920 from Micromeritics equipped with a vapour generator. A sample of 100 mg catalyst were loaded into a quartz tube. The catalyst was activated in a stream of 30 ml/min of pure H₂ by increasing the temperature to 350 °C at a heating rate of 10 °C/min and reducing the catalyst for 30 min. The temperature was decreased to 120 °C at a heating rate of 10 °C/min under a flow of 10 ml/min He and the sample was dried for 1 h. The sample temperature was decreased to 110 °C where pyridine pulse adsorption was performed. 15 pulses of 5.1 ml of He saturated with pyridine at 60 °C were dosed to the activated catalyst in 5 min intervals. The pyridine uptake was monitored with a TCD detector. Weakly adsorbed pyridine was removed by flowing 50 ml/min of pure He over the catalyst for 1 h. Pyridine desorption was carried out by increasing the temperature to 900 °C at a heating rate of 10 °C/min in a stream of 50 ml/min He, and monitoring the tail gas with a TCD detector.

The pyridine concentration (p_{Py}) at the saturation temperature of 60 °C was calculated using the Antoine equation and substituting the appropriate Antoine constants for

pyridine [73, 74]:

$$\ln(p_{Py}) = 4.16 - \frac{1371.35}{-58.49 - (60 + 273.15)\text{K}}$$

$$p_{Py} = 0.148 \text{ bar}$$

Hence, the mole fraction of pyridine (y_{Py}) is

$$y_{Py} = \frac{p_{Py}}{1 \text{ atm}} = \frac{0.148}{1.01} = 0.146 \quad (5.7)$$

The loop was heated to 110 °C and its volume is 5.1 ml therefore the amount of pyridine in the loop (N_{Py}) is:

$$V_{Py} = V_{\text{loop},STP} \cdot y_{Py} \cdot \frac{T_{STP}}{T_{\text{loop}}} = 0.612 \text{ ml} \quad (5.8)$$

$$N_{Py} = \frac{V_{Py}}{22.41/\text{mol}} = 27 \mu\text{mol} \quad (5.9)$$

Fischer-Tropsch synthesis was performed in a 1 l slurry reactor. 3-5 g of the catalyst were activated ex situ in a flow of hydrogen with a space velocity of 12 l/h/g_{cat}. The temperature was increased to 350 °C at a constant heating rate of 1 °C/min, and the catalyst was reduced for 10 h. The activated catalyst was cooled to room temperature and then transferred to 30 g hot wax in an argon atmosphere. The catalyst-wax was cooled to room temperature, and the mass of the reduced catalyst ($m_{\text{cat,red}}$) was determined by differential weighing of the wax tablet before and after addition of the catalyst. The reactor was filled with 250 g molten wax and the catalyst-wax tablet was loaded into the reactor. The reactor was pressurised with argon to 20 bar, and the temperature was increased to 220 °C at a stirring speed of 350 RPM. When the desired temperature and pressure was reached, syngas (H₂/CO=2) containing 25 vol% argon was introduced. The inorganic products were analysed on-line with a micro GC equipped with a TCD detector to determine the CO conversion and methane selectivity. Gaseous samples were taken in pre-evacuated ampoules [75] at regular intervals, and the samples were analysed off-line by GC-FID.

Experimental conditions for the GC-TCD and -FID analyses, as well as the flow diagram for the slurry reactor, can be found in Appendix D.

Inorganic products were analysed with a Varian CP-4900 micro GC equipped with a thermal conductivity detector. The GC was calibrated using a mixture of 10.1 vol% Ar, 5.2 vol% N₂, 15.2 vol% CH₄, 20.1 vol% CO, 9.8 vol% CO₂ and 30.6 vol% H₂ and response factors (f_i) for CH₄, CO and CO₂ were calculated using Ar as an internal reference.

$$\frac{F_i}{F_{\text{Ar}}} = f_i \frac{A_i}{A_{\text{Ar}}} \quad (5.10)$$

, where f_i is the response factor for compound i ; F_i and F_{Ar} are the molar flow rates of compound i and Ar, respectively; and A_i and A_{Ar} are the areas in the TCD chromatogram of compound i and Ar, respectively.

The CO conversion can be calculated according to

$$X_{\text{CO}} = \frac{F_{\text{CO},in} - F_{\text{CO},out}}{F_{\text{CO},in}} \quad (5.11)$$

, where X_{CO} is the conversion of CO and $F_{\text{CO},in}$ and $F_{\text{CO},out}$ is the molar flow rate of CO in the feed and tail gas, respectively.

The methane selectivity (S_{CH_4}) was calculated according to

$$S_{\text{CH}_4} = \frac{F_{\text{CH}_4,out}}{F_{\text{CO},in} \cdot X_{\text{CO}}} \quad (5.12)$$

Organic products were analysed using a Varian CP-3800 GC equipped with a flame ionization detector (FID). Sample ampoules were crushed in an ampoule breaker by a hydraulic piston, and the sample was injected onto the GC column in a flow of nitrogen. Compounds were identified using known FID-chromatograms of FT products as reference. The signal intensity of hydrocarbons in the FID is proportional to the number of carbon atoms and the number of carbon atoms bonded to oxygen. Kaiser [76] developed an incremental method of calculating the response factor by assigning every carbon-carbon bond a value of 1, a carbon-oxygen single-bond a value of 0.55 and a carbon-oxygen double-

bond is assigned a value of 0:

$$f_i = \frac{N_{C,i}}{N_{C,C-C} + 0.55N_{C,C-O} + 0N_{C,C=O}} \quad (5.13)$$

, where f_i is the response factor for compound i , $N_{C,i}$ is the number of carbon atoms in the compound i ; and $N_{C,C-C}$, $N_{C,C-O}$ and $N_{C,C=O}$ is the number of carbon atoms bonded to carbon, single bonded to oxygen and double bonded to oxygen, respectively. The quantity of compound i can then be calculated, using methane as an internal reference, on a molar basis according to

$$F_i = F_{CH_4} \cdot \frac{N_{C,CH_4}}{N_{C,i}} \cdot \frac{f_i \cdot A_i}{f_{CH_4} \cdot A_{CH_4}} = \frac{F_{CH_4}}{N_{C,i}} \cdot \frac{f_i \cdot A_i}{A_{CH_4}} \quad (5.14)$$

or on a carbon basis:

$$F_{C,i} = F_i \cdot N_{C,i} = F_{CH_4} \cdot \frac{f_i \cdot A_i}{A_{CH_4}} \quad (5.15)$$

The selectivity (S_i) for compound i can be calculated according to

$$\begin{aligned} S_i &= \frac{F_i}{F_{CO,in} \cdot X_{CO}} = \frac{F_{CH_4}}{F_{CO,in} \cdot X_{CO}} \cdot \frac{f_i \cdot A_i}{N_{C,i} \cdot A_{CH_4}} \\ &= S_{CH_4} \cdot \frac{f_i \cdot A_i}{N_{C,i} \cdot A_{CH_4}} \end{aligned} \quad (5.16)$$

The C_{5+} selectivity was calculated as:

$$C_{5+} = 100 - \sum_{i=1}^4 S_{C,i} \quad (5.17)$$

Catalytic activity was determined as a function of the mass of reduced catalyst loaded into the reactor. The water-gas shift activity of cobalt is negligible. Thus the rate of the FT synthesis (r_{FT}) can be simplified to the rate of CO consumption ($-r_{CO}$):

$$r_{FT} = -r_{CO} = \frac{F_{CO,in} \cdot X_{CO}}{m_{cat,red}} \quad (5.18)$$

Taking into account the degree of reduction and the alumina loading, the weight fraction of cobalt in the reduced catalyst can be determined. The cobalt time yield (CTY) can

then be calculated according to:

$$\begin{aligned} \text{CTY} &= \frac{F_{\text{CO},in} \cdot X_{\text{CO}}}{N_{\text{Co}^0}} \quad \left[\frac{\text{mol CO}}{\text{mol Co} \cdot \text{s}} \right] \\ &= \frac{F_{\text{CO},in} \cdot X_{\text{CO}}}{\frac{m_{\text{cat,red}} \cdot w_{\text{Co}^0}}{M_{\text{Co}}}} = \frac{-r_{\text{CO}}}{\frac{w_{\text{Co}^0}}{M_{\text{Co}}}} \end{aligned} \quad (5.19)$$

The turn over frequency (TOF) was determined as the rate of CO consumption per mole of surface cobalt:

$$\begin{aligned} \text{TOF} &= \frac{F_{\text{CO},in} \cdot X_{\text{CO}}}{N_{\text{Co,surf}}} \\ &= \text{CTY} \cdot \frac{N_{\text{Co,bulk}}}{N_{\text{Co,surf}}} = \frac{\text{CTY} \cdot 100}{D[\%]} \quad \left[\frac{\text{mol CO}}{\text{mol Co}_{\text{surf}} \cdot \text{s}} \right] \end{aligned} \quad (5.20)$$

The rate of the FT synthesis may be described as a pseudo first-order reaction with respect to hydrogen [11]:

$$r_{\text{FT}} = -r_{\text{CO}} = k \cdot p_{\text{H}_2} \quad (5.21)$$

The H_2/CO ratio was kept constant. The partial pressure of H_2 depends on the CO conversion, the dilution with inert carrier (e.g. Ar) and the formation of gaseous product. 1-Olefin formation is generally agreed to be the major FT pathway [77]. Hence, the FT reaction may be simplified as:



The partial pressure of H_2 can then be determined as:

$$\begin{aligned} y_{\text{H}_2} &= \frac{p_{\text{H}_2}}{p} \\ &= \frac{N_{\text{H}_2}}{N_{\text{CO}} + N_{\text{H}_2} + N_{\text{C}_n\text{H}_{2n+2}} + N_{\text{H}_2\text{O}} + N_{\text{Ar}}} \\ &= \frac{2n(1 - X_{\text{CO}})}{n(1 - X_{\text{CO}}) + 2n(1 - X_{\text{CO}}) + X + nX + m} = \frac{2n(1 - X_{\text{CO}})}{3n - X_{\text{CO}}(2n - 1) + m} \\ &= \frac{2(1 - X_{\text{CO}})}{3 - X_{\text{CO}}(2 - \frac{1}{n}) + \frac{m}{n}} \end{aligned} \quad (5.22)$$

It follows that:

$$k = \frac{-r_{\text{CO}}}{p \cdot y_{\text{H}_2}} \quad (5.24)$$

The activation energy can now be determined from the slope of a plot of $\ln(k)$ vs. $1/T$ by using the Arrhenius equation:

$$k = Ae^{\frac{E_a}{RT}} \quad (5.25)$$

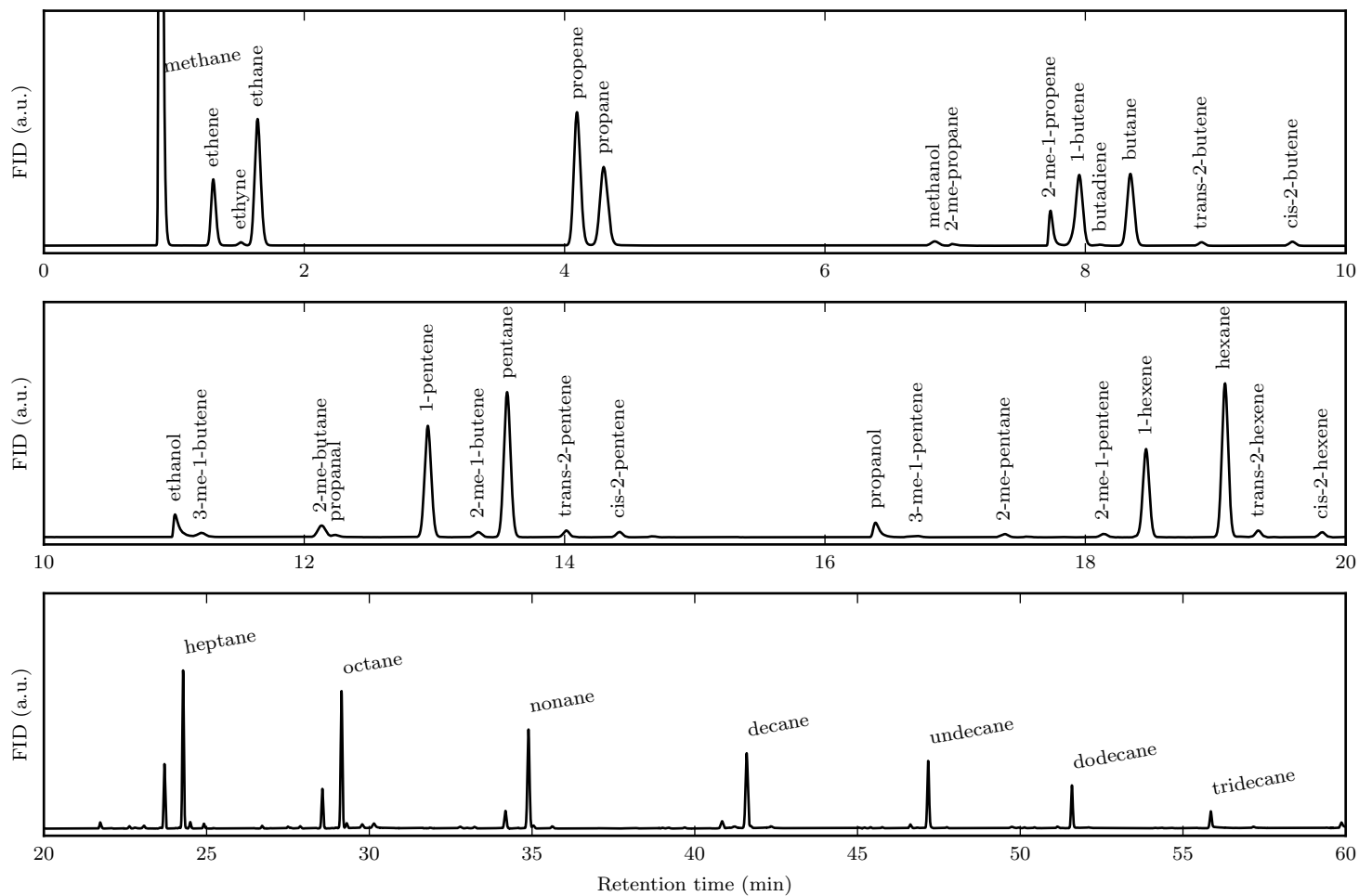


Figure 5.2: Representative FID chromatogram of Fischer-Tropsch product. Product sample taken after 208 h TOS for catalyst 0.0Al300.

5.4 Results

5.4.1 Degree of reduction

FT catalysts need to be activated by a reductive treatment to transform the precursor into the catalytically active metallic form. A compromise has to be found between a temperature high enough to achieve complete catalyst reduction within a reasonable time, and a temperature low enough to prevent excessive sintering. This often leads to catalysts being incompletely reduced after activation. For alumina-supported cobalt catalysts which show strong metal-support interactions a degree of reduction below 60% is not uncommon [25, 37, 78]. In order to obtain accurate information on the catalytic activity, the degree of reduction (DOR) has to be determined.

Cobalt catalysts are typically reduced at temperatures of 350-450 °C in H₂ [37, 78]. In this study, the aim was to apply mild reduction conditions to minimise metal sintering and at the same time adhere to conventional activation procedures in order to achieve a better comparison to the literature. According to the H₂-TPR experiments discussed in Section 4.4.2, 350 °C was determined as an adequate temperature to achieve a high DOR for all catalysts.

The degree of reduction (DOR) was determined by performing a H₂-TPR experiment on the activated catalysts. The TPR profiles of the *activated* catalysts are shown in Figure 5.3. A reduction peak is visible in all cases, indicating that all catalysts were incompletely reduced. The peak area corresponds to the hydrogen consumption and correlates with the DOR.

The DOR decreased with increasing alumina loading from 96% to 86% for catalyst 0.0Al300 and 2.5Al300, respectively. With increasing alumina loading the peak maxima shifted to higher temperatures, and the total peak area increased. For instance, catalyst 2.5Al300 showed a peak maxima at 252 °C, which corresponds to a peak shift of more than 100 °C, compared to 0.0Al300.

The reduction of bulk Co₃O₄ to metallic cobalt proceeds in two steps, via the formation of CoO [6]. Hence, the reduction of Co₃O₄ shows two (sometimes strongly overlapping) reduction peaks, while the reduction of CoO, shows only one peak [79]. Catalyst 0.0Al300 and 0.1Al300 had virtually the same DOR, and only showed one reduction peak at 147 °C

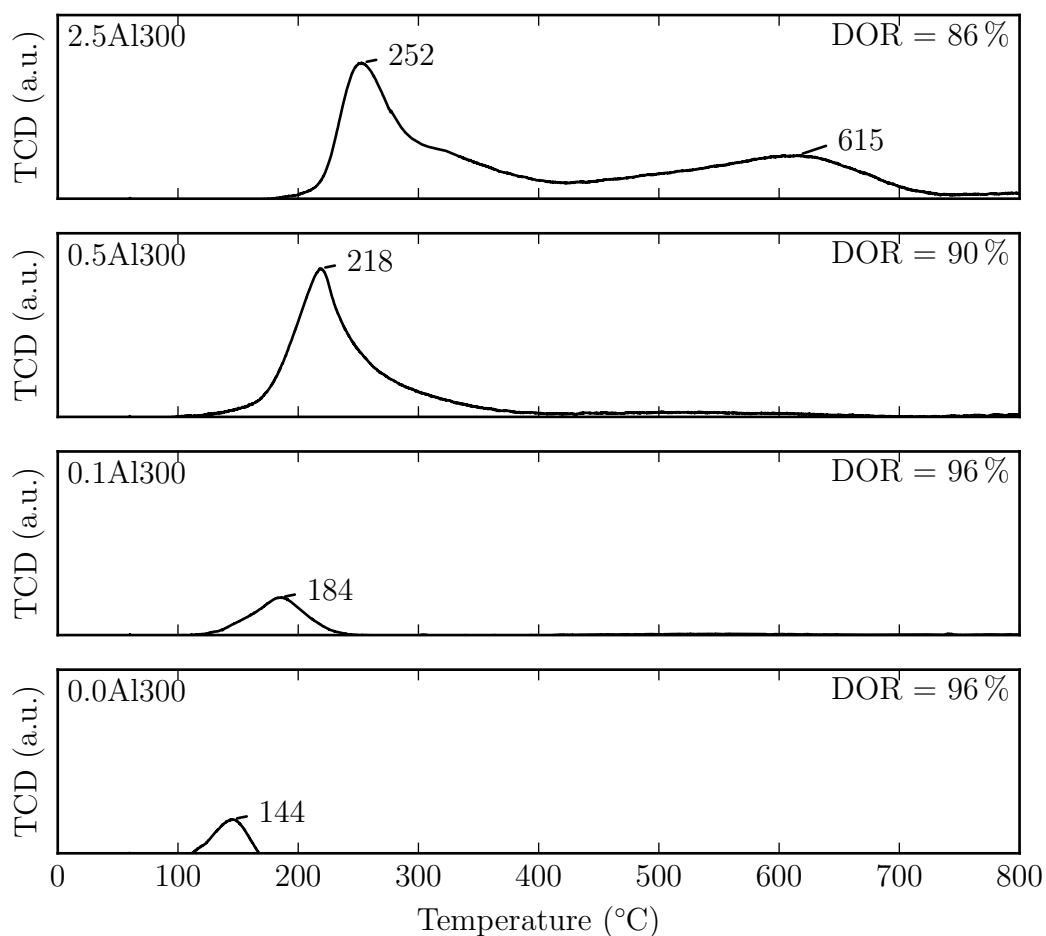


Figure 5.3: TPR experiments of activated catalysts after reduction at 350 °C for 10 h. The hydrogen consumption can be determined from the peak area and gives information on the degree of reduction.

and 184 °C, respectively. It is concluded, that the unreduced fraction of cobalt atoms was present exclusively as Co^{2+} (not Co^{3+}), in accordance with results from the *in situ* XRD experiments (see Figure 4.18 on page 76). In the case of 0.0Al300, CoO is expected to be the only phase present after activation.

The reduction peak of catalyst 0.1Al300 was broadened which indicates two consecutive reduction processes were taking place [8, 80]. For catalyst 0.5Al300 and 2.5Al300, the second reduction step was visible as a shoulder around 300 °C. The reduction profile of 2.5Al300 showed an additional peak at 615 °C. This indicates that more than one cobalt phase was present in the alumina-modified catalysts after activation. In these catalysts, Co^{2+} may be present as CoO, as well as a non-stoichiometric cobalt-alumina surface phase,

with slower reduction kinetics. This cobalt-alumina surface phase likely consisted of Co^{2+} in octahedral coordination, which is more difficult to reduce than pure CoO , but easier to reduce than cobalt-alumina phases with Co^{2+} in tetrahedral coordination [8].

The reduction profile of 2.5Al300 showed a large portion of the reduction was taking place above $300\text{ }^\circ\text{C}$. This indicates that a substantial fraction of the Co^{2+} ions may have been coordinated to alumina. *In situ* XANES experiments (see Section 4.5.2) showed no evidence for the presence of Co^{2+} ions in tetrahedral coordination below a reduction temperature of $550\text{ }^\circ\text{C}$. It is therefore hypothesised that the cobalt-alumina phase in catalyst 2.5Al300 after activation contained Co^{2+} in octahedral coordination, just like in catalyst 0.1Al300 and 0.5Al300, albeit in a higher concentration. The reduction peak at $615\text{ }^\circ\text{C}$ can be assigned to a cobalt-alumina phase with tetrahedrally coordinated Co^{2+} ions which was formed during the TPR experiment, and was not present in the activated catalyst.

In situ XRD experiments showed complete reduction to metallic cobalt for catalysts containing less than 2.5 wt% Al (see Figure 4.18 on page 76). Only for catalyst 2.5Al300 CoO was visible in the XRD at temperatures up to $400\text{ }^\circ\text{C}$. The TPR experiments, however, revealed that neither of the catalysts was completely reduced. This indicates that part of the Co^{2+} phase formed during the reduction may have been X-ray amorphous, either because the phase lacked long-range order, or because the crystallite size was too low to diffract the beam coherently. Hence, XRD experiments may overestimate catalyst reducibility. Furthermore, it should be noted that the XRD capillary set-up exhibits near perfect plug-flow conditions, which may not be the case for the set-up of the TPR experiments. However, the conditions in the TPR are better comparable to conditions during the *ex situ* catalyst activation performed for catalyst testing.

It is curious that the reduction profiles of the activated catalysts have peaks at temperatures below the activation temperature of $350\text{ }^\circ\text{C}$. It appears as though the reducibility of the catalysts was increased after catalyst activation. This may be explained by the removal of adsorbed water from the catalyst surface during the experiment. High partial pressures of water are known to decrease catalyst reducibility [81]. This is because adsorbed water or OH species may block active sites necessary for H_2 dissociation. During the reduction of metal oxides, oxygen atoms are removed as water from the metal oxide lattice. This may lead to the surface being increasingly covered with adsorbed OH species. In the TPR

experiments the catalysts were reduced *in situ*. After the reduction the catalysts had to be cooled and flushed with Ar in order to remove H₂ from the environment. In this process water may desorb from the catalyst surface rendering it more active for H₂ dissociation. H₂ dissociation may be facilitated on the clean catalyst surface and reduction peaks appear at lower temperatures.

It should be noted that other experimental procedures exist to determine the DOR of cobalt catalysts. Different methods may give slightly different results (due to their inherent limitations and uncertainties), which is why sometimes more than one experiment is performed to obtain a complete picture [82]. Possibly the most frequently applied method to determine the DOR is by oxygen titration. Oxygen titration experiments are often believed to be more precise, because the oxygen consumption can be determined very accurately when small pulses of an oxidising gas mixture are dosed during an isothermal experiment, resulting in sharp peaks. However, oxygen titration of bulk cobalt catalysts is not feasible, because it leads to the formation of an oxide layer on the surface, which passivates the catalyst and inhibits further oxidation of the bulk (see Appendix C). Therefore, oxygen titration may underestimate the DOR. Thus TPR experiments performed on the activated catalysts were chosen as the most accurate method to determine the DOR.

5.4.2 Cobalt metal dispersion

The metal dispersion and metal crystallite size were determined by H₂-chemisorption. The obtained H₂-adsorption isotherms are shown in Figure 5.4.

The adsorption isotherms are expected to follow the Langmuir equation [83] adapted to dissociative adsorption

$$V_{\text{H}_2,\text{ad}} = \frac{V_{\text{H}_2,\text{mono}}\sqrt{Kp_{\text{H}_2}}}{1 + \sqrt{Kp_{\text{H}_2}}} \quad (5.26)$$

, where $V_{\text{H}_2,\text{ad}}$ is the volume of H₂ adsorbed (H₂ uptake), $V_{\text{H}_2,\text{mono}}$ is the volume of H₂ adsorbed at a monolayer coverage (maximum coverage), p_{H_2} is the partial pressure of H₂ and K is the adsorption constant.

According to the Langmuir equation, the H₂ uptake is expected to increase with increas-

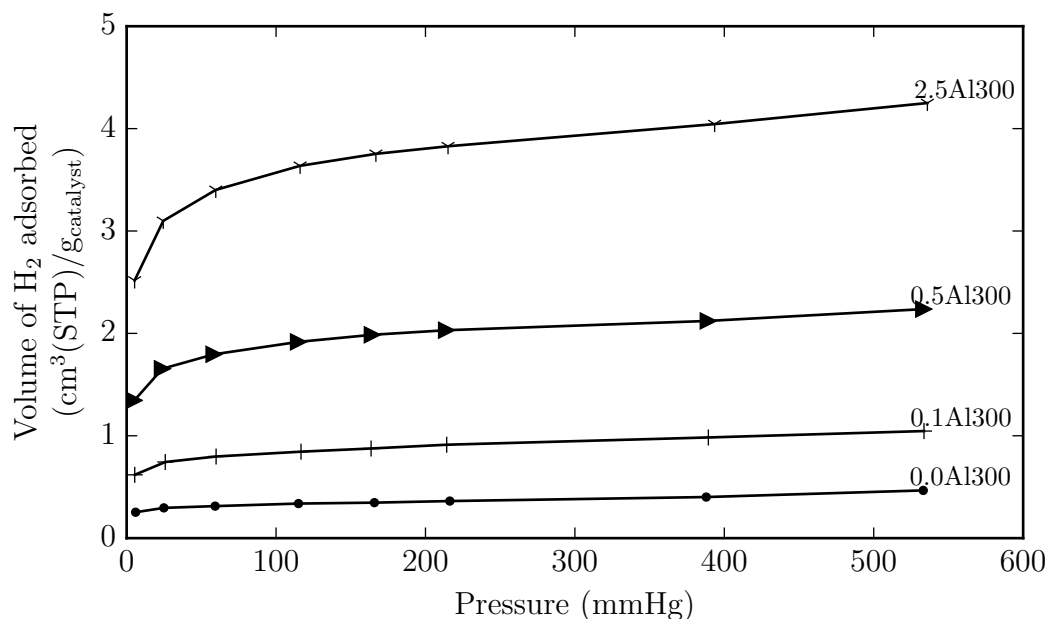


Figure 5.4: H₂-chemisorption experiments of a series of alumina-modified catalysts after reduction at 350 °C.

ing pressure up to the saturation pressure, at which point the surface is completely covered, and no further chemisorption can take place. The cobalt surface is expected to be saturated at a coverage of one monolayer of H atoms. Adsorption of more than one monolayer would essentially require H₂ condensation, which is not possible as the experiments are carried out at 120 °C, which is above the critical temperature of H₂ ($T_{crit} = -243$ °C [84]). Hence, the number of H atoms adsorbed at monolayer coverage corresponds to the number of cobalt atoms present at the catalyst surface (metal dispersion).

The H₂-adsorption isotherms obtained during H₂-chemisorption deviate from the Langmuir-adsorption isotherm. The H₂ uptake was not found to plateau, but increased slightly with increasing pressure. This observation is not uncommon when measuring H₂-chemisorption on supported catalysts and has been attributed to a spillover effect [85]. Hydrogen-spillover describes the effect of H₂ being dissociated on a metal centre and then migrating to the support material. The support is thus providing additional sites for H₂ adsorption, and the measured H₂ uptake may exceed the monolayer coverage.

In this study, the deviation from the Langmuir-adsorption isotherm was observed for all catalysts, including unmodified Co₃O₄. Hence, the deviation can not be explained

by hydrogen-spillover. Instead, the deviation may simply be a measurement artefact, for example, caused by small leaks within the instrument².

Therefore, the volume of the monolayer coverage was calculated by performing an empirical fit according to

$$V_{\text{H}_2,ad} = \frac{V_{\text{H}_2,mono} \sqrt{K p_{\text{H}_2}}}{1 + \sqrt{K p_{\text{H}_2}}} + cf \cdot p_{\text{H}_2} \quad (5.27)$$

, where $cf \cdot p_{\text{H}_2}$ is a linear correction term, to account for the deviation from the Langmuir equation. The fitting parameters are reported in Appendix B.

The metal crystallite size was determined from the metal dispersion as

$$d_{\text{Co}} = \frac{96}{D(\%)} \text{ nm} \quad (5.28)$$

, where d_{Co} is the cobalt metal crystallite size in nm and D is the metal dispersion in % [86]. The DOR was taken into account when calculating the metal dispersion.

The metal dispersions and metal crystallite sizes determined from the chemisorption experiments are reported in Table B.1. The catalysts studied in this work were essentially bulk cobalt catalysts. Therefore, the catalysts were expected to sinter extensively during catalyst activation. The metal dispersion, as determined by H₂-chemisorption experiments, varied between 0.23 % (\approx 421 nm) and 3.30 % (\approx 29 nm) and increased with increasing alumina loading. In contrast, for conventional alumina-supported catalysts with a 10-20 wt% loading of cobalt, metal dispersions above 10 % can be achieved [37].

However, the effect of the alumina modification on the metal dispersion is surprisingly large. The 0.0Al300 catalyst had a metal dispersion of 0.23 %, the addition of 0.1 wt% Al almost tripled the dispersion to 0.64 % and adding 2.5 wt% Al resulted in a 14-fold increase in the metal dispersion to 3.3 %. In comparison, Jacobs et al. [37] reported a similar metal

²The H₂ uptake is calculated from the difference between the measured and the expected increase in pressure after addition of a known volume of H₂ to the evacuated sample tube. Prior to the analysis, a leak test is performed, whereby the sample tube is evacuated and then isolated and the pressure is monitored over 30 min. The most likely point of failure are O-rings around the quartz tube, which would result in air leaking into the tube. An increase in pressure over 10 μ mHg leads to cancellation of the measurement. A leak through the valve connecting the sample tube with the remaining instrument, which remains under vacuum may result in a slight pressure decrease, which is not accounted for by a leak test. A leak causing a pressure decrease may lead to an increase in the determined H₂ uptake with increasing pressure.

dispersion of 2.4 % for a 33 wt% Co catalyst supported on a low surface area ($100 \text{ m}^2/\text{g}$) Al_2O_3 support (reduced at $350 \text{ }^\circ\text{C}$). Their catalyst had a DOR of 67 %, whereas the DOR for catalyst 2.5Al300 was 86 %. This indicates a large degree of interaction between the cobalt and alumina phase. In order to achieve this degree of interaction, the alumina phase has to remain on the catalyst surface, in direct contact with the cobalt phase throughout the reduction of Co_3O_4 to metallic cobalt. Furthermore, this demonstrates that the introduction of small amounts of alumina to Co_3O_4 can drastically reduce catalyst sintering while achieving a high DOR.

Table 5.3: Results of H_2 -chemisorption of alumina-modified cobalt catalysts performed at $120 \text{ }^\circ\text{C}$ on activated catalysts.

w_{Al} (wt%)	$V_{\text{H}_2, \text{mono}}$ ($\text{cm}^3(\text{STP})/\text{g}$)	$N_{\text{Co, surf}}$ ($\text{mmol}/\text{g}_{\text{cat}}$)	Dispersion (%)	d_{Co}^a (nm)	$d_{\text{Co}_3\text{O}_4}^b$ (nm)
0.0	0.32	0.028	0.23	421	14
0.1	0.88	0.078	0.64	150	14
0.5	2.07	0.185	1.63	59	14
2.5	3.94	0.352	3.30	29	14

^aCo crystallite size determined from H_2 -Chemisorption using equation (5.6)

^b Co_3O_4 crystallite size prior to catalyst activation determined by XRD from FWHM of the (220) reflection peak using the Scherrer equation.

Equation (5.28) used to determine the cobalt metal crystallite size assumes spherical crystallites of fcc cobalt, with an average cobalt site density of 14.6 nm^2 [86]. The equation was developed for supported catalysts and is not expected to be strictly applicable to bulk cobalt. Heavy sintering taking place during catalyst activation is expected to result in a catalyst composed of a highly aggregated conglomerate of cobalt crystallites, possibly forming inaccessible cavities, with an irregular shape.

Moreover, it should be considered that the metal surface is decorated with alumina, which may block cobalt metal sites. Thus the crystallite size calculated from H_2 -chemisorption may be larger than the actual metal crystallite size. Cobalt metal site blockage by metal oxide promoter has been reported by Johnson et al. [87]. They were able to estimate the amount of metal oxide promoter on the metal surface using HAADF-STEM/STEM-EDS.

However, the H_2 -chemisorption experiments reveal the number of metal sites available for H_2 adsorption, which can render information on the intrinsic catalyst activity. The

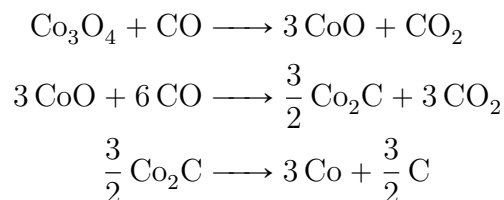
metal crystallite sizes are merely reported to serve as a direct measure for comparison of the crystallite sizes in the activated and calcined catalysts.

In cobalt-based FT synthesis crystallite size effects only play a role for cobalt crystallite sizes below 6-10 nm ($D = 9 - 16\%$). In this study dispersions below $< 4\%$ were observed with a minimum crystallite size of 29 nm. Hence, the metal crystallite size can safely be assumed to be above 10 nm so that crystallite size effects can be ruled out.

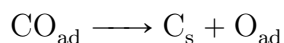
5.4.3 Boudouard reaction

Cobalt-based FT catalysts are almost always activated in H_2 , whereas iron-based FT catalyst may also be activated in CO or syngas [11, 88]. The activation of iron catalysts in CO is favourable because the thus formed iron carbides are believed to be the active phase. Cobalt carbides, however, do not show significant FT activity, and reductive treatments in CO may lead to excessive catalyst sintering due to the increased mobility of the cobalt phase by formation of cobalt carbonyls [47], hence the strong preference for H_2 -activation. In this study, the reducibility of cobalt catalysts in CO was studied in a series of CO-TPR experiments. The aim was not to investigate the feasibility of CO activation, but to establish a relationship between the alumina modification and the activity towards CO dissociation, by following the surface catalysed Boudouard reaction.

The reduction of Co_3O_4 to metallic cobalt in CO atmosphere may proceed via the formation of cobalt carbide according to:

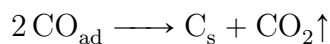


CO may dissociate on metallic cobalt to form surface carbon according to:



At temperatures above $400^\circ C$, CO may dissociate on cobalt via the surface catalysed

Boudouard reaction to form surface carbon and CO₂ [89]:



Dissociation of CO only forms a single layer of surface carbon, while the Boudouard reaction may form multi-layered carbon deposits [90].

Figure 5.5 shows the CO-TPR results for the series of alumina-modified catalysts calcined at 300 °C. The 0.0Al300 catalyst showed three partly overlapping peaks below 350 °C and a separate broad feature above 500 °C. At 300 °C a very sharp peak was observed. The CO reduction profile of 0.1Al300 showed essentially the same features, but the high-temperature peak was twice as large and shifted to a lower temperature. The 0.5Al300 catalyst showed additional features between 350-400 °C. Here, the onset of the high-temperature peak was shifted to slightly lower temperatures and was more pronounced, compared to 0.1Al300. The profile of the catalyst with the highest weight loading, 2.5Al300, differed strongly from the others. The sharp peak, which appeared at 295 °C for the catalyst with lower Al contents was shifted towards 373 °C, while the high temperature features, which were separated by almost 300 °C for the other catalysts, overlaps with the reduction peaks around 400 °C.

The high-temperature features are ascribed to the surface catalysed Boudouard reaction, while features appearing below 350-450 °C are ascribed to the reduction of Co₃O₄ to metallic cobalt in multiple steps. The first peak appearing around 200 °C to 250 °C corresponds to the formation of CoO. The sharp peak appearing around 300 °C to 380 °C corresponds to the formation of Co₂C, which consumes six times as much CO as the formation of CoO, thus explaining the high intensity of this peak. Peaks corresponding to the cobalt oxide reduction shifted to higher temperatures with increasing alumina content, except for catalyst 0.1Al300. This is in line with the H₂-TPR experiments discussed in Section 4.4.2, where alumina was found to decrease the catalyst reducibility by decreasing the rate of the Co₃O₄ and CoO reaction, except for catalyst 0.1Al300, which showed a slight acceleration for the rate of reduction.

The high-temperature feature appearing around 400-500 °C can be attributed to a surface catalysed Boudouard reaction, where CO disproportionates to CO₂ and carbon. The

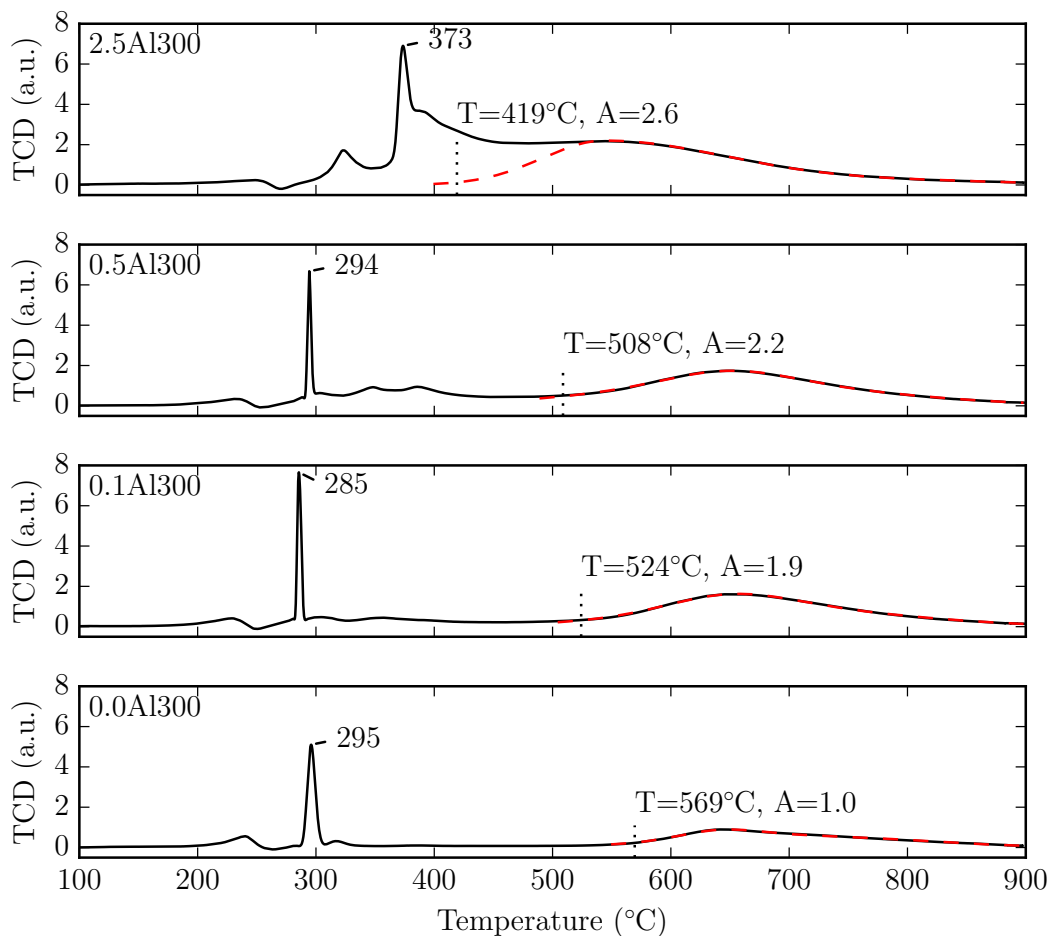


Figure 5.5: Results of CO-TPR experiments of a series of alumina-modified cobalt catalysts calcined at 300 °C. - -: Boudouard reaction - peak area (A) reported as fraction of the peak area for catalyst 0.0Al300.

onset of the reaction shifted to lower temperatures and the corresponding peak area increased with increasing alumina loading. The onset of the reaction was shifted from 569 °C to 419 °C, while the peak area increased by 160 % upon modification with 2.5 wt% Al.

The increase in peak area may be ascribed to the increase in metal dispersion upon alumina modification as determined by H₂-chemisorption. An increase in metal dispersion increases the number of cobalt sites and thus increases the activity per gram cobalt. However, the shift of the surface catalysed Boudouard reaction to lower temperatures indicates a change in the activation energy or pre-exponential factor and thus a facilitated CO dissociation. Crystallite size effects are not expected to be relevant in these catalysts, as the crystallite size is $\gg 10$ nm. Hence, it is proposed that alumina modification facilitates CO

dissociation and thus increases the activity for the surface catalysed Boudouard reaction.

CO dissociation may not be the rate-limiting step for the FT synthesis. Hence, facilitating the CO dissociation may not influence the intrinsic activity for the FT synthesis. A higher rate of CO dissociation, however, may change the surface coverage of C on the catalyst surface, which may affect the product selectivity.

Carbon deposition by the Boudouard reaction was confirmed by TEM imaging of a catalyst sample after CO-TPR as shown in Figure 5.6. The image shows metal crystallites encapsulated by material appearing like multi-wall carbon nanotubes. The d-spacing of this material was determined to be 3.4 Å, which is consistent with graphitic carbon [90, 91].

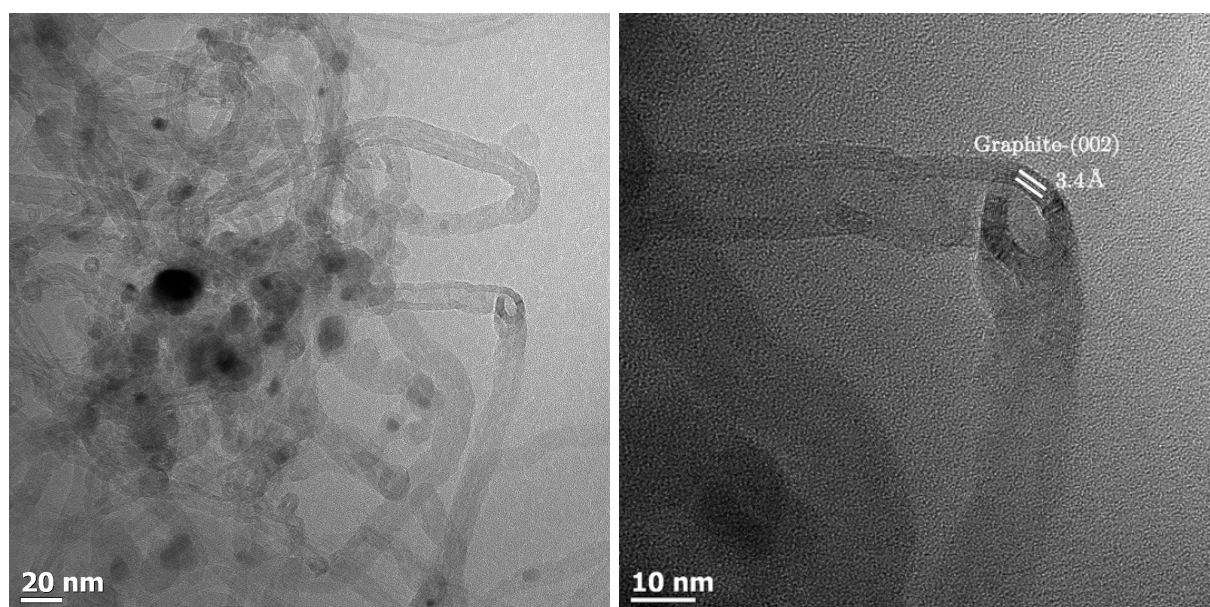


Figure 5.6: TEM image of 0.5Al300 ex CO-TPR showing metal particles encapsulating in multiwall carbon nanotubes.

The assignment of the reduction peaks during the TPR experiment was confirmed by *in situ* XRD reduction experiments of the 0.0Al300 reference catalyst in CO, which are shown in Figure 5.7. The XRD showed the reduction of Co_3O_4 to CoO taking place between 200 °C and 250 °C. Starting at 300 °C, the CoO phase was directly reduced to Co_2C . The Co_2C phase decomposed to metallic cobalt showing a sharp phase transition at 350 °C. This is in agreement with Claeys et al. [92] who reported decomposition of Co_2C between 300 °C and 350 °C, when heated in argon.

The formation of Co_2C gave rise to a very sharp peak in the TPR, due to the large consumption of CO during this process. The XRD experiments showed thermal decom-

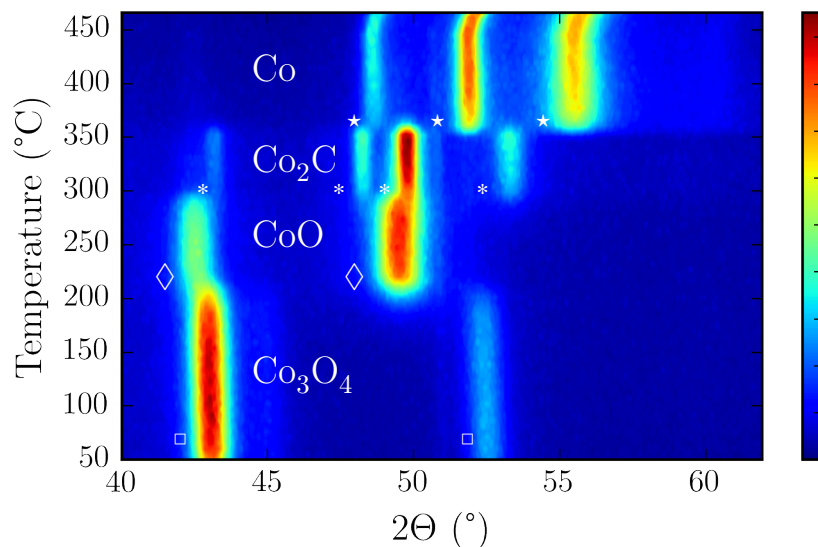


Figure 5.7: *In situ* XRD reduction experiments of 0.0Al300 in CO atmosphere. XRD shows the transition of Co_3O_4 (□) to CoO (◇) to Co_2C (*) and then decomposition into metallic cobalt (★).

position of Co_2C at 350 °C. Decomposition of Co_2C to metallic cobalt and carbon does neither consume CO, nor produce CO_2 . Therefore, it does not contribute to a change in the composition of the reaction gas and can not be measured with a TCD detector. Hence, this phase transition was not visible in the TPR experiments.

The catalysts containing 0.5 and 2.5 wt% Al show additional features between 350 °C and 450 °C, which are assigned to the reduction of a non-stoichiometric cobalt-alumina surface phase. These species were directly reduced to metallic cobalt, as Co_2C is not stable at these temperatures [92].

5.4.4 Catalyst acidity

Alumina is known to exhibit Lewis acidity. The number and strength of Lewis acid sites depend on the crystal structure and surface area [66]. Thus it is proposed, that alumina modification may introduce Lewis acid sites, and the acidity of the activated catalysts was investigated by pyridine-TPD as shown in Figure 5.8.

The activated catalysts were saturated with pyridine by pulse chemisorption, and the pyridine uptake ($N_{py,ad}$) was determined. A blank experiment was performed, which con-

firmed that no pyridine uptake and desorption was observed on the quartz wool or sample tube. The pyridine uptake of the unmodified catalyst during pulse chemisorption was $30\ \mu\text{mol/g}$. Pyridine desorption took place at a low temperature of $269\ ^\circ\text{C}$. This indicates that pyridine was weakly adsorbed or physisorbed, on the unmodified cobalt catalyst.

Catalyst 0.1Al300 contained only 0.1 wt% Al. The pyridine uptake of this catalyst was low, and the TPD signal had a low signal to noise ratio, when the experiment was performed with the standard amount of sample of 100 mg. Therefore, the experiment was repeated using a larger amount of 400 mg catalyst, and both experiments are compared in Figure 5.8. A slightly lower pyridine uptake of $48\ \mu\text{mol/g}$ was determined for the experiment with 400 mg catalyst, compared to the experiment with 100 mg catalyst ($63\ \mu\text{mol/g}$). The value of $48\ \mu\text{mol/g}$ calculated is probably more reliable, because the signal to noise ratio was larger, as more catalyst was used.

The pyridine uptake increased with increasing alumina loading. When taking the catalyst with the lowest alumina loading as a reference, the alumina uptake followed the ratio of 1 : 1.5 : 4.1 for 0.1Al300:0.5Al300:2.5Al300, while the Al ratio followed 1 : 5 : 25. Hence, the pyridine uptake did not increase in proportion to the alumina loading. It has frequently been observed that the strength of the individual acid sites decreases as the number of acid sites is increased [93]. Hence, the catalyst acidity is not expected to increase linearly with increasing alumina loading.

It should be noted, that the pyridine uptake determined during pulse chemisorption accounts for weakly bound (physisorbed) and strongly bound (chemisorbed) pyridine. Therefore, the experiments cannot be used to calculate the exact number of acid sites.

During pyridine-TPD, a sharp peak between $350\ ^\circ\text{C}$ to $500\ ^\circ\text{C}$ was observed for the alumina-modified catalysts. Sharp peaks above $350\ ^\circ\text{C}$ have been reported to correspond to decomposition of pyridine to N_2 and CO_2 [94, 95]. Because this peak is not caused by desorption of pyridine but by its decomposition, the position of the peak is expected to correlate with the rate of pyridine decomposition, and the peak area correlates with the thermal conductivity of the decomposition products. The amount of desorbed pyridine calculated from the peak area, suggested a volume of pyridine desorbed about five times larger than the amount of pyridine adsorbed, which is unreasonable. The catalyst had also darkened after the experiment, which may suggest carbon deposition [95]. Hence, it

is proposed that pyridine decomposition occurred during the experiment.

Decomposition of pyridine at temperatures below 500 °C, in an inert atmosphere, is only catalysed by strong acid sites [95, 96]. However, as the high-temperature peak may be due to decomposition, and not desorption of pyridine, its position cannot be directly correlated with the strength of the acid site [94]. Thus, the experiment is not suited to determine the order of acid site strength among the alumina-modified catalysts; e.g. it is not clear whether the acid sites on catalyst 0.1Al300 are stronger or weaker compared to catalyst 2.5Al300.

However, measurable quantities of pyridine were adsorbed on the alumina-modified catalysts, and the quantity of pyridine adsorbed increased with increasing alumina loading. This shows that the alumina modification introduced acid sites, and that the number of acid sites increased with increasing alumina loading. The pyridine-TPD experiments indicate that the acid sites were strong enough to catalyse the decomposition of pyridine at temperatures below 500 °C.

It should be noted, that pyridine exhibits both Lewis and Brønsted basic character. Thus, pyridine can probe both types of acid sites [94]. Alumina does mostly display Lewis acid character, but the presence of Brønsted acid sites cannot be ruled out [97].

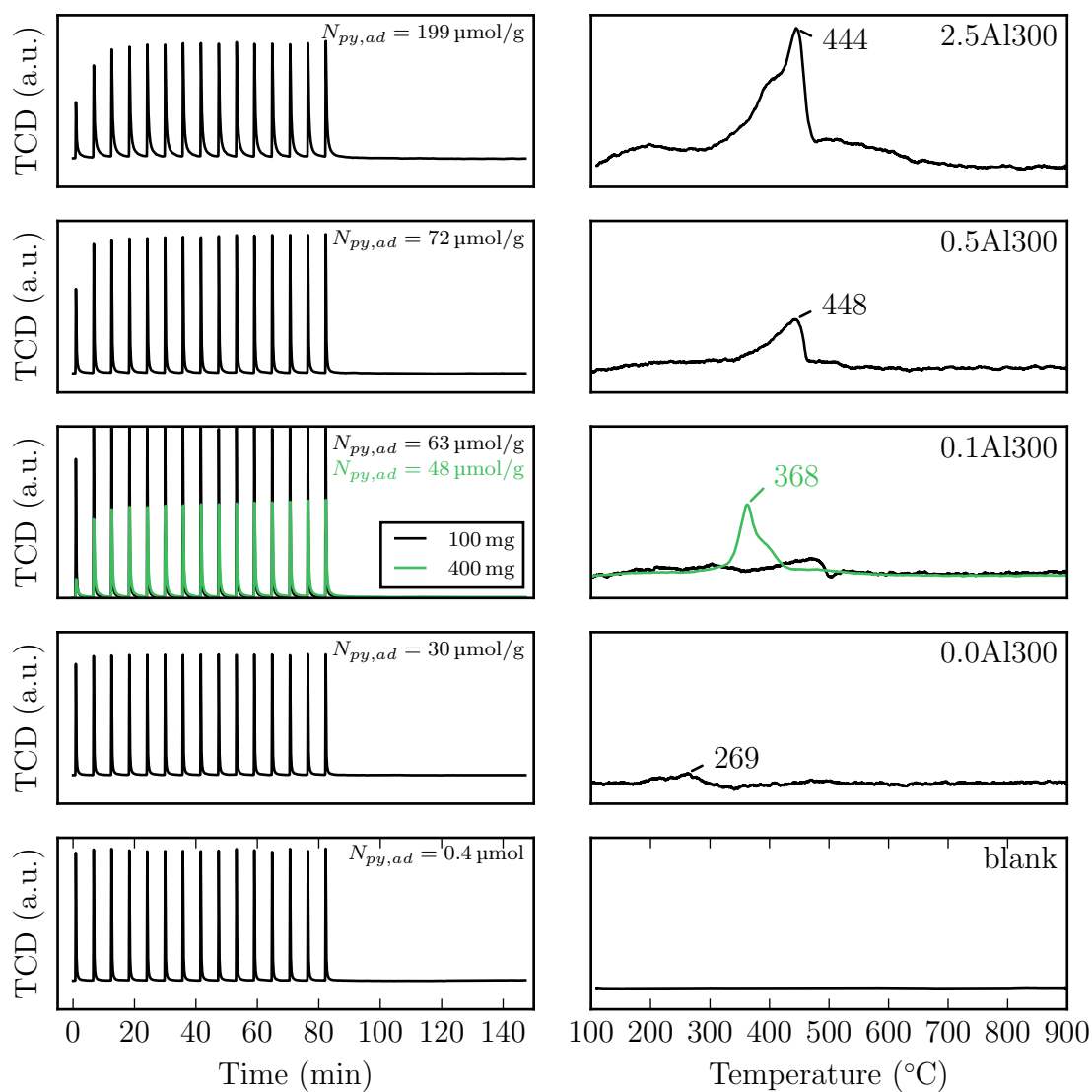


Figure 5.8: Pyridine pulse chemisorption (left) followed by temperature programmed desorption/decomposition of pyridine (right) on unmodified and alumina-modified catalysts.

5.4.5 Fischer-Tropsch synthesis

Activity and catalyst deactivation

The catalytic performance for the Fischer-Tropsch synthesis was tested in a slurry reactor at a pressure of 20 bar and temperatures between 220 °C and 240 °C. The space velocity was adjusted so that the selectivity could be compared at similar levels of conversion.

Figure 5.9 shows the catalytic activity as a function of time on stream (TOS) during the start-up of the reaction. The results are tabulated in Table 5.4.

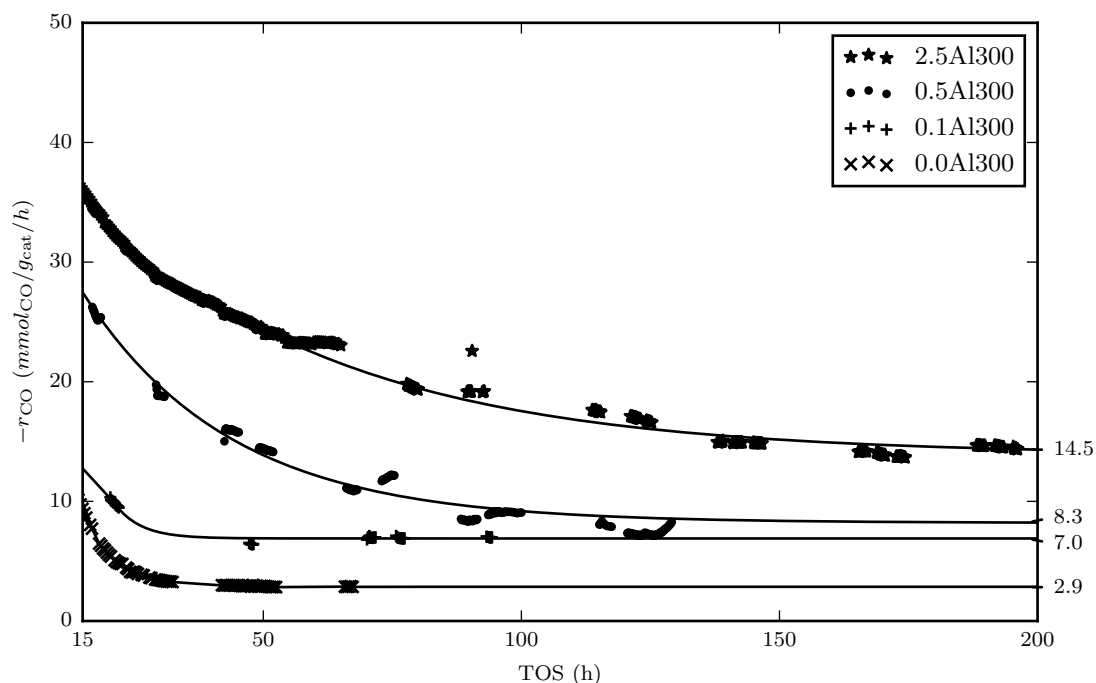


Figure 5.9: Activity for the Fischer-Tropsch synthesis determined in a slurry reactor at 220 °C and a $H_2/CO=2:1$. The steady-state activity for each catalyst is demarcated on the right axis.

Table 5.4: Activity of the Fischer-Tropsch reaction at 220 °C and 20 bar conducted in a slurry reactor.

w_{Al} (wt%)	Initial activity			steady-state activity			Deactivated catalyst		
	$-r_{CO}$ ($mmol_{CO}/g_{cat,red}/h$)	CTY ($10^{-4}s^{-1}$)	TOF ($10^{-2}s^{-1}$)	$-r_{CO}$ ($mmol_{CO}/g_{cat,red}/h$)	CTY ($10^{-4}s^{-1}$)	TOF ($10^{-2}s^{-1}$)	$-r_{CO}$ ($mmol_{CO}/g_{cat,red}/h$)	CTY ($10^{-4}s^{-1}$)	TOF ($10^{-2}s^{-1}$)
0	8.6	15	65	2.9	5	22	2.7	5	20
0.1	12.8	22	34	7.0	12	19	5.5	10	15
0.5	26.9	51	31	8.3	16	10	7.4	14	9
2.5	35.5	74	23	14.5	30	9	6.2	13	4

The initial activity was determined at 16 h TOS, which corresponds to double of the break-through time. Due to the long break-through time, the values for the initial activity may have been affected by catalyst sintering. The initial activity increased with increasing alumina loading from 8.6 to 35.5 mmol_{CO}/g_{cat,red}/h, corresponding to a cobalt time yield (CTY) of $15 \cdot 10^{-4} \text{ s}^{-1}$ and $74 \cdot 10^{-4} \text{ s}^{-1}$, for catalyst 0.0Al300 and 2.5Al300, respectively. The initial turn over frequency (TOF) was found to decrease with increasing alumina loading from $65 \cdot 10^{-2} \text{ s}^{-1}$ to $23 \cdot 10^{-2} \text{ s}^{-1}$ for catalyst 0.0Al300 and 2.5Al300, respectively.

Steady-state conditions were defined at the point where the CO conversion varied by $\leq 2.5\%$. Reported steady-state conversions correspond to the averaged value. Steady-state was reached after 20-135 h TOS. The steady-state activity also increased with increasing alumina loading from 2.9 to 14.5 mmol_{CO}/g_{cat,red}/h, corresponding to a CTY of $5 \cdot 10^{-4} \text{ s}^{-1}$ and $30 \cdot 10^{-4} \text{ s}^{-1}$, for catalyst 0.0Al300 and 2.5Al300, respectively. On average, the steady-state activity was $\approx 40\%$ of the initial activity, independent of alumina loading. The time necessary to achieve steady-state increased with increasing alumina loading. Hence, a slower catalyst deactivation was observed for the alumina-modified catalyst. Initial catalyst deactivation is typically attributed to catalyst sintering [46, 98]. It may thus be speculated that the alumina modification reduced the rate of catalyst sintering.

Figure 5.10 shows the CO conversion and methane selectivity achieved at various conditions. All catalysts were tested consecutively at 220 °C, 230 °C, 240 °C and again at 220 °C. The catalyst at steady-state during the first test at 220 °C shall be referred to as the *fresh catalyst*. The catalyst tested at the final stage at 220 °C shall be referred to as the *deactivated catalyst*.

For catalyst 2.5Al300 the space velocity was changed throughout the experiment to adjust the level of conversion. The CO conversion was relatively stable after the initial period of catalyst deactivation, except for catalyst 2.5Al300. Catalyst 2.5Al300 showed a continuous drop in activity, especially at 240 °C. The activity of the deactivated catalyst, after 650 h TOS, corresponded to only 17% of the initial activity, and 43% of the activity of the fresh catalyst. Catalysts with lower alumina loadings were tested for shorter periods (less than 300 h TOS). The activity of the deactivated catalyst for catalysts with $\leq 0.5 \text{ wt}\%$ Al, was within 80-90% of the activity of the fresh catalyst.

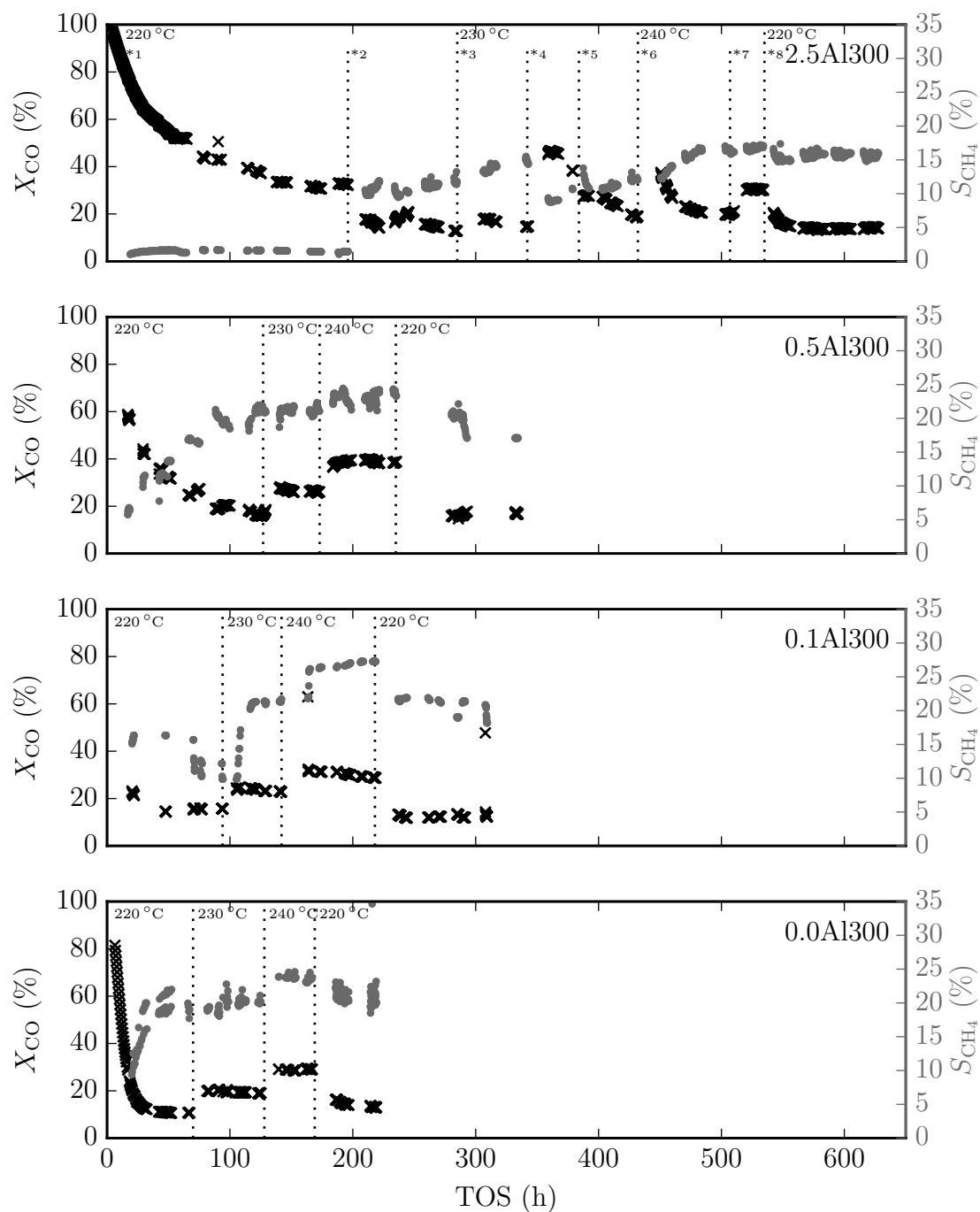


Figure 5.10: Conversion (X_{CO}) and methane selectivity (S_{CH_4}) for the Fischer-Tropsch synthesis at 20 bar and reaction temperatures of 220 °C, 230 °C and 240 °C. Where necessary the space velocity was adjusted to achieve the desired conversion. A detailed list of reaction conditions is reported in Table 5.5.

Table 5.5: Summary of FT conditions, activity and methane selectivity as determined by TCD analysis. * refers to the experimental condition in Figure 5.10.

w_{Al} (wt%)	$m_{cat,red}$ (g)	T (°C)	$v_{Ar,in}$ (ml/min)	$v_{CO,in}$ (ml/min)	$v_{H_2,in}$ (ml/min)	X_{CO} (%)	S_{CH_4} (%)
0	2.69	220	50	50	100	10 ± 0.2	19 ± 1.2
		230	50	50	100	19 ± 0.4	19 ± 0.7
		240	50	50	100	28 ± 0.3	23 ± 0.3
		220	35	35	70	14 ± 1.1	21 ± 2.9
0.1	1.72	220	50	50	100	15 ± 0.1	12 ± 3.4
		230	50	50	100	23 ± 0.2	19 ± 4.4
		240	50	50	100	29 ± 0.8	27 ± 0.4
		220	50	50	100	12 ± 0.5	20 ± 1.3
0.5	1.73	220	50	50	100	18 ± 1.8	20 ± 1.0
		230	50	50	100	26 ± 0.4	21 ± 0.4
		240	50	50	100	38 ± 0.6	23 ± 0.7
		220	50	50	100	16 ± 0.5	17 ± 2.6
2.5	2.19	* ₁ 220	50	50	100	32 ± 1.0	1 ± 0.7
		* ₂ 220	50	100	200	16 ± 2.3	10 ± 0.7
		* ₃ 230	50	100	200	17 ± 0.8	13 ± 0.5
		* ₄ 230	50	60	120	45 ± 2.6	9 ± 0.6
		* ₅ 230	100	100	200	19 ± 0.5	12 ± 0.3
		* ₆ 240	100	100	200	19 ± 0.1	16 ± 0.2
		* ₇ 240	50	50	100	30 ± 0.3	16 ± 0.3
		* ₈ 220	50	50	100	13 ± 0.3	15 ± 0.4

Activation energy

The reaction constant (k) for the FT synthesis was calculated using Equations (5.24) and (5.23). The activation energy was determined by linear regression of the Arrhenius equations, as shown in Figure 5.11. Two data points are present at 220 °C, which correspond to the fresh and deactivated catalyst, respectively. The activation energy for the fresh and deactivated catalyst was determined, by linear regression through the respective data point at 220 °C. $E_{a,deac}$ for all catalysts was higher than $E_{a,fresh}$. The difference between $E_{a,deac}$ and $E_{a,fresh}$ increased in the order 0.0Al300 < 0.5Al300 < 0.1Al300 < 2.5Al300. This correlates directly to the degree of deactivation observed in the catalyst.

Catalyst 2.5Al300 deactivated throughout the FT experiment, especially at 240 °C. Catalyst deactivation resulted in the scattering of the k values observed in the Arrhenius plot. Linear regression through all data points resulted in unreasonable results with very

large errors for catalyst 2.5Al300. Therefore, $E_{a,\text{deac}}$ was calculated by linear regression through the data points at 240 °C and the data point of the deactivated catalyst at 220 °C, while $E_{a,\text{fresh}}$ was calculated by linear regression through the data points at 230 °C and the data point of the fresh catalyst at 220 °C. The value of $E_{a,\text{fresh}}$ has a very large error ($R^2 = 0.20$). It is reported only for the sake of completeness, and should be interpreted with caution. However, the linear regression for the $E_{a,\text{deac}}$ value achieved an acceptable goodness of fit ($R^2 = 0.98$).

Overall the activation energy for the alumina-modified catalyst is lower compared to the unmodified catalyst. $E_{a,\text{fresh}}$ increased in the order 0.1Al300 < 0.5Al300 < 0.0Al300. $E_{a,\text{deac}}$ increased in the order 2.5Al300 < 0.1Al300 < 0.5Al300 < 0.0Al300. $E_{a,\text{deac}}$ for catalyst 2.5Al300 was 106 kJ/mol, which was 15 % lower than the value of 124 kJ/mol for catalyst 0.0Al300. This seems to suggest that the alumina modification affected the kinetics of the FT reaction.

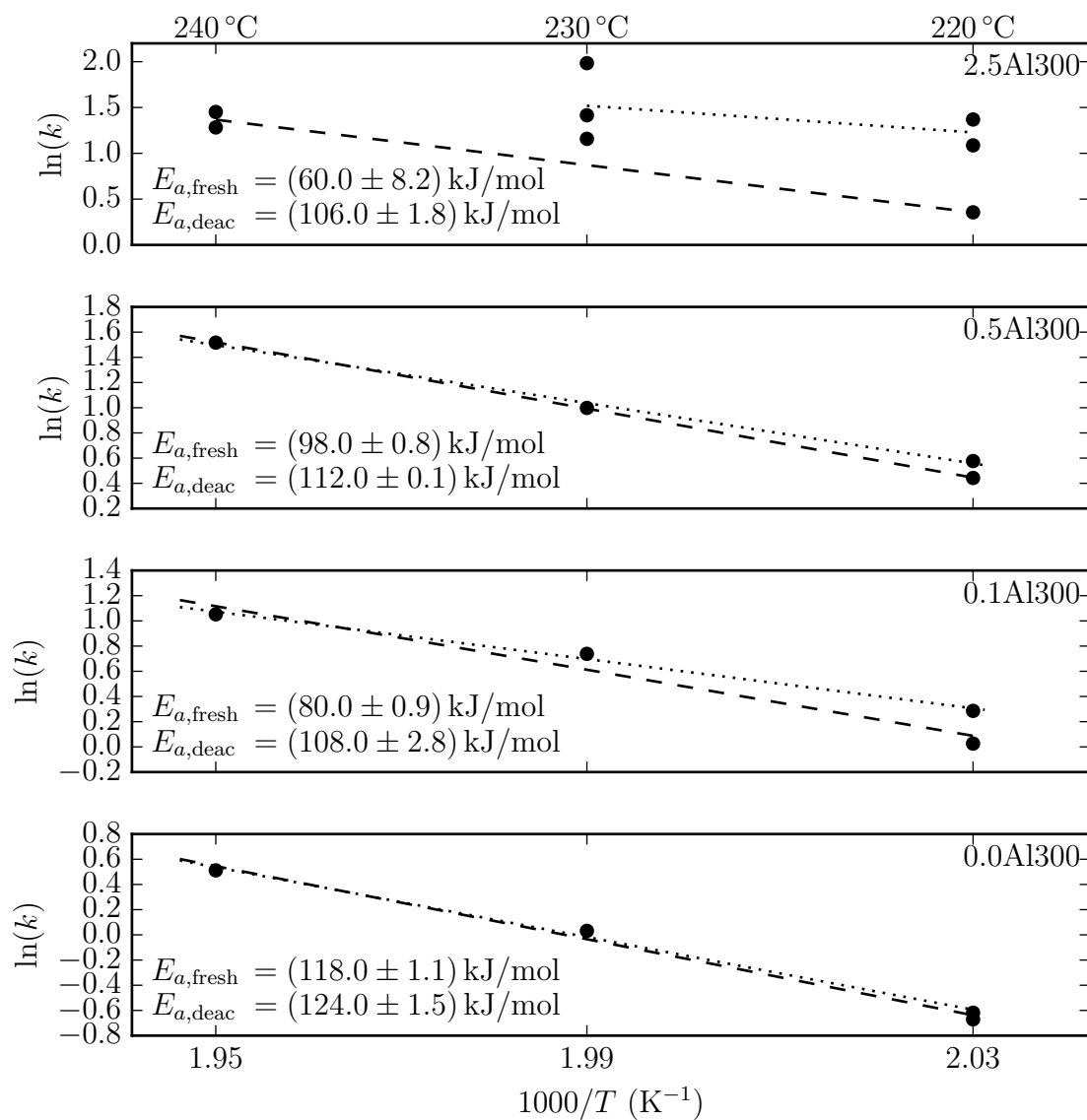


Figure 5.11: Arrhenius plot for the Fischer-Tropsch reaction. Activation energies are reported for the fresh ($E_{a,\text{fresh}}$) and deactivated ($E_{a,\text{deac}}$) catalyst. k -values for catalyst 2.5Al300 scatter strongly, possibly due to catalyst deactivation.

Product selectivity

The selectivity of the organic FT product was determined by FID analysis of the tail gas, sampled in pre-evacuated ampoules. All values reported were determined at steady-state. The selectivity was evaluated in terms of the methane selectivity, the C_{5+} selectivity, chain growth probability, the olefin selectivity and the selectivity for branched compounds. Product selectivities were determined by using methane as a reference according to Equation (5.16). The selectivity of oxygenated products and CO_2 was low, as expected for cobalt catalysts. The C_{5+} selectivity was determined according to Equation (5.17). α values were calculated from $C_4 - C_7$, as product condensation in the hot-trap and inside the gas-ampoule decreased the concentration of high molecular weight products in the FID.

The olefin selectivity was investigated in terms of the linear olefin to linear hydrocarbon ratio ($C_n^=/C_n$), the 1-olefin to linear hydrocarbon ratio ($C_n^{1=}/C_n$) and the 2-olefin to 1-olefin ratio ($C_n^{2=}/C_n^{1=}$) in a carbon number fraction. 2-olefin selectivity was determined as the ratio of 2-olefin to 1-olefin because 2-olefins are secondary products, which mainly form via double bond isomerisation of 1-olefins.

The selectivity for branched compounds was evaluated as the ratio of branched compounds to linear hydrocarbons (C_n^Y/C_n) and the ratio of branched compounds to 1-olefins ($C_n^Y/C_n^{1=}$) in the carbon number fraction. The ratio of branched compounds to 1-olefins may give information on the formation of branched compounds via skeletal isomerisation of 1-olefins.

The activity of all catalysts was relatively low, as can be expected from catalysts with low metal dispersions. In order to achieve an accurately measurable level of conversion ($> 10\%$), catalytic testing was restricted to low space velocities. The amount of catalyst used was restricted by the amount of catalyst that could be loaded into the calcination set-up used for catalyst activation ($< 5\text{ g}$). In order to achieve a reasonably small duration for product retention in the reactor, a relatively large dilution of syngas with argon was used (25%). This, in turn, resulted in difficulties in determining very low methane selectivities. Catalyst 2.5Al300 displayed a comparably high activity and low methane selectivity. In the initial stages of the reaction, the CO conversion exceeded 30% at 220°C , and a methane selectivity of $1 \pm 0.7\%$ was measured. In this case, the methane

concentration in the tail gas was too low to be accurately determined. The space velocity was increased, and the argon dilution was decreased to 15% in order to increase the methane concentration and achieve more accurate results for the methane selectivity. As a result, this catalyst was exposed to a slightly higher partial pressure of CO and H₂ for part of the FT experiment.

The product distribution is expected to change as a function of reaction temperature and CO conversion [99]. Figure 5.12 shows the product selectivity for the different catalysts as a function of reaction temperature. The CO conversion and methane selectivity increased, while the C₅₊ selectivity decreased, with increasing reaction temperature.

For catalyst 0.0Al300 a slight increase in C₅₊ selectivity was observed from 220 °C to 230 °C. This can be explained by the increase in CO conversion. An increase in CO conversion typically leads to a decrease in methane selectivity and increase in C₅₊ selectivity [99]. As the CO conversion increased at 230 °C, the C₅₊ selectivity was also found to increase, despite the increase in temperature.

The selectivity for linear olefins is plotted as a function of carbon number. The selectivity for total linear olefins, as well as the selectivity for linear 1-olefins (C_n¹⁼/C_n), decreased with increasing reaction temperature. The increase in C_n¹⁼/C_n was more pronounced in catalyst 0.0Al300 and 2.5Al300 compared to catalyst 0.1Al300 and 0.5Al300. The C_n²⁼/C_n¹⁼ ratio increased with increasing reaction temperature, for all catalyst except 0.1Al300 and 0.5Al300. For catalyst 0.1Al300 and 0.5Al300, which showed a higher C_n²⁼/C_n¹⁼ ratio, compared to the other catalysts, no clear trend between reaction temperature and 2-olefin selectivity was observed.

Usually, an increase in secondary reactions and products with increasing reaction temperature is expected [99]. This may lead to a decrease in 1-olefin and increase in 2-olefin selectivity. However, the effect of temperature on olefin selectivity is not entirely understood. Different studies reported an increase in olefin selectivity with increasing temperature, the opposite or no effect [23].

The C₄^Y/C₄ decreased, while the C_n^Y/C_n for $n > 4$ increased slightly with increasing reaction temperature. The same trend was observed for the C_n^Y/C_n¹⁼ ratio. Long chain hydrocarbons have a longer retention time in the reactor, which may increase the probability for secondary reaction [22]. This may explain the increase in the selectivity to branched

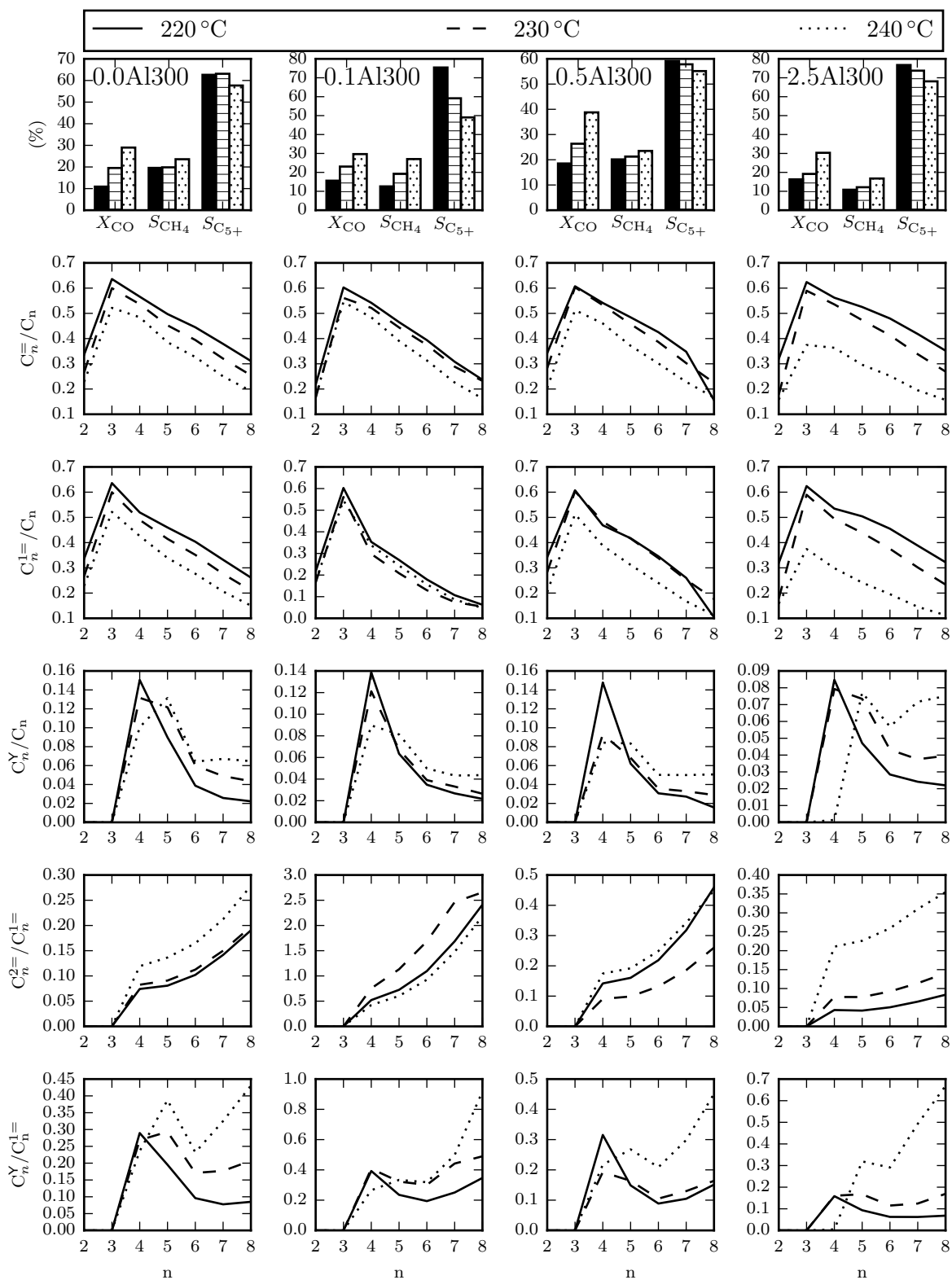


Figure 5.12: FT product distribution as a function of reaction temperature.

compounds with increasing carbon number.

Figure 5.13 shows the product selectivity for the fresh and deactivated catalysts (220 °C). Catalyst 0.0Al300 had a very low activity. The space velocity for the deactivated catalyst was decreased to ensure that conversion and product formation were sufficiently high, to be accurately determined. Therefore, the CO conversion reported for the deactivated catalysts was slightly higher, compared to the fresh catalyst. For the other catalysts, the CO conversion for the deactivated catalysts was lower, as expected.

For catalyst 0.0Al300 and 0.5Al300 the methane and C₅₊ selectivity varied by only 2-4 % between the fresh and deactivated catalysts. For catalyst 0.1Al300 and 2.5Al300 a significant increase in methane selectivity and drop in C₅₊ selectivity was observed. These changes in selectivity may be partly ascribed to the change in CO conversion. However, it should be noted that an increase in methane selectivity due to catalyst deactivation has frequently been reported [99].

Catalyst 2.5Al300 had the lowest methane selectivity and highest C₅₊ selectivity compared to the other catalysts in its fresh and deactivated state. A significant loss in olefin selectivity was observed for this catalyst upon deactivation. A drop in activity and olefin selectivity was already observed when the catalyst was tested at 240 °C. It is hypothesised, that irreversible catalyst deactivation occurred at the increased temperature, which resulted in the loss of catalyst activity and selectivity at 220 °C (2).

It should be noted, that not only a change in the catalyst, but also a change in the slurry phase inside the reactor may contribute to a change in product selectivity. Long chain hydrocarbons may accumulate inside the reactor with increasing TOS, which may change the composition of the slurry phase [23]. An increase in long-chain olefins in the slurry may increase the retention time of long-chain olefins, and thus increase olefin re-adsorption and secondary reactions [23]. This may lead to an increase in C₅₊ selectivity. Thus, the slight increase in C₅₊ selectivity, despite the drop in CO conversion observed in the deactivated catalyst 0.5Al300, which was tested for over 300 h, may be explained by a change in the composition of the slurry phase.

Figure 5.14 shows the product distribution as a function of alumina loading at different reaction temperatures. The catalysts responded differently to a change in temperature, so that different trends were observed at different temperatures. Catalyst 2.5Al300 had the

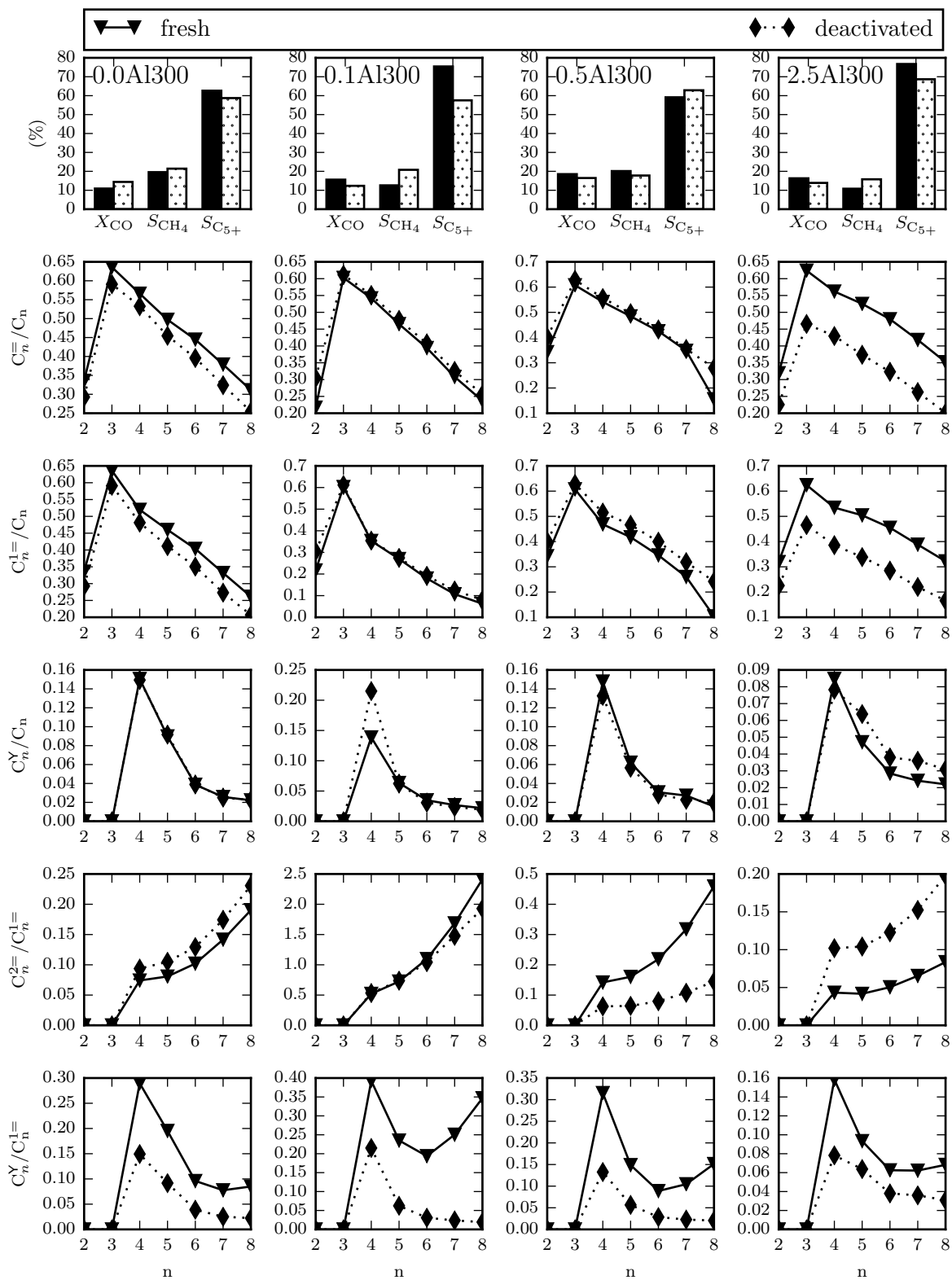


Figure 5.13: Comparison of the FT product distribution of fresh and deactivated catalysts at a reaction temperature of 220 °C.

highest methane and highest C_{5+} selectivity, and catalyst 0.1Al300 had a relatively high 2-olefin selectivity and high $C_n^Y/C_n^{1=}$ ratios in comparison to the C_n^Y/C_n ratios, throughout the experiment.

At the start-up of the reaction at 220 °C, the methane selectivity decreased in the order 0.0Al300 \approx 0.5Al300>0.1Al300>2.5Al300. The C_{5+} selectivity increased in the opposite order. Catalyst 2.5Al300 had the highest olefin selectivity. Catalyst 0.1Al300 and 0.5Al300 had the lowest linear olefin and 1-olefin selectivities and the highest $C_n^{2=}/C_n^{1=}$ ratios. Furthermore, the $C_n^Y/C_n^{1=}$ ratio was higher, especially for large carbon numbers, compared to the C_n^Y/C_n ratio. This points towards secondary olefin-isomerisation being the primary mechanism for the formation of branched compounds in these catalysts.

At a reaction temperature of 230 °C similar trends in the selectivity of olefins and branched compounds were observed, although the differences between the catalysts were smaller. When the reaction temperature was increased to 240 °C, the 1-olefin selectivity of catalyst 2.5Al300 and 2-olefin selectivity of catalyst 0.1Al300 dropped considerably. This change in selectivity may be attributed to irreversible catalyst deactivation, as the selectivities remained low after reducing the reaction temperature to 220 °C.

For the deactivated catalysts (220 °C (2)) the methane selectivity increased in the order 2.5Al300<0.5Al300<0.1Al300 \approx 0.0Al300 and the opposite trend was observed for the C_{5+} selectivity. The olefin selectivity decreased in the order 0.5Al300>0.1Al300>0.0Al300 »2.5Al300. For catalyst 0.5Al300 the 1-olefin selectivity increased, whereas the 2-olefin selectivity decreased compared to the fresh catalyst.

Figure 5.15 shows the chain growth probability (α_{4-7}) at different reaction temperatures (at a comparable level of conversion). The concentration of high molecular weight products determined by analysis of the tail gas was found to decrease strongly for high carbon numbers. This may be due to condensation of products in the hot-trap and inside the gas-ampoule, and increased retention of high molecular weight products in the slurry phase. Hence, α values were determined for relatively low carbon numbers of $C_4 - C_7$.

The chain growth probability increased with increasing alumina loading at the start of the reaction. Only small variations in chain growth probability as a function of temperature were observed for catalyst 0.0Al300. For catalyst 2.5Al300 the chain growth probability decreased with increasing temperature. This is in line with the trends in C_{5+} and methane

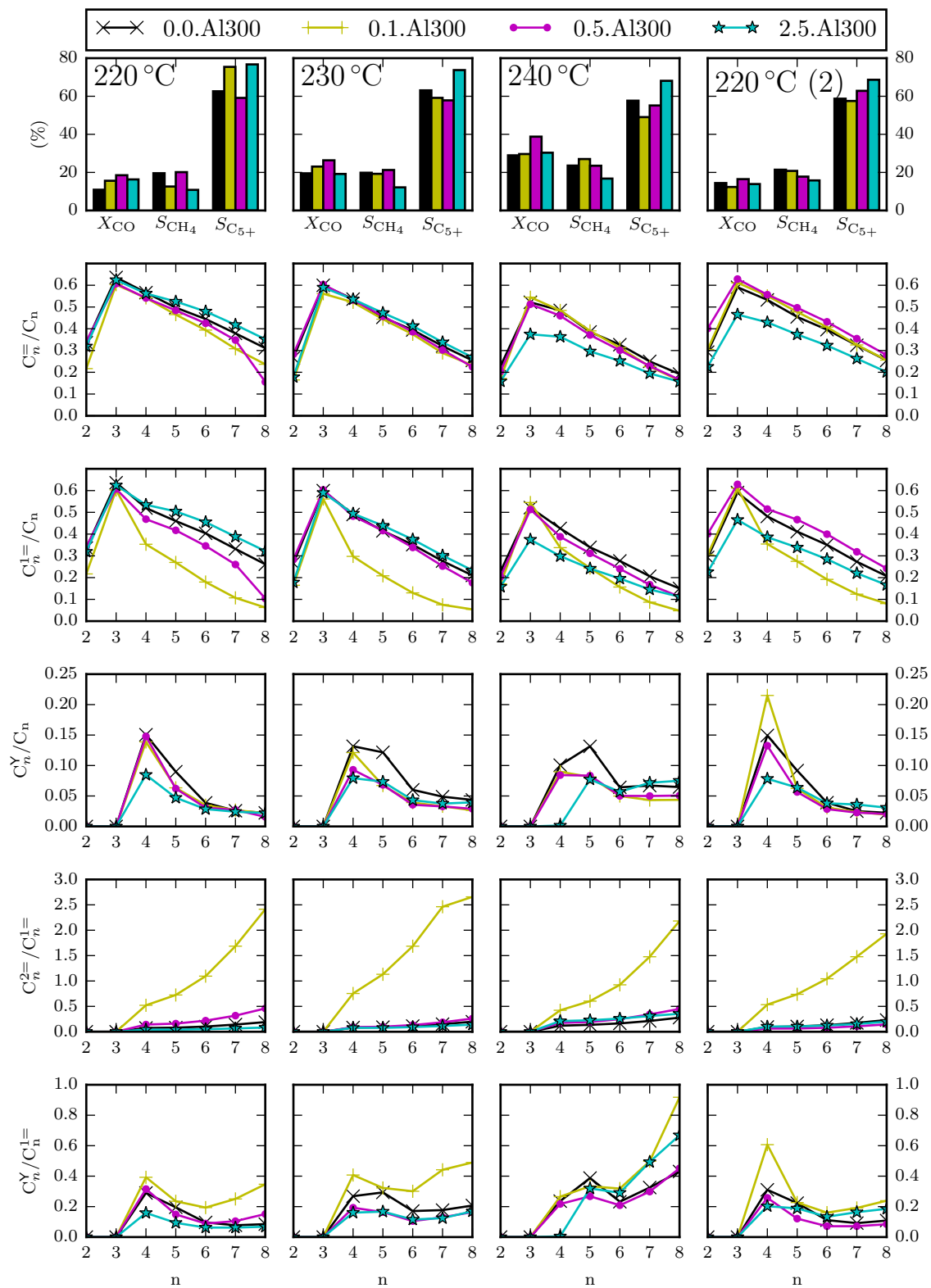


Figure 5.14: Product distribution as a function of alumina loading at a reaction temperature of 220 °C, 230 °C and 240 °C.

selectivity for this catalyst. The strong decrease in chain growth probability may be related to the observed catalyst deactivation. For catalyst 0.1Al300 and 0.5Al300 the chain growth probability unexpectedly increased during the course of the reaction. This may, again, be explained by an increased solubility and retention time of long-chain olefins. The increased retention time may lead to increased olefin re-adsorption and further chain growth, resulting in an increased chain growth probability [23].

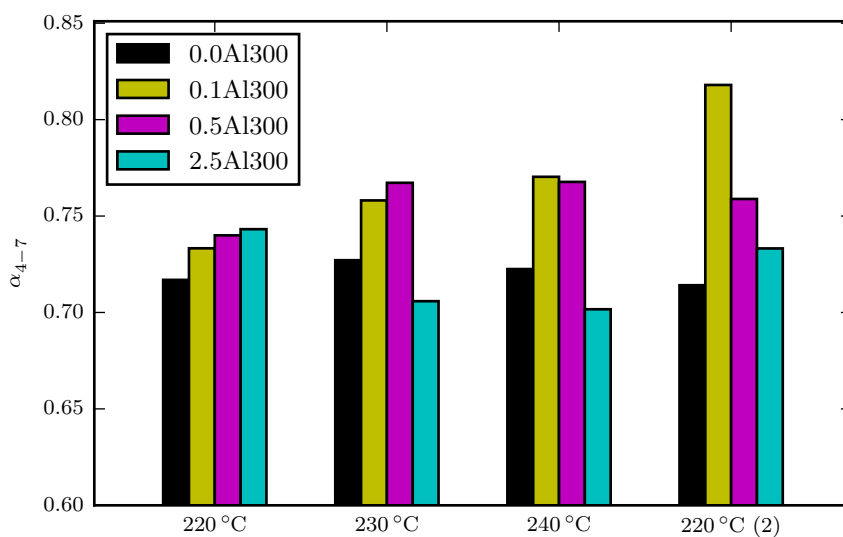


Figure 5.15: Chain growth probability (α_{4-7}) as a function of the reaction temperature.

5.4.6 Spent catalyst characterisation

After completion of the FT experiments, the spent catalyst was unloaded from the reactor inside a wax tablet. The wax coat was removed using xylitol, and spent catalysts were characterised by TEM and XRD. The XRD of the spent catalysts are shown in Figure 5.16. Crystalline phases corresponding to fcc cobalt, hcp cobalt and CoO were detected. CoO was only detected for catalyst 2.5Al300, and a CoO content of 8 wt% was estimated by Rietveld refinement.

The peak broadening increased with increasing alumina loading indicating a decrease in crystallite size. In all catalysts, diffraction peaks corresponding to fcc cobalt were sharper than those of hcp cobalt. This is similar to observations made during *in situ* XRD reduction experiments.

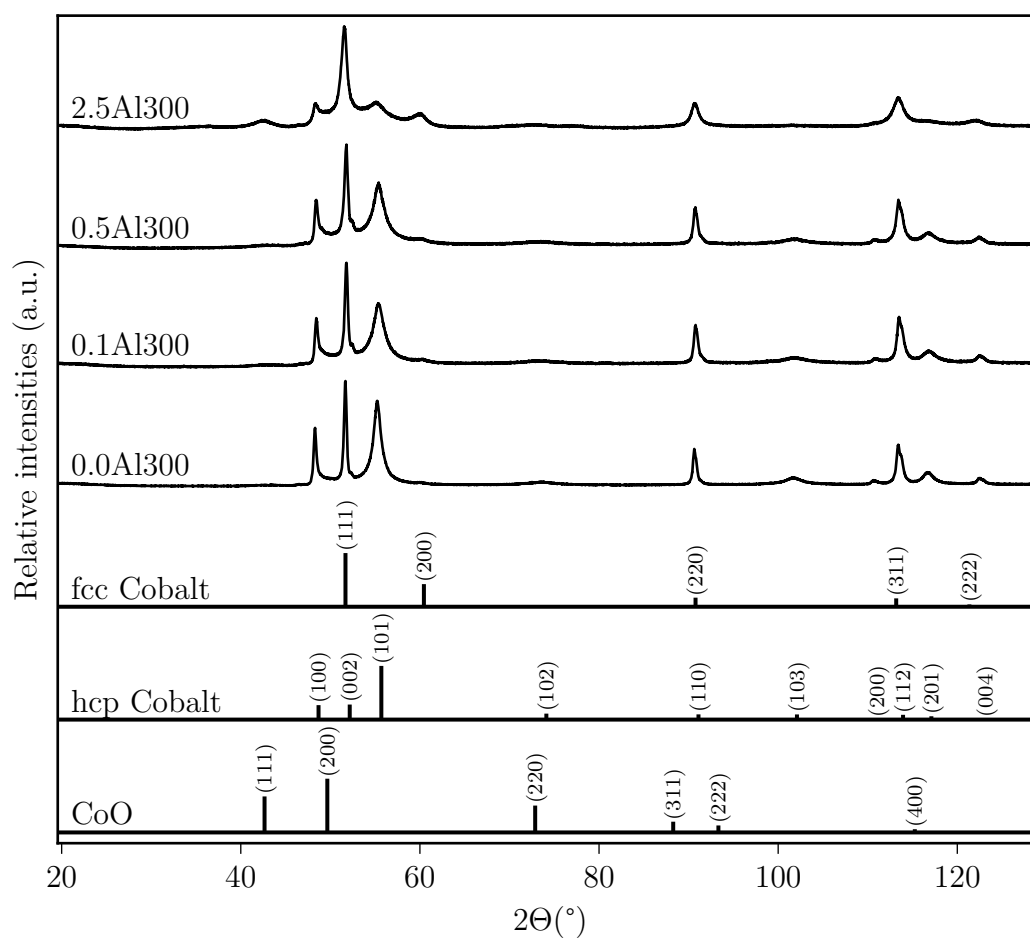


Figure 5.16: XRD of spent catalysts showing crystalline phase of CoO (PDF - 00-043-1004), fcc Cobalt (PDF - 01-071-4651), and hcp Cobalt (PDF - 01-071-4239).

Rietveld refinement indicated crystallite domain sizes between 2-4 nm for hcp cobalt and 14-38 nm for fcc cobalt. These crystallite sizes are much smaller compared to the ones estimated from the H₂-chemisorption experiments. It should be noted that the sizes derived by XRD reflect the size of crystal domains. In large crystallites, multiple crystal domains may be present. Furthermore, the cobalt phase may be distorted showing fcc and hcp domain inter-grown through stacking faults [100], in which case results from Rietveld refinement may be inaccurate [101, 102]. Hence, the results of the Rietveld refinement may not be used to estimate the metal surface area.

Figure 5.17 shows TEM images of the spent catalysts. The images show very large crystallites with crystallite sizes > 50 nm for the alumina-modified catalysts, and crystallites $\gg 100$ nm for the unmodified catalyst. This confirms that the crystal domain size derived from Rietveld refinement did not accurately represent the crystallite size of the catalysts.

The spent catalysts consisted of large networks of merged cobalt crystallites of various sizes. This indicates that crystallites sintered by crystallite coalescence. Some crystallites show a pattern of dark lines. These may constitute stress fringes, which may appear due to the high shear stress upon coalescence of small metal crystallites [103].

Obtaining an accurate measure of the crystallite size of a large network of merged crystallites is not feasible. Hence, TEM imaging cannot be used to estimate the metal dispersion³.

The surface of the cobalt particles seemed to be decorated with small crystallites appearing in a lighter shade. The lattice fringes around these areas had a d-spacing of 2.1 Å or 2.4 Å which is consistent with the (200) and (111) crystal plane of CoO, respectively. This indicates that the surface of the catalysts was partly oxidised. Bulk reoxidation of cobalt during the FT synthesis is only relevant for cobalt crystallites smaller than ≈ 4 nm [54], but surface reoxidation may take place, and has been reported to contribute to catalyst deactivation [104]. It should be noted, that the spent catalysts were exposed to air. After wax-removal, the surface of the spent catalysts is expected to remain passivated by a thin layer of wax. Previous studies have shown that long-term oxidation of spent catalysts, after

³It is nearly impossible to strip the spent catalysts completely from the reaction wax. This complicates spent catalyst characterisation. The wax residue may cause damage to analytical instruments, such as the Micromeritics analysers, which is why no H₂-chemisorption experiments were performed on spent catalysts.

wax removal, stored in air for ten months was negligible [105]. However, surface oxidation of the catalysts upon exposure to air cannot be ruled out.

Images of the 2.5Al300 spent catalyst show a large number of very small grey coloured crystallites. The grey colour indicates a lower electron density. Thus, this phase may be oxidic. EDS mapping of these areas showed the presence of cobalt, aluminium and oxygen, as shown in Figure 5.18. Thus, these regions appear to correspond to a mixed-cobalt alumina phase. This is in agreement with TPR experiments, which showed the formation of a mixed-cobalt alumina phase during catalyst reduction. This phase was visible to a lesser extent in images of catalyst 0.5Al300, and was not observed for catalyst 0.1Al300 and 0.0Al300.

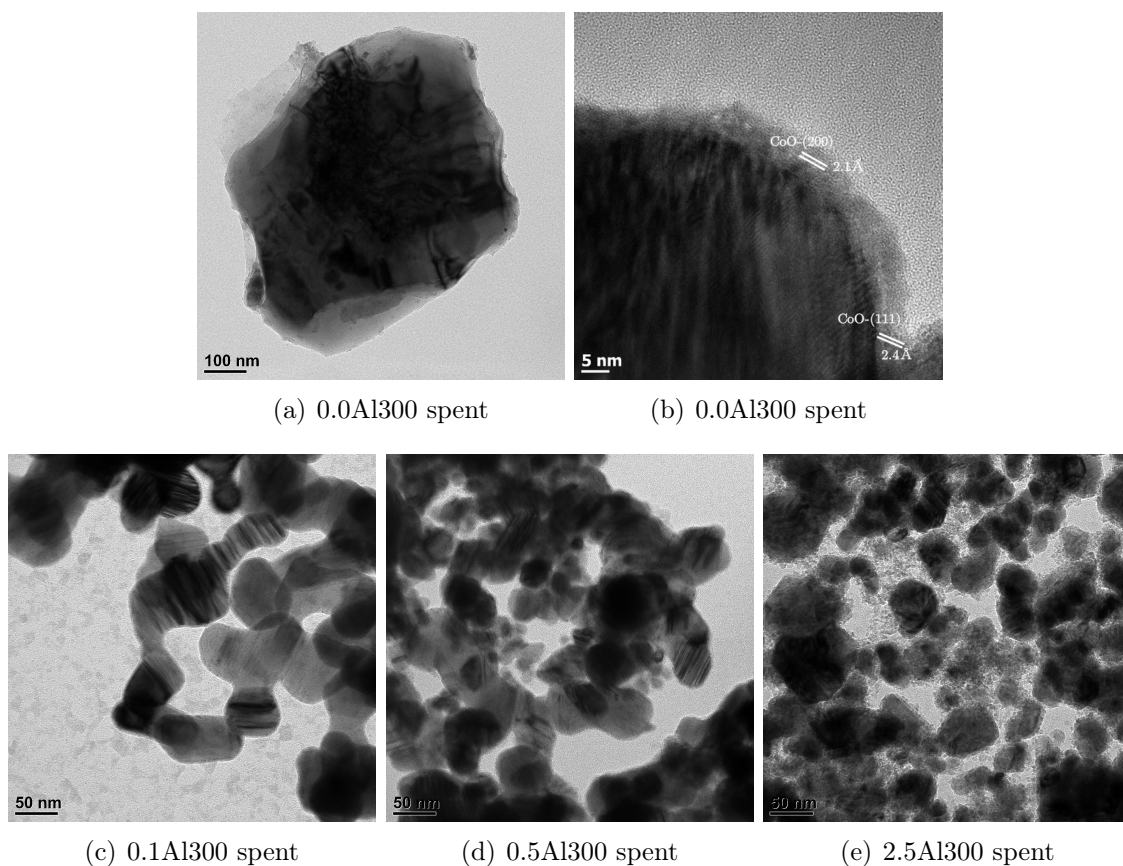
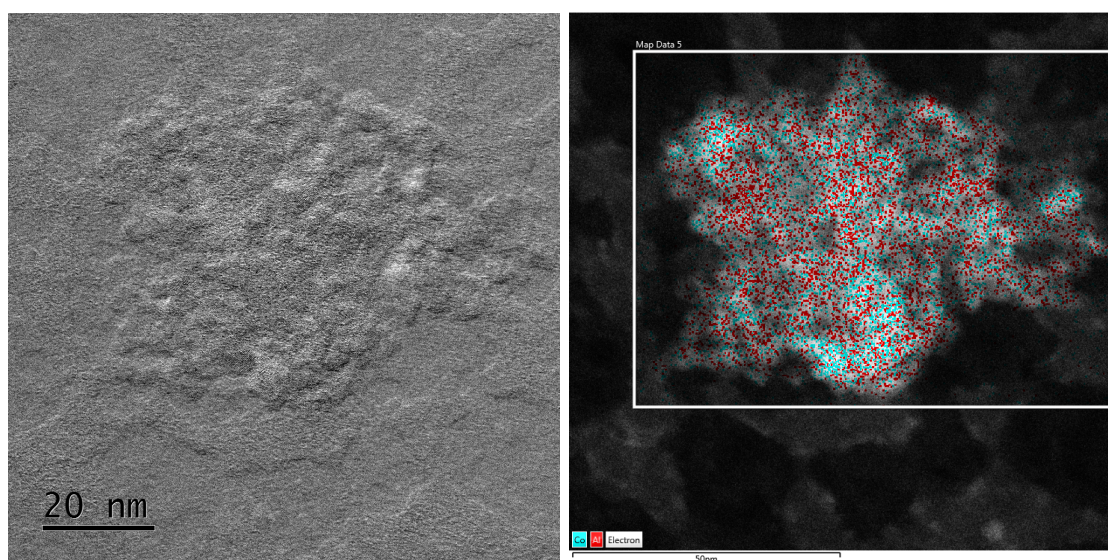
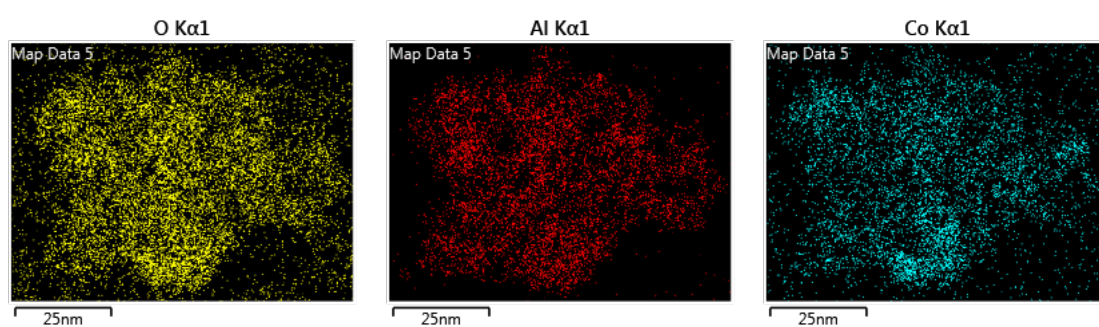


Figure 5.17: TEM images of spent catalysts. Large agglomerates of cobalt particles visible. Small crystallites on particle surface show lattice indicating CoO phase.



(a) 2.5Al300 spent bright field STEM-EDS.

(b) Co and Al mapped using EDS



(c) O map

(d) Al map

(e) Co map

Figure 5.18: Bright-field STEM and EDS mapping of spent 2.5Al300 catalyst.

5.5 Discussion

5.5.1 Fischer-Tropsch activity

The activity of alumina-modified catalysts for the Fischer-Tropsch (FT) synthesis was investigated under industrially relevant conditions in a slurry reactor at temperatures between 220 °C and 240 °C at a pressure of 20 bar. The results conclusively showed that alumina modification increased the activity per unit mass of cobalt and decreased the activation energy for the FT reaction.

In this study, activation energies between 98-124 kJ/mol were determined for the FT synthesis. Values for the activation energy reported in the literature typically vary between 80-105 kJ/mol [11, 106, 107], although values as high as 176 kJ/mol have been reported [38]. Hence, although the values obtained in this study are rather high, they fall well within the expected range.

For the unmodified cobalt catalyst, a conversion of 19 % was achieved at a space velocity of 3.3 L/h/g_{cat}. This compares well with Das et al. [108], who reported a conversion of 18 % for a bulk cobalt catalyst tested in a CSTR at a space velocity of 3 L/h/g_{cat}. The literature on the activity of unsupported cobalt catalysts is scarce, but the cobalt time yield (CTY) and turn over frequencies (TOF) observed in this study, compare well with values reported in the literature for supported catalysts. The CTY at steady-state varied between $5 \cdot 10^{-4} \text{ s}^{-1}$ to $30 \cdot 10^{-4} \text{ s}^{-1}$, compared to values of $5 \cdot 10^{-4} \text{ s}^{-1}$ to $15 \cdot 10^{-4} \text{ s}^{-1}$ reported in the literature [39]. The TOF at steady-state varied between $9 \cdot 10^{-2} \text{ s}^{-1}$ to $22 \cdot 10^{-2} \text{ s}^{-1}$, compared to values of $4 \cdot 10^{-2} \text{ s}^{-1}$ to $20 \cdot 10^{-2} \text{ s}^{-1}$ reported in the literature [33, 109–111].

The initial CTY increased from $15 \cdot 10^{-4} \text{ s}^{-1}$ to $74 \cdot 10^{-4} \text{ s}^{-1}$ upon modifying cobalt with 2.5 wt% Al. However, the initial TOF was found to decrease with increasing alumina loading from $65 \cdot 10^{-2} \text{ s}^{-1}$ to $23 \cdot 10^{-2} \text{ s}^{-1}$ for catalyst 0.0Al300 and 2.5Al300, respectively. Due to the rather low space velocity (ergo long break-through time), the initial activity could only be determined after 16 h TOS. In this large time period, the available metal surface area may have decreased due to sintering [46] or irreversible adsorption of unreactive product intermediates [112]. Hence, the available metal surface area determined by H₂-chemisorption experiments of the activated catalysts may have overestimated the available metal surface area under operating conditions; and thus the values of the initial TOF may

not reflect the actual intrinsic activity of the catalyst.

CO-TPR experiments indicated that alumina modification facilitated CO dissociation (see Section 5.4.3). It is typically assumed that CO and H₂ adsorb competitively on the cobalt surface [113, 114]. Hence, an increased rate of CO dissociation may lead to an increase in surface coverage with C and O, and decrease in H coverage. Chen et al. [115] investigated the effect of CO coverage on the CO consumption rate using SSITKA experiments. They showed that the rate of CO consumption decreased with increasing CO pressure due to a decrease in free sites. Interestingly, they also reported a decrease in the activation energy with increasing partial pressure of CO. This correlates well with the observations made in this study, where the activation energy was found to decrease with increasing alumina loading. Hence, it is possible that alumina modification may have decreased the intrinsic rate of CO consumption by decreasing the number of free sites.

5.5.2 Catalyst deactivation

Catalyst deactivation takes place in two stages [18, 46]. In the first stage, fast deactivation, typically due to catalyst sintering is observed. In the second stage, slow deactivation takes place which may be ascribed to catalyst poisoning, reoxidation or the build-up of polymeric carbon deposits.

In this study, fast catalyst deactivation was observed for the first 20-135 h TOS. This is consistent with Peña et al. [116], as well as Overett et al. [98] and Khodakov et al. [30], who reported a decrease in the catalytic activity within the first 1-15 d when the FT synthesis was carried out in a slurry reactor. These long periods of deactivation observed in slurry reactors are partially due to the large gas volumes and high solubility of long-chain products in the FT wax, which increase the time necessary to achieve steady-state [117–119].

The duration of the first stage of catalyst deactivation increased with increasing alumina loading, while the total loss in activity was about 40%, independent of alumina loading. Hence, the alumina modification decreased the rate of catalyst deactivation.

Sintering has been established to be the main cause for catalyst deactivation during the first stage of the catalytic reaction [46]. Sadeqzadeh et al. [49] developed a kinetic model to describe sintering of alumina-supported cobalt catalysts in a slurry reactor, which showed

that sintering affects the catalytic activity during the first days on stream and then levels off.

Alumina modification was found to prevent sintering during calcination (see Section 4.5.2), and during reduction as evident from the increased metal dispersion of the activated catalyst determined by H₂-chemisorption. TEM imaging showed that the cobalt crystallite size in spent catalysts was smaller for the alumina-modified catalysts. Thus, it is proposed that alumina modification prevented sintering during the FT reaction. This may also explain the increase in the CTY with increasing alumina loading.

The activity of catalyst 2.5Al300 decreased abruptly when the reaction temperature was increased to 240 °C (see Figure 5.10 on page 139). Bertole et al. [120] reported irreversible deactivation of unsupported cobalt catalysts at high partial pressures of water. Treatment of the deactivated catalyst with H₂ partially restored activity but not CO adsorption capacity suggesting a decrease in the metal dispersion. Das et al. [108] reported irreversible catalyst deactivation of bulk cobalt catalysts after addition of 30 % water. A partial pressure of water ($p_{\text{H}_2\text{O}}/p_{\text{H}_2}$) of 30 % is reached at a CO conversion of 37 %, which is close to the conversion of catalyst 2.5Al300 at 240 °C. Hence, it is proposed that catalyst deactivation at this stage of the FT experiment, was induced by a combination of the high reaction temperature and a high partial pressure of water.

During the second stage of catalyst deactivation, catalyst activity dropped by only 10 % for catalyst 0.0Al300, 0.1Al300 and 0.5Al300, but by 56 % for catalyst 2.5Al300. The increased catalyst deactivation observed for catalyst 2.5Al300 may be explained by the longer exposure of this catalyst to FT conditions (630 h TOS vs. \approx 300 h TOS) and by the additional sintering observed due to the high CO conversions of this catalyst at 240 °C.

The second stage of slow catalyst deactivation is typically ascribed to deactivation by carbon deposition or catalyst reoxidation [41, 46]. Analysis of the spent catalysts did not show signs of excessive cobalt reoxidation.

XRD experiments showed a CoO content of 8 wt% in the spent catalyst 2.5Al300, which corresponds to a DOR of 95 %. This constitutes an increase from the DOR of 86 % determined for the activated catalyst. The other catalysts showed no CoO phase in the XRD. This would indicate that the catalysts were reduced, rather than reoxidised, during the FT synthesis. This is in agreement with existing studies who reported an increase in

the degree of reduction during the FT synthesis for cobalt catalysts with a crystallites size above 6 nm [41, 121].

TEM imaging showed a surface layer of small CoO crystallites in all catalysts. The CoO phase seen in the TEM images was possibly X-ray amorphous (e.g. < 3 nm) and thus not detected by the XRD. Furthermore, H₂-TPR experiments indicated the presence of unreduced cobalt in a non-stoichiometric cobalt-alumina phase after catalyst activation (see Section 5.4.1). STEM-EDS mapping of the spent catalyst 2.5Al300 showed small crystallites with a high concentration of cobalt, aluminium and oxygen, which may correspond to such a non-stoichiometric cobalt-alumina phase. These mixed metal-support phases often lack long-range order, and are therefore X-ray amorphous [61, 122]. Hence, the actual DOR of the spent catalysts may be lower than suggested by XRD experiments. Therefore, surface reoxidation may have contributed to slow catalyst deactivation.

XRD and TEM did not show any signs of graphitic carbon. However, polymeric carbon deposition may not be revealed by these techniques. Formation of polymeric carbon increases with increasing partial pressures of CO [18]. Peña et al. [116] found a higher concentration of 1-olefins on the surface of spent catalysts, compared to the concentration in the FT product. They suggested that 1-olefins may act as precursors for the formation of polymeric carbon. Hence, the increased rate of CO dissociation and high selectivity for 1-olefins observed for catalyst 2.5Al300 may have led to polymeric carbon deposition which blocked active sites. This may have contributed to the larger catalyst deactivation, and relatively low TOF determined for this catalyst.

5.5.3 Fischer-Tropsch product selectivity

In this study, methane selectivities between 11-20 % were observed at a reaction temperature of 220 °C. This is in good agreement with values of 7-21 % for unpromoted Co/Al₂O₃ reported in the literature [30, 123, 124]. The olefin selectivity in the C₃-fraction varied between 60-63 %, and the C₅₊ selectivity varied between 58-76 %, which is also in good agreement with values reported for other cobalt-based catalysts [124]. This demonstrates that the product selectivity of the inverse-model catalysts prepared in this study was comparable to a regular Co/Al₂O₃ catalyst.

The effect of temperature and TOS on the product selectivity was particular to each investigated catalyst. Thus, slightly different trends were observed at different reaction temperatures. In general, the product selectivity observed for different catalysts was more similar to each other at a higher reaction temperature, so that the largest differences in product selectivity were observed at the lowest reaction temperature of 220 °C.

It has been suggested, that the effects of CO conversion, partial pressure of water and temperature on the product selectivity may vary depending on the support and preparation method [23, 99]. Hence, the observed variations in product selectivity as a function of temperature and TOS may be explained by the different degree of cobalt-alumina interaction in the catalyst.

Figure 5.19 shows the product distribution for the fresh catalysts at a reaction temperature of 220 °C as a function of alumina loading. The methane selectivity decreased, whereas C_{5+} selectivity and chain growth probability increased for catalyst 0.1Al300 and 2.5Al300, while those parameters are similar for catalyst 0.0Al300 and 0.5Al300. The 1-olefin selectivity was higher in catalyst 2.5Al300 compared to the reference catalyst 0.0Al300. Catalyst 0.1Al300 and 0.5Al300 had a large $C_n^{2=}/C_n^{1=}$ and $C_n^Y/C_n^{1=}$ ratio. $C_n^{2=}/C_n^{1=}$ ratio increased from 0.06 to 0.14 and 0.42 upon modifying the catalyst with 0.5 wt% and 0.1 wt% Al, respectively. Noticeable was also the increase in alcohol (ethanol) selectivity in the C_2 -fraction of the alumina-modified catalysts.

Due to the increase in the initial deactivation period with increasing alumina loading, the duration of the FT experiment increased with increasing alumina loading. Catalyst 2.5Al300 was tested for about 630 h, while catalyst 0.0Al300 was only tested for about 250 h. Product accumulation inside the reactor may affect the retention time and thus the extent of secondary reactions of FT products [125]. The retention increases with increasing chain lengths due to their increased solubility in the liquid phase [22]. The different rate of catalyst deactivation in combination with differences in product accumulation complicate the comparison of the product selectivity. Thus, the best correlation between the product selectivity and alumina loading was observed when comparing the catalysts at a similar TOS. Figure 5.20 shows the product selectivity at TOS \approx 250 h. It should be noted, that this means comparing catalyst 0.0Al300, 0.1Al300 and 0.5Al300 in their deactivated state (220 °C(2)) to catalyst 2.5Al300 in its fresh state (220 °C). In this case, the methane

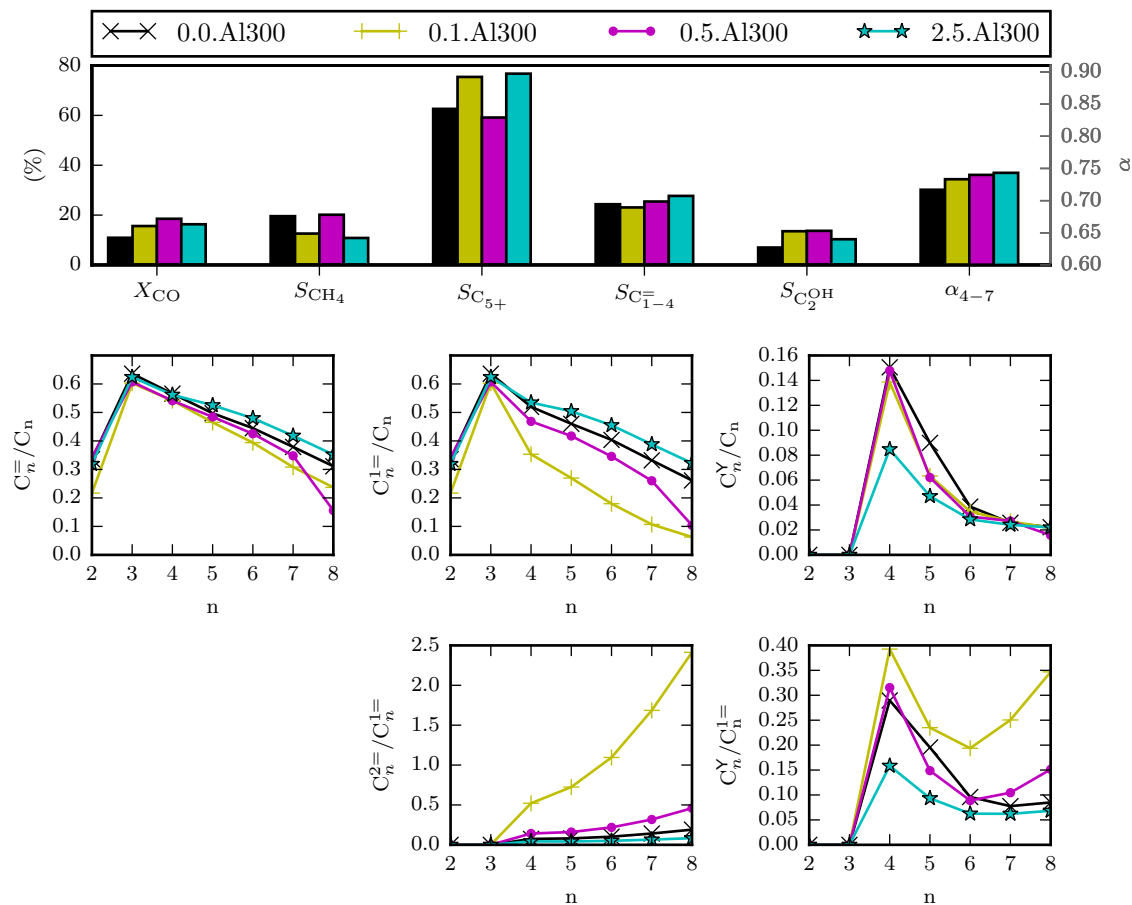


Figure 5.19: Product distribution for the fresh catalyst at a reaction temperature of 220 °C as a function of alumina loading.

selectivity decreased, while C₅₊ selectivity and olefinicity in the C₁–C₄-fraction increased with increasing alumina loading.

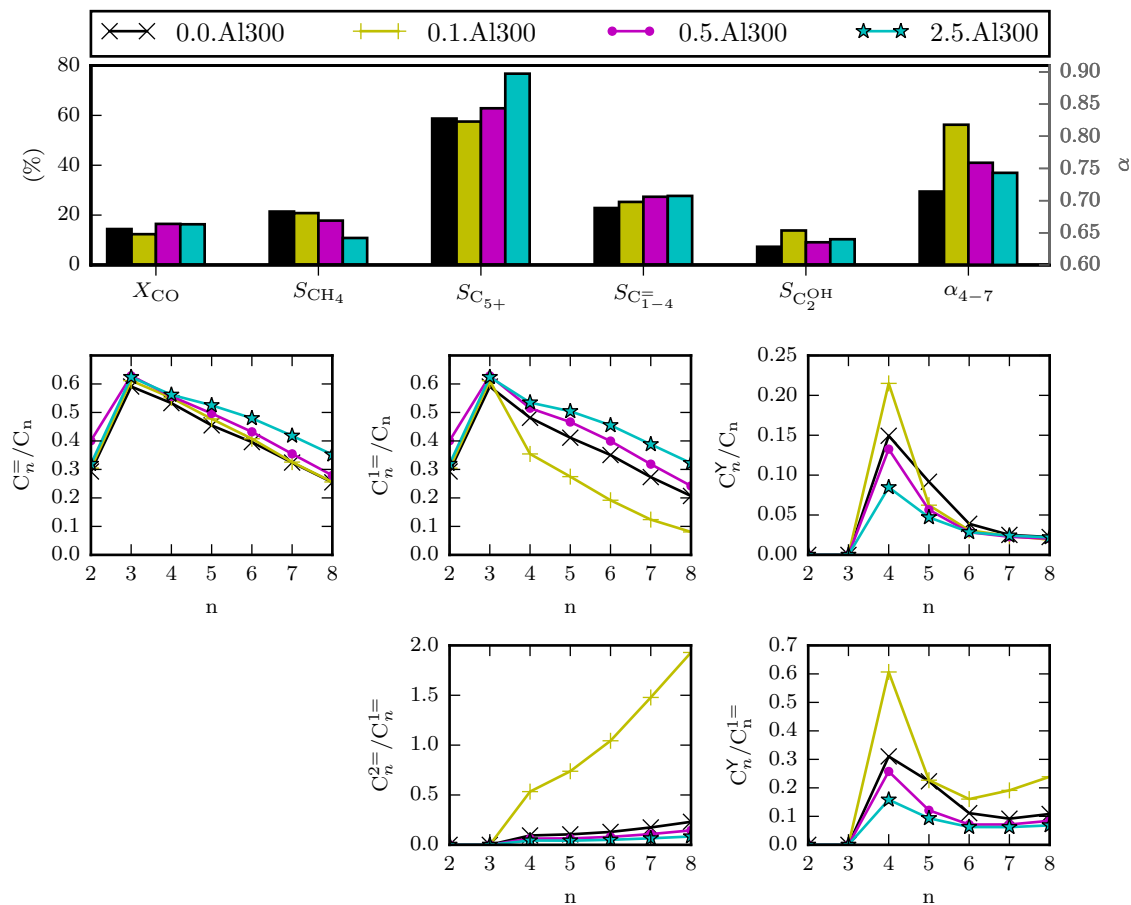


Figure 5.20: Product distribution at a reaction temperature of 220 °C as a function of alumina loading determined at TOS \approx 250 h.

In conclusion, a different FT product selectivity was observed for the alumina-modified catalysts, compared to the unmodified bulk cobalt catalyst. The catalysts had a low cobalt dispersion, so that crystallite size effects are not expected to play a role [25, 29, 34–36]. Hence, the change in product selectivity may be attributed to the alumina modification.

CO-TPR experiments showed an increased rate of the surface catalysed Boudouard reaction which led to the hypothesis that the alumina modification facilitated CO dissociation. It has been proposed, that CO dissociation on cobalt may be facilitated by Lewis acid sites [77, 126]. A DFT study performed by van Heerden and van Steen [127] showed facilitated CO dissociation on a Co fcc (111) surface modified with OAl(OH)₂-ligands.

Pyridine-TPD experiments revealed the presence of acid sites in the alumina-modified catalysts. The number of acid sites increased with increasing alumina loading. CO may act as a weak Lewis base donating electrons from the 4 σ -molecular orbital to the Al cation [128].

The 4σ -molecular orbital is a bonding orbital; thus electron withdrawal results in weakening of the C-O bond. Thus it is proposed, that the alumina modification showed a synergistic effect, by introducing Lewis acid sites to the cobalt surface, which facilitated CO dissociation by interaction of the Lewis acid site with the oxygen atom of CO molecules adsorbed on a cobalt site, as depicted in Figure 5.21. This is in agreement with previous studies, which reported the promotion of CO dissociation on metal-support boundary sites for noble metal catalysts [129, 130].

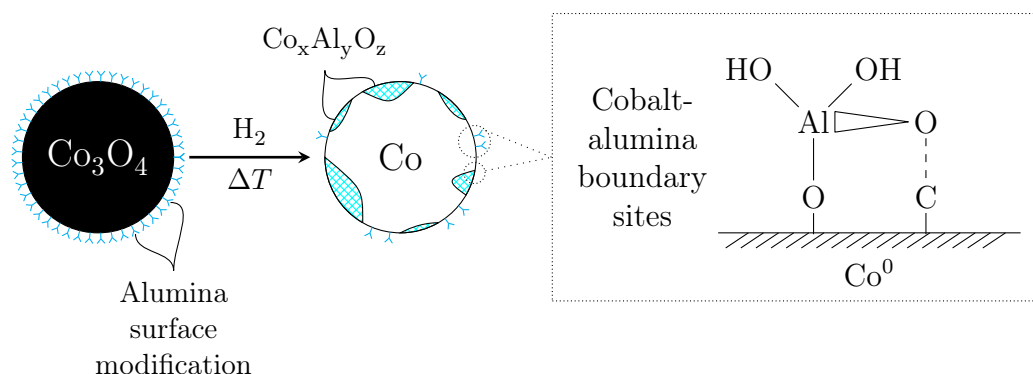


Figure 5.21: Schematic representation of the effect of alumina modification on the cobalt catalyst. Alumina may be present as isolated alumina groups and a mixed cobalt-alumina phase ($\text{Co}_x\text{Al}_y\text{O}_z$), which introduce Lewis acid sites. Lewis acid sites at the boundary of the alumina and cobalt phase facilitate CO dissociation on a cobalt site.

The increased rate of CO dissociation, may have resulted in a high coverage of the cobalt surface with C and O. Bertole et al. [131, 132] used isotope transient experiments to measure changes in surface composition after addition of water and found that water addition leads to an increase in the 'surface inventory of active carbon' [120]. This was explained by an increased rate of CO dissociation without a change in reactivity of the active carbon intermediates. The methane selectivity decreased and chain growth probability increased with increasing surface concentration of active carbon caused by increased partial pressures of water.

Weststrate et al. [114] described this effect in terms of availability of surface H. Adsorbed CO was found to decrease the adsorption capacity for H and inhibit dissociative H_2 adsorption. A high coverage of surface H favoured formation of methyl species and fast methane formation.

Thus, surface crowding of carbon on the catalyst surface, may decrease the availabil-

ity of H thus inhibiting chain termination and promoting chain growth, which decreases methane but increases C_{5+} selectivity, as was observed for the alumina-modified catalysts. Decreased availability of H on the cobalt surface is also expected to inhibit chain termination as paraffins, and thus promote the primary formation of 1-olefins. This was observed by Tristantini et al. [133], who studied the effect of H_2/CO ratio and found that a decrease in the H_2/CO ratio increased C_{5+} selectivity and olefin selectivity, which was explained by a decrease in surface H.

The increase in C_{5+} selectivity observed for the alumina-modified catalyst was coupled with an increase in the 1-olefin selectivity. Chain growth may be promoted by secondary reactions of 1-olefins [27]. Thus, a decrease in the 1-olefin selectivity with increasing C_{5+} selectivity is often observed [99, 134]. The increase in the C_{5+} accompanied by an increase 1-olefin selectivity observed in this study supports the hypothesis that chain growth was promoted by an increased C, and decreased H availability.

In Chapter 4 it was discussed how alumina modification decreased the reducibility of the catalysts. Correlations between the reducibility and catalyst selectivity, have been reported in the literature [135–137]. Promotion of cobalt catalysts with noble metals increases reducibility by facilitating H_2 dissociation, which may result in a higher methane selectivity, lower chain growth probability, and higher selectivity towards 2-olefins [135]. On the other hand addition of Mn to cobalt catalysts was found to decrease reducibility, but increase 1-olefin selectivity and chain-growth probability [136, 137]. Modification of Co/Al_2O_3 catalysts with zirconia was also found do decrease the reducibility and increase the C_{5+} selectivity [138]. This is in agreement with the trends observed in this study.

It should be noted, that catalyst 0.1Al300 showed a different reduction behaviour and different product selectivity (high selectivity of 2-olefins and branched compounds) compared to catalysts with higher alumina loadings. In catalyst 0.5Al300 and 2.5Al300 reducibility was decreased because the pre-exponential factor decreased, and hence the hydrogen dissociation (as well as nucleation) was hindered. In catalyst 0.1Al300 the pre-exponential factor increased, and hence the hydrogen dissociation was facilitated promoting the formation of CoO and metallic cobalt, but small amounts of a mixed metal-support compound were formed resulting in an overall loss in reducibility (see Section 4.5.2). Hence, a higher hydrogenation activity could be predicted for catalyst 0.1Al300, which may explain

a decrease in olefinicity and increased secondary reaction. However, the methane selectivity typically increases with increasing hydrogenation activity, which was not observed for catalyst 0.1Al300.

Furthermore, the H₂-TPR experiments on the *activated* catalyst (see Section 5.4.1) showed a peak shift to higher temperatures compared to the unmodified catalyst and the presence of a mixed cobalt-alumina phase. For the mixed-cobalt alumina phases, a decrease in the pre-exponential factor was observed (see Section 4.5.2). This suggests that the cobalt oxide phases, which showed an increased hydrogen dissociation ability in the calcined catalyst, were reduced during catalyst activation, and are not any longer present in the *activated* 0.1Al300 catalyst. However, these experiments indicate that the effect of very low alumina loadings may be fundamentally different to high alumina loadings.

For the formation of a mixed cobalt-alumina phase, which contains Co²⁺, the concentration of alumina on the surface needs to be sufficiently large to significantly affect the CoO reducibility and allow for diffusion of Co²⁺ ions into the alumina structure. Thus, it is hypothesised, that apart from the mixed cobalt-alumina phases observed, isolated alumina groups may be formed on the surface of metallic cobalt, where the local alumina concentration was very low. These isolated alumina groups have a large contact area with the metallic cobalt phase, and may thus have a stronger effect on the catalyst selectivity. The concentration of these isolated alumina groups may be higher on catalysts with a low alumina loading.

The high product selectivity of 2-olefins and branched compounds observed for catalyst 0.1Al300 is non-typical for cobalt catalysts, which are expected to have a very low selectivity for secondary products, especially branched compounds. Branched compounds may form as primary compounds [33] or secondary compounds by 1-olefin re-adsorption [139], which is believed to be the prominent reaction pathway for cobalt-based catalysts [12]. For catalyst 0.1Al300, a low 1-olefin selectivity and increase of branching and 2-olefin selectivity with increasing carbon number was observed, which support secondary reactions of 1-olefins as the main reaction pathway. Prieto et al. [140] reported a decrease in the 1-olefin content with increasing acidity of the catalyst support and concluded that the acid-base character of the support may determine the extent of secondary reactions of 1-olefins.

Isomerisation of 1-olefins to 2-olefins or branched compounds can be catalysed by acid

sites (Brønsted acids, or strong Lewis acids) [141]. Olefins have Lewis basic character. They can donate electrons from the double bond to a Lewis acid site forming a carbo-cation. Secondary carbo-cations are more stable than primary carbo-cations resulting in the preference for secondary carbo-cations. Thus, a double bond isomerisation from a 1- into a 2-olefin may take place. The activated olefins could also react with a surface methyl group on the cobalt surface to form branched compounds. It is hypothesised, that isolated alumina groups on the surface of metallic cobalt affected the reactivity of olefins on a cobalt site. This may have contributed to the low selectivity of 1-olefins and high selectivity of 2-olefins and branched compounds observed for catalyst 0.1Al300, and partly for catalyst 0.5Al300.

It should be noted, that the Lewis acid sites of the alumina-modified catalysts are not proposed to act in isolation but in conjunction with a cobalt site, as depicted in Figure 5.21. Hence, alumina is proposed to have a synergistic effect by creating Lewis acid sites which may change the metal-adsorbate bond strength on a neighbouring cobalt site. By themselves, they may not show any catalytic activity under FT conditions.

Growth of the isolated alumina groups into larger islands, or formation of a mixed cobalt-alumina phase through reoxidation decreases the number of boundary sites between the Lewis acid and metallic cobalt phase, which may lead to loss of selectivity. Catalyst 0.5Al300 showed a product selectivity similar to 0.1Al300 at the start of the FT experiment, but the selectivity for secondary products decreased when the reaction temperature was increased to 230 °C and remained low throughout the experiment (see Figure 5.12 on page 145). For catalyst 2.5Al300 fast catalyst deactivation was observed at a reaction temperature of 240 °C, which led to a decrease in the 1-olefin and C₅₊ selectivity and increase in methane selectivity. The selectivity was not recovered when the reaction temperature was decreased to 220 °C. It is proposed, that growth of alumina islands or formation of mixed-cobalt alumina phases promoted by high reaction temperatures and high partial pressures of water (high conversion) led to an irreversible loss of selectivity caused by a decrease in the number of boundary sites between Lewis acid and metallic cobalt sites.

Similar effects of Lewis acidity on cobalt-based FT catalysts have been reported in the literature [87, 93, 126, 137]. Johnson et al. [87] studied the effect of metal oxide promoters with varying Lewis acidity on the FT performance of Co/SiO₂ catalysts. A

strong positive correlation was found between the C_{5+} selectivity and the Lewis acidity of the promoter metal cations, suggesting that the promotional effects are a consequence of Lewis acid-base interactions between the reaction intermediates and the promoter metal cations. In particular modification with Mn was found to decrease the reducibility but promote the Boudouard reaction and increase the CO adsorption constant, which resulted in catalysts with improved C_{5+} and methane selectivities, as well as a higher olefin to paraffin ratio [126, 137].

Zhao et al. [93] investigated the carburization of alumina co-pillared montmorillonite as cobalt support material. The acidity of the support varied with the alumina to carbon ratio. Support with a high alumina content showed increased acidity with mainly weakly acidic sites, and a high carbon content showed an overall lower acidity with a small amount of strong acidic sites. The reducibility was found to decrease, and the C_5-C_{20} selectivity was found to increase with increasing alumina content of the support.

In contradiction to these studies, the opposite trend has been observed by Zhang et al. [68, 69]. Comparison of the product selectivity of Co supported on γ - Al_2O_3 with a different number of acid sites led to the conclusion that the methane selectivity decreased with decreasing acidity of the alumina support [69]. Although this study is compelling, it should be noted that the alumina supports did differ in the pore size distribution and cobalt oxide crystallite size. The catalyst with the highest and lowest number of acid sites contained small pores. A crystallite size of 10 nm was reported for the low-acidity catalyst, which was comparable to its pore size, while a crystallite size of 15 nm was reported for the high-acidity catalyst, which was larger than its pores size. It is possible that cobalt crystallites on the low-acidity catalyst were located within the porous structure, while cobalt crystallites on the high-acidity catalysts may have been located on the outside of the porous structure. Hence, the increased C_{5+} selectivity observed for the low-acidity catalysts may have been partly caused by mass-transfer limitations [27].

The number of Lewis acid sites on alumina is expected to decrease in the order $\gamma > \theta > \delta > \alpha$ - Al_2O_3 [67]. Rane et al. [64] noted that, as the expected support acidity decreases, the observed olefin to paraffin ratio and the C_{5+} selectivity increase. Hence, opposite to what was observed in this study, cobalt supported on α - Al_2O_3 , which has low acidity, typically shows the largest C_{5+} and lowest methane selectivity. It has been proposed, that

the high selectivity of cobalt supported on α -Al₂O₃ may be due to low crystal strain of the cobalt crystallites on low surface area supports [25].

In this study, it was proposed that the acid sites need to be in contact with an active cobalt site in order to affect the product selectivity. Hence, the effect of support acidity may be strongly linked to the number of boundary sites between the support and the metal phase, and thus may be strongly affected by the metal dispersion and catalyst preparation. The controversy around the reasons for and the direction of support effects on the FT reaction demonstrate that the study of metal-support interaction remains a relevant research topic.

5.6 Conclusions

Alumina surface-modified cobalt catalysts were prepared by impregnation of cobalt oxide with aluminium sec-butoxide. The alumina modification was found to decrease the catalyst reducibility and increase metal dispersion. This shows that only small amounts of alumina are necessary to prevent metal sintering. As a result the alumina-modified catalysts showed a higher CTY for the FT synthesis.

Furthermore, alumina was found to have a promotional effect on the catalyst selectivity. Pyridine-TPD experiments showed that alumina modification introduced acid sites. The number of acid sites increased with increasing alumina loading. It is proposed, that alumina may act as a Lewis acid, which facilitates CO dissociation by weakening the C-O bond due to electron withdrawal. Facilitated CO dissociation on alumina-modified catalysts was evident from an increased activity for the Boudouard reaction studied by CO-TPR. The increased rate of CO dissociation on the cobalt surface may increase the availability of surface C and decrease the availability of surface H, thereby promoting chain growth and suppressing hydrogenation. Thus, an increase in the olefinicity and C₅₊ selectivity, and decrease in the methane selectivity was observed for alumina-modified catalysts.

The Lewis acid sites are proposed to change the reactivity of CO and reaction intermediates on a neighbouring cobalt site. Hence, the Lewis acid sites are not proposed to act in isolation, but in conjunction to a cobalt site. It is hypothesised, that that mixed cobalt-alumina phases as well as isolated alumina groups on the surface of metallic cobalt were introduced by the alumina modification. The number of isolated alumina groups may increase with decreasing alumina loading. These isolated alumina groups have a large contact area with the metallic cobalt phase, and may thus display increased reactivity. It is proposed that isolated alumina groups on the catalyst containing only 0.1 wt% Al promoted secondary reactions of 1-olefins, and were responsible for the large selectivity of 2-olefins and branched compounds, observed for this catalyst. Hence, the synergistic effect of alumina may be dependent on the alumina loading.

High reaction temperatures and high partial pressures of water (high conversion) may induce growth of alumina islands or the formation of mixed-cobalt alumina phases, which may decrease the number of boundary sites between Lewis acid sites and metallic cobalt.

This may result in a loss of olefin and C₅₊ selectivity, as observed for catalyst 0.5Al300 and 2.5Al300.

Recently, alumina-surface modification of less-reactive supports such as silicon carbide or silica, have been reported to successfully increase metal dispersion while maintaining a high degree of reduction, thus improving catalytic activity [5, 142]. This study shows that alumina modification may also promote the catalytic selectivity. This underlines the possibility of using alumina-surface modification as a method to tune catalyst properties and achieve a more desirable product selectivity.

5.7 References

- [1] Leckel, D. *Energy & Fuels*, 23(5):(2009) 2342–2358
- [2] Dry, M. E. *Applied Catalysis A: General*, 276(1–2):(2004) 1–3
- [3] Gates, B. C. *Chemical Reviews*, 95(3):(1995) 511–522
- [4] Xiong, H., Motchelaho, M. A. M., Moyo, M., Jewell, L. L. and Coville, N. J. *Journal of Catalysis*, 278(1):(2011) 26–40
- [5] Lacroix, M., Dreibine, L., de Tymowski, B., Vigneron, F., Edouard, D., Bégin, D., Nguyen, P., Pham, C., Savin-Poncet, S., Luck, F., Ledoux, M.-J. and Pham-Huu, C. *Applied Catalysis A: General*, 397(1–2):(2011) 62–72
- [6] Jacobs, G., Ji, Y., Davis, B. H., Cronauer, D., Kropf, A. J. and Marshall, C. L. *Applied Catalysis A: General*, 333(2):(2007) 177–191
- [7] Arnoldy, P. and Moulijn, J. A. *Journal of Catalysis*, 93(1):(1985) 38–54
- [8] Wang, W. J. and Chen, Y. W. *Applied Catalysis*, 77(2):(1991) 223–33
- [9] Liu, P., Qin, R., Fu, G. and Zheng, N. *Journal of the American Chemical Society*, 139(6):(2017) 2122–2131
- [10] Schulz, H. *Applied Catalysis A: General*, 186:(1999) 3–12
- [11] Laan, G. P. V. D. and Beenackers, A. A. C. M. *Catalysis Reviews*, 41(3):(1999) 255–318
- [12] Claeys, M. and van Steen, E. *Studies in Surface Science and Catalysis*, 152:(2004) 601–680
- [13] Fischer, F. and Tropsch, H. *Brennstoff-Chemie*, 7:(1926) 97–104
- [14] Bukur, D. B., Mukesh, D. and Patel, S. A. *Industrial & Engineering Chemistry Research*, 29(2):(1990) 194–204
- [15] Kaminsky, M. P., Winograd, N., Geoffroy, G. L. and Vannice, M. A. *Journal of the American Chemical Society*, 108(6):(1986) 1315–1316
- [16] Erley, W., McBreen, P. H. and Ibach, H. *Journal of Catalysis*, 84(1):(1983) 229–234
- [17] Dry, M. E. *Catalysis Today*, 6(3):(1990) 183–206
- [18] Moodley, D. J. *On the deactivation of cobalt-based Fischer-Tropsch synthesis catalysts*. Ph.D. thesis, TU Eindhoven (2008)
- [19] Lögberg, S., Lualdi, M., Järås, S., Walmsley, J. C., Blekkan, E. A., Rytter, E. and Holmen, A. *Journal of Catalysis*, 274(1):(2010) 84–98
- [20] Schulz, H. *Catalysis Today*, 214:(2013) 140–151

- [21] Weststrate, C. J., Ciobica, I. M., van de Loosdrecht, J. and Niemantsverdriet, J. W. *Journal of Physical Chemistry C*, 120(51):(2016) 29210–29224
- [22] Schulz, H. and Claeys, M. *Applied Catalysis A: General*, 186(1):(1999) 71–90
- [23] Bukur, D. B., Lang, X., Akgerman, A. and Feng, Z. *Industrial & Engineering Chemistry Research*, 36(7):(1997) 2580–2587
- [24] Rytter, E., Tsakoumis, N. E. and Holmen, A. *Catalysis Today*, 261:(2015) 3–16
- [25] Rytter, E. and Holmen, A. *Catalysis Today*, 275:(2016) 11–19
- [26] Iglesia, E., Soled, S. L. and Fiato, R. A. *Journal of Catalysis*, 137(1):(1992) 212–224
- [27] Fratolocchi, L., Visconti, C. G., Lietti, L., Tronconi, E. and Rossini, S. *Applied Catalysis A: General*, 512:(2016) 36–42
- [28] Johnson, B. G., Bartholomew, C. H. and Goodman, D. W. *Journal of Catalysis*, 128(1):(1991) 231–247
- [29] Borg, Ø., Dietzel, P. D. C., Spjelkavik, A. I., Tveten, E. Z., Walmsley, J. C., Diplas, S., Eri, S., Holmen, A. and Rytter, E. *Journal of Catalysis*, 259(2):(2008) 161–164
- [30] Khodakov, A. Y., Chu, W. and Fongarland, P. *Chemical Reviews*, 107(5):(2007) 1692–1744
- [31] Niemantsverdriet, J. W. *Applied Physics A*, 61(5):(1995) 503–509
- [32] Patanou, E., Tveten, E. Z., Chen, D., Holmen, A. and Blekkan, E. A. *Catalysis Today*, 214:(2013) 19–24
- [33] Fischer, N., Van Steen, E. and Claeys, M. *Journal of Catalysis*, 299:(2013) 67–80
- [34] Bezemer, G. L., Bitter, J. H., Kuipers, H. P. C. E., Oosterbeek, H., Holewijn, J. E., Xu, X., Kapteijn, F., van Dillen, A. J. and de Jong, K. P. *Journal of the American Chemical Society*, 128(12):(2006) 3956–3964
- [35] Fischer, N., van Steen, E. and Claeys, M. *Catalysis Today*, 171(1):(2011) 174–179
- [36] Wang, Z.-J., Skiles, S., Yang, F., Yan, Z. and Goodman, D. W. *Catalysis Today*, 181(1):(2012) 75–81
- [37] Jacobs, G., Das, T. K., Zhang, Y., Li, J., Racoillet, G. and Davis, B. H. *Applied Catalysis A: General*, 233(1–2):(2002) 263–281
- [38] Reuel, R. C. and Bartholomew, C. H. *Journal of Catalysis*, 85(1):(1984) 78–88
- [39] Oukaci, R., Singleton, A. H. and Goodwin Jr., J. G. *Applied Catalysis A: General*, 186(1–2):(1999) 129–144
- [40] Storsæter, S., Borg, Ø., Blekkan, E. A. and Holmen, A. *Journal of Catalysis*, 231(2):(2005) 405–419

-
- [41] van de Loosdrecht, J., Balzhinimaev, B., Dalmon, J. A., Niemantsverdriet, J. W., Tsybulya, S. V., Saib, A. M., van Berge, P. J. and Visagie, J. L. *Catalysis Today*, 123(1–4):(2007) 293–302
- [42] Ciobîcă, I. M., van Santen, R. A., van Berge, P. J. and van de Loosdrecht, J. *Surface Science*, 602(1):(2008) 17–27
- [43] Sparks, D. E., Jacobs, G., Gnanamani, M. K., Pendyala, V. R. R., Ma, W., Kang, J., Shafer, W. D., Keogh, R. A., Graham, U. M., Gao, P. and Davis, B. H. *Catalysis Today*, 215:(2013) 67–72
- [44] de Smit, E. and Weckhuysen, B. M. *Chemical Society Reviews*, 37(12):(2008) 2758–2781
- [45] Pendyala, V. R. R., Gnanamani, M. K., Jacobs, G., Ma, W., Shafer, W. D. and Davis, B. H. *Applied Catalysis A: General*, 468:(2013) 38–43
- [46] Saib, A. M., Moodley, D. J., Ciobîcă, I. M., Hauman, M. M., Sigwebela, B. H., Weststrate, C. J., Niemantsverdriet, J. W. and van de Loosdrecht, J. *Catalysis Today*, 154(3–4):(2010) 271–282
- [47] Ouyang, R., Liu, J.-X. and Li, W.-X. *Journal of the American Chemical Society*, 135(5):(2013) 1760–71
- [48] Geus, J. W. In *Materials Science Research - Sintering and Catalysis*, volume 10, 29–62. Plenum Press (1975)
- [49] Sadeqzadeh, M., Chambrey, S., Piché, S., Fongarland, P., Luck, F., Curulla-Ferré, D., Schweich, D., Bousquet, J. and Khodakov, A. Y. *Catalysis Today*, 215(0):(2013) 52–59
- [50] Ruckenstein, E. and Pulvermacher, B. *Journal of Catalysis*, 29(2):(1973) 224–245
- [51] Borkó, L., Horváth, Z. E., Schay, Z., Guzzi, L., Bellot Noronha, F., Schmal, M. and Falabella Sousa-Aguiar, E. In *Studies in Surface Science and Catalysis*, volume 167, 231–236. Elsevier (2007)
- [52] Niemelä, M. K. and Krause, A. O. I. *Catalysis Letters*, 42(3):(1996) 161–166
- [53] Zonneville, M. C., Geerlings, J. J. C. and van Santen, R. A. *Surface Science*, 240(1):(1990) 253–262
- [54] van Steen, E., Claeys, M., Dry, M. E., van de Loosdrecht, J., Viljoen, E. L. and Visagie, J. L. *The Journal of Physical Chemistry B*, 109(8):(2005) 3575–3577
- [55] van Berge, P., van de Loosdrecht, J., Barradas, S. and van der Kraan, A. *Catalysis Today*, 58(4):(2000) 321–334
- [56] Moodley, D. J., Saib, A. M., van de Loosdrecht, J., Welker-Nieuwoudt, C. A., Sigwebela, B. H. and Niemantsverdriet, J. W. *Catalysis Today*, 171(1):(2011) 192–200

- [57] Levin, I. and Brandon, D. *Journal of the American Ceramic Society*, 81(8):(1998) 1995–2012
- [58] Zhou, R. S. and Snyder, R. L. *Acta Crystallographica Section B*, 47(5):(1991) 617–630
- [59] Sirijaruphan, A., Horváth, A., Goodwin, J. G. and Oukaci, R. *Catalysis Letters*, 91(1):(2003) 89–94
- [60] Kurajica, S., Popović, J., Tkalčec, E., Gržeta, B. and Mandić, V. *Materials Chemistry and Physics*, 135(2–3):(2012) 587–593
- [61] Jongsomjit, B., Panpranot, J. and Goodwin, J. G. *Journal of Catalysis*, 204(1):(2001) 98–109
- [62] Rane, S., Borg, Ø., Yang, J., Rytter, E. and Holmen, A. *Applied Catalysis A: General*, 388(1–2):(2010) 160–167
- [63] Borg, Ø., Eri, S., Blekkan, E. A., Storsæter, S., Wigum, H., Rytter, E. and Holmen, A. *Journal of Catalysis*, 248(1):(2007) 89–100
- [64] Rane, S., Borg, Ø., Rytter, E. and Holmen, A. *Applied Catalysis A: General*, 437–438:(2012) 10–17
- [65] Liu, C., Li, J., Zhang, Y., Chen, S., Zhu, J. and Liew, K. *Journal of Molecular Catalysis A: Chemical*, 363–364:(2012) 335–342
- [66] Digne, M., Sautet, P., Raybaud, P., Euzen, P. and Toulhoat, H. *Journal of Catalysis*, 226(1):(2004) 54–68
- [67] Sung, D. M., Kim, Y. H., Park, E. D. and Yie, J. E. *Research on Chemical Intermediates*, 36(6):(2010) 653–660
- [68] Zhang, J., Chen, J., Ren, J. and Sun, Y. *Applied Catalysis A: General*, 243(1):(2003) 121–133
- [69] Zhang, J., Chen, J., Ren, J., Li, Y. and Sun, Y. *Fuel*, 82(5):(2003) 581–586
- [70] Rytter, E., Salman, A. u. R., Tsakoumis, N. E., Myrstad, R., Yang, J., Logdberg, S., Holmen, A. and Roenning, M. *Catalysis Today*, 299(1):(2018) 20–27
- [71] Claeys, M. and Fischer, N. PCT patent WO 2013/005180 A1 (2013)
- [72] Fischer, N., Clapham, B., Feltes, T., van Steen, E. and Claeys, M. *Angewandte Chemie International Edition*, 53(5):(2014) 1342–1345
- [73] Antoine, C. *Comptes Rendus des Séances de l'Académie des Sciences*, 107:(1888) 681–684
- [74] McCullough, J. P., Douslin, D. R., Messerly, J. F., Hossenlopp, I. A., Kincheloe, T. C. and Waddington, G. *Journal of the American Chemical Society*, 79(16):(1957) 4289–4295

-
- [75] Nehren, H. S. S. *Erdöl, Kohle, Erdgas, Petrochemie*, 39:(1986) 93–94
- [76] Kaiser, R. *Methoden der Physikalischen Analyse*, 5:(1969) 357
- [77] Maitlis, P. M. and Zanotti, V. *Chemical Communications*, 13:(2009) 1619–1634
- [78] Xiong, H., Zhang, Y., Wang, S. and Li, J. *Catalysis Communications*, 6(8):(2005) 512–516
- [79] Tang, C.-W., Wang, C.-B. and Chien, S.-H. *Thermochimica Acta*, 473:(2008) 68–73
- [80] Lapidus, A., Krylova, A., Kazanskii, V., Borovkov, V., Zaitsev, A., Rathousky, J., Zukal, A. and Jančálková, M. *Applied Catalysis*, 73(1):(1991) 65–81
- [81] Zhang, Y., Wei, D., Hammache, S. and Goodwin Jr., J. G. *Journal of Catalysis*, 188(2):(1999) 281–290
- [82] Øyvind, B., Magnus, R., Sølvi, S., Wouter, v. B. and Anders, H. *Studies in Surface Science and Catalysis*, 163:(2007) 255–272
- [83] Fogler, H. S. *Essentials of Chemical Reaction Engineering*, 420–425. Pearson (2011)
- [84] Onnes, H. K., Crommerlin, C.-A. and Cath, P. G. *Proceedings of the Koninklijke Nederlandse Akademie Van Wetenschappen*, 20(178-184)
- [85] Scholten, J. J. F. *Studies in Surface Science and Catalysis*, 3:(1979) 685–714
- [86] Reuel, R. C. and Bartholomew, C. H. *Journal of Catalysis*, 85(1):(1984) 63–77
- [87] Johnson, G. R. and Bell, A. T. *Journal of Catalysis*, 338:(2016) 250–264
- [88] Anderson, R. B. *The Fischer-Tropsch Synthesis*. Academic Press (1984)
- [89] Nakamura, J., Toyoshima, I. and Tanaka, K.-i. *Surface Science*, 201(1):(1988) 185–194
- [90] Bremmer, M., Zacharaki, E., Sjastad, A. O., Navarro, V., Frenken, J. W. M. and Kooyman, P. J. *Faraday Discussions*, 197:(2017) 337–351
- [91] Kharissova, O. V. and Kharisov, B. I. *RSC Advances*, 4(58):(2014) 30807–30815
- [92] Claeys, M., Dry, M. E., van Steen, E., du Plessis, E., van Berge, P. J., Saib, A. M. and Moodley, D. J. *Journal of Catalysis*, 318:(2014) 193–202
- [93] Zhao, Y.-H., Song, Y.-H., Hao, Q.-Q., Wang, Y.-J., Wang, W., Liu, Z.-T., Zhang, D., Liu, Z.-W., Zhang, Q.-J. and Lu, J. *Fuel Processing Technology*, 138:(2015) 116–124
- [94] Stevens Jr., R. W., Chuang, S. S. C. and Davis, B. H. *Thermochimica Acta*, 407(1–2):(2003) 61–71
- [95] Příbylová, L. and Dvořák, B. *Journal of Chromatography A*, 1216(18):(2009) 4046–4050

- [96] Barzetti, T., Selli, E., Moscotti, D. and Forni, L. *Journal of the Chemical Society, Faraday Transactions*, 92(8):(1996) 1401–1407
- [97] Rascon, F., Wischert, R. and Coperet, C. *Chemical Science*, 2(8):(2011) 1449–1456
- [98] Overett, M. J., Breedts, B., du Plessis, E., Erasmus, W. and van de Loosdrecht, J. *Preprints - American Chemical Society, Division of Petroleum Chemistry*, 53(2):(2008) 126–128
- [99] Yang, J., Ma, W., Chen, D., Holmen, A. and Davis, B. H. *Applied Catalysis A: General*, 470:(2014) 250–260
- [100] Ducreux, O., Rebours, B., Lynch, J., Roy-Auberger, M. and Bazin, D. *Oil & Gas Science and Technology - Rev. IFP*, 64(1):(2009) 49–62
- [101] Tsakoumis, N. E., Voronov, A., Rønning, M., Beek, W. v., Borg, Ø., Rytter, E. and Holmen, A. *Journal of Catalysis*, 291:(2012) 138–148
- [102] Braconnier, L., Landrивon, E., Clémentçon, I., Legens, C., Diehl, F. and Schuurman, Y. *Catalysis Today*, 215:(2013) 18–23
- [103] Thölén, A. R. In *Materials Science Research - Sintering Processes*. Plenum Press (1979)
- [104] Schanke, D., Hilmen, A. M., Bergene, E., Kinnari, K., Rytter, E., Ådnanes, E. and Holmen, A. *Catalysis Letters*, 34(3-4):(1995) 269–284
- [105] Chonco, Z. H. *Investigation of the promotional effect of Cu and Ag on iron-based Fischer-Tropsch catalysts using ferrites as model catalysts*. Ph.D. thesis, University of Cape Town (2014)
- [106] Chu, W., Chernavskii, P. A., Gengembre, L., Pankina, G. A., Fongarland, P. and Khodakov, A. Y. *Journal of Catalysis*, 252(2):(2007) 215–230
- [107] Herranz, T., Deng, X., Cabot, A., Guo, J. and Salmeron, M. *The Journal of Physical Chemistry B*, 113(31):(2009) 10721–10727
- [108] Das, T. K., Conner, W., Jacobs, G., Li, J., Chaudhari, K. and Davis, B. H. *Studies in Surface Science and Catalysis*, 147:(2004) 331–336
- [109] Prieto, G., Concepción, P., Murciano, R. and Martínez, A. *Journal of Catalysis*, 302:(2013) 37–48
- [110] Shimura, K., Miyazawa, T., Hanaoka, T. and Hirata, S. *Applied Catalysis A: General*, 494:(2015) 1–11
- [111] Yang, J., Froeseth, V., Chen, D. and Holmen, A. *Surface Science*, 648:(2016) 67–73
- [112] Schanke, D., Vada, S., Blekkan, E. A., Hilmen, A. M., Hoff, A. and Holmen, A. *Journal of Catalysis*, 156(1):(1995) 85–95
- [113] Yates, I. C. and Satterfield, C. N. *Energy & Fuels*, 6(3):(1992) 308–14

-
- [114] Weststrate, C. J. and Niemantsverdriet, J. W. *Faraday Discuss.*, 197:(2017) 101–116
- [115] Chen, W., Filot, I. A. W., Pestman, R. and Hensen, E. J. M. *ACS Catalysis*, 7(12):(2017) 8061–8071
- [116] Peña, D., Griboval-Constant, A., Lancelot, C., Quijada, M., Visez, N., Stephan, O., Lecocq, V., Diehl, F. and Khodakov, A. Y. *Catalysis Today*, 228:(2014) 65–76
- [117] Dictor, R. A. and Bell, A. T. *Industrial & Engineering Chemistry Process Design and Development*, 22(4):(1983) 678–681
- [118] Bukur, D. B. and Brown, R. F. *The Canadian Journal of Chemical Engineering*, 65(4):(1987) 604–612
- [119] Caldwell, L. and Van Vuuren, D. S. *Chemical Engineering Science*, 41(1):(1986) 89–96
- [120] Bertole, C. J., Mims, C. A. and Kiss, G. *Journal of Catalysis*, 210(1):(2002) 84–96
- [121] Saib, A. M., Borgna, A., van de Loosdrecht, J., van Berge, P. J. and Niemantsverdriet, J. W. *Applied Catalysis A: General*, 312:(2006) 12–19
- [122] Chin, R. L. and Hercules, D. M. *The Journal of Physical Chemistry*, 86(3):(1982) 360–367
- [123] Hemmati, M. R., Kazemeini, M., Khorasheh, F. and Zarkesh, J. *Journal of the Taiwan Institute of Chemical Engineers*, 44(2):(2013) 205–213
- [124] Nabaho, D., Niemantsverdriet, J. W., Claeys, M. and van Steen, E. *Catalysis Today*, 275:(2016) 27–34
- [125] Masuku, C., Shafer, W., ma, W., G, M. K., Jacobs, G., Hildebrandt, D., Glasser, D. and Davis, B. *Journal of Catalysis*, 287:(2012) 93–101
- [126] Dinse, A., Aigner, M., Ulbrich, M., Johnson, G. R. and Bell, A. T. *Journal of Catalysis*, 288:(2012) 104–114
- [127] van Heerden, T. and van Steen, E. *Faraday Discussions*, 197:(2016) 87–99
- [128] Hadjiivanov, K. I. and Vayssilov, G. N. *Advances in Catalysis*, 47:(2002) 307–511
- [129] Boffa, A. B., Lin, C., Bell, A. T. and Somorjai, G. A. *Catalysis Letters*, 27(3):(1994) 243–249
- [130] Hayek, K., Fuchs, M., Klotzer, B., Reichl, W. and Rupprechter, G. *Topics in Catalysis*, 13(1-2):(2000) 55–66
- [131] Bertole, C. J., Mims, C. A. and Kiss, G. *Journal of Catalysis*, 221(1):(2004) 191–203
- [132] Bertole, C. J., Kiss, G. and Mims, C. A. *Journal of Catalysis*, 223(2):(2004) 309–318
- [133] Tristantini, D., Lögdberg, S., Gevert, B., Borg, Ø. and Holmen, A. *Fuel Processing Technology*, 88(7):(2007) 643–649

- [134] Bukur, D., Pan, Z., Ma, W., Jacobs, G. and Davis, B. *Catalysis Letters*, 1–6
- [135] Nabaho, D. *Hydrogen spillover in the Fischer-Tropsch synthesis*. Ph.D. thesis, University of Cape Town (2015)
- [136] Iqbal, S., Davies, T. E., Hayward, J. S., Morgan, D. J., Karim, K., Bartley, J. K., Taylor, S. H. and Hutchings, G. J. *Catalysis Today*, 272:(2016) 74–79
- [137] Johnson, G. R., Werner, S. and Bell, A. T. *ACS Catalysis*, 5:(2015) 5888–5903
- [138] Rohr, F., Lindvag, O. A., Holmen, A. and Blekkan, E. A. *Catalysis Today*, 58(4):(2000) 247–254
- [139] Schulz, H., Erich, E., Gorre, H. and van Steen, E. *Catalysis Letters*, 7(1):(1990) 157–167
- [140] Prieto, G., De Mello, M. I. S., Concepción, P., Murciano, R., Pergher, S. B. C. and Martínez, A. *ACS Catalysis*, 5(6):(2015) 3323–3335
- [141] Asensi, M. A., Corma, A. and Martínez, A. *Journal of Catalysis*, 158(2):(1996) 561–569
- [142] Koo, H.-M., Lee, B. S., Park, M.-J., Moon, D. J., Roh, H.-S. and Bae, J. W. *Catalysis Science & Technology*, 4:(2014) 343–351

Chapter 6

Concluding remarks

6.1 Summary and conclusions

This study aimed to gain fundamental insights into the effects of metal-support interactions on the reducibility and catalytic performance of cobalt alumina based FT catalysts. This was achieved by using an inverse-model catalyst which isolates the effect of the metal-support interaction from possible clouding effects of the metal crystallite size or support porosity.

Inverse-model catalysts were prepared by incipient wetness impregnation of cobalt oxide with aluminium sec-butoxide, followed by calcination at 300 °C or 500 °C. Weight loadings of 0.1, 0.5 and 2.5 wt% Al were investigated. TEM-EDS imaging confirmed that alumina was homogeneously distributed over the surface of Co_3O_4 .

Alumina modification did not affect the structure of bulk Co_3O_4 , but stabilised small cobalt oxide and cobalt crystallites, thereby preventing metal sintering during calcination, reduction and the FT synthesis. After catalyst activation, the catalysts had low metal dispersions < 4 %, as determined by H_2 -chemisorption. However, the metal dispersion increased with increasing alumina loading. Sintering occurred during the FT synthesis and may be responsible for catalyst deactivation observed in the first 20-135 h TOS. However, the rate of catalyst deactivation decreased with increasing alumina loading. TEM imaging of spent catalysts showed smaller cobalt crystallites present in the alumina-modified, compared to the unmodified catalyst, which indicates that alumina modification decreases the rate of cobalt sintering in the FT synthesis.

The effect of alumina modification and varying calcination temperature on the reducibility was investigated using H₂-TPR as well as *in situ* XRD and *in situ* XANES experiments. The reducibility of the catalysts decreased with increasing calcination temperature and increasing alumina content.

The decrease in reducibility with increasing calcination temperature was attributed to an increase in the Co₃O₄ crystallite size. It should be noted that this effect is opposite to a common observation in supported catalysts, where reducibility decreases with *decreasing* cobalt oxide crystallite size. This is because in supported catalysts the reducibility is dominated by metal-support interactions, which increases with decreasing crystallite size, due to a larger contact area of the metal oxide crystallite with the support [1–3]. This emphasises the difference in the reduction behaviour of bulk and supported cobalt oxide. Astonishingly, the reduction profile of Co₃O₄ containing small amounts of 2.5 wt% Al has a stronger resemblance to the reduction profile of a supported cobalt catalyst, than the reduction profile of bulk Co₃O₄.

Alumina modification was found to decrease the rate of reduction by decreasing the pre-exponential factor for the reduction process, and not by a decrease in the activation energy. This means, that alumina hinders hydrogen activation and/or nucleation of reduced cobalt phases, possibly by blocking of active sites or hindering cobalt diffusion. Thus, the reduction peaks corresponding to the reduction of Co₃O₄ and CoO in the TPR were shifted to higher temperatures. In conclusion, the position of the Co₃O₄ and the CoO reduction peak in the TPR profile may indicate the strength of the metal-support interaction.

Furthermore, alumina modification led to the appearance of additional reduction peaks at temperatures between 400 °C to 600 °C, which were caused by the formation of a mixed cobalt-alumina phase with cobalt occupying octahedral sites. This is supported by the absence of tetrahedrally coordinated Co²⁺ ions below 550 °C in the *in situ* XANES experiments. Reduction peaks at temperatures between 600 °C and 800 °C were assigned to a non-stoichiometric cobalt-alumina phase with cobalt in tetrahedral coordination.

The effect of alumina modification on the FT synthesis was investigated in a slurry reactor under industrially relevant conditions. The activity and selectivity of the alumina-modified catalysts were comparable to the performance of conventional cobalt catalysts supported on alumina [4–6]. This shows that inverse-model catalysts can adequately em-

ulate the effect of the support on the catalytic reaction.

Alumina modification was found to increase the cobalt time yield (CTY), and decrease the activation energy for the FT synthesis. This indicates that alumina may affect the kinetics of the FT reaction. The increase in activity is attributed to an increase in the metal dispersion upon alumina modification, as determined by H₂-chemisorption.

Furthermore, the alumina modification was found to promote the catalytic selectivity. Alumina-modified catalysts showed an increased olefinicity and C₅₊ selectivity, and a decreased methane selectivity. At low alumina loadings, secondary reactions were promoted, and a high selectivity of 2-olefins and branched compounds was observed. These effects are believed to be due to a synergistic effect of Lewis acid sites introduced by the alumina modification.

Pyridine-TPD revealed that alumina modification introduced acid sites to the catalyst. The number of acid sites increased with increasing alumina loading. CO adsorbed in the vicinity of an alumina site may act as a Lewis base by donating electrons from the oxygen to the aluminium cation. This leads to weakening of the C–O bond and may facilitate CO dissociation. This was confirmed by CO-TPR experiments, which showed an increased activity of the alumina-modified catalysts for the surface catalysed Boudouard reaction. It is concluded that the alumina modification facilitated CO dissociation on metallic cobalt.

Facilitation of CO dissociation may lead to an increase in the coverage of the metal surface with carbon, and a decrease of the coverage of the metal surface with hydrogen, thereby reducing the hydrogenation activity. This leads to a shift in the selectivity towards a more olefinic and higher molecular weight product.

The Lewis acid sites are not believed to act in isolation but in conjunction with a cobalt metal site. Hence, the promotional effect of alumina is limited to the cobalt-alumina boundary sites. The effect may depend strongly on the alumina loading, as evident from the different selectivity observed for the catalyst with 0.1 wt% Al.

In conclusion, this study demonstrated a facile approach to prepare inverse-model catalysts for the study of metal-support interactions. Alumina-modification was found to introduce Lewis acid sites and promoted the catalytic activity and selectivity. These findings suggest that the surface chemistry of alumina may promote the catalytic performance of cobalt catalysts via a synergistic effect. It has been shown that metal-support bound-

ary sites on supported noble metals, may affect the strength of the metal-adsorbate bond, which may affect the catalytic activity and selectivity [7, 8]. This study indicates that these effects may also play a role in cobalt alumina catalysts. It also supports recent findings that suggest that Lewis acid sites may promote the selectivity of cobalt-based FT catalysts [9–12].

6.2 Recommendations

This study demonstrated a facile technique to prepare inverse-model catalysts for the study of metal-support interactions on cobalt alumina based FT catalysts. It was shown that alumina could have a promotional effect on the FT synthesis. Hence, inverse-model catalyst systems may be well suited to study other catalyst promoters, such as potassium or manganese, as well as other support materials, such as titania or silica.

The promotional effect of alumina could be further investigated by elucidating the electronic structure of alumina, and how it is affected by the metal-support interaction. This may be accomplished with synchrotron-based X-ray absorption experiments on the aluminium edge.

The model catalyst was prepared by surface modification of Co_3O_4 which had to be activated by a reductive treatment to render the catalytically active metal phase for the FT synthesis. Sintering of the metal phase during reduction and catalytic reaction made it difficult to determine the intrinsic activity of the catalyst. It is recommended to investigate the use of alumina-modified cobalt oxide crystallites for other catalytic reactions which proceed on the Co_3O_4 phase, thereby avoiding excessive sintering. Co_3O_4 is active for oxidation reactions. Suitable catalytic reactions are for example the preferential oxidation of CO [13] or the selective oxidation of alcohols to aldehydes [14].

Alternatively, it should be considered to study the direct modification of metallic cobalt nanoparticles with alumina. However, it is hypothesised that these catalysts would still undergo sintering during the FT synthesis, resulting in much of the same problems.

The effect of acidity on the FT synthesis is still a largely unexplored topic. This study has shown that Lewis acid sites can increase the selectivity for high weight products as well as branched products, which may be desired for fuel production, due to their large octane

number [15]. It is recommended to continue to investigate the effect of Lewis acidity of support materials on the FT product selectivity. Suitable support materials may include boron-doped carbon supports [16, 17].

6.3 References

- [1] Ji, L., Lin, J. and Zeng, H. C. *The Journal of Physical Chemistry B*, 104(8):(2000) 1783–1790
- [2] Jacobs, G., Ma, W. and Davis, B. H. *Catalysts*, 4:(2014) 49–76
- [3] Roe, G. M., Ridd, M. J., Cavell, K. J., Larkins, F. P., D. M. Bibby, R. F. H., C. D. Chang and Yurchak, S. *Studies in Surface Science and Catalysis*, 36:(1988) 509–515
- [4] Khodakov, A. Y., Chu, W. and Fongarland, P. *Chemical Reviews*, 107(5):(2007) 1692–1744
- [5] Hemmati, M. R., Kazemeini, M., Khorasheh, F. and Zarkesh, J. *Journal of the Taiwan Institute of Chemical Engineers*, 44(2):(2013) 205–213
- [6] Nabaho, D., Niemantsverdriet, J. W., Claeys, M. and van Steen, E. *Catalysis Today*, 275:(2016) 27–34
- [7] Hayek, K., Kramer, R. and Paál, Z. *Applied Catalysis A: General*, 162(1–2):(1997) 1–15
- [8] Campbell, C. T. *Nature Chemistry*, 4(8):(2012) 597–598
- [9] Johnson, G. R. and Bell, A. T. *Journal of Catalysis*, 338:(2016) 250–264
- [10] Johnson, G. R., Werner, S. and Bell, A. T. *ACS Catalysis*, 5:(2015) 5888–5903
- [11] Dinse, A., Aigner, M., Ulbrich, M., Johnson, G. R. and Bell, A. T. *Journal of Catalysis*, 288:(2012) 104–114
- [12] Zhao, Y.-H., Song, Y.-H., Hao, Q.-Q., Wang, Y.-J., Wang, W., Liu, Z.-T., Zhang, D., Liu, Z.-W., Zhang, Q.-J. and Lu, J. *Fuel Processing Technology*, 138:(2015) 116–124
- [13] Khasu, M., Nyathi, T., Morgan, D. J., Hutchings, G. J., Claeys, M. and Fischer, N. *Catalysis Science & Technology*, 7(20):(2017) 4806–4817
- [14] Mate, V., Shirai, M. and V. Rode, C. *Catalysis Communications*, 33:(2013) 66–69
- [15] Dry, M. E. *Applied Catalysis A: General*, 276(1–2):(2004) 1–3
- [16] Kawai, S., Saito, S., Osumi, S., Yamaguchi, S., Foster, A. S., Spijker, P. and Meyer, E. *Nature Communications*, 6:(2015) 8098
- [17] Osumi, S., Saito, S., Dou, C., Matsuo, K., Kume, K., Yoshikawa, H., Awaga, K. and Yamaguchi, S. *Chemical Science*, 7(1):(2016) 219–227

Appendix A

Evaluation of TPR experiments

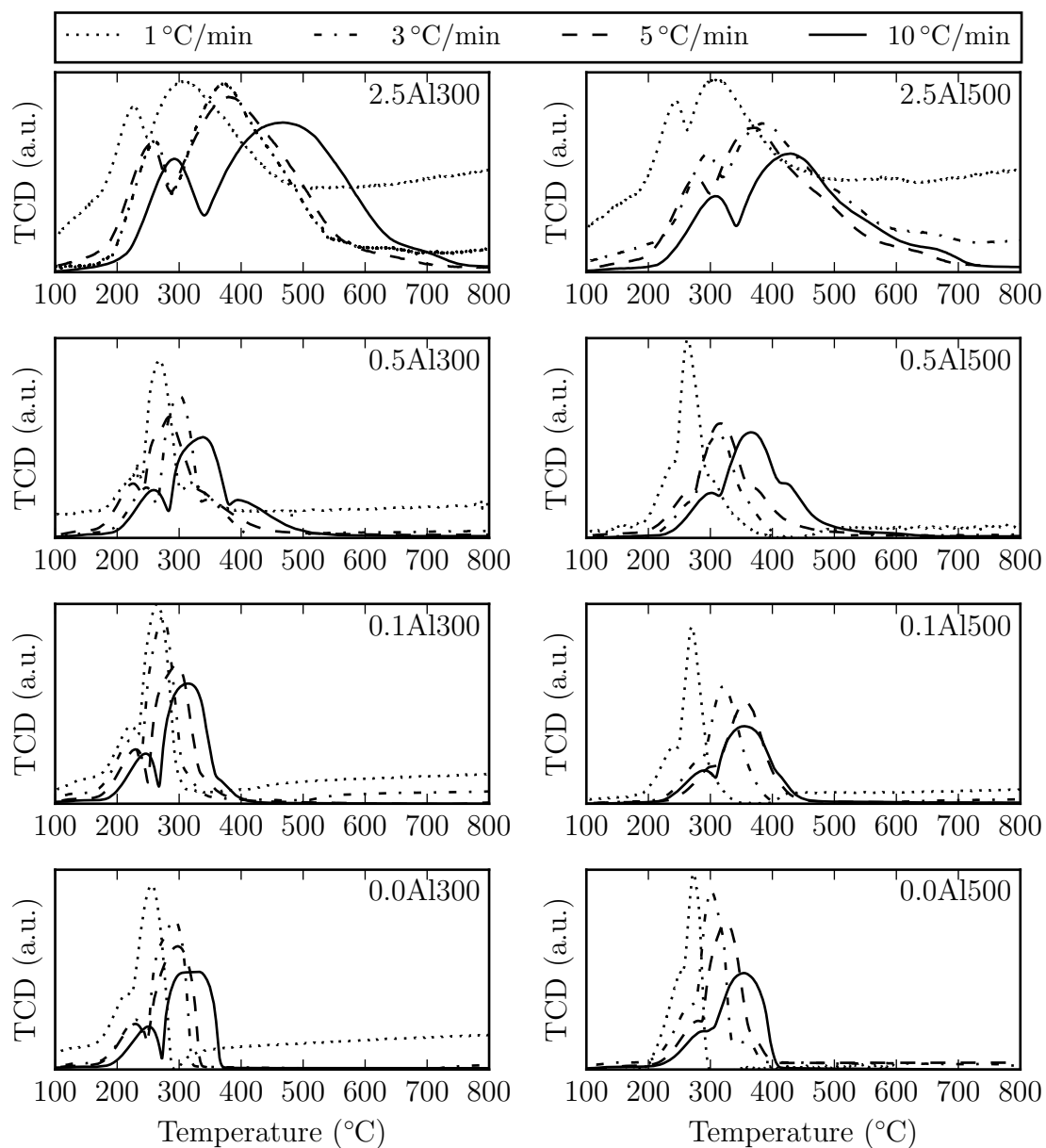


Figure A.1: Reduction profile as measured for catalyst calcined at 300°C (left) and 500°C (right).

Table A.1: Evaluation of reduction profiles measured by TPR.

β (K/min)	T_{cal} (°C)	w _{Al} (wt%)	T_1^a (°C)	T_2^a (°C)	T_3^a (°C)	T_4^a (°C)	Area (TCD*min)
1	300	0	222	257	-	-	70
		0.1	223	264	-	-	58
		0.5	228	268	318	378	41
		2.5	226	308	-	480	37
	500	0	252	271	-	-	56
		0.1	242	269	306	-	57
		0.5	242	263	299	-	55
		2.5	243	306	460	572	50
3	300	0	230	290	-	-	66
		0.1	223	274	315	-	63
		0.5	245	301	344	-	51
		2.5	260	367	-	602	63
	500	0	267	301	352	-	66
		0.1	278	321	-	-	59
		0.5	268	310	358	-	46
		2.5	295	382	522	628	59
5	300	0	228	298	-	-	65
		0.1	231	295	342	-	62
		0.5	226	283	336	-	60
		2.5	254	379	-	635	72
	500	0	280	324	371	-	68
		0.1	300	356	-	-	59
		0.5	267	316	369	-	65
		2.5	278	374	469	615	62
10	300	0	250	315	329	-	63
		0.1	245	314	368	-	63
		0.5	258	338	394	-	61
		2.5	292	467	-	685	77
	500	0	288	353	-	-	58
		0.1	290	354	412	-	63
		0.5	302	366	417	-	73
		2.5	309	428	536	646	57

^aTemperature at peak maximum determined by evaluating first and second derivative of reduction profile

Table A.2: Kinetic evaluation using Kissinger method from TPR profiles (no peak deconvolution).

T_{cal} (°C)	w _{Al} (wt%)	Peak	E_a (kJ/mol)	A (s^{-1})	k (min^{-1})	R^2 (a.u.)
300	0	1	143	1.4E+14	44.1	0.86
		2	92	4.3E+07	17.4	0.99
	0.1	1	159	8.5E+15	46.9	0.83
		2	100	3.0E+08	22.4	0.95
		3	60	1.5E+04	10.2	0.99
	0.5	1	79	1.7E+07	15.2	0.60
		2	65	9.5E+04	13.2	0.82
		3	76	2.3E+05	14.2	0.85
	2.5	1	71	1.1E+06	17.3	0.94
		2	40	8.1E+01	6.2	0.96
		4	50	3.0E+01	3.3	0.97
	500	0	1	140	5.8E+12	29.8
2			69	1.3E+05	13.4	0.99
0.1		1	75	1.4E+06	9.3	0.87
		2	54	4.2E+03	6.7	0.93
		3	61	8.1E+03	9.5	1.00
0.5		1.0	83	1.4E+07	20.8	0.95
		2	55	6.0E+03	10.7	0.98
		3	54	1.9E+03	8.3	0.99
2.5		1	66	1.7E+05	11.1	0.86
		2	51	8.6E+02	7.1	0.95
		3	71	3.5E+03	5.3	0.60
		4	165	5.1E+08	11.5	0.91

Table A.3: Results of peak deconvolution for TPR of catalysts calcined at 300 °C

Peak	w _{Al} (wt%)	Heating rate (°C/min)	T_{max} (°C)	Area (%)	Peak	w _{Al} (wt%)	Heating rate (°C/min)	T_{max} (°C)	Area (%)		
1	0	1	209	24.9	2	0	1	255	75.1		
		3	226	24.9			3	286	75.1		
		5	225	24.9			5	294	75.1		
		10	244	24.7			10	320	75.3		
	0.1	1	218	25.0		0.1	1	265	75.0		
		3	215	25.0			3	272	73.0		
		5	223	25.0			5	292	72.5		
		10	238	24.8			10	314	73.3		
	0.5	1	232	24.9		0.5	1	269	60.5		
		3	244	25.0			3	299	54.2		
		5	225	25.0			5	281	43.0		
		10	256	24.9			10	332	52.6		
	2.5	1	217	13.3		2.5	1	310	78.0		
		3	250	20.2			3	353	38.1		
		5	243	19.1			5	357	43.4		
		10	283	20.7			10	423	42.2		
	3	0.1	3	322		2.0	3	0.1	3	322	2.0
			5	357		2.5			5	357	2.5
			10	382		1.9			10	382	1.9
		0.5	1	326		14.5		0.5	1	326	14.5
3			355	20.8	3	355			20.8		
5			335	32.0	5	335			32.0		
10			412	22.5	10	412			22.5		
2.5		1	408	8.8	2.5	1		408	8.8		
		3	436	39.5		3		436	39.5		
		5	455	35.7		5		455	35.7		
		10	533	34.8		10		533	34.8		
4		2.5	3	609	2.2	4		2.5	3	609	2.2
	5		617	1.8	5		617		1.8		
	10		683	2.3	10		683		2.3		

Table A.4: Results of peak deconvolution for TPR of catalysts calcined at 500 °C

Peak	w _{Al} (wt%)	Heating rate (°C/min)	T _{max} (°C)	Area (%)	Peak	w _{Al} (wt%)	Heating rate (°C/min)	T _{max} (°C)	Area (%)		
1	0	1	235	25.0	2	0	1	272	75.0		
		3	257	25.0			3	304	75.0		
		5	276	25.0			5	326	75.0		
		10	283	24.9			10	354	75.1		
	0.1	1	233	25.0		0.1	1	270	62.0		
		3	275	25.0			3	323	65.0		
		5	300	25.0			5	357	68.1		
		10	284	25.1			10	352	58.5		
	0.5	1	234	25.0		0.5	1	266	52.8		
		3	272	25.0			3	310	47.2		
		5	267	25.0			5	316	46.0		
		10	300	25.0			10	362	39.2		
	2.5	1	229	21.3		2.5	1	309	54.7		
		3	282	20.8			3	380	49.7		
		5	261	15.4			5	362	53.3		
		10	292	17.9			10	422	59.3		
	3	0.1	1	300		13.0	3	0.1	1	307	22.2
			3	364		10.0			3	352	26.7
			5	406		6.8			5	371	28.3
			10	398		16.4			10	417	32.9
0.5		1	400	19.7	0.5	1		400	19.7		
		3	485	24.2		3		485	24.2		
		5	469	24.9		5		469	24.9		
		10	541	17.6		10		541	17.6		
2.5		3	422	1.1	2.5	3		422	1.1		
		5	447	0.6		5		447	0.6		
		10	529	2.9		10		529	2.9		
		10	529	2.9		10		529	2.9		
4	2.5	1	550	4.2	4	2.5	1	550	4.2		
		3	615	5.3			3	615	5.3		
		5	595	6.4			5	595	6.4		
		10	652	5.2			10	652	5.2		

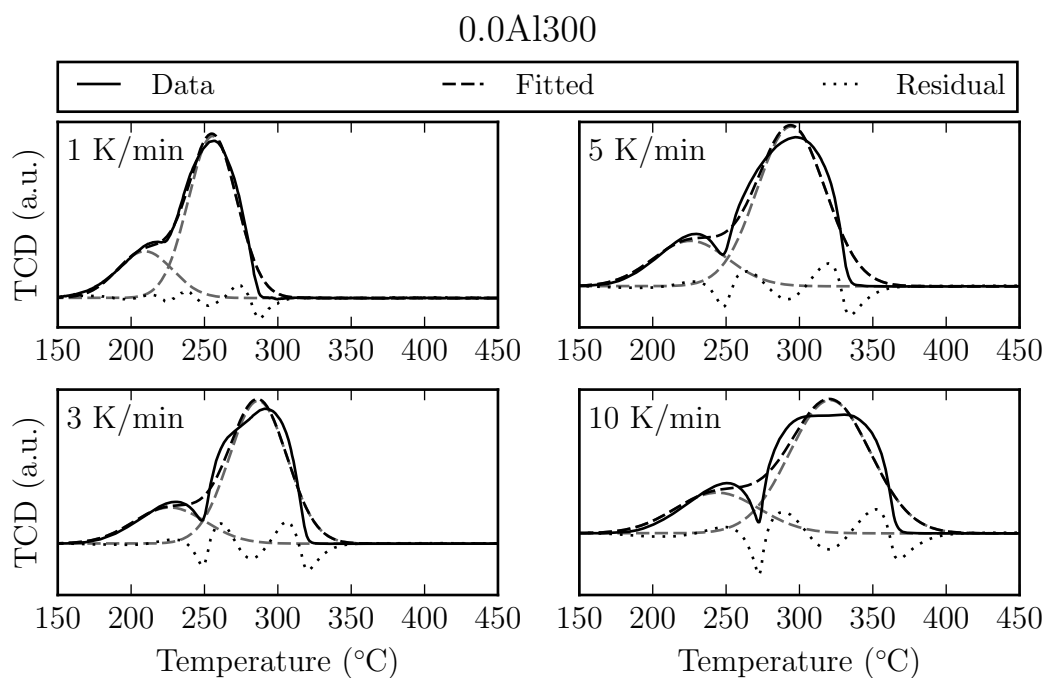


Figure A.2: Peak deconvolution of TPR of catalyst 0.0Al300.

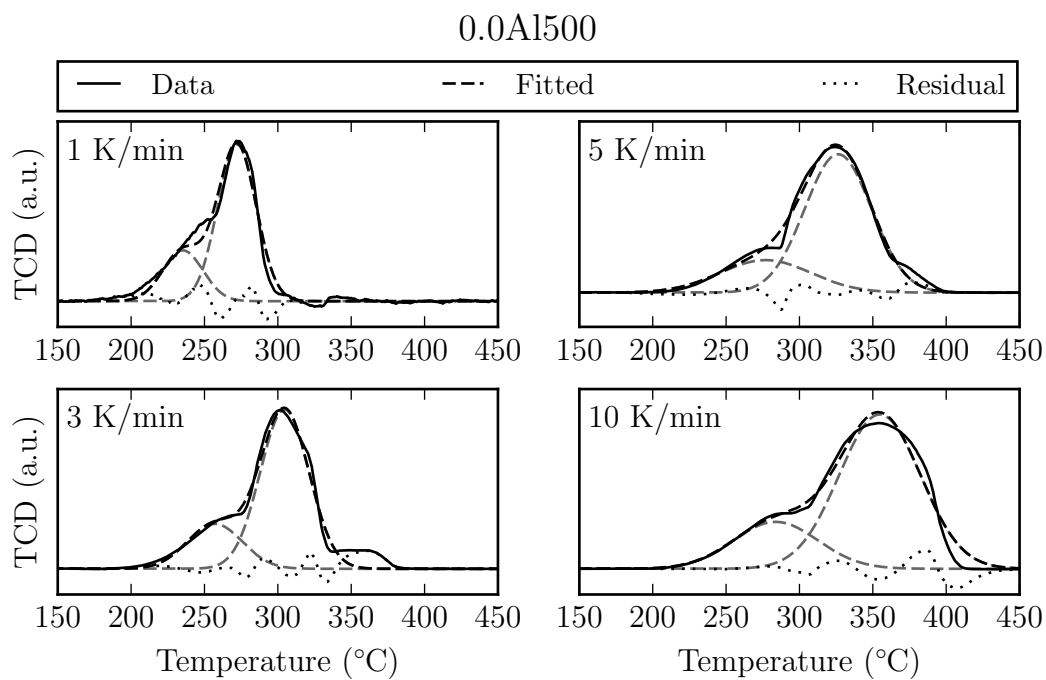


Figure A.3: Peak deconvolution of TPR of catalyst 0.0Al500.

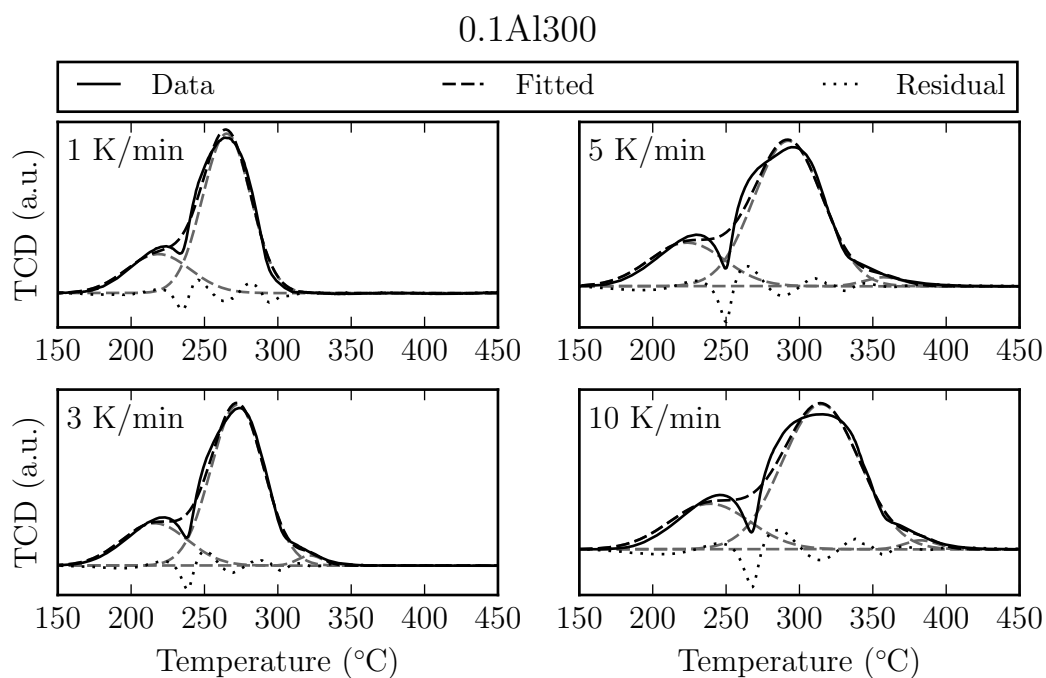


Figure A.4: Peak deconvolution of TPR of catalyst 0.1Al300.

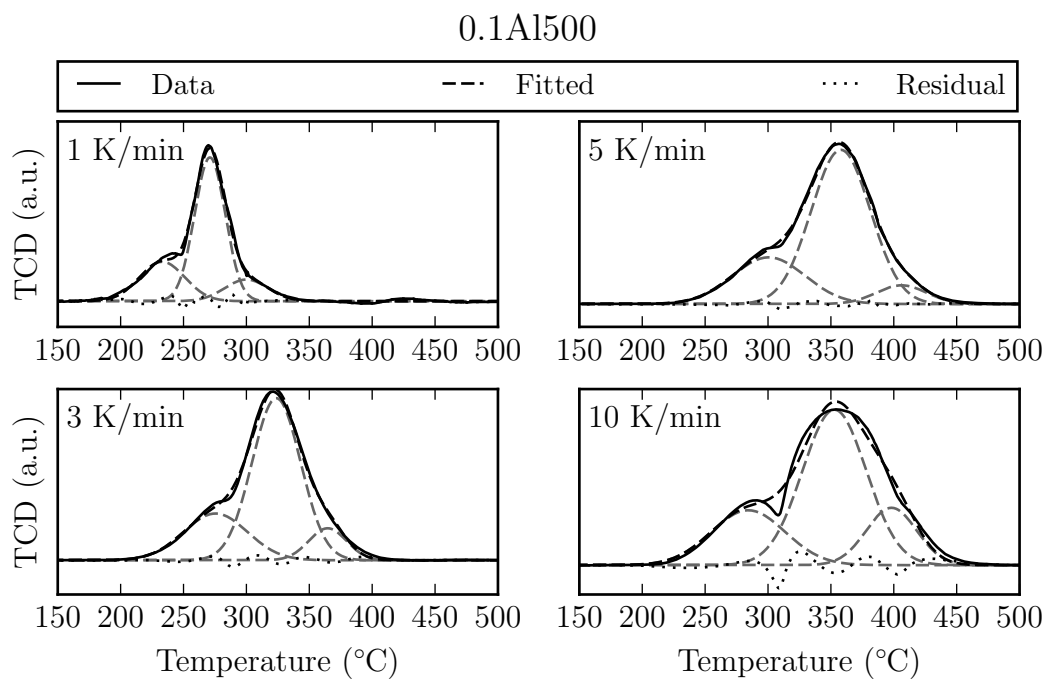


Figure A.5: Peak deconvolution of TPR of catalyst 0.1Al500.

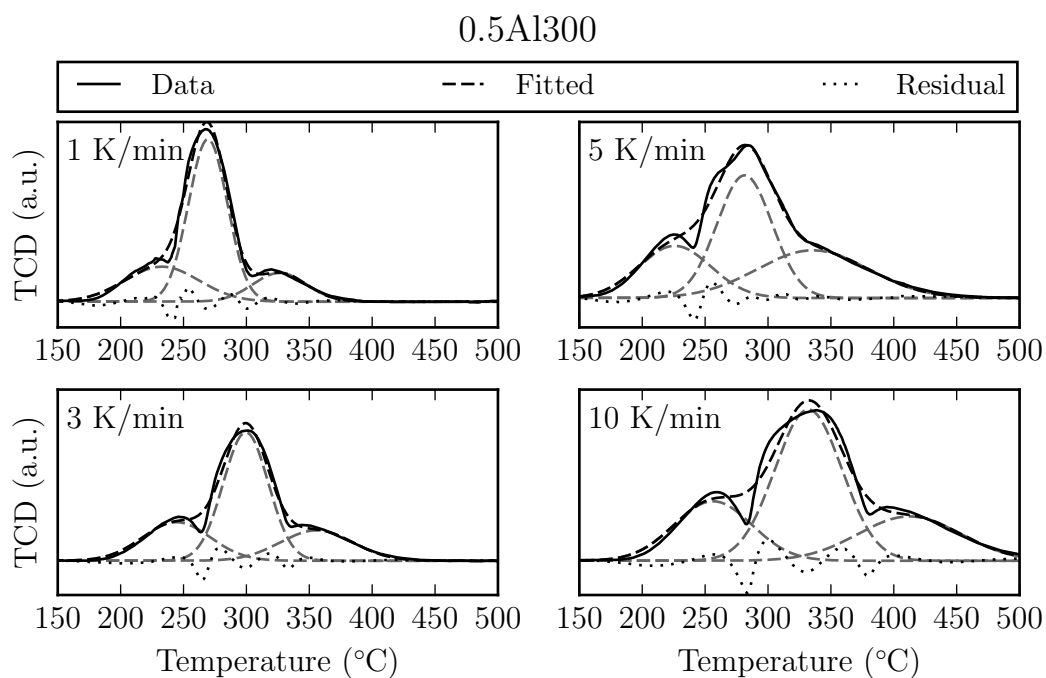


Figure A.6: Peak deconvolution of TPR of catalyst 0.5Al300.

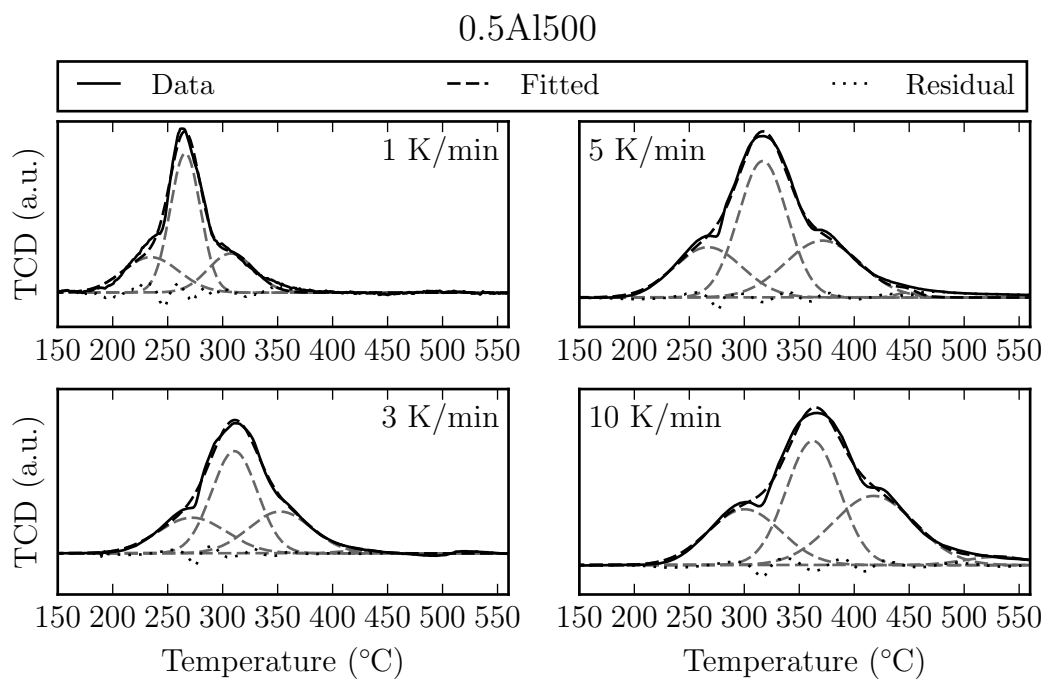


Figure A.7: Peak deconvolution of TPR of catalyst 0.5Al500.

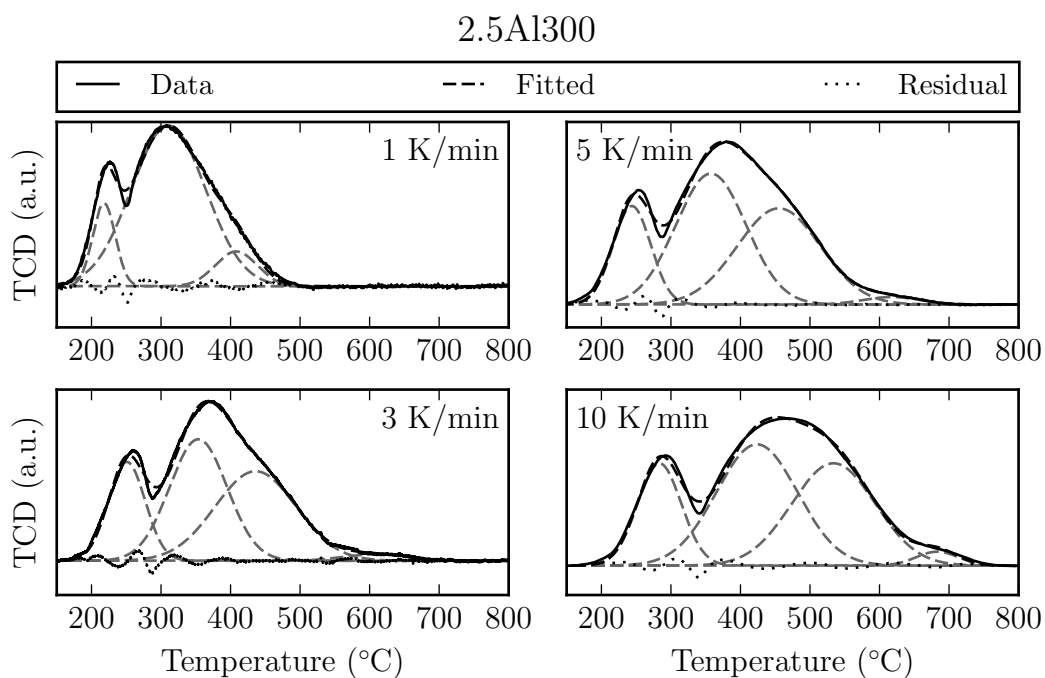


Figure A.8: Peak deconvolution of TPR of catalyst 2.5Al300

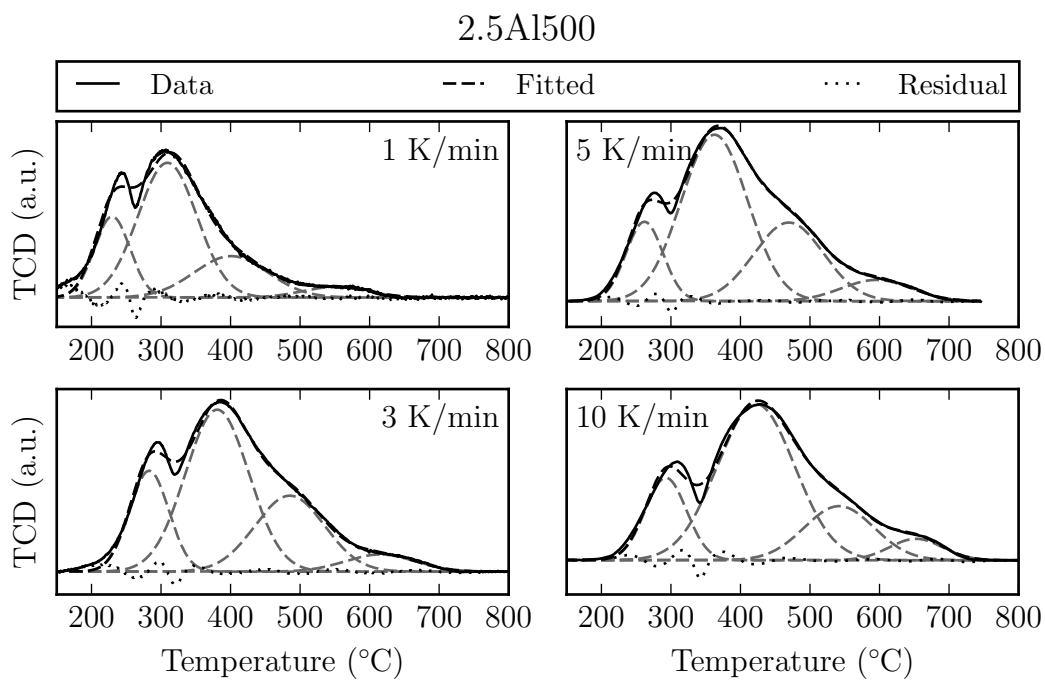


Figure A.9: Peak deconvolution of TPR of catalyst 2.5Al500.

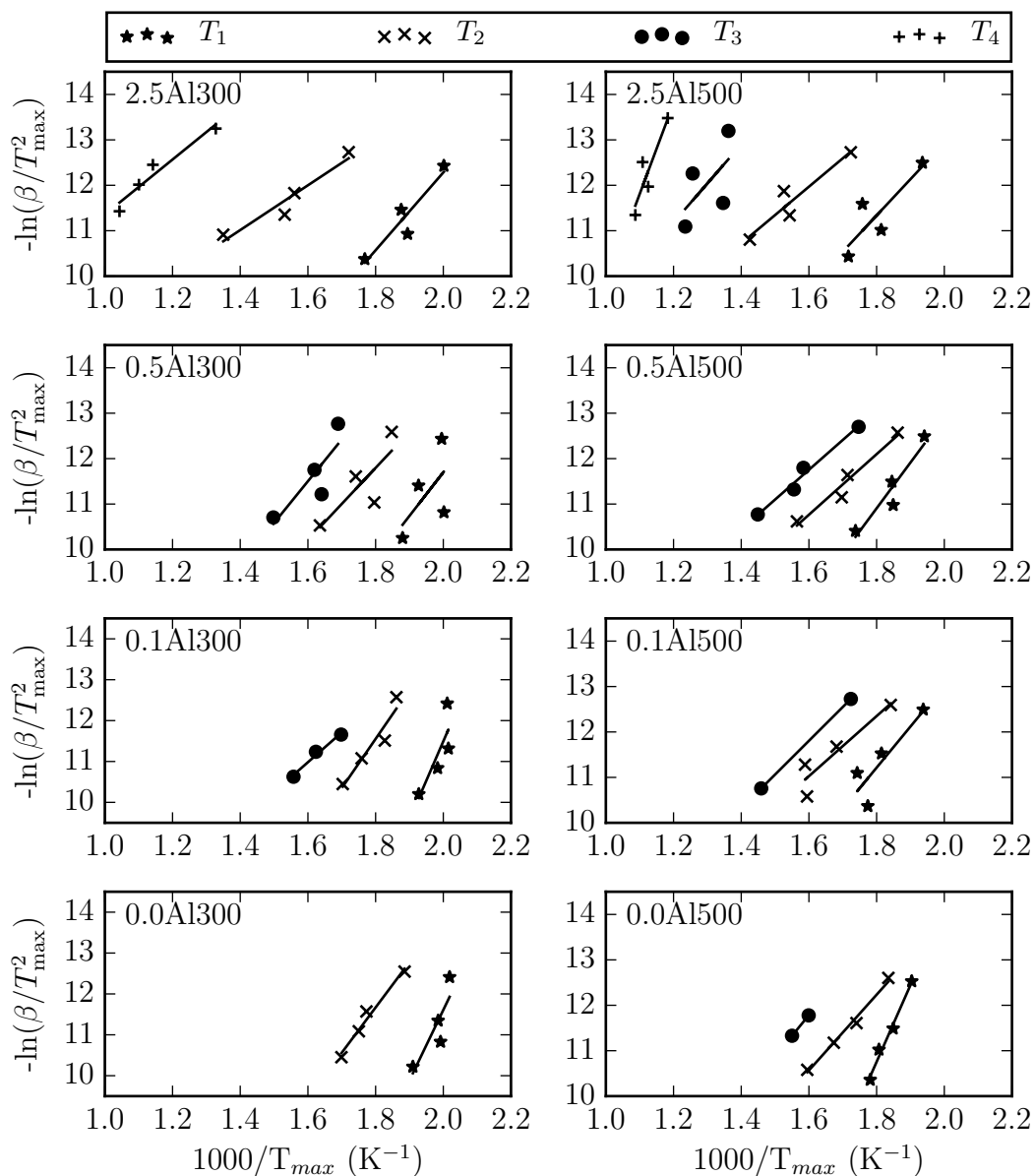


Figure A.10: Kissinger plot from TPR experiments. T_{max} was determined by evaluating first and second derivative of the TCD signal.

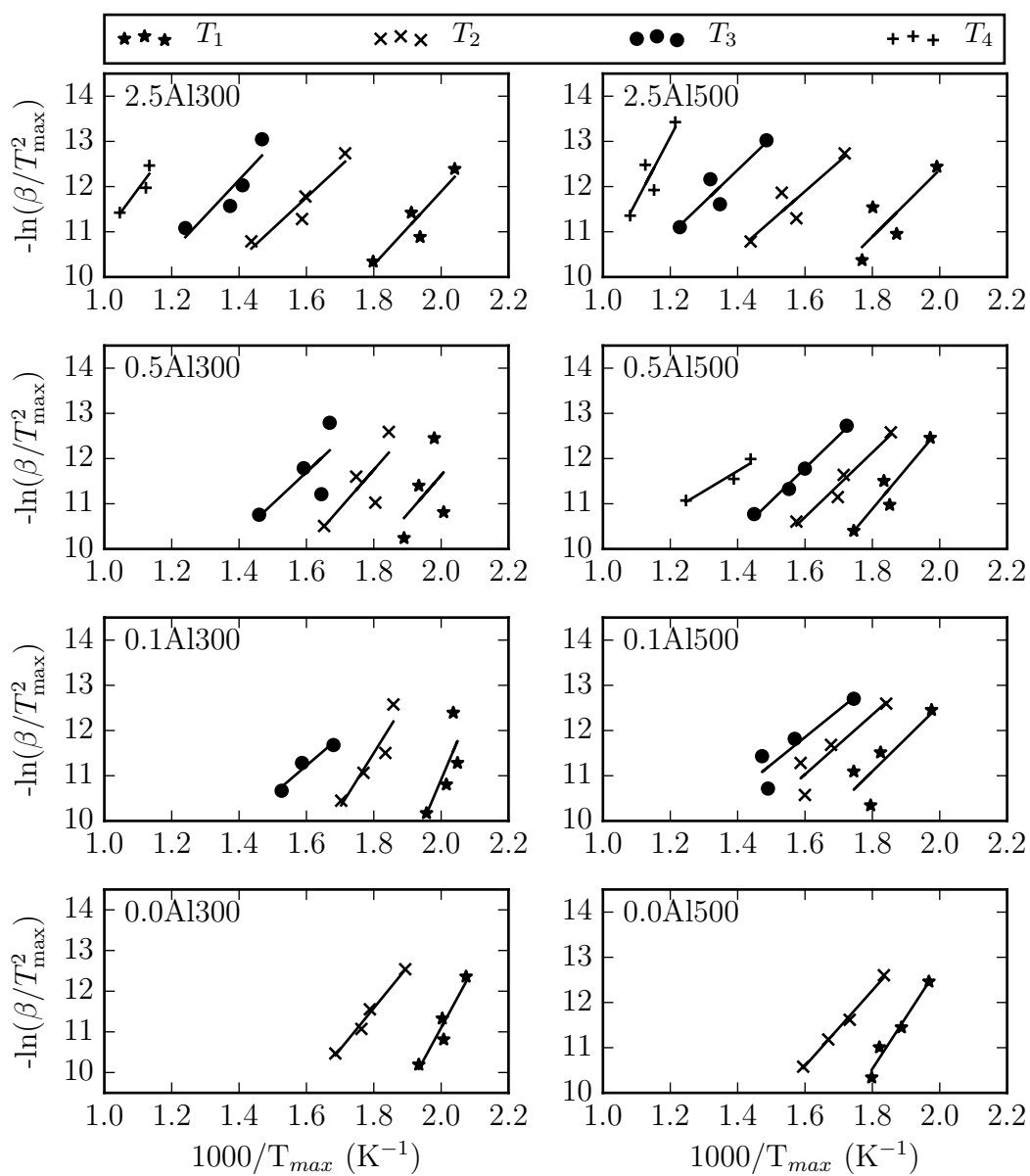


Figure A.11: Kissinger plot of results from peak deconvolution of TPR experiments.

Appendix B

Effect of calcination temperature on metal dispersion

The metal dispersion reported here were determined without taking into account the degree of reduction (DOR), according to:

$$D[\%] = \frac{N_{Co,surface}}{N_{Co,bulk}} \cdot 100 = \frac{N_{H,ad}}{N_{Co,bulk}} \cdot 100 \quad (B.1)$$

$$= \frac{\frac{2V_m}{22.41 \text{ l/mol}}}{\frac{g_{cat} \cdot w_{Co}}{M_{Co}}} \quad (B.2)$$

The metal dispersions and metal crystallite sizes determined from the chemisorption experiments are reported in Table B.1. The values for catalysts calcined at 300 °C deviate slightly from the values reported in Section 5.4.2, because the DOR was not taken into account.

All catalysts had very low metal surface areas with dispersions below $\leq 4\%$, corresponding to crystallite sizes between 27 nm and 697 nm. The metal dispersion increased with increasing alumina loading from 0.22 to 2.85 %, for catalysts 0.0Al300 and 2.5Al300 and from 0.14 to 3.5 % for catalysts 0.0Al500 and 2.5Al500, respectively. This shows that the alumina modification prevented metal sintering during reduction.

The effect of the calcination temperature on the final metal dispersion was not as distinct as the effect of alumina modification. When comparing the metal dispersion of

the catalysts calcined at 500 °C which each other, the dispersion increased with increasing alumina content from 0.14 % to 3.5 %. When comparing the 2.5Al300 catalyst, with the 2.5Al500 catalyst, which had a similar Co_3O_4 crystallite size and the same alumina weight loading, the metal dispersion of the catalyst calcined at 500 °C is about 15 % higher, than the catalyst calcined at 300 °C. However, the initial Co_3O_4 crystallite size of catalysts calcined at 500 °C with lower alumina weight loadings was larger than the Co_3O_4 crystallite size of the catalysts calcined at 300 °C. Hence, the final metal dispersion in these catalysts decreased for the higher calcination temperature. It is reasonable to assume that the Co_3O_4 crystallite size effects the final metal dispersion. In supported catalyst with low metal-support interactions, small cobalt crystallites would be expected to be more mobile on the support and therefore sinter more severely. The situation is different for bulk catalysts. In bulk catalysts, the metal oxide will form agglomerates. Sintering takes place by particle coalescence, and larger oxide crystallites may form larger agglomerates which sinter into larger metal crystallites.

Table B.1: Results of hydrogen chemisorption of alumina-modified cobalt catalysts performed at 120 °C on activated catalysts.

T_{cal} (°C)	w_{Al} (wt%)	$V_{\text{H}_2, \text{mono}}$ ($\text{cm}^3(\text{STP})/\text{g}$)	$N_{\text{Co, surf}}$ ($\text{mmol}/\text{g}_{\text{sample}}$)	Dispersion (%)	d_{Co}^a (nm)	$d_{\text{Co}_3\text{O}_4}^b$ (nm)
300	0.0	0.32	0.028	0.22	427	14
300	0.1	0.88	0.078	0.62	155	14
300	0.5	2.07	0.185	1.47	65	14
300	2.5	3.94	0.352	2.85	33	14
500	0.0	0.20	0.017	0.14	697	30
500	0.1	0.78	0.069	0.55	174	29
500	0.5	1.11	0.099	0.78	122	25
500	2.5	4.85	0.433	3.50	27	16

^aCo crystallite size determined from H_2 -Chemisorption using equation (5.6)

^b Co_3O_4 crystallite size determined by XRD from FWHM of the (220) reflection peak using the Scherrer equation.

Table B.2: Evaluation of hydrogen chemisorption experiments.

T_{cal} (°C)	w _{Al} (wt%)	m_{sample} (g)	K^a -	V_{mono}^a (cm ³ /g)	cf^a -	K^b -	V_{mono}^b (cm ³ /g)
300	0.0	0.12	2.632	0.319	$2.7 \cdot 10^{-4}$	0.152	0.448
300	0.1	0.106	1.035	0.876	$4.0 \cdot 10^{-4}$	0.250	1.054
300	0.5	0.061	0.637	2.075	$5.0 \cdot 10^{-4}$	0.304	2.300
300	2.5	0.057	0.558	3.943	$9.5 \cdot 10^{-4}$	0.262	4.395
500	0.0	0.113	10.883	0.195	$7.8 \cdot 10^{-6}$	7.956	0.198
500	0.1	0.107	0.557	0.778	$-8.6 \cdot 10^{-5}$	0.831	0.741
500	0.5	0.096	0.975	1.108	$-6.1 \cdot 10^{-5}$	1.200	1.083
500	2.5	0.111	1.208	4.846	$8.9 \cdot 10^{-4}$	0.640	5.210

^a Parameters obtained by empirical fit according to Equation 5.27

^b Parameters obtained by fitting the Langmuir isotherm to experimental data.

Appendix C

Determining degree of reduction

The degree of reduction can be determined by TPR experiments, if the hydrogen consumption can be obtained from the tcd signal. The hydrogen consumption as a function of the peak area was determined on the Autochem 2920 using Ag_2O :

$$\text{H}_2 \text{ consumption} = 2.8 \cdot 10^{-5} + \text{peak area (tcd*min)} \cdot 2.3 \cdot 10^{-4} \quad (\text{C.1})$$

Complete reduction of 1 mole of Co_3O_4 requires 4 mole of hydrogen. The amount of hydrogen consumed during the reduction of the activated catalyst gives information about the amount of oxidised cobalt remaining in the catalyst. The degree of reduction is then calculated according to:

$$\text{DOR} = 100 - \frac{\text{H}_2, \text{consumed}}{4N_{\text{Co}_3\text{O}_4}} \cdot 100\% \quad (\text{C.2})$$

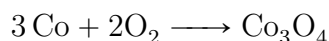
Table C.1: Degree of reduction determined from TPR experiments on activated catalysts

T_{cal} (°C)	w_{Al} (wt%)	m_{sample} (mg)	$N_{\text{Co}_3\text{O}_4}$ (mmol)	Peak area (tcd*min)	H_2 consumption (mmol)	DOR (%)
300	0.0	51	0.21	8.8E-03	3.0E-02	96(.4)
300	0.1	78	0.32	6.1E-02	4.2E-02	96(.7)
300	0.5	49	0.20	2.2E-01	7.9E-02	90(.2)
300	2.5	56	0.22	4.0E-01	1.2E-01	86(.4)

Additional experiments were performed to determine the feasibility of determining the DOR by pulse oxidation (oxygen titration) experiments. The loop volume ($V_{loop}=5.1$ ml) and peak area ($A_{peak,av} = 0.22$ tcd * min) were calibrated by manual injection of 5 ml of 5.1 % O₂ in Helium. The total oxygen consumption was determined as:

$$X_{O_2} = \sum_1^n \frac{A_{peak,n}}{A_{peak,av}} \cdot 8.3 \cdot 10^{-6} \text{ mol}$$

, where n is the peak number. Assuming complete oxidation of metallic cobalt to Co₃O₄:



the DOR can be calculated as:

$$\text{DOR} = \frac{X_{O_2}}{0.66N_{\text{Co}_3\text{O}_4}} \cdot 100 \% \quad (\text{C.3})$$

The catalyst was diluted with SiC to prevent excessive sintering and activated in a flow 10 ml/min H₂ by heating the catalyst to 350 °C at a heating rate of 1 °C/min, and holding for 10 h. The sample was cooled to 60 °C under hydrogen. Then the temperature was raised to 750 °C and the sample was reoxidised by introducing pulses of 5.1 ml of a mixture of 5.2 % O₂ in Helium while recording the TCD signal. The pulses were integrated and the DOR calculated according to Equation (C.3).

After pulse oxidation the catalyst was cooled to 60 °C and kept at 60 °C while flowing 5 % H₂ in Argon for 50 min. The temperature was increased to 900 °C at a heating rate of 10 °C/min, and the tcd signal recorded. If the catalyst was completely reoxidised during the pulse oxidation experiment, the DOR calculated from the TPR experiment (according to C.2), should be 100 %.

Figure C.1 shows the pulse oxidation followed by TPR experiment of catalyst 2.5Al300 after activation. The DOR determined by pulse oxidation was 68 %, which is much lower than expected. The TPR experiment performed on the reoxidised catalysts show that only 85 % of the catalyst had been reoxidised during the pulse oxidation experiment. This proves that the catalyst can not be reoxidized completely at 750 °C. Increasing the temperature

of the pulse oxidation experiment is not feasible as the auto-decomposition of Co_3O_4 to CoO may take place at temperatures above 850°C . It should be noted, that these results merely indicate the stability of the catalyst towards *bulk reoxidation* and no conclusion can be drawn about the stability of the *metal surface* towards reoxidation.

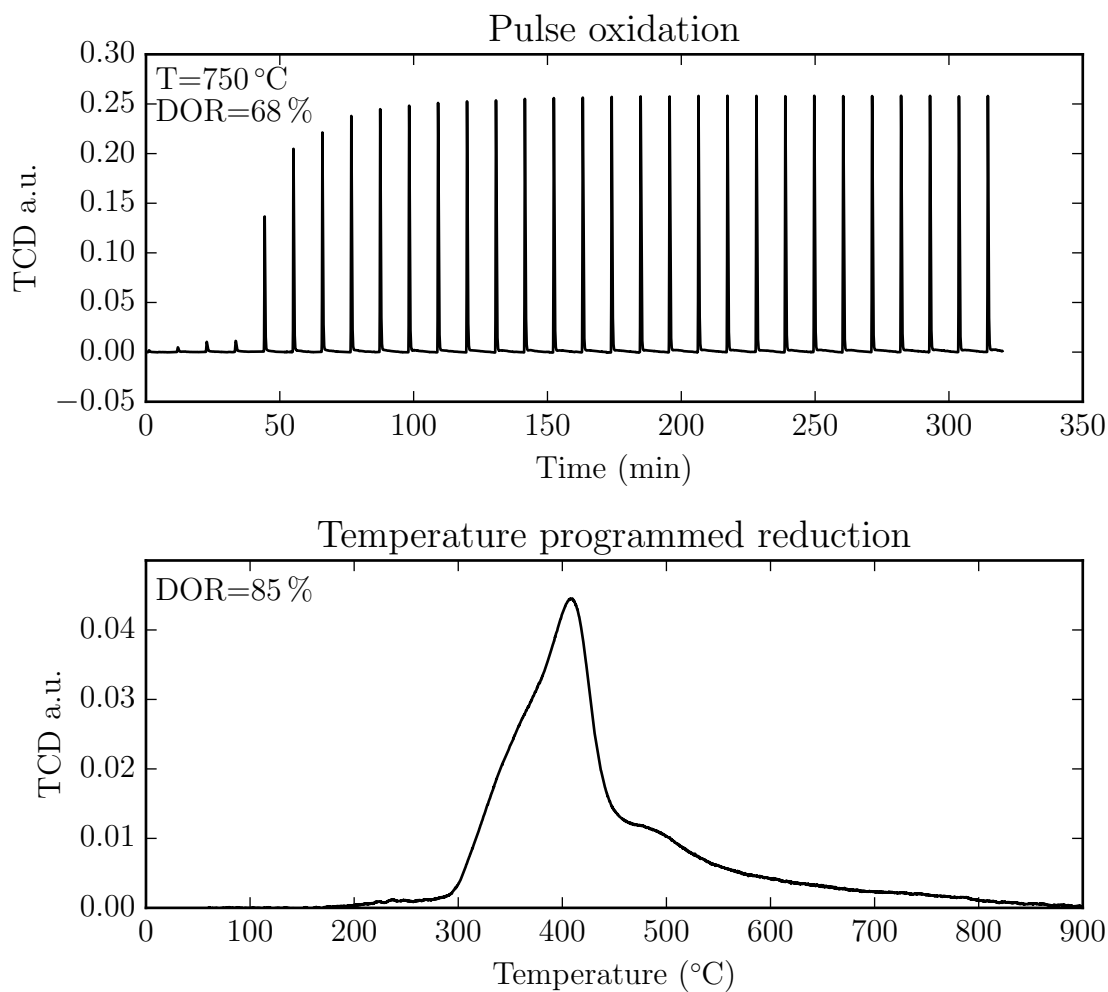


Figure C.1: Experimental results of oxygen titration experiments of catalyst 2.5Al300 after activation. After oxygen titration the reoxidized catalyst was reduced in a H_2 -TPR experiment in order to estimate the degree of reoxidation. The experiment showed that the catalyst was not completely reoxidised at 750°C .

Appendix D

Conditions and GC-analysis of Fischer-Tropsch experiments

Table D.1: Experimental conditions of GC-TCD analysis on Varian CP-4900

Channel	A	B
Detector	Thermal conductivity detector	Thermal conductivity detector
Column Type	Molsieve 5 Å, 20 m	PoraPlot Q, 10 m
Carrier gas	H ₂	H ₂
Temperature	80 °C	60 °C
Pressure	150 kPa	100 kPa
Duration	220 s	220 s
Analysed gases	Ar, CH ₄ , CO	CO ₂

Table D.2: Experimental conditions of GC-FID analysis on Varian CP-3800

Detector	Flame ionisation detector (FID)		
Detector temperature	200 °C		
Column	Varian Capillary Column CP-Sil 5CB, 25 m, 0.15 mm, 2 µm		
Column pressure	1.72 bar		
Flame gas	H ₂ at 30 ml/min		
Makeup gas	N ₂ at 25 ml/min		
Air flow	300 ml/min		
Coolant	CO ₂ , liquid		
Temperature programme:	Heating rate (°C/ min)	Temperature (°C)	Time (min)
	initial	-55	1.5
	10	0	8
	5	100	29
	2	120	40
	5	180	54
	5	200	61
	10	240	70
	20	310	83.5

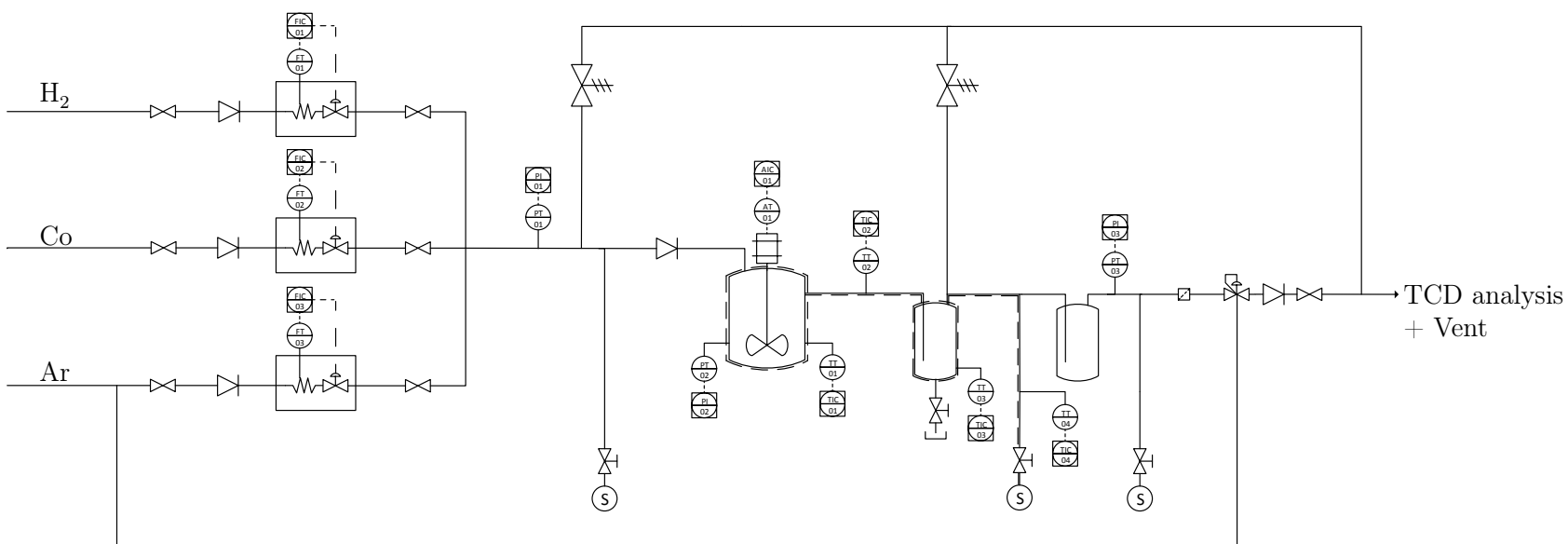


Figure D.1: Flow diagram of the slurry reactor used for the Fischer-Tropsch experiments.

Table D.3: Overview of activity and selectivity of the prepared catalysts for the Fischer-Tropsch synthesis.

w_{Al} (wt%)	$m_{cat,red}$ (g)	T (°C)	Ar (ml/min)	CO (ml/min)	H ₂ (ml/min)	X_{CO} (%)	S_{CH_4} (%)	C_{5+} (C%)	α_{4-7}	C_{1-4}^- (C%)	C_{1-4}^{Oxy} (C%)	n=1 C_n^{OH}/C_n	n=2 C_n^{OH}/C_n $C_n^{1=}/C_n$		n=3 C_n^{OH}/C_n $C_n^{1=}/C_n$		n=4 C_n^{OH}/C_n $C_n^{1=}/C_n$ C_n^Y/C_n $C_n^{2=}/C_n^{1=}$ $C_n^X/C_n^{1=}$				
0	2.69	220	50	50	100	10	19	62.6	0.717	24.4	2.7	1.5	7.0	33.6	3.3	63.6	2.0	52.0	15.1	7.4	29.0
		230	50	50	100	19	19	63.1	0.727	21.9	2.6	1.4	8.1	26.6	3.4	60.0	1.8	49.0	13.2	8.3	26.9
		240	50	50	100	28	23	58.1	0.719	18.9	2.3	1.2	7.0	28.4	2.9	53.4	1.8	42.5	10.7	12.0	25.2
		240	50	50	100	28	23	57.7	0.723	18.4	2.2	1.2	7.4	22.9	3.1	52.2	1.8	42.6	10.1	11.9	23.6
		220	35	35	70	14	21	58.7	0.714	22.8	2.7	1.4	7.3	29.3	3.4	59.1	2.0	48.1	14.9	9.4	31.0
0.1	1.72	220	50	50	100	15	12	75.4	0.733	23.1	3.1	1.0	13.5	21.7	3.9	60.3	2.1	35.3	13.9	52.1	39.3
		230	50	50	100	23	19	59.2	0.758	23.1	3.9	1.2	15.3	16.5	4.3	56.1	2.9	29.8	12.1	75.4	40.7
		240	50	50	100	29	27	49.1	0.770	19.8	2.6	0.9	10.4	17.1	3.2	54.5	1.8	33.8	9.0	42.3	26.5
		220	50	50	100	12	20	57.5	0.818	25.3	3.7	1.0	13.8	30.5	4.8	61.2	3.2	35.4	21.5	53.4	60.7
0.5	1.73	220	50	50	100	18	20	59.1	0.740	25.4	3.2	1.2	13.7	34.2	3.9	60.7	2.2	46.9	14.8	14.2	31.5
		230	50	50	100	26	21	57.8	0.767	23.9	2.6	1.1	9.8	28.3	3.2	60.3	2.0	48.3	9.3	9.1	19.3
		240	50	50	100	38	23	55.2	0.768	19.5	2.4	0.9	10.0	20.4	3.0	51.3	1.8	38.8	8.4	17.4	21.7
		220	50	50	100	16	17	62.9	0.759	27.4	2.8	1.1	9.1	40.1	3.5	62.9	2.1	51.5	13.3	6.3	25.8
2.5	2.19	220	50	50	100	32	1.0	97.6	0.737	29.0	2.4	1.2	8.2	28.7	2.6	62.6	1.8	51.0	3.8	7.7	7.5
		220	50	100	200	16	10	76.7	0.743	27.7	2.8	1.2	10.3	31.9	2.9	62.4	2.1	53.5	8.5	4.3	15.8
		230	50	100	200	17	13	72.8	0.752	22.8	2.7	1.3	10.2	26.1	2.8	55.2	2.2	46.3	8.3	8.5	18.0
		230	50	60	120	45	9	79.9	0.770	20.3	5.9	1.0	11.9	17.4	3.3	50.9	2.3	39.2	0.4	14.8	0.9
		230	100	100	200	19	12	73.8	0.706	25.2	2.7	1.2	11.2	17.8	2.7	59.0	1.7	49.4	7.9	7.8	16.0
		240	100	100	200	19	16	69.1	0.735	17.7	2.1	1.3	6.5	27.0	2.2	43.5	1.4	36.5	7.8	15.2	21.5
		240	50	50	100	30	16	68.1	0.702	14.7	1.3	1.4	2.1	15.8	1.0	37.5	0.4	29.9	0.1	21.1	0.5
220	50	50	100	13	15	68.7	0.733	19.4	2.4	1.4	8.5	22.6	2.4	46.5	1.6	38.6	7.8	10.2	20.3		

ANNA PAULA PETERSEN

born: Rio de Janeiro, Brazil, 27 March 1986
nationality: German, Brazilian
e-mail: a.p.petersen@gmx.net

EDUCATION

Ph.D. 2013-Present University of Cape Town, South Africa
Department of Chemical Engineering
Thesis: *Alumina-modified cobalt catalysts for the Fischer-Tropsch synthesis*
Advisors: Eric van Steen & Michael Claeys

M.Sc. 2009-2012 Utrecht University, The Netherlands
Nanomaterials Chemistry and Physics
Department of Inorganic Chemistry
Thesis: *Understanding the effect of iron oxide particle size on activity, selectivity and stability of carbon nanofiber supported Fischer-Tropsch to olefin catalysts*
Advisors: Hirsra M. Torres & Harry J. Bitter

B.Sc. Chemistry 2005-2008 University of Leipzig, Germany
Department of Technical Chemistry
Thesis: *Multifunctional coating materials based on hierarchical designed photo-catalysts*
Advisors: Roger Gläser

High School -2005 Heinrich-Heine Gymnasium, Munich, Germany
Specialisation in Chemistry and French

AWARDS AND SCHOLARSHIPS

2012-2017 Bursary · DST-NRF Centre of Excellence in Catalysis (c*change)

2016 CATSA International Student Travel Grant · Catalysis Society of South Africa (CATSA)

2015 Best Poster Presentation Award · Annual Conference of the Catalysis Society South Africa, Stellenbosch, South Africa

2015 Best Poster Presentation Award · Syngas Convention, Cape Town, South Africa

2014 Best Poster Presentation Award · Annual Conference of the Catalysis Society South Africa, Pretoria, South Africa

PUBLICATIONS

Catalysis Letters *Effect of alumina modification on the reducibility of Co₃O₄ crystallites studied on inverse-model catalysts* · accepted manuscript
Authors: Anna P. Petersen, Roy P. Forbes, Sandeeran Govender, Patricia J. Kooyman and Eric van Steen

in preparation *Effect of alumina modification of cobalt on the Fischer-Tropsch synthesis*
Authors: Anna P. Petersen, Roy P. Forbes, Sandeeran Govender, Patricia J. Kooyman, Michael Claeys, Eric van Steen

ORAL PRESENTATIONS

- 2016 Annual Conference of the Catalysis Society South Africa (CATSA), Drakensberg, South Africa
- 2016 DST-NRF Centre of Excellence in Catalysis (c*change) Workshop, Drakensberg, South Africa
- 2016 Natural Gas Conversion Symposium, Tromsø, Norway
- 2015 DST-NRF Centre of Excellence in Catalysis (c*change) Workshop, Stellenbosch, South Africa
- 2014 DST-NRF Centre of Excellence in Catalysis (c*change) Workshop, Pretoria, South Africa
- 2013 DST-NRF Centre of Excellence in Catalysis (c*change) Workshop, Port Edward, South Africa

POSTER PRESENTATIONS

- 2017 Faraday Discussions, Cape Town, South Africa
- 2015 Annual Conference of the Catalysis Society South Africa, Stellenbosch, South Africa
- 2015 Syngas Convention, Cape Town, South Africa
- 2014 Annual Conference of the Catalysis Society South Africa, Pretoria, South Africa
- 2014 5th IUPAC International Conference on Green Chemistry, Durban, South Africa
- 2013 Annual Conference of the Catalysis Society South Africa, Port Edward, South Africa
- 2013 2nd International Summer School Catalysis for Sustainability, Kerkrade, The Netherlands

July 11, 2018

A handwritten signature in blue ink, appearing to be 'P. W.' with a long horizontal stroke extending to the right.

*"Diga o que você pensa com esperança.
Pense no que você faz com fé.
Faça o que você deve fazer com amor!"*
Ana Carolina

*"Talk of what you think with hope.
Think of what you do with faith.
Do what you need to do with love!"*